UNIVERSITAT DE BARCELONA

Theoretical and experimental approaches for the initiation and propagation of activity in spatially embedded neuronal cultures

Lluís Hernandez Navarro

Theoretical and experimental approaches for the initiation and propagation of activity in spatially embedded neuronal cultures

Lluís Hernández Navarro

Advisor
Jordi Soriano Fradera

UNIVERSITAT DE
BARCELONA

Estudis teòrics i experimentals sobre la iniciació i propagació d'activitat en cultius neuronals amb restriccions espacials

Lluís Hernández Navarro

Director

Jordi Soriano Fradera

Tutor

Jaume Casademunt Viader

Programa de Doctorat en Física

Facultat de Física

February 2018

Als meus pares i al meu germà.

“ Caminante, no hay camino, se hace camino al andar."

Antonio Machado

Acknowledgements

First of all, I would like to thank my advisor Jordi Soriano for his guidance and constant support during the whole, long process of creation of this PhD thesis. I would like to thank Antoni Planes for his tutoring along the first three years of my PhD, as well as Jaume Casademunt for being my tutor in the last year.

Also, I would like to thank Javier G. Orlandi for his collaboration, help and advice in the study of metric effects on neuronal cultures, as well as thank Tanguy Fardet for giving his permission to reproduce his work in simulated patterned cultures in one of the figures of this thesis.

Per altra banda, segurament aquesta tesis s'hauria quedat en molt menys sense l'ajuda, els ànims, la companyia i l'amistat de les meves companyes, companys i excompanys de laboratori. Moltes gràcies Sara per la teva paciència els primers dies que estava aprenent el funcionament del laboratori, i també pel teu recolzament i per ajudar-me quan no tenia ànims per tirar la tesis endavant, ja sigui per temes personals o professionals. Gràcies per les interessantíssimes converses sobre literatura de ciència ficció, idees, filosofia i, en general, passió per la ciència. I també (no ens n'oblidem) per la publicitat que em vas fer al final dels teus encontres amb el tercer cicle, amb aquella foto meva tan formal XDDD. Ah, i espero algun dia poder organitzar-me i venir a alguna actuació teva de ball!!! ^^. Per suposadíssim: moltes gràcies a tu també, Elisenda, per aquests primers tres o quatre anys de convivència al laboratori, per tots els ànims i moltíssims consells que em vas donar tot aquest temps, i per les converses sobre hobbies comuns (com ara les excursions i el

futbol), que demostraven que existeix vida fora del laboratori, i que aquesta pot ser un (o "el") gran motiu per tirar endavant dia a dia. Perdona les segades i faltes que t'hagi pogut fer en els partits de futbol setmanal XDDD i espero que coincidim sovint, a veure si al final m'apunto al teu grup excursionista :). Et trobem a faltar al laboratori, doctora! Però ens alegrem de que estiguis fent una feina que t'apassiona, i de que segurament hagis trobat la teva vocació ^^. Por supuestísimo también: muchísimas gracias Espef(i) XD por aguantarme este último año y medio, y por ser la persona que me salvó de la soledad en el laboratorio cuando sólo yo lo usaba como despacho :). Por compartir las penas y frustraciones de laboratorio, por todas las veces que me has ayudado con las pequeñas dudas q nos consultamos, y por las mini clases de técnicas de canto y las anécdotas sobre Acu :D. Sobretodo siento que no hayamos tenido más tiempo para conocernos aún más antes de que me fuera, pero esto no es una despedida! Os seguiré haciendo visitas de tanto en tanto :). També vull agrair l'ajuda i companyia a en Marc Montalà (fes tanta companyia com puguis a l'Estef, que se'ns queda sola al lab! XD), and also I would like to thank Adrian for our conversations (either go–related or not XD), així com a en Dani, Marc Duque, Ana, Gemma, i tanta altra gent de biofísica que no sóc capaç d'enumerar.

Moltíssimes gràcies a tots els amics de planta 7 de la facultat, amb qui he viscut tantíssims dinars i berenars, 'fireflys', sopars temàtics, calçotades, algunes excursions, aniversaris, viatges per recargar bateries, etc. :DDDDD tant a tots els qui ja s'han anat, com aquells que encara hi sou. Sou tants que la tesis s'hauria d'escriure en *un parell* de volums XD. Gràcies Dani del Ser, per tots els anys i anys d'experiències compartides, tant a dins com a fora de la universitat :DD, A ti Nico por tu amistad y tus consejos para ser un buen italiano :D, a Núria (i Núries XD) per ser la nostra hater oficial ;P, a la iaia Casamiquela XP, a l'Edgar per votar a gent amb dos dits de front XD, a l'Alfred tantes gràcies com a s'amo Pep de sa sínia XDD, Dani Pacheco, Jose, Roger, Ignasi, Víctor, etc etc etc. Gràcies a tots, perdoneu per tots els

noms que m'he deixat (sóc un despiste, ja em coneixeu XD), i espero que ens seguim veient! I feu un ús responsable del calçador!!! XDD

També vull agrair a la resta de gent de la facultat, com els companys de carrera amb qui hem coincidit durant el doctorat (Albert, Carambola, Cucco, Frede...), als companys de màster (Joan, Xavi, Albert, Ricard...), als companys dels partits de futbol setmanal que tant m'ha ajudat a desestressar-me (Julià, Lluís, Alex, Martí...), als col·legues organitzadors de les JIPI, i a tota la gent de la coral de física *Cor–Iolis*!

Com no pot ser d'una altra manera, aquesta tesis li deu molt al Rashevsky club, altrament dit EPSJC (shhh!!!), per tota la inspiració, discussió teòrica i bàsicament motivació XD. I especialment al seu formal president, Jordi Piñero (P.D.: praise Tong!).

Tampoc em puc oblidar de tots els amics de fora de l'àmbit acadèmic, sense el suport dels quals definitivament no hauria pogut fer la tesis :), i que difícilment podria mencionar en un sol paràgraf, ni enmumerar totes les experiències que hem viscut junts en aquests anys de doctorat :DDD. Moltes gràcies a tots!!! Octavi i Víctor; Manu; Alex Ace^{TM} (XD); tots vosaltres 'I–mans'; Jose, Jenny, Alba, Brian, Dani, Desis, Xusep, Anna...; els Mairenos; i un molt llarg etcètera. I igualment voldria agrair a aquells amics amb els qui vaig perdre el contacte fa temps, però que en part també m'han ajudat a arribar fins aquí.

Finalment, mai podria arribar a expressar tot l'agraïment que sento per la meva família, que m'ho ha donat tot i a qui dec tot el que sóc :). Amb una menció especial pel meu germà (sí, tu també Sergi ;P, dueeeneduene...duonoduón, ajajaj salu2). Y por último, muchas gracias a ti, mi amor, porque sin tu apoyo, tu inquebrantable confianza en mí, y tu cariño, los frutos de mi esfuerzo nunca habrían llegado a tanto.

Ha estat un grandíssim plaer i honor compartir aquests anys amb tots vosaltres :).

Table of contents

Chapter 1

Introduction

1.1 Conceptual framework

The brain might be the most complex system known to mankind, able to receive and store exceptional amounts of coded information, retrieve and modify it with great adaptability, and process it to finally generate actions and thoughts (Ornstein and Thompson, 1991). Unveiling the fundamental mechanisms that allow our Central Nervous System (CNS) to perform such sophisticated functions is an extraordinarily defying challenge. The difficulty of this task may be epitomized by the famous quote: *"If the human brain were so simple that we could understand it, we would be so simple that we couldn't"*, by the physicist Emerson M. Pugh (1938).[1]

The human brain is composed of 10^{11} neurons and 10^{14} synapses between cell pairs (Pakkenberg et al., 2003), which form the *neuronal circuitry*, based

[1]The quote highlights that the complete information of a structure (such as exact cell locations and type, connected cell pairs, or dynamic single–cell states in our case) cannot be stored and codified in the same structure, or in another of lower capacity. However, a less–demanding approach relying on abstraction and theoretical description, without the need for explicit information, may suffice to "understand" the brain. That is, in the same sense as *Thermodynamics* and *Statistical Physics* describe the behavior of billions and billions and billions of particles without the specific individual information for each of them.

on the propagation of electric signals and chemical interactions. The organization of the brain provides not only a high and complex interconnectivity, but also an extremely wide range of sustained dynamical states; either at a single–neuron microscale, at a scale of tens of neurons, at populations in the mesoscale, or at a macroscopic extent, and for a a wide spectrum of timescales. The vast dynamic spectrum emerges as a collective phenomena of interacting communities, which is thought to be the cornerstone of brain's huge computational capacity, since slow single–neuron dynamics alone cannot account for the fast processing of information in the CNS (Von Neumann, 2012; Yuste, 2015).

The first measurements of activity of neuronal populations in the brain, which started around the 30's of the past century (Fox and Raichle, 2007), changed the former concept of the neuron as the fundamental computing element. Else, neuronal assemblies emerged as the main ingredient for information processing through the complex, non–linear interaction of its constituting parts.

One of the main cerebral regions that excels in computational power is the cortex. It holds $\sim 80\%$ of all brain mass (Herculano-Houzel, 2009) and presents a particularly wide dynamical spectrum (Buzsáki and Draguhn, 2004; Honey et al., 2007). As illustrated in Fig. 1.1, the cortex exhibits a highly organized anisotropic structure, where mini–columns, of $\sim 50\ \mu m$ in diameter and composed of ~ 100 neurons, are considered its minimum functional elements (de Lorente, 1933; DeFelipe et al., 2012; Mountcastle, 1998). Indeed, the cortex displays strikingly different functional properties between areas separated no more than $\sim 100\ \mu m$ in the horizontal plane, while those features are kept constant in the vertical direction (Mountcastle, 1978). In turn, cellular minicolumns tend to connect laterally into dense, afferent macrocolumns of $\sim 300\ \mu m$ in diameter, forming microcircuits of high functional specialization, often called *modules*, and that can be found iteratively within each area of the cortex.

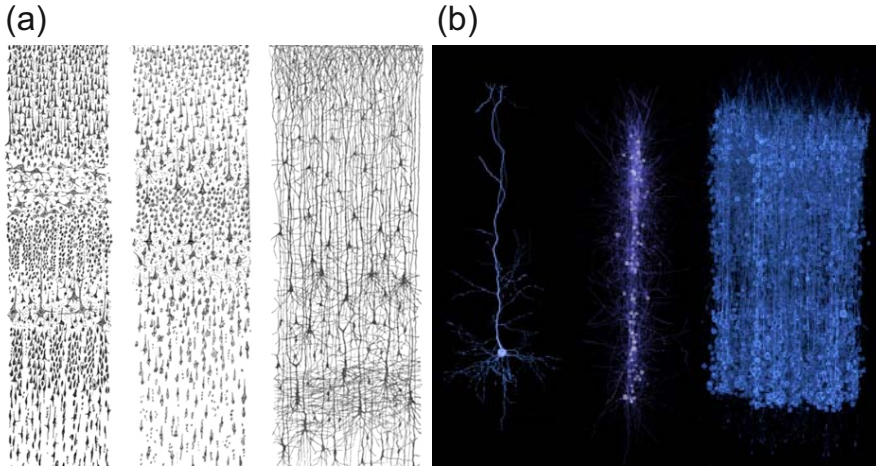

Fig. 1.1 Culture preparation. (a) Sketch of the structure of cortical columns in the brain. Drawing by Ramon y Cajal (1899). **(b)** Single neuron (left), mini-column (middle), and macrocolumn (right) in cortical circuitry.

In order to understand the mechanisms governing the brain, two main strategies have been developed. The first one (top–down approach) focuses on the macroscopic study of the CNS, starting from behavioral studies and/or large–scale activity recordings to understand and identify the contribution of smaller subsets. The second strategy (bottom–up approach) relies on the extensive knowledge at the single–neuron level, and on the study of gradually larger ensembles of neurons to assess the emergence of collective phenomena, most notably spontaneous activity, at the mesoscale. This thesis is grounded on this bottom–up approach, and is presented in the context of *cortical neuronal cultures*.

1.2 Cortical neuronal cultures

As a Neurophysics thesis, this work is grounded on the biological characteristics of the neurons, always taking into account this framework and its implications in the study, but without getting lost in the biochemical complexity of the cells. Often, generalizations are needed, approximations are used,

and simplifications are performed in order to extract the essential foundations of the non–trivial collective activity of neuronal populations.

Cortical neuronal cultures are a valuable tool to study living neuronal circuits in a controlled manner, with much better accessibility than in the brain, a feasible closed number of elements to study ($10^1 - 10^6$ cells), low–cost, and a high reproducibility. Although the *in vivo* complex connectivity circuitry of the mature cortex —coarsely shaped through genetic cues and refined through experience— is lost in *in vitro* preparations, neuronal phenotypes and sensing capabilities are preserved (Kriegstein and Dichter, 1983). This maintenance of the fundamental building blocks facilitates that spontaneous dynamics in neuronal cultures resembles the one of the neuronal circuits in the brain (Mazzoni et al., 2007). Therefore, cortical neuronal cultures are an adequate platform —despite structural simplicity— to investigate the basis of universal phenomena in neuronal systems, in particular the emergence of collective activity and its spatio–temporal characteristics.

The use of cortical cultures is widespread, as asserted by the large amount of works published in this field. For example, some research groups investigaged the self–organization potential of neuronal cultures during development (Soriano et al., 2008), as well as the emergence and overall features of spontaneous activity (Orlandi et al., 2013; Pasquale et al., 2008). Plasticity was an additional feature investigated (Turrigiano and Nelson, 2004; Van Pelt et al., 2004). Others studies treated synchronized activity (Baruchi et al., 2008) and oscillations (Czarnecki et al., 2012); while some others analyzed the cultures under percolative approaches (Breskin et al., 2006; Cohen et al., 2010; Soriano et al., 2008). On the other hand, criticality in neuronal networks was also explored through cortical cultures (Tetzlaff et al., 2010), which also served as interesting platforms to prospect new ideas in network theory (Teller et al., 2014). Another contribution of cultures was the optimization of network reconstruction algorithms that used neuronal activity to infer the real, ground truth connectivity blueprint (Orlandi et al., 2014; Stetter et al., 2012). The

in vitro networks also served as a valuable tool to study neuronal diseases in a simplified environment, as in the case of Alzheimer's disease (Huang and Mucke, 2012; Teller et al., 2015). And finally, cultures proved also useful for drug toxicity tests (Frega et al., 2012).

Two cultures types have been interrogated to address different features in an optimal way. A first kind, namely *aggregated cultures* or *clustered cultures*, presents the spontaneous self–assembly of multiple clumps of cells constituted by hundreds of neurons, i.e. *neurospheres* or *clusters*, that are interconnect by bundles of axons and dendrites, i.e. *neurites*, specifically called *axonal highways*. The diameter of those neurospheres in typical two–dimensional cultures is on the order of $\sim 100\mu m$, and their formation is governed by neurites' pulling forces, which are strong enough to overcome neuronal adhesion to the substrate (Segev et al., 2003). The morphology of these cultures allow for the study of their spontaneous assembly (Shefi et al., 2002), which is conceptually similar to the high modularity in the cortex. Furthermore, their activity is also modular, and its study provides a better insight in the dynamic repertoire that neuronal populations are capable of (Shein Idelson et al., 2010; Tsai and Chang, 2008; Yvon et al., 2005).

The second kind of interrogated cultures are the *homogeneous cultures*, which consist of networks of homogeneously distributed neurons on a substrate (Cohen et al., 2008; Orlandi et al., 2013; Tibau et al., 2013b), and that are the main focus of this thesis. Homogeneous cultures are particularly useful for assessing the initiation and propagation of spontaneous activity in neuronal networks, since they provide a simple neuronal model where single–cell activity can be isolated and investigated, unlike in the neurospheres case of clustered cultures. Although this thesis concentrates in activity and connectivity in this homogeneous cultures, they have also been used in other contexts, such as the study of plasticity (Madhavan et al., 2006, 2007; Turrigiano and Nelson, 2004), or the study of age–dependend dynamical patterns (Van Pelt et al., 2004; Wagenaar et al., 2006).

1.3 Spontaneous activity in homogeneous cortical cultures

In homogeneous cultures, neurons' individual activity is usually presented as a short series of concatenated action potentials, i.e. *a train of spikes* or *burst*. Eventually, the interaction of those individual bursts might evoke a quasi–synchronous activation of the whole culture in the form of a spontaneous *network burst* (Kamioka et al., 1996; Wagenaar et al., 2006), a phenomenon that has also been observed in the hippocampus (Mazzoni et al., 2007), the spinal cord (Streit et al., 2001), or the retina (Harris et al., 2002). The exact mechanisms underlying network burst' initiation, and that dictates the subsequent propagation of activity, are still an open research field, within which falls the aim of this thesis.

1.3.1 Initiation of spontaneous activity

Although a detailed, complete theoretical framework of the initiation of network bursts has not been yet developed, it is known that spontaneous collective phenomena are grounded on synaptic interactions, since the blockage of excitatory currents totally suppresses them (Robinson et al., 1993). Even at a single–neuron level, it seems that the spontaneous activation of individual cells is prevented at similar blocking conditions (Cohen et al., 2008; Serra et al., 2010). Indeed, individual activations apparently arise from *synaptic noise*, mainly in the form of spontaneous release of neurotransmitters in input neurons, that generates miniature post–synaptic currents (Otsu and Murphy, 2003; Serra et al., 2010), and whose magnitude is comparable to that of evoked currents (Ivenshitz and Segal, 2010).

The difficulty for uncovering the mechanisms that shape spontaneous activity is reflected in the number of models and explanations that have been proposed along the last 15 years. These models were grounded on experimental observations, which made even more difficult the elaboration of

a unified view. A first of group of models suggested the existence of network burst initiation areas that are formed during development (Feinerman et al., 2007; Lonardoni et al., 2017). A second group proposed some sort of neuronal population interactions that triggered network activity (Eytan and Marom, 2006; Segev et al., 2004). A third group suggested the formation of functional hubs that elicited network bursts (Sun et al., 2010). A fourth one introduced the presence of subnetworks of *leader neurons*, some sort of specialized neurons that orchestrate activity, and that shape the initiation of collective bursts (Eckmann et al., 2008, 2010; Ham et al., 2008). Finally, a fifth group came up with the idea of a *noise–focusing scenario*, which suggests that synaptic neuronal noise, and subsequent spontaneous activations, become amplified through inherent connectivity topological traits and dynamical nucleation, routing activity towards foci of attraction where network bursts are finally triggered (Orlandi et al., 2013).

The attractiveness of the noise–focusing scenario is that it rules out the need of *ad hoc* ingredients such as leader neurons. Noise–focusing just assumes that there is sufficient noise and connectivity–amplification features for spontaneous activity to initiate. Interestingly, these connectivity features emerge naturally in the form of connectivity correlations among neurons during development. As we will elaborate later, spatial embedding and metric–inherited correlations play a pivotal role in shaping these connectivity features.

1.3.2 Structure of propagating activity fronts

Independently of the actual initiation mechanisms that shape the emergence of network bursts, their propagation has been extensively investigated. In order to assess this kind of collective activity, simultaneous recordings of multiple neurons were necessary, although some groups were able to assess activity patterns by monitoring one neuron at a time (Habets et al., 1987). Thus, the first results were obtained in simultaneous recordings of $2-3$

neurons, e.g. as in (Dichter, 1978). Afterwards, and through the improvement of various techniques, the total number of monitored neurons substantially increased (Ogura et al., 1987), and with techniques that were expanded and consolidated years later (Murphy et al., 1992).

It was then when Robinson et al. (1993) confidently reported the presence of whole–culture quasi–synchronized bursts and the existence of activity propagation fronts, with apparently random onset locations for each network burst. However, other posterior studies concentrated on full–synchronization approaches (Opitz et al., 2002; Segev et al., 2004; Wagenaar et al., 2006), disregarding the suggested propagation profile, since their setups focused on a more local scale. We remark that a large–scale propagation event may be wrongly assessed as simultaneous activations for insufficient spatio–temporal resolution.

Major steps towards the quantitative description of networks bursts' propagation were performed on simple, one–dimensional homogeneous neuronal cultures, and whose length was much larger than the average extension of axons ~ 1 *mm* (Eckmann et al., 2007; Feinerman and Moses, 2003). In this experimental condition, fast neuronal propagations of activity of ~ 80 mm/s were preceded by a slow recruitment (~ 20 mm/s) of asynchronous activations. It has been suggested that the two former velocities basically depended on the excitation–inhibition balance in the network, strength of connections, and synaptic depression (Alvarez-Lacalle and Moses, 2009). Moreover, the initiation of network bursts took place in highly specific (and usually dense) locations of the culture, which were therefore labeled as *bursts initiation zones* (Feinerman et al., 2005, 2007).

The experiments presented and analyzed in this thesis are grounded on neuronal cultures grown on two–dimensional substrates, as is the aforementioned work of Robinson et al. (1993). When characterizing avalanches of activity in these large cortical cultures ($\phi \geq 3$ mm), one realizes that network bursts are activity fronts that nucleate on specific finite areas (~ 0.3 mm^2), and then prop-

agate to encompass the whole neuronal network at $v \sim 10 - 100$ mm/s (Orlandi et al., 2013). In homogeneous cultures, this propagation is usually observed as a circular front that activates the entire system in a short time window (Maeda et al., 1995; Orlandi et al., 2013), although some studies alleged that temporal activations are power–law distributed and with complex spatio–temporal structure (Mazzoni et al., 2007; Okujeni et al., 2017; Pasquale et al., 2008; Pu et al., 2013; Tetzlaff et al., 2010).

1.4 Connectivity

Substantial efforts have been devoted to study the connectivity blueprint of neuronal networks, i.e. their *connectome*. However, it is generally assumed that the information of the complete structure of the network does not suffice to properly characterize neuronal activity. Another crucial element is the dynamics of the system. Neuronal activity, together with noise, and the interplay of these elements throughout the structure of the network, may dictate not only the dynamic behavior of cortical cultures and cortical slices *in vitro*, but also the cortex or the whole CNS *in vivo*. The physical wiring of the neuronal circuit is bast and the flow of activity through it do not necessarily explore all possible paths. Therefore, it is necessary to discern between *structural* and *functional* connectivity, where the latter reflects the flow of information during activity. Both connectivities are not independent and may influence one another, for instance due to plasticity.

1.4.1 Structural connectivity

The structural connectivity of a neuronal network is directly related with the architecture that arises from axons and dendrites. It is the exact map of physical connexions between all cell–pairs, with an specific excitatory (inhibitory) action and particular strength (Abbott and Nelson, 2000).

One of the first, major successes in the study of the structural connectivity in neuronal networks was the entire reconstruction of the nervous system of a nematode, the *Caenorhabditis elegans*, with exactly 302 neurons and ~ 5000 connections between them (Varshney et al., 2011; White et al., 1986). Two decades later, the structure of a cortical column was completely characterized in the context of the *Blue Brain Project* (Markram, 2006). And in the present decade, the USA's *BRAIN initiative* (Insel et al., 2013) and the European *Human Brain Project* (Markram, 2012) aimed to boost neuroscience in the development of techniques and the detailed characterization and simulation of gradually larger regions of the human brain.

In this context, dissociated cortical cultures emerge as a very appealing platform to study structural connectivity. Their manipulability and accessibility allow for a detailed characterization of topological traits, and even provide the possibility to tune neuronal wiring to some extent (Wheeler and Brewer, 2010). The latter is achieved in the context of *patterned cultures*, where a heterogeneous substrate induces a heterogeneous connectivity with rich resulting dynamical patterns. The heterogeneity may be chemical (Macis et al., 2007; Sorkin et al., 2006) or physical (Baruchi et al., 2008; Gabay et al., 2005; Tibau et al., 2013a), but independently of the employed methods, the main goal of patterned cultures is to investigate the relation between the dictated connectivity and subsequent dynamics (Eckmann et al., 2007).

1.4.2 Functional connectivity: topology–function interplay

As previously mentioned, the relation between neuronal wiring structure and the corresponding dynamics is not straightforward. On the one hand, single neurons present themselves sophisticated, non–linear dynamics (Brunel et al., 2014). On the other, their interaction generates emergent phenomena where the collective system presents a greater complexity than the sum of its parts. For example, a fixed connectivity structure of a neuronal population provides a wide spectrum of sustained dynamical states (Battaglia et al., 2012; Deco

and Jirsa, 2012), i.e. *functional multiplicity*; whereas similar dynamic regimes may arise from strikingly different structural blueprints (Stetter et al., 2012), i.e. *structural degeneracy*. Accordingly, one has to discern between the structural connectivity and the so–called *functional connectivity*.

The *functional connectivity* is the connectivity defined by means of statistical relations in activity between nodes (either single–cells, network modules, neuronal populations, or macroscopic brain regions) (Friston, 2011). When further assumptions are made, and causal relationships are inferred, the resulting network wiring is called *effective connectivity* (Friston, 2011).

Extractions of macroscopic functional networks in the brain have been performed through a wide variety of activity imaging techniques. For instance, neuronal activity have been positively correlated with blood flow, and then inferred by means of *functional magnetic resonance imaging* (fMRI) (Cordes et al., 2000; Deco et al., 2011; Van Den Heuvel and Pol, 2010). Another possible procedure is the use of extremely sensitive instruments to record the electric and magnetic fields resulting from neuronal currents in the brain, i.e. *electroencephalography* (EEG) and *magnetoencephalography* (MEG) respectively, and whose application in the study of functional connectivity is reviewed in Sakkalis (2011). And a third approach could be *calcium imaging*, a technique that monitors neuronal activity in terms of the intracellular calcium concentration (Gobel and Helmchen, 2007; Smetters et al., 1999), able to record activity *in vivo* at single–cell resolution, as performed for instance in the whole brain of the larval zebrafish (Ahrens et al., 2013). In calcium imaging, single–cell internal Ca^{+2} concentration is measured by means of fluorescent probes, which can be either chemical calcium indicators (Paredes et al., 2008), or genetically encoded calcium indicators (GECIs) (Kotlikoff, 2007).

Regarding neuronal cultures, and provided their attractiveness for neuronal network researches, two main techniques have become central in the study and inference of cultures' functional connectivity. *Multi–electrode arrays*

(MEAs) consist of large ensembles of electrodes (from tens to thousands) that directly record changes in the membrane potential of neurons, with an inter–electrode spacing of typically $\sim 10\ \mu$m. They are extensively used in neuronal cultures due to their high temporal resolution and good spatial accuracy (after proper *spike sorting* to identify single–neuron contributions) (Bettencourt et al., 2007; Ito et al., 2014; Maccione et al., 2012). The second technique consist of the aforementioned *calcium imaging* applied at the culture level, with a superior spatial resolution and sufficient temporal sensitivity to infer functional and effective connectivity (Lütcke et al., 2013; Tibau et al., 2013b; Wrosch et al., 2017).

1.5 Spatial embedding and metrics

The architecture of the mammalian brain combines two– and three–dimensional circuits in a complexly embedded three–dimensional space. This spatial embedding certainly constrains the layout of network connectivity, either by guiding connections or by restraining them, and plays a pivotal role in shaping brain function and computational power (Horvát et al., 2016). Additionally, the kilometers of brain wiring have a substantial energetic cost, and therefore evolution has sought for strategies to minimize it while preserving flexible function. The difficulty for understanding the influence of spatial embedding in neuronal networks *modus operandi* has brought this aspect to the front–line of modern neuroscience research.

Indeed, the functionality of the brain, and particularly the cortex, seems to be linked to a *segregation–integration* balance in neuronal circuitry (Stam, 2014; Tononi et al., 1994, 1998). Apparently, simple functions are localized in specific regions of the cortex (Hubel and Wiesel, 1968), while more complex processes require contributions from multiple, distinct areas (Luria, 2012). This provides a hierarchical network (Hilgetag et al., 2000) with a *small–world* blueprint (Watts et al., 1998), where local connectivity is enhanced while long

distance connections become bounded and optimized, i.e. high *clustering* and short *path lengths* (Achard et al., 2006; Hagmann et al., 2008; Meunier et al., 2010; Sporns and Zwi, 2004). Moreover, brain networks present distribution of connections close to a scale–free scenario (Eguiluz et al., 2005) with an efficient information flow via highly connected hubs (Sporns, 2013).

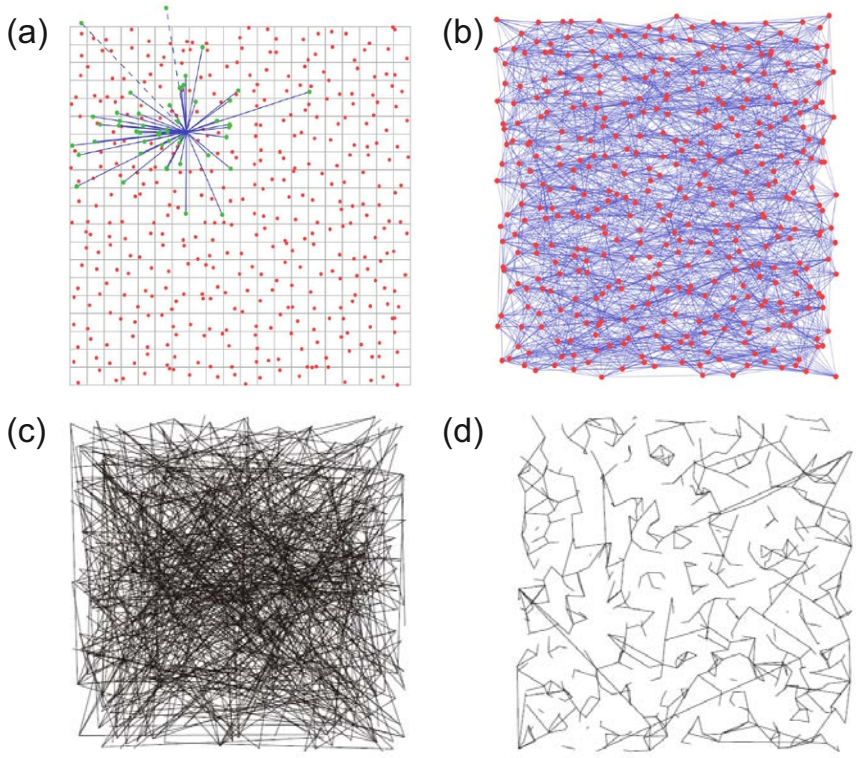

Fig. 1.2 Spatial networks. **(a)-(b)**, The left plot illustrates the neighborhood of possible candidates for a neuron to connect to. Targets are drawn from a probability distribution that favors short–range connections, but some long–range connections are still possible. The right plot shows the final network. Adapted from Cahalane et al. (2011). **(c)-(d)**, Examples of spatial networks where the connectivity probability is a function of the euclidean distance between nodes, which scales as a power law with exponent $-\alpha$. The left plot corresponds to $\alpha = 0$, and the right one to $\alpha = 10$. Adapted from Schmeltzer et al. (2014).

The previous networks might be naturally constructed under an optimization of wiring costs (Chen et al., 2006; Chklovskii et al., 2002; Horvát et al.,

2016), that would finally shape the topology–function interplay in terms of an accurate balance between local and global connectivity. Cortical cultures help understand the natural rules that modulate this cost–efficiency compensation at a smaller scale, where metrics dictates a distance–dependent probability of connection between single neurons, as illustrated in Fig. 1.2a–b. In this *in vitro* framework, genes do not regulate major connectivity pathways, as opposed to what is observed in the brain (Paul et al., 2007). However, neuronal morphology still provides a specifically bounded connectivity, yet governed by general trends, that give rise to the observed multiple activity dynamics in cultures.

Modeling spatial networks is a challenging task. In many studies, the connection probability between two nodes (i, j) of a random network is given by a function of the euclidean distance l between them, $f(l_{ij})$, which is often chosen to be a power law $f(l_{ij}) \sim l_{ij}^{-\alpha}$ (Schmeltzer et al., 2014). This choice is particularly attractive from a neuroscience perspective since the probability for two neurons to connect rapidly decays with their physical separation. As illustrated in Fig. 1.2c–d, for $\alpha = 0$ the network is random (Erdös–Rény graph), but for $\alpha > 1$ or higher the network is gradually more local. In addition to the metric constraints, spatial embedding could alter degree–degree correlations. A prominent example of such correlations is assortativity (Teller et al., 2014), which describes networks in which nodes preferably attach to other nodes with similar degree. Assortativity is believed to play an important role in brain networks since it may provide a subnetwork of highly connected nodes where information flow can be reorganized in case of damage.

1.6 Outlook of the present thesis

Spatial embedding and inherited metric constraints are a fundamental trait of biological neuronal circuits. However their role in shaping connectivity

and dynamics has been often disregarded, with models of neuronal networks paying much more attention to the distribution of connections in the quest for understanding network's behavior. In this thesis we aim at filling this gap by studying the importance of metric features in the complex connectivity–dynamics–noise interplay that shapes spontaneous neuronal activity.

Thus, the main goals of this thesis is to assess the importance of metric correlations in dissociated cortical cultures. Given the relevance of spatial embedding, we want to move a step further towards its understanding by developing a new theoretical model grounded on Ising Models (Dorogovtsev et al., 2002; Hopfield, 1982; Schneidman et al., 2006) to assess metric effects in neuronal cultures' behavior, and in the context of percolation approaches (Breskin et al., 2006; Cohen et al., 2010; Soriano et al., 2008). Once metric effects are settled, we illustrate their relevance in shaping spontaneous activity by perturbing the structural connectivity blueprint of neuronal cultures. This is achieved by patterning the substrate where neurons grow, and by using topographical molds that dictate the connectivity of the network. Next, and since the initiation of bursting activity is governed in great manner by a complex amplification mechanism that involves metric correlations and noise, we focus on the metric–driven amplification of spontaneous single–neuron noise to derive an analytical model that predicts the frequency of bursting events in neuronal cultures. We then further investigate in an experimental context the contribution of noise to the observed activity patterns, and through a moderate electrical stimulation that increases the level of activity noise in cultures. Finally, the latter study is completed with experiments regarding the specific role of inhibition in neuronal networks, in order to provide a wider understanding in the mechanisms that govern the initiation and propagation of activity fronts in cortical cultures.

Chapter 2

Experimental Setup and Procedure

Neuronal cultures are the simplest experimental system of real, living neuronal networks that show collective phenomena, prominently in the form of spontaneous avalanches of neuronal activity, and that is shaped from the interaction among interconnected cells. Although spontaneous activity is a primordial feature of the Human Brain (Deco et al., 2011), it is a truly universal feature that has been observed in all living neuronal assemblies.

The fact that a neuronal culture is a closed, highly controllable and manipulable system, allows experimentalists to reliably extract information of its functional and even structural connectivity traits. Additionally, the behavior of neuronal cultures can be also perturbed, by electrical, chemical or other means, to monitor its response and analyze properties such as resilience to damage. In the framework of bottom–up approaches in Neuroscience, the understanding of the complex, collective activity that arises in neuronal cultures is the first step to understand Brain's activity and its functioning.

In this Chapter we describe the experiments that establish the foundation of this thesis. We will present and discuss the different experimental tools,

strategies and procedures that were carried out to prepare and monitor primary cortical cultures.

2.1 Cultures

All the neuronal cultures were prepared, maintained and monitored at Porf. Jordi Soriano's NeuroPhysics Lab, at the Faculty of Physics of the University of Barcelona.

This thesis essentially deals with a particular kind of neuronal cultures known as *homogeneous cultures*, in which neurons cover uniformly (although with some fluctuations) the substrate where they sit. The protocols for the preparation of these cultures are detailed in Breskin et al. (2006); Cohen et al. (2010); Soriano et al. (2008) and summarized below. These homogeneous cultures contrast with the *clustered* ones, in which neurons tend to concentrate in highly–dense aggregates (or *clusters*) connected among them. This kind of cultures will be sporadically covered along the thesis. The protocols for their preparation were developed by Prof. Jordi Soriano and Dr. Sara Teller, and are detailed in Teller et al. (2014).

All the experimental procedures were approved by the Ethical Committee for Animal Experimentation of the University of Barcelona in 2010, under order DMAH-5461, and were revised and updated periodically in accordance to the regulations of the Generalitat de Catalunya and the European Commission.

2.1.1 Culture preparation

In our laboratory, we used neurons extracted from the cortical tissue of dissected Sprague–Dawley rat embryos at $18-19$ days of development. We typically prepared 24 cultures each week, and cultured them for a period of $2-3$ weeks.

The choice of cortical neurons obeys two reasons. On the one hand, embryonic cortices are one of the most accessible brain regions during dissection

due to their peripheral location and large size. On the other, cortical neurons mainly present a combination of two neuronal cell types: excitatory, pyramidal neurons (≈75-80%) and inhibitory interneurons (≈15-20%). This last feature ensures reproducibility in the experiments since identically–prepared cultures robustly maintain the same ratio of cell types (Soriano et al., 2008).

The justification for using embryonic instead of adult brains is two–fold. First, neurons in the perinatal period (or *neuroblasts*) are still able to divide and proliferate, therefore increasing the survival of the cultures. Second, neuroblasts' axons and dendrites (also called *neurites*) are not extensively developed in embryonic brains and thus neurons can be dissociated by gentle mechanical pipetting. This procedure contrasts with the aggressive rupture of connections through chemical action such as trypsin application, as required in maturer brains (Chen et al., 2008; Choi et al., 1987; Walicke et al., 1986).

Rats were bred at the animal farm of the Faculty of Pharmacy of the University of Barcelona. Pregnant rats were deceased with CO_2 at the same facility, and then transported to Soriano's lab to perform the dissection in the oxygen rich, ice–cold L–15 medium, which preserves the health of the neurons. This process was carried out as fast as possible in order to ultimately avoid tissue deterioration and neuronal death. The extraction of the cortical tissue was carried out manually for each embryo, as well as the dissociation of neurons through repeated mechanical pipetting with progressively narrow pipette tips, up to $\sim$50 μm wide.

The result of the dissection and dissociation processes was a dense suspension of disconnected neurons in *plating medium*. For clarity, the different chemicals that we used for the preparation of our cultures are summarized in Table 2.1. The obtained suspension was diluted and distributed among 24 wells, each of them containing a previously cleaned 13 mm borosilicate glass coverslip (Marienfield–Superior). In some experiments, the glass was bound to a polydimethylsiloxane (PDMS) mold to either consider cultures with a

topographical pattern, or to simply prepare multiple, small *mini–cultures* over the same glass.

Neurons spontaneously settled over the substrate, and started the growth of neurites within 24 h to form a *de novo* neural network. The initial, nominal density of neurons on the cavities was ≈ 2500 neurons/mm^2, although the final density at the time of the experiment was about ≈ 400 neurons/mm^2 due to neuronal death. Details on the preparation of the glass coverslips and the PDMS molds are provided in Section 2.1.3, and a sketch of the cell culture preparation is provided in Figure 2.1A.

2.1.2 Homogeneous and aggregated cultures

Primary cells usually present several anionic groups in the glycoproteins and glycolipis of their membrane, providing an overall negative surface charge. This natural feature, together with the prevailing negative charge of glass coverslips, hinders the adhesion of primary neurons onto a substrate. A number of strategies have been developed to overcome this difficulty, and mostly focused to treat chemically or physically the substrate prior plating. In our case, glasses were immersed in 65% nitric acid during 2 h and afterwards washed two times in double–distilled water (DDW); then, the coverslips were sonicated in ethanol for 20 min, and finally dried with a methane gas torch. These procedures equilibrated charges, increased glass porosity, and facilitated an hydrophilic behavior of the substrate.

When the neurons are plated on coverslips, the tension between the somas (applied by the new, recently–projected neurites) overcomes the surface adhesion and shapes a spontaneous aggregation mechanism (de Santos-Sierra et al., 2014; Segev et al., 2003). The *clustered cultures* outlined above are created in this manner, configuring a set of neuronal clusters, i.e. *neurospheres*, that extend acroos the substrate. Examples of this configuration are provided in Figure 2.1B(top) and Figure 2.7b.

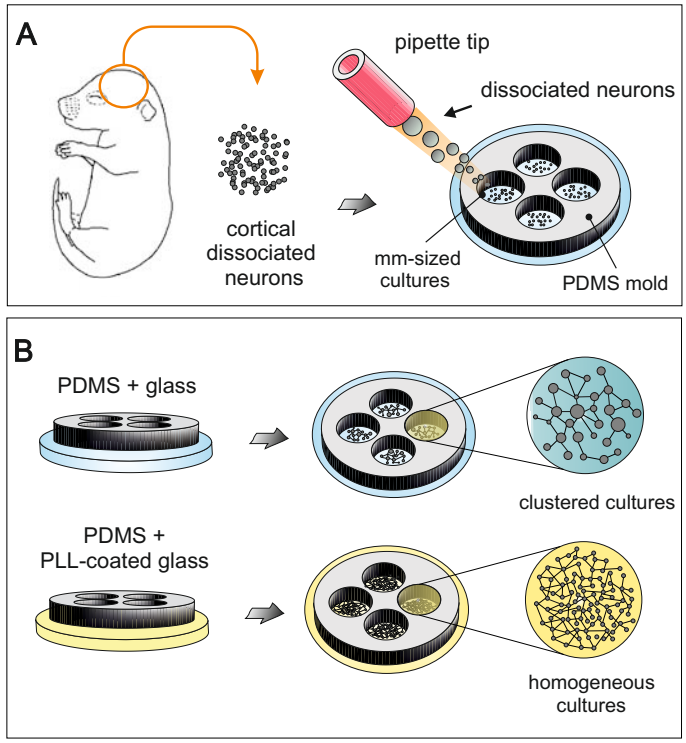

Fig. 2.1 Culture preparation. A, Cortices from embryonic rat brains were dissected and neurons dissociated by pipetting. Neurons were then suspended in plating medium and seeded onto previously prepared PDMS–glass structures 13 mm in diameter, and containing 4 cavities, each 3 mm in diameter. **B,** Each culture well contained 4 networks (minicultures), which could be neatly isolated by adjusting the height of the PDMS walls. Two main cultures could be prepared. In the absence of the adhesive protein PLL (top), neurons moved and aggregated, shaping the clustered configuration. The coating of the glasses with PLL (bottom) gave rise to the homogeneous networks. This Figure was adapted from Sara Teller's PhD Thesis.

In the case of *homogeneous cultures*, which are the main focus of this thesis, an additional protocol was necessary to restrict the motility of the neurons, and therefore ensure a homogeneous spatial distribution of the neuronal bodies (or *somas*) on the two-dimensional substrate [Figure 2.1B(bottom) and Figure 2.2]. The protocol consisted in applying a coating of poly–L–lysine (PLL, Sigma-Aldrich) over the substrate to improve cell adhesion, overcome neurites' tension, and restrict the motility of the neurons. The coating was

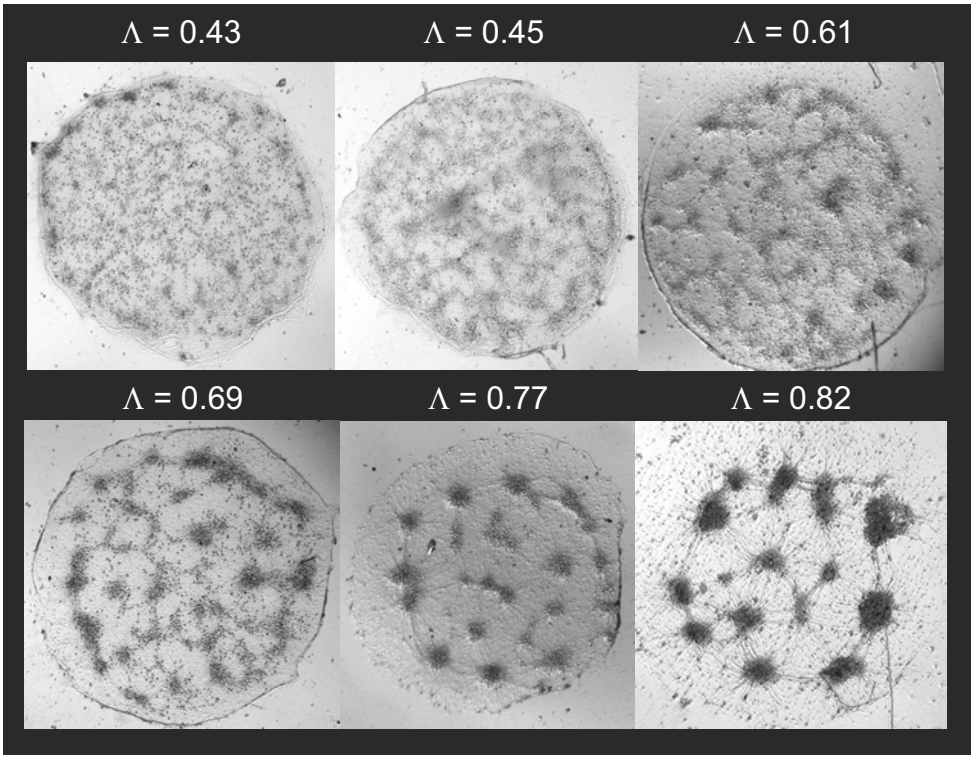

Fig. 2.2 Neuronal cultures with different degree of aggregation. Optical images of cultures with different degrees of aggregation: homogeneous ($\Lambda \approx 0.43$, 0.45), semi–aggregated ($\Lambda \approx 0.61$, 0.69) and aggregated ($\Lambda \approx 0.77$, 0.82). The diameter of the cultures is ϕ=3 mm. This Figure was adapted from Elisenda Tibau's PhD Thesis.

performed by overnight immersion of the substrate in a 1 ml PLL–diluted solution. The solution was prepared by mixing PLL-4957 (0.1 mg/ml) and Borate Buffer (pH 8.4) in a proportion of 1:12 in volume. Afterwards, the coverslips were gently washed with DDW and finally stored in *plating medium*. For our $\phi = 13$ mm cultures, the maximal homogeneity was found at a saturating PLL concentration of $\sim 10\ \mu$g/ml. We note that, despite using a strong concentration of PLL, neurons always exhibited some small, *stochastic* aggregation, and therefore perfectly homogeneous cultures were impossible with our current protocols.

In our lab, we modulated the degree of aggregation of our neuronal cultures by controlling the PLL concentration, being able to prepare not only the extreme cases of homogeneous or clustered cultures, but also cultures that covered a full spectrum of *aggregation degrees*, as illustrated in Figure 2.2.

We quantified the degree of aggregation in our cultures in order to provide a parameter for such a spatial trait. This degree of aggregation, that we termed Λ, was established through the 'Lorenz curves' of neuronal physical arrangement (Figure 2.3). These curves are constructed by first setting a unit area in the system, on the order of $100 \times 100\ \mu m^2$ (about 10 cell somas). Then, the number of neurons at each unit area is quantified, and the values sorted out in a descending order, to finally represent their cumulative fraction N_f as a fraction of the explored area fraction A_f. In this construction, a perfectly homogeneous configuration corresponds to the bisector of the plot $N_f(A_f)$. To properly quantify the degree of aggregation of a culture as $\Lambda \in [0,1]$ we considered the 'Gini coefficient', given by the area between the bisector and the Lorenz curve after normalization with respect to its maximum possible value of $1/2$. Typically, the best homogeneous cultures exhibited a degree of aggregation of $\Lambda \approx 0.2$, while the most clustered ones presented $\Lambda \approx 0.8$.

2.1.3 Glass–PDMS mold preparation

The silicone–based PDMS is a transparent, non–toxic polymer. In our lab, one of its uses was to restrict the size of the cultures and prepare several networks in different cavities, of $\phi = 3$ mm and $h = 1-4$ mm each, on the same glass substrate (Figure 2.1B). In this context, PDMS molds were a powerful tool since they provided independent, identically–prepared neuronal cultures that could be monitored simultaneously and selectively perturbed if needed. Furthermore, culture size could be set to match optical demands of our imaging system.

On the other hand, PDMS molds were also employed to dictate neuronal connectivity. As stated in Section 2.1.2, the connectivity could be tuned to

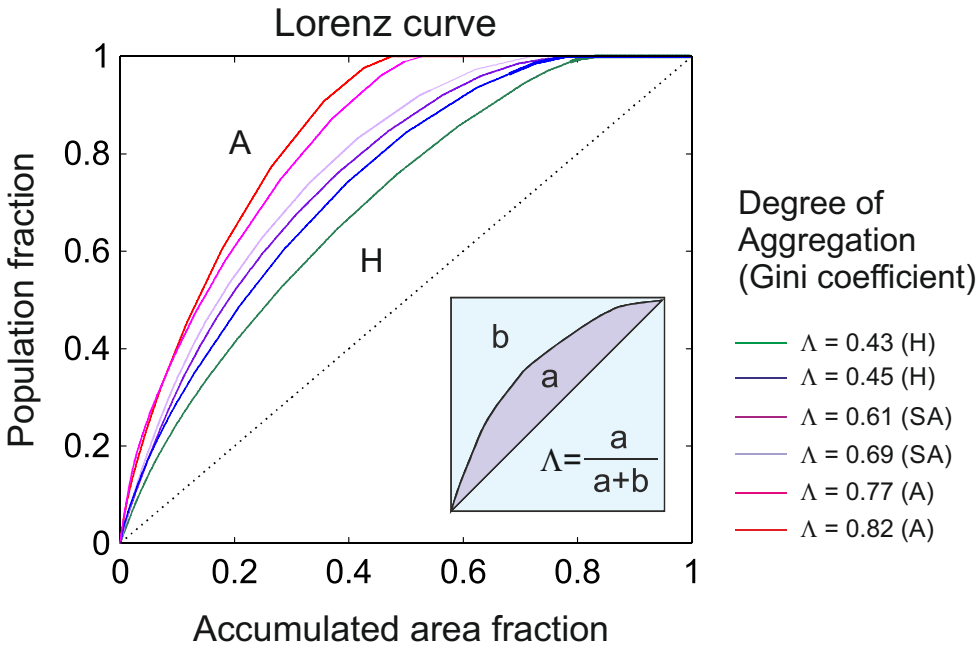

Fig. 2.3 Lorenz curves. Degree of aggregation Λ for different Lorenz curves. These curves plot the cumulative fraction of neurons per unit area, where the bisector corresponds to a perfectly homogeneous spatial distribution. The deviation from the bisector accounts for spatial heterogeneity, i.e. spatial aggregation. Λ is quantified as the 'Gini coefficient': the normalized area between the bisector and the corresponding Lorenz curve. **H** means homogeneous, **SA** semi–aggregated, and **A** aggregated. This Figure was adapted from Elisenda Tibau's PhD Thesis.

some extent via the modulation of the degree of aggregation Λ. However, this concept solely altered the heterogeneity of the spatial location of the neurons, without additional adjustment or guidance of the local or global isotropy of the network. *Patterned* molds of PDMS, which functioned as two–height topographical molds with specific designs, guided neuronal connections and were able to provide a new framework for the modulation of the connectivity in neuronal cultures. Examples of PDMS molds are presented in Figure 2.4.

PDMS structures were fabricated from the Silicone Elastomer Kit PDMS Sylgard 184 of Dow Corning (USA), which consists of a resin base and a

curing agent. When vigorously mixed as 10:1 ratio, and after 8 hours cure time, one could obtain solid structures of desired designs.

To restrict culture size, we placed the PDMS–liquid mixture in ϕ=100 mm flat petri dishes. When solidified, we extracted circular sections of PDMS with a stainless steel puncher of the same diameter as the glass coverslips ($\phi = 13$ mm), and then pierced 3 mm holes in it with an additional, sterile puncher (Integra-Miltex). The height of the PDMS mask is fixed by the total mass of mixture applied at the 100 mm flat petri dish. In the case of the patterned PDMS molds, the desired topography was produced by placing the liquid mixture on a solid, photolithographic–designed model.

Once the PDMS molds were prepared, they were placed on the glass coverslips and autoclaved at 105 °C in order to both sterilize the polymer and bond it to the glass.

The optimal thickness of the PDMS mold depended on the experimental conditions. In the context of PDMS molds used to restrict cultures size, we were interested in recording the activity of several, independent small cultures. Therefore, the thickness of the polymer had to be thick enough to ensure that neurites were not able to overcome the height of the PDMS layer, and

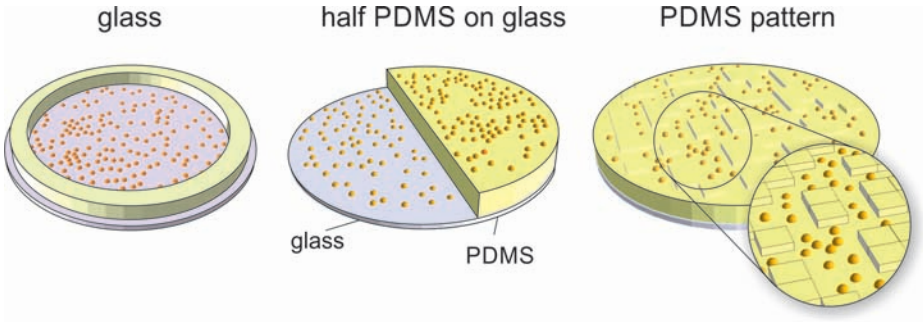

Fig. 2.4 Patterned experiments. Left: sketch of a typical homogeneous culture whose size is constrained by a PDMS ring. **Center**: 'half–PDMS-on–Glass' configuration, where a PDMS slab $\simeq$ 1 mm high attached over glass introduces a sharp vertical step that separates the culture into two regions. **Right**: 'PDMS patterned' culture, which provides a topographical disorder constructed with unit squares 250 μm lateral size and 100 μm height.

thin enough to ensure a good attachment between the PDMS and the glass substrate. Typical experiments procured heights in the range $1 \lesssim h \lesssim 2$ mm.

In patterned PDMS molds, the selected depth of the top–bottom topographical pattern is a crucial factor that strongly modulates the connectivity blueprint. Depths too low procured PDMS patterns that did not significantly affect the guidance of neurites; and depths too high caused the top–bottom layers to be effectively independent, giving rise to mutually excluded sub–cultures.The optimal working range, assessed experimentally, was $0.1 \lesssim h \lesssim 1$ mm.

2.1.4 Culture maintenance

A plate of 24 wells was prepared in each dissection. Each well had a diameter of 15 mm, and allocated the corresponding ϕ=13 mm glass–PDMS structure. After neuronal seeding was completed, and neurons were placed in the wells with 'plating medium' , the plate was put inside our lab's incubator (Memert), set at 37 °C, 5% CO_2 and 95% humidity, for the cultures to develop.

Along the first days *in vitro* (DIV) the tension emerging from the newly developed neurites favored cell–cell attachment. As already discussed, for low PLL concentrations, this inter–cells tension overcame cell attachment, gradually promoting the formation of compact neuronal assemblies. The cultures were maintained up to 3 weeks, with periodic changes in the culture media to ensure healthy, active neuronal cultures.

Cortical tissue extracted from rat embryos contained both neuroblasts and glioblasts. The former derived into neurons, and formed the networks of our interest. The latter are the precursors to glial cells present in the cortex, i.e. astrocytes and oligodendrocytes. In order to survive and grow, cultures needed a well balanced ratio between those two cellular populations, typically of 2:1 glia to neuron ratio as in the adult rat cortex. Although neuroblasts rapidly differentiated into neurons and lost their ability to divide, glial cells preserved their capacity to proliferate for long time. This imbalance had to be corrected

by substituting the initial 'plating medium' by 'changing medium' at 5 DIV, a medium that contained a cocktail of FUDR and Uridine that stopped all cell proliferation through cell division inhibitors. Afterwards, at 8 DIV, culture medium was changed to 'final medium', which was periodically refreshed every 3 days up to the time of the experiment.

All used mediums are summarized in Table 2.1.

Product Name	Description	Provider	Role
L15+2G	L15 enriched with 0.6% glucose and gentamicin	Sigma-Aldrich	Maintains physiological pH conditions before plating
MEM+3G	Essential Medium Eagle's-L-glutamate enriched with gentamicin, glutamate and glucose	Sigma-Aldrich	Main buffer for cell culturing and development
Plating medium	MEM+3G with 5% of foetal calf serum (FCS), 5% of horse serum (HS), and 0.1% B27	FCS and HS, Invitrogen B27, Sigma-Aldrich	Neuronal growth
Changing medium	MEM+3G with 0.5% FUDR, 0.5% Uridine, and 10% HS	FUDR and Uridine, Sigma-Aldrich	Limits glia cell division
Final medium	MEM+3Gwith 10% HS	HS Invitrogen	Maintains a proper environment to keep cultures healthy for long time
EM	500ml DDW with 128mM NaCl, 1mM CaCl2, 1mM MgCL2, 45 mM sucrose, 10mM glucose, and 0.01M Hepes; pH 7.4	--	Recording solutions i.e. pH-stable buffer for actual experiments

Table 2.1 Cell culture media and recording solutions. The table summarizes the different media used for the preparation and maintenance of the cultures, as well as to record activity. We also include the manufacturer of the product and the role of the different products. This Table was adapted from Sara Teller's PhD Thesis.

2.2 Experimental setup

Neuronal activity in Soriano's lab was recorded by means of *Multi–Neuron Fluorescence Calcium Imaging*, a technique that uses calcium–sensitive dyes

to monitor changes in the intracellular concentration of calcium. Since calcium is taken by neurons upon activity, this technique allows an easy identification of neuronal firings (Grienberger and Konnerth, 2012; Rochefort et al., 2008; Smetters et al., 1999). The term 'multi–neuron' refers to the ability of the optical system to resolve single neurons in the culture and follow their activity. Fluorescence Calcium Imaging has been widely used *in vitro* for neuronal cultures (Breskin et al., 2006; Ganguly et al., 2001; Orlandi et al., 2013; Tibau et al., 2013b), *ex vivo* for brain slices (Carrillo-Reid et al., 2008; Ikegaya et al., 2004), and *in vivo* for specific brain regions or small animal brains (Ahrens et al., 2013). This technique not only frames the basis of our collected experimental data, but it was also the main data acquisition tool in E. Moses' group (Weizmann Institute of Science, Israel) for the *quorum percolation experiments* that were reanalyzed in Chapters 3 and 4 of this thesis.

2.2.1 Fluorescence Calcium Imaging

The membrane potential of neurons arises from a complex biophysical mechanism in which different ionic species (prominently K^+, Na^+, Ca^{2+} and Cl^-) maintain a different concentration inside and outside the neuron's membrane. Through the action of membrane pumps and channels, the membrane potential is increased during the arrival of inputs from upstream connected neurons, and peaks after reaching a given threshold, emitting a spike. Specifically for the context of calcium imaging, neurons at rest present a very low intracellular calcium concentration.

When a neuron fires, several voltage–gated channels become open, providing a high intake of calcium up to two orders of magnitude above its resting intracellular concentration (Berridge et al., 2000). Fluorescence Calcium Imaging takes advantage of this increase by using a fluorescent molecule that fluoresces solely upon bindiug with Ca^{2+} ions. The fluorescent molecule therefore acts as a Calcium indicator for neuronal firing. When a neuron fires,

its fluorescence emission sharply increases as the membrane depolarizes in few milliseconds. Afterwards, the fluorescence signal of the neuron decays in a rather complex dynamics, since not only Ca^{2+} has to return to its resting concentration, but also the fluorescent molecule has to unbind Calcium. Altogether, fluorescence imaging can detect well the initiation of neuronal firing with $1-10$ ms resolution, but full recovery of resting fluorescence levels may require $1-10$ s, often hindering the precise identification of concatenated spikes.

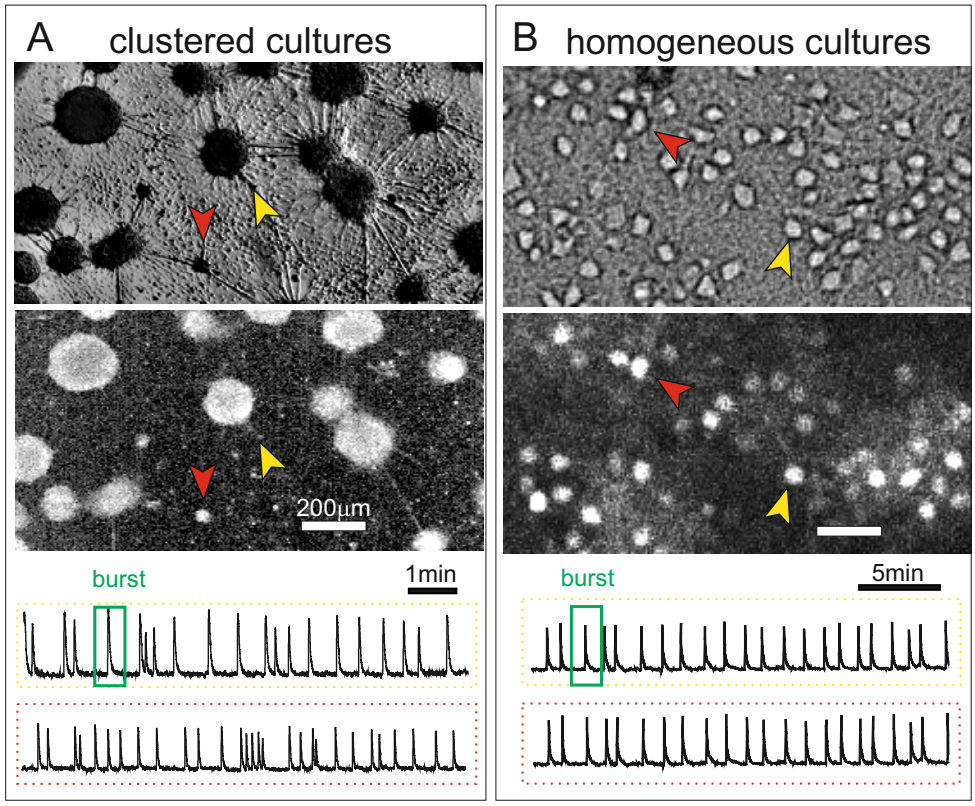

Fig. 2.5 Calcium Imaging in our neuronal cultures. A, Bright field image of a clustered culture (top), its corresponding calcium fluorescence signal (center), and two representative fluorescence traces (bottom) of the neuronal clusters marked with yellow and red arrows. **B,** Equivalent representation for a homogeneous neuronal network. Scale bars apply to all images. This Figure was adapted from Sara Teller's PhD Thesis.

The most extensively used indicators in fluorescence imaging are *chemical calcium probes* and *genetically encoded calcium indicators* (GECIs) (Knöpfel, 2012). Chemical indicators consist in relatively simple molecules that reshape their structure upon binding with calcium, becoming fluorescent; they are usually toxic and have to be loaded in the cytoplasm through solvents such as DMSO. Conversely, genetically encoded calcium indicators are proteins expressed by the cell itself, which ensures no damage to the cells since fluorescent dye loading is avoided. Genetic encoding is typically performed through viral gene transfer. The procedure may initially stress the cells, but it is much less pernicious at a long run. Chemical indicators are cheap and easy to handle, and are perfect for short experiments, on the order of hours. GECIs, on the contrary, are expensive and require special safety regulations; they are therefore adequate for recordings on the order of days. The first group has been widely used in our research lab since its foundation, and the second has been recently implemented to our neuronal cultures, with excellent results.

For the experiments carried out in this thesis we used Fluo–4–AM as fluorescent probe (F14201, Life) (Gee et al., 2000; Paredes et al., 2008), which is excited at a wavelength of 485 nm and emits light at ≈506 nm. The increase in fluorescence upon neuronal firing is sufficiently high to ensure a good signal–to–noise ratio in the acquired data, although with constraints associated with the optical system (such as spatial area covered or light intensity) and camera settings (such as frame rate or pixel binning). Fluo–4 had to be dissolved in DMSO at 1 μg/ml in order to make the cell membrane permeable. To carry out actual calcium fluorescence measurements, cultures were first placed on a ϕ=35 mm petri dish with 1 ml of 'external medium' (EM), a solution that maintains the culture stable during recording. Then, 3.5 μl of DMSO–Fluo–4 solution were applied to the culture medium, and the petri dish was gently stirred using an orbital shaker (Termo-Fischer) at 40 rpm, for a 30 min incubation of the fluorescence probe. Once inside the cell, Fluo–4 was spontaneously split by cell enzimes and became impermeable

to the cell membrane, being trapped in the soma of the neurons. Finally, the culture was totally refreshed with new 4 ml EM, washing out any residual Fluo–4 in the extracellular medium. At this step, the experimental protocol provided neuronal cultures with calcium indicators present solely inside the cells, and therefore we were ready to perform recordings of fluorescent neuronal activity. Representative fluorescence images of our cultures, together with their corresponding bright–field counterparts and typical fluorescence activity traces, are shown in Figure 2.5.

The main drawback of Calcium imaging is the slow unbinding and biological outflow of Ca^{2+} after neuronal firing. This implies a limitation in the temporal resolution of the technique, in the sense that it cannot resolve single spikes within a window of $\tau \sim 1$ s. Neuronal activity in cultures was usually presented in the form of *network bursts*, i.e. highly coherent whole–culture activations, with each neuron emitting several spikes (*neuron bursts*) during these episodes. Thus, the timing of individual spikes was very difficult to resolve, although the initiation of neuron bursting could be resolved well. Another disadvantage of this Calcium imaging is that the duration of the experiments is substantially limited —to 4h at most— due to degradation of neurons. This degradation is both due to DMSO toxicity and photo–damage during light exposure. DMSO toxicity can be avoided using GECIs, but the reduction of photo–damage requires the shortening of the recordings and the minimization of light intensity. The latter aspects cannot be eaily overcome, since they may compromise the statistics of the experiment and the quality of the data.

In conclusion, although Fluorescence Calcium Imaging is not optimal, it is a cheap technique to assess neuronal activity in large populations (typically 400 neurons per mm^2) with single-neuron spatial resolution, large fields of view (16×12 mm^2 in our system), and recordings of typically 1 h long. Our camera settings sufficed to extract the onset times of activation (typically with

5 – 15 ms resolution), but could not reliably provide the times of individual spikes.

2.2.2 Main alternative to Calcium Imaging: MEAs

Although most of Calcium Imaging drawbacks could be easily amended by means of Multi–Electrode Arrays (MEAs), both techniques are very different, and therefore some specific advantages provided by the fluorescence technique would be lost.

MEAs have been widely used either in neuronal cultures (Bettencourt et al., 2007; Downes et al., 2012; Raichman and Ben-Jacob, 2008) and brain slices (Beggs and Plenz, 2003; Carmeli et al., 2013). Its typical structure consists in a grid of 8×8 microelectrodes, 30 μm in diameter each, with a microelectrode interdistance of 200 μm. MEAs quantify neuronal activity through measurement of the extracellular local field potentials (LFP).

The acute temporal resolution of this technique, in the order of 10^1–10^2 μs, provides an accurate detection at a single–spike level. Furthermore, MEAs measurements are non–toxic for the cells, and therefore is an excellent tool for long–time recordings along several days, perfect for assessing changes during the development of cultures.

On the other hand, MEAs' spatial resolution is largely compromised since its LFP readings can arise from several sources. This includes aggregates of cells at the vicinity of an electrode, or neurites touching an electrode whose corresponding neuron soma is far–located. In order to reduce the spatial uncertainty and unveil single–neuron locations, complex data analysis is needed in a process named *spike sorting* (Lewicki, 1998). Moreover, and given the spatial configuration of the electrodes, only a limited number of ∼10 neurons per electrode is accessible through MEAs recordings. And finally, MEAs are overall much more expensive when compared to Fluorescence Imaging.

Efforts have been poured to overcome the scanty spatial resolution and limited number of recorded neurons in MEAs. Some examples are the high–

density MEAs composed of 512 microelectrodes of Ito et al. (2014), able to record ∼100 neurons simultaneously; and the CMOS Multi–Transistor Arrays of Hierlemann et al. (2011). However, these technologies have not been widely used due to their high manufacturing cost and challenging analysis.

In conclusion, MEAs an Calcium Imaging provided complementary measurements of activity. A combined setup consisting of both techniques would be ideal for neuronal activity recordings but, unfortunately, it was not possible to implement such an idea in our lab. Therefore, Calcium Imaging was chosen over MEAs due to its better spatial resolution, straightforward data processing, excellent extraction of onset times of activations, accessibility to large neuronal ensembles, and economical viability.

2.3 Experimental procedure

Here we present a detailed description of the experimental setup and data acquisition procedure, together with an overview of the different groups of experiments carried out along the thesis.

We first note that, after substantial preliminary testing, the optimal range for monitoring neuronal activity was set in the range $6-18$ DIV. Previous developmental stages neither presented spontaneous activity nor exhibit responding neurons to electric stimulation. At the other extreme, cultures at $21-28$ DIV were already starting to degrade and exhibited erratic activity. We remark that around ∼60% of the performed experiments had to be discarded due to insufficient signal–to–noise ratio or total absence of neuronal activity. Taking into account the complexity of neuronal cultures and their intrinsic variability, and although samples with identical culturing conditions exhibited some differences in activity, our lab had been able to achieve an outstanding experimental reproducibility.

As a whole, the experiments presented in this thesis, performed under the direction of Jordi Soriano, comprised four main groups: (I) *Inhibition–blocked*

experiments, (II) *Patterned experiments*, (III) *Electric stimulation experiments*, and (IV) *Quorum percolation experiments*. The first set of experiments involved the blockade of inhibition with the corresponding antagonists; the second one consisted in cultures grown over PDMS topographical patterns to modulate the connectivity blueprint; the third one dealt with the stimulation of cultures through a pair of bath electrodes, and the fourth one was related with the measurement of the highest group of neurons that responded together to an external stimulation.

We would like to remark that some experiments, specifically those belonging to the *quorum percolation* group and reanalyzed in the framework of the Neuronal Network Ising model of Chapter 3, were performed by Jordi Soriano in the group of Elisha Moses at the Weizmann Institute of Israel, and along the period 2005–2008. The corresponding experimental protocols are described in Section 2.3.5.

2.3.1 Experimental setup

Experiments were performed in a Zeiss Axiovert C25 inverted microscope. Initially, the available objectives were in the range $2.5-10\times$. Afterwards, during this thesis, our lab purchased a $1.25\times$ objective that increased the field of view to cover almost entirely the ϕ=13 mm cultures. This provided the possibility to record whole–culture fluorescence at once with an improved characterization of the dynamics of activity propagation, and without the need to restrict system size through PDMS–molds. Additionally, our microscope included an adjustable optical zoom in the range $0.32-0.88\times$ for further tuning of the field of view. Neuronal activity was monitored through an Orca Flash 2.8 camera (Hamamatsu, 960×720 pixels image size) attached to the microscope. Data was acquired at a typical acquisition rates in the range $20-50$ frames per second. Taking into account the different objectives, optical zoom and camera configurations, the spatial resolution of the setup in our experiments varied between 8.5 and 16.7 μm/pixel, sufficient to resolve

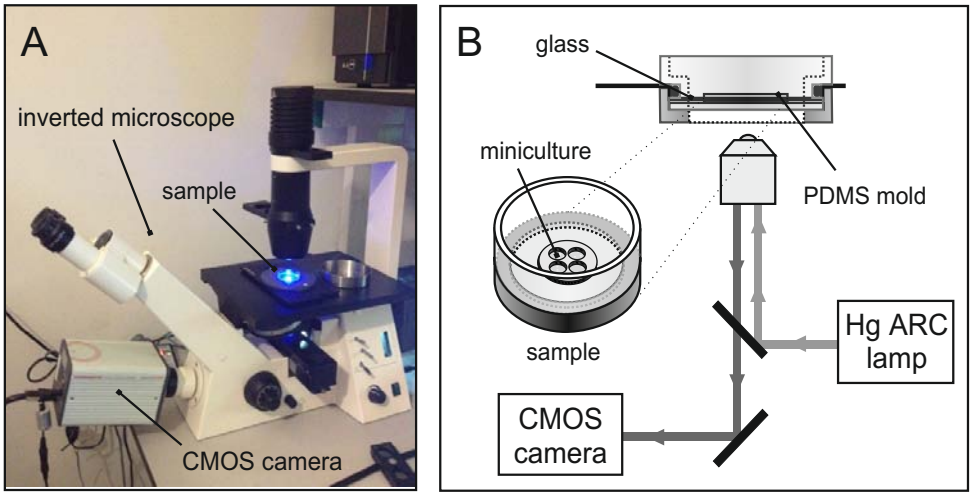

Fig. 2.6 Experimental setup at Jordi Soriano's Lab. A, Standard configuration used in most of the experiments, showing the inverted microscope and the attached CMOS camera. The culture to be studied sits the in center of the $x-y$ stage and appears blue due to the excitation light for fluorescence. **B,** Detailed sketch of the experimental system. In this case, the observation chamber contains 4 minicultures and is filled with EM. An arc lamp excites the fluorescence with a filtered wavelength of 485 nm (blue). Fluorescence light is emitted at 520 nm (green), which is captured by the camera. Figure adapted from Sara Teller's PhD thesis.

individual neurons. The blue light for excitation ($\lambda = 485$ nm) was applied through a mercury arc lamp combined with appropriate filters. Fluorescence emission was in green ($\lambda = 530$ nm). The basic experimental setup is pictured in Figure 2.6.

The culture recording chamber consisted of a ϕ=35 mm petri dish with a ϕ=14 mm cavity in its center, hermetically sealed from below by a thin cover glass (Fig. 2.7a). This design effectively provided a crevice that minimized the movement of the culture during experiments, and ensured optimum optical quality of the recording due to the glass surface at the bottom (instead of plastic). The measured culture, which were previously incubated with the Fluo–4 fluorescent probe (Section 2.2.1), was placed in the 14 mm crevice and bathed in 4 ml of EM.

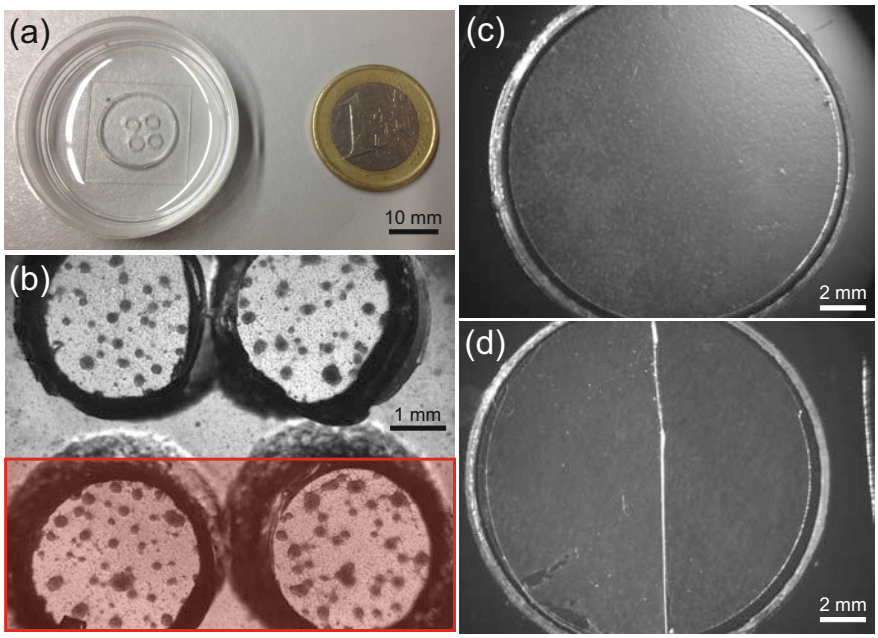

Fig. 2.7 Observation chamber and culture configurations. (a) Picture of the observation chamber compared to 1 euro coin. On the center of the chamber there is a glass–PDMS mold structure showing 4 PDMS–cavities, each 3 mm in diameter. **(b)** Bright field image of 4 aggregated networks. Red area depicts the recording field of view. **(c)** Bright field image of a 13 mm homogeneous culture. The monitored area is equal to the whole area of the picture. **(d)** Bright field image of a half–PDMS–on–GLASS patterned culture, with recorded area equal to whole area. Figure (a) and (b) adapted from Sara Teller's PhD thesis.

Configuration for 4 minicultures 3 mm in diameter. This configuration was used to record a number of cultures simultaneously and maximize data statistics. Experiments were carried out with a 2.5× objective combined with the 0.32× optical zoom. Images were acquired as 8-bits gray–scale, and acquisition speed could be set up to 100 fps. A larger frame rate was not possible without excessive loss of signal–to–noise ratio due to low exposition time of the camera. The field of view resulted in 8.1×3.4 mm and 940×400 pixels, with a spatial resolution of 8.51 μm/pixel (red area in Fig. 2.7b). A subset of the *electric stimulation experiments* were performed with this configuration. Since we were specially focused on initiation and propagation of activity, a high acquisition frequency was needed to properly

assess activity dynamics in a small 3 mm culture. However, one could not increase fps at all costs, for it would have resulted in a dramatic decrease of data quality. We concluded that this configuration provided an appropriate balance between image resolution, light and acquisition speed.

Configuration for 13 mm cultures. This configuration was implemented once the lab acquired the 1.25× objective, therefore allowing for a large field of view, whole–culture recording. The optical zoom used in this case was the lowest one of 0.32× amplification, and the acquisition speed was set to 20–50 fps, where the first value provided a higher light intensity and the latter ensured a slightly better temporal resolution. In these experiments, a higher fps was not necessary since the large size of the culture with respect to the mean axonal length (ϕ=13 mm to $\langle a \rangle \approx$1 mm) ensured a proper determination of activity propagation. The field of view covered an area of 16×12 mm, almost fitting the entire coverslip. For this acquisition speed, the image size in pixels was 960×720, which entailed a spatial resolution of 16.67 μm/pixel (Figure 2.7c). The majority of the final set of experiments presented in this thesis were performed using this configuration.

We remark that the blue light that excited the fluorophore in the neuronal cultures had to be often attenuated to avoid extreme photo–damage and photo–bleaching. This aspect, together with the large data storage needed, limited the duration of the experiments to about $2-3$ h, with an average duration of 1 h. Indeed, the large size of the data and its posterior processing resulted in a total of ∼300 GB storage space for each performed activity measure. Large data was necessary for sufficiently detailed monitoring of activity, but led to a slow painstaking data analysis.

2.3.2 Inhibition–blocked experiments

In a typical *homogeneous experiment* of whole–culture monitoring of activity, we focused on the characterization of activity fronts initiation and propagation.

The main goal of these *inhibition–blocked experiments* was to assess the changes in activity fronts between an initial, excitatory–inhibitory neuronal network (E+I), and its corresponding excitatory–only (E) network analog.

As stated in Section 2.1.1, rat cortical primary cultures presented a reproducible neuronal type distribution of roughly ∼80% excitatory pyramidal neurons and ∼20% inhibitory interneurons. Dale's principle establishes that neuronal type —either excitatory or inhibitory— remains constant in time, and that excitatory (inhibitory) neurons have only an excitatory (inhibitory) role. In our case, a remark has to be made regarding inhibitory interneurons. Their depolarization action is excitatory at early developmental stages, and switches to its definitive inhibitory action by 5 DIV (Ganguly et al., 2001; Soriano et al., 2008; Tibau et al., 2013b). Provided that we performed experiments at $6-18$ DIV, we solely observed the interneuron's inhibitory action.

This switch in interneurons action is termed 'GABA switch', where GABA stands for *γ-Aminobutyric acid*, the main inhibitory neurotrasmitter in the brain. In order to fully block inhibition and to obtain the 'E–only' condition, we applied the $GABA_A$–receptor antagonist *bicuculline* (Sigma) to the cultures at a concentration of 40 μM.

In summary, a characteristic experiment consisted of an initial recording at standard, 'E–I' condition for ∼20–30 min; followed by the application of the drug bicuculline and 5 min of rest for culture stabilization; and a final monitoring of activity in 'E–only' condition for another ∼20–30 min.

2.3.3 Patterned experiments

The main aim of our *patterned experiments* was to guide neuronal connections and induce specific dynamic regimes. Patterning was established through a two–height topographical mold. Conceptually, these experiments follow a bottom–up approach, in the sense that we tuned *microscopic* connectivity to frame *macroscopic* activity fronts. To understand the behavior of neurons

and connections with a topographical mold, we first focused on the simplest possible configuration, consisiting of a single PDMS–topographical step, as shown in Figs. 2.4(center) and 2.7d. Since that step effectively split the culture in two interconnected sides, one on the high PDMS–mold and the other on glass, these experiments helped to unveil both the influence of different substrates and the resulting dynamics of two interdependent neural networks. Once the behavior of neurons and connections in this basic configuration was understood, we studied richer configurations in which a series of low–height topographical obstacles (*pattern* or *disorder*) were used as substrate of the neuronal cultures. Figure 2.4(right) illustrates these kind of patterns. In all cases, changes in the connectivity were indirectly assessed by characterizing the emergent dynamical activity of the networks.

Neurons were plated by sedimentation, therefore gravity played some role in initially distributing the neurons over the pattern. Indeed, we note that neurons slightly move before anchoring to the substrate, and therefore some top neurons easily fell to the bottom areas, resulting often in a higher density of neurons at the bottom of the pattern. Despite this process, however, once the neurons were attached to the substrate and started growing axons and dendrites, the leading forces were substrate adhesion (enhanced with previous PLL–coating) and tension between neurites, without significant contribution of gravity. Thus, neurites were able to grow either vertically or horizontally through the PDMS–step; yet, the vertical wall of the obstacle was seen different from either bottom or top neurites. The bottom ones tended to deflect in contact with the obstacle and kept exploring the substrate, or grow along the obstacle. Therefore, solely a small fraction of the axons were projected from the base of the pattern to its top part, for instance from glass to PDMS in the simplest experiments; whereas axons from the top PDMS layer could easily reach the glass base and then get trapped. We concluded that an appropriately sized PDMS–step would foster an asymmetric, PDMS–to–glass enhanced connectivity in our cultures.

In an effort to understand the impact of obstacle height to the interconnectivity of top–bottom parts, we carried out experiments with preset heights between a glass substrate and PDMS, in the range 100–1500 μ m, to assess the impact of this parameter on the connectivity blueprint and its asymmetry. For experiments with a complex pattern, i..e a set of obstacles, their height was set to 100 μm and both bottom and top parts were PDMS.

Concerning activity, *patterned experiments* consisted of a ∼20–30 min whole–culture recording. If overall spontaneous activity was poor, *bicuculline* was applied to strengthen it (see Section 2.3.2). For the glass–PDMS experiments, and after the first recording, a cut was made along the base of the PDMS–step in order to physically separate the two sides and obtain independent cultures. Then, another recording of ∼20–30 min was conducted.

2.3.4 Electric stimulation experiments

The central goal for our *electric stimulation experiments* was to enhance and modulate neuronal activity by the application of an electric, sub–threshold stimulation, which was meant to increase uncorrelated spontaneous individual firings, i.e. background activity that could be seen as *noise*. The threshold of stimulation V_{th} was defined as the stimulation value above which network bursting was automatically triggered.

The electric stimulation setup consisted of a custom–made hollow plastic cylinder, with an outer diameter ϕ_{outer} ≈35 mm that fitted in the special recording petri dish (see Section 2.3.1), and an inner diameter of ϕ_{inner} ≈20 mm to make room for water and light. A pair of parallel, conductive platinum wires crossed the central hole of the cylinder diametrically, at the bottom of the structure, as close as possible to the culture. Those two wires effectively acted as bath electrodes to deliver the electric stimulation to the neuronal network; their platinum nature was chosen due to its conductivity and biocompatibility. Figure 2.8a shows a detailed sketch of the electric stimulation setup, adapted from Soriano et al. (2008); a picture of the setup is presented in Figure 2.8b.

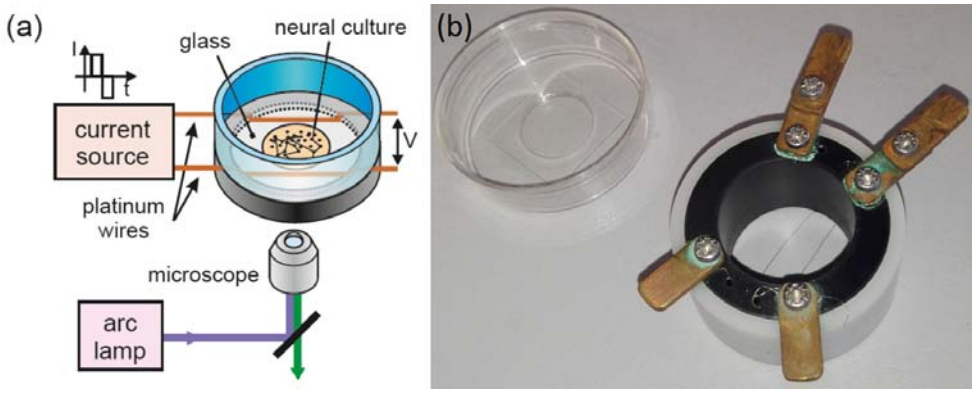

Fig. 2.8 Electric stimulation setup. (a) Sketch of the electric stimulation setup. Current is applied through bath electrodes, and the fluorescent activity is recorded through the inverted microscope. **(b)** Picture of the setup and the observation chamber. The outer and inner diameters of the plastic polymer cylinder are ϕ_{outer} ≈34.5 mm and ϕ_{inner}=20 mm, and the separation between platinum macroelectrodes is ∼ 5 mm.

The applied stimuli were controlled through an Agilent DSO-X 2002A oscilloscope. The wave generator of the oscilloscope provided the chosen electric potential to one of the electrodes, while the other was kept at 0 V. Preliminary experiments were performed to set the optimal conditions to monitor cultures' response upon sub–threshold electric stimulation:

Threshold of stimulation V_{th}. To extract the threshold for our specific setup we recorded the activity of cultures upon biphasic pulses of $\Delta t = 50$ μs and fixed semi–amplitude V, and we assessed the voltage value that triggered bursts. Interestingly, our threshold of stimulation presented a robust value of V=5 V that, within the experimental range explored in our lab, was roughly independent of DIV, degree of aggregation and average culture density. Pulses were biphasic to preserve a neutral electrical charge upon stimulation.

Culture viability upon stimulation. Given the short 50 μs timescale of the aforementioned pulses, the cultures seemed to increase neuronal activity but did not increase activity noise in the network, as in stochastic resonance. Instead, a long–lasting stimulation provided an effective increase in neuronal

noise, and therefore DC and AC stimulations were tested on experiments. In DC, positive–solely (or negative–solely) stimulation applied to the recording medium generated persistent currents of positive (negative) ions converging to the charged electrode, while negative (positive) ones dispersed from it; DC current also promoted water electrolysis. Both features provided cell death even at low V and short recordings, discarding DC as a viable stimulation for living neuronal cultures. On the other hand, AC stimulation provided no net charge for time windows larger than its period and, for semi–amplitudes lower than V<3 V and recordings of $\Delta t \lesssim 1$ h, it was not lethal.

Taking into account the above preliminary tests, the experimental protocol developed for our *electric stimulation experiments* was finally arranged. First, the stimulation setup was fitted in the recording petri dish with the culture sample bathed in EM. Secondly, a no–stimulation standard recording of 20–30 min was performed at a typical frequency acquisition of 20–50 fps. Then, a sinusoidal stimulation of semi–amplitude $V_{1/2}$=0.5 V and period T=10 s was generated with the oscilloscope, increased four times by a signal amplifier ($V_{1/2}$=2 V), and directly applied to the electrodes during 20–30 min for a second recording. And lastly, if the culture still fired, an optional 20–30 min monitoring of activity was carried out.

We note that cultures with no initial activity were disinhibited with *bicuculline*. If spontaneous activity emerged in consequence, the previous protocol was conducted.

2.3.5 Experiments at Weizmann Institute

The main objective of the *experiments at Weizmann Institute* was to assess the connectivity blueprint of neuronal cultures through a stimulation protocol combined with a graph–theoretical analysis, allowing the extraction of microscopic information such as the average connectivity of the neurons.

This set of experiments were performed by Jordi Soriano and coworkers in the group of Elisha Moses at the Weizmann Institute of Israel, along 2005–2010. The protocols, from which our lab was inspired, are described in detail in Soriano et al. (2008). The fundamental differences with respect to the protocol in previous Section 2.3.4 is that, first, the electric stimulation at Weizmann Institute was limited to the biphasic pulse scenario, and second, the excitatory connectivity in the culture was gradually weakened by application of appropriate antagonists.

To gradually disintegrate the connectivity, the excitatory AMPA α*–amino–3–hydroxy–5–methyl–4–isoxazolepropionic acid* receptors were targeted with increasing concentrations of their antagonist CNQX *6–cyano–7–nitroquinoxaline–2,3–dione*. We note that the AMPA excitatory neurotransmitters represented an 80% of the excitatory receptors of the neurons, the other 20% being NMDA *N–methyl–D–aspartate* receptors. To fully control network disintegration, NMDA receptors had to be previously blocked, and therefore their antagonist APV *2–amino–5–phosphonovalerate* was formerly applied to the cultures at 20 μM concentration. Table 2.2 summarizes the main neurotransmitter receptors in rat cortical cultures, their antagonists and role.

Receptor	Antagonist	Action
AMPA-glutamate	CNQX	Reduces excitation
NMDA	APV	Blocks non-glutamate excitation
$GABA_A$	Bicuculline	Blocks inhibition

Table 2.2 Basic neurotransmitter receptors present in neuronal cultures, their respective antagonists applied in our experiments, and their major action. Table extracted from Sara Teller's PhD thesis.

The electric stimulation was necessary since cultures did not spontaneously burst for [CNQX]$\gtrsim$300 nm. The stimulation was also applied at lower concentrations of the drug for consistency in the conditions of the experiments. In the latter case, where spontaneous activity was present, the

biphasic pulse was applied when the network fully recovered from the last burst, i.e. a minimum of $\sim 10\ s$ elapsed.

A typical experiment consisted in an initial blockade of NMDA receptors through application of 20 μM APV and 5 min rest; disinhibition through *bicuculline* could be then applied if appropriate. In the next step, spontaneous activity was recorded at [CNQX]=0 nM. Afterwards, the lowest non–zero CNQX concentration was applied, followed by a resting period of 5–10 min, and a recording of activity upon biphasic pulse stimulation. The latter was then repeated for increasing concentrations of CNQX, up to the total disintegration of the network at [CNQX]$\sim$10 μM.

2.4 Data Analysis

Once the experiments were performed, and the activity was recorded, a posterior analysis was needed to extract single–neuron activation times in network bursts. The latter information was then processed to extract bursts initiation points, as well as to assess the velocity of the propagating activity front. Additional treatments have been applied to the data to get extra information in specific cases, such as the characterization of the propagation profile in patterned cultures.

2.4.1 Raw data

Raw experimental fluorescence images were obtained with the program *HOKAWO 2.5–2.8*, in format files type '.HIS'. Data was recorded in 8 or 16 bits gray–scale. For further treatment, HIS files had to be converted to a stack of bitmap images '.BMP'; a process that lasted around $1-2\ h$ for $\sim 45\ min$ of monitored activity, which was equivalent to $\sim 50-100\ Gb$ of data depending on the recording frame rate.

2.4.2 NeuroImages: ROIs selection

Since the experimental field of view could vary between experiments, samples could present different substrates, and, in summary, the experimental *regions of interest* (ROIs) were culture–specific, a manual selection of the ROIs was needed. This selection of pixel subsets was performed with the custom program *NeuroImages*, a software based in C language and developed by my advisor Dr. Jordi Soriano.

A typical data processing in NeuroImages involved the following steps. First, experimental data (in BMP format) was loaded. Secondly, ROIs were selected, either by manual selection of the individual position for each ROI or by specification of a rectangular/circular ROI grid. The former was chosen for sparse, low–density cultures; and the latter was performed in high–density cultures, were single–cell selection was unfeasible provided the large number of recorded neurons ($10^3 - 10^4$ neurons). We would like to remark that manual selection of single–cells' locations required no less than 30 *min*, and sometimes lasted up to 2 *h*. And finally, in the third step, NeuroImages calculated the average fluorescence intensity for each frame and for all pixels enclosed in each ROI ($\sim$ 90 *min* of computing time). The output data consisted of two files: first the fluorescence intensity matrix in an ASCII '.DAT' file, where rows depicted ROI index and columns indicated temporal frame; and secondly the ROIs file, where each row depicted ROI index and columns indicated ROI's horizontal and vertical positions in pixels. Figure 2.9 depicts the NeuroImages interface.

We note that the selection of a ROI grid provided a coarse–grained average fluorescence, since each ROI encompassed a fixed area instead of labeling individual neurons. Therefore, each ROI could enclose one, zero, or multiple neurons. Although this procedure generated dead cells artifacts and spurious 'single–cell' multiple spikes, we observed that it was an efficient method when characterizing global initiation points and propagating fronts in the context of homogeneous cultures.

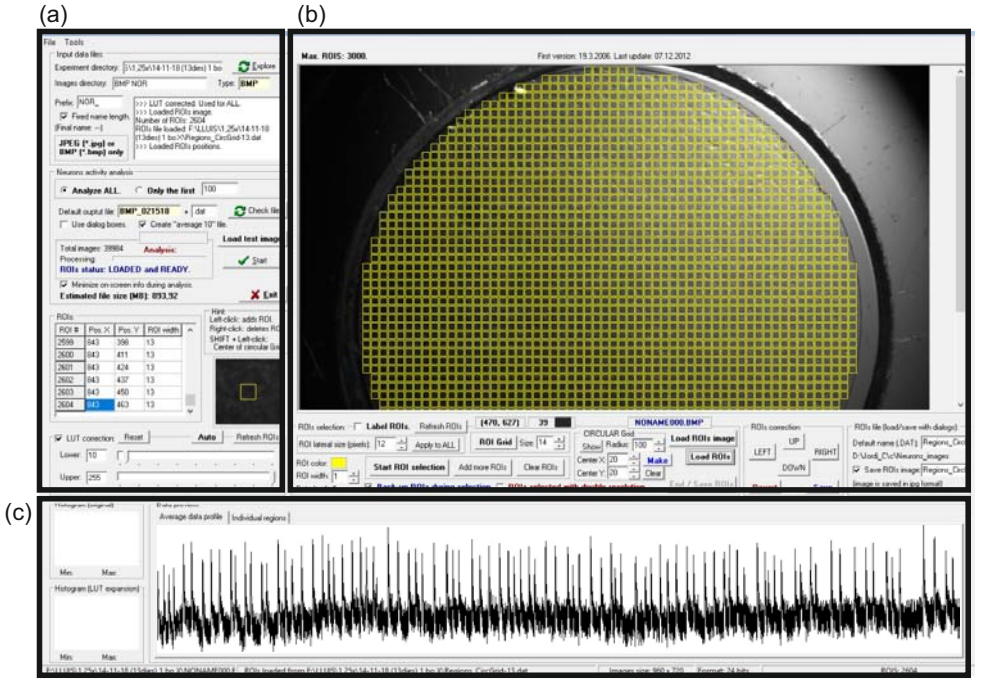

Fig. 2.9 NeuroImages interface for ROIs selection and fluorescence data processing. ROIs selection and extraction of fluorescence data for a typical homogeneous culture. **(a) Load panel.** Input BMP fluorescence images loading and output files saving options. **(b) ROIs selection panel.** Circular grid of square ROIs selected on an optical image of the homogeneous culture. Culture size is $\phi = 13$ *mm*; the total number of ROIs is 2604, and their individual lateral size 200 μm. **(c) Average fluorescent activity trace.** Mean fluorescence trace averaged over all output ROIs' traces, and for the whole 20 *min* recording of activity. Vertical axis in arbitrary units.

Figure 2.10 illustrates NeuroImages' output single–ROI fluorescence activity traces, and for typical homogeneous and patterned cultures. Activity in homogeneous networks presents whole–network bursts with high similarity between ROIs. Patterned cultures exhibit more complex activity, with a richer repertoire of dynamical patterns and multiple subsets of highly coordinated neurons.

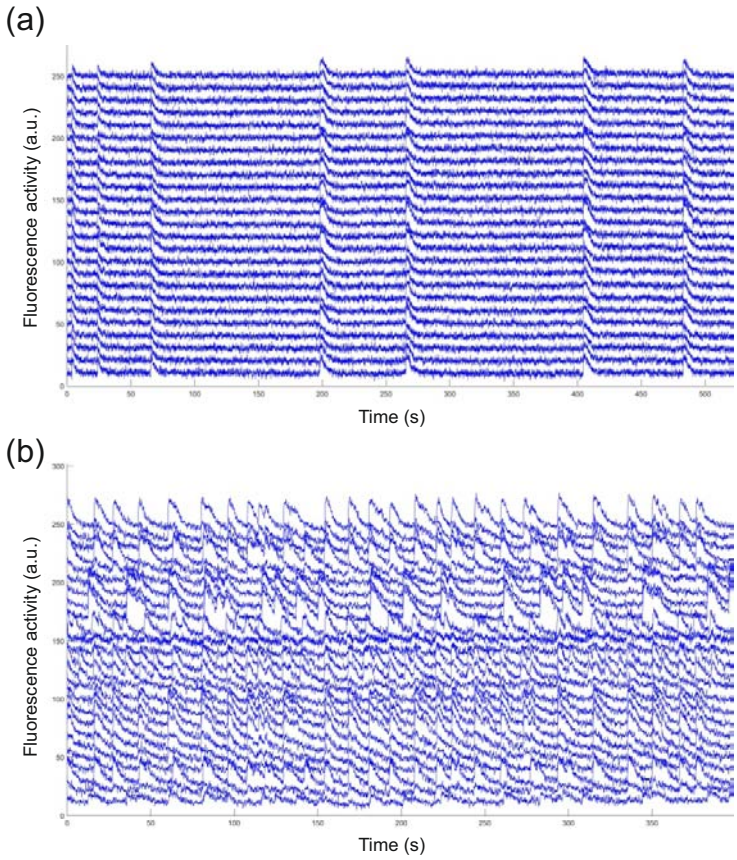

Fig. 2.10 Single–ROI fluorescence data. Illustrative fluorescence activity plots of NeuroImages' output data. **(a) Homogeneous data.** Typical fluorescence traces for 25 ROIs in a homogeneous culture. **(b) Patterned data.** Typical fluorescence traces for 25 ROIs in a patterned culture.

2.4.3 NeuroDynamics: individual activation times

The determination of individual times of activation for each neuron (ROI) in each network burst was performed using *NeuroDynamics*, a software also written by Dr. Jordi Soriano. Initially, I developed a custom program that was able to extract activation times in a automatized, faster, yet slightly less accurate manner. Nevertheless, we finally opted for NeuroDynamics due to its better performance.

NeuroDynamics required the aforementioned fluorescence intensity matrix file, as well as the ROIs location file. Once both files were loaded, fluorescence traces were explored manually in order to find the ROI with best signal–to–noise ratio, and that contributed to all network bursts. When the optimal ROI was discriminated, we manually identified each burst in its fluorescence profile. Next, for each observed burst we manually discriminated the fluorescence baseline and the sudden fluorescence increase in this ROI. The former was stated as a linear fit in a certain time range immediately previous to the firing of the ROI, and the latter was derived as a linear fit of the slope corresponding to the fast activation of the ROI. Finally, NeuroDynamics automatically extracted those linear fits for the remaining ROI, and provided the activation time of each region of interest in this network burst as the intersection between its baseline and its burst–slope linear regression. A snapshot of NeuroDynamics interface is shown in Fig. 2.11.

The former steps were repeated for each burst. Taking into account the necessary manual implementations and computing time, and the usually large number of observed bursts (~ 100), the whole process lasted between 1 and 3 hours. The final output data consisted of an ASCII '.DAT' matrix file for each burst, where rows defined ROI index, and columns indicated x–positions, y–positions and activation times.

2.4.4 Cone fit: initiation points and velocity of propagation

The previously mentioned NeuroDynamics also provided a rough measure for focusing points and velocity of network bursts. Those results derived the center of mass of the three first firing ROIs to determine bursts' initiation points. And the propagation velocity was then obtained by calculating the center of mass of the last three firing ROIs, deriving the euclidean distance to the initiation point, and finally dividing it by the total elapsed time. This method disregarded the majority of the spatio–temporal information, since it relied solely on initial and final data points.

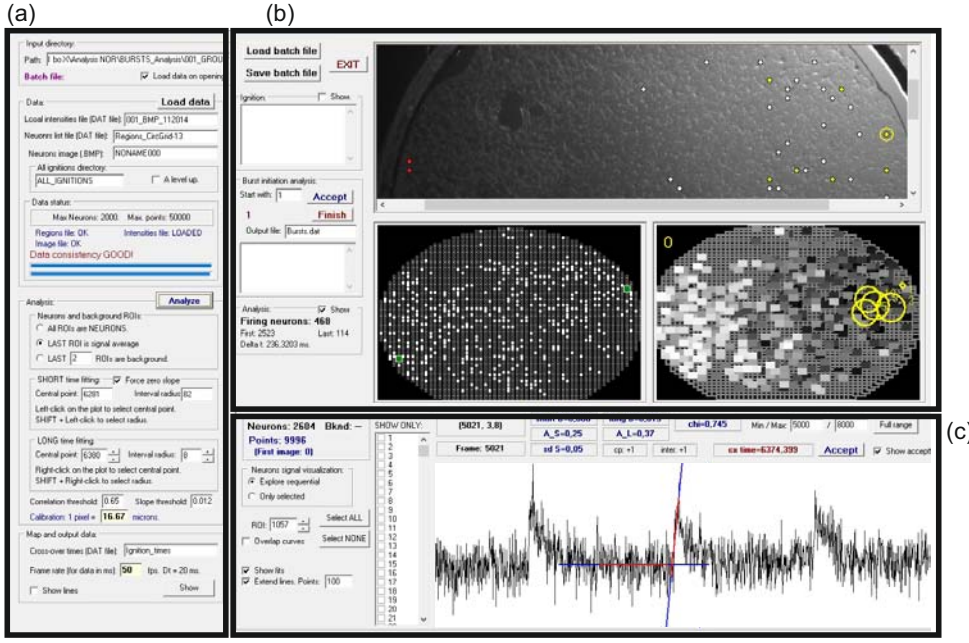

Fig. 2.11 NeuroDynamics interface for bursts' initiation and propagation analysis. ROIs activation times extraction for a typical homogeneous culture. **(a) Load, save and parameters panel.** Input fluorescence activity matrix (from NeuroImages) loading panel, output saving details, and parameter tunning options. **(b) Visual analysis panel.** Upper plot: optical image of the culture with ROIs' location displayed as white dots; first (last) 10 active ROIs in this particular burst are portrayed as yellow (red); first active ROI is encircled; total culture size is $\phi = 13$ *mm*. Bottom–left plot: sketch of discarded (gray) and accepted (white) ROIs in terms of their signal–to–noise ratio. Bottom–right plot: grayscale map of ROIs activation times; first to last firing ROIs plotted as black to white rectangles; yellow circles depict 1, 2, 3, 5, and 10 first active ROIs, with center at their respective center of mass and radius equal to the corresponding standard deviation. **(c) Fluorescent activity trace for the best ROI.** Fluorescence trace for best signal–to–noise ratio ROI; horizontal axis is 1 *min* long; vertical axis in arbitrary units; horizontal red line shows the fitted baseline for this ROI in this burst; almost–vertical red line portrays the activation slope for this ROI in this burst; final activation time for this ROI is assessed as the temporal coordinate of intersection between the two red lines.

In order to confidently extract both the initiation points and the propagation velocity, I developed a new analysis method, grounded on the assumption that bursts' propagation took the form of circular activity fronts with isotropic constant velocity. In this framework, a three–dimensional representation of

the analyzed data would display an inverted cone (Fig. 2.12). X and Y axis would plot the position of the ROIs, and Z axis would represent the corresponding activation times. Therefore, the initiation points and the propagation velocity would be accurately extracted from the parameters of the fit between the processed data and the equation of an inverted cone. That is,

$$t = 1/v \cdot \sqrt{(x-x_0)^2 + (y-y_0)^2} + t_0, \tag{2.1}$$

where t was the activation time, and x and y were the coordinates of the ROI. The parameters of the fit were: v the velocity of propagation, x_0 and y_0 the coordinates of the initiation point, and t_0 the onset time of the network burst.

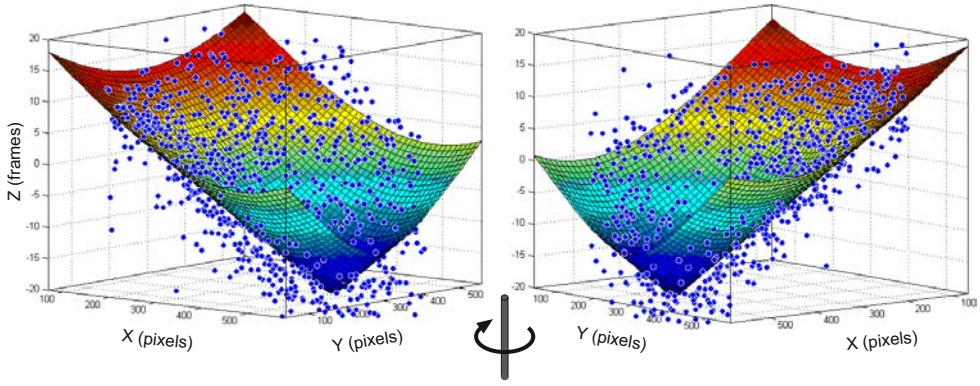

Fig. 2.12 Extraction of the initiation point and propagation velocity in a slow network burst. Two perspectives for the same, three–dimensional inverted cone (surface with color gradient) fit to experimental data (blue dots) for a typically slow network burst in a homogeneous network. X and Y axis are the two–dimensional coordinates of the analyzed ROIs in the experimentally recorded images, in pixels. $X-Y$ values are determined when selecting ROIs with NeuroImages. Z axis is the activation time for each ROI in this specific burst, in frames, shifted so that axis' origin coincides with the average activation time. Onset times of activation are obtained with NeuroDynamics. Estimated initiation point coordinates are given by the tip of the inverted cone, i.e. $(x_0, y_0) \approx (450, 300)\ pixels = (6.8, 5.1)\ mm$ for a spatial resolution of 17 $\mu m/pixel$. Propagation velocity is provided by the inverse of the slope of the inverted cone, i.e. $v \approx 15\ pixels/frame = 13\ mm/s$ for a frequency of acquisition of 50 $frames/s$.

We note that Eq. 2.1 was only valid for homogeneous cultures, since the assumption of a circular front of constant velocity did not hold for patterned or clustered cultures. However, in this particular context, this analysis arose as an efficient, robust method, able to extract confident results even from highly noisy data.

The probability density functions (pdf) of the location of initiation points in a recorded experiment were estimated from gaussian mixture distributions (MATLAB 2017a), with each gaussian's center and sigma extracted from the initiation point's coordinates and uncertainty in the corresponding cone fit.

As a final remark, we would like to highlight the great amount of time devoted to experimental data analysis. Taking into account all the aforementioned steps, a complete analysis of a single experimental recording of activity lasted no less than 7 hours. And for experiments that consisted of multiple recordings and different substrate regions, the total time of analysis added up to $\sim 30\ h$. This, together with the actual time invested in the performance of experiments, and the $1-2$ weeks for culture maturation, might show the great effort dedicated to the experimental part of this thesis.

Chapter 3

Ising Model to Quantify Average Connectivity in Neuronal Cultures

In this Chapter we introduce a novel Random Field Ising Model, grounded on previous experimental observations, to assess the behavior of cortical circuits *in vitro* and extract information of their connectivity in a percolation framework. The study shown here was an initial suggestion from Benedetta Cerruti and Eduard Vives, at the University of Barcelona, whose research in magnetic materials provided the initial mathematical model and analysis tools.

3.1 The problem of connectivity inference

We have pinpointed in previous chapters the existence of robust, well–timed spontaneous activity patterns in neuronal cultures. These patterns emerge from a complex interplay between connectivity, intrinsic neuronal dynamics and noise. Despite the robustness of spontaneous activity, the mechanisms that initiate and sustain it, as well as the role of the different actors, are still not fully understood. In the quest for identifying these mechanisms and develop modeling scenarios, a fundamental ingredient is the characterization of the

connectivity blueprint of a neuronal network. Since the precise identification of all neuron–to–neuron synaptic links is unpractical for networks with $\sim 10^3$ neurons or larger, a major effort has been devoted to seek for strategies to bring to light such an information, a challenge that has become by itself an active field of research in Physics and Neuroscience.

A first group of strategies include the use of model–free *reconstruction* tools to infer structural connections from activity data via transfer–entropy (Garofalo et al., 2009; Orlandi et al., 2014; Stetter et al., 2012) or mutual information (Bettencourt et al., 2007); and the use of model–based approaches that take into account the properties of spiking neurons (Burioni et al., 2014; Goltsev et al., 2010; Lee et al., 2014).

A second group, and that falls within the aim of this Chapter, applies concepts from phase transitions (Lee et al., 2014) and critical phenomena (Dorogovtsev et al., 2008), most notably in the context of percolation transitions (Goltsev et al., 2006, 2008; Nagler et al., 2011) and spin models (Dorogovtsev et al., 2002, 2008).

On the one hand, percolation models explored theoretically (Achlioptas et al., 2009; Baxter et al., 2010; Nagler et al., 2011; Tlusty and Eckmann, 2009) and experimentally (Breskin et al., 2006; Cohen et al., 2010; Soriano et al., 2008) the transition from an assembly of connected neurons to a disconnected population as the connectivity probability between neurons gradually reduced. These models considered as order parameter the size of the largest group of connected neurons (*giant component*), and investigated the characteristics of both the transition curve and point to assess the major structural features of the network, in particular the distribution and average number of connections (Cohen et al., 2010; Jacobi et al., 2009; Soriano et al., 2008).

On the other, neuronal spin models map the on/off nature of the neurons onto spin states that interact through the connectivity. Initially, Hopfield (1982) applied a spin model to simulate neuronal networks of $N \sim 40$ ele-

ments in order to analyze content–addressable memory based in multiple locally stable states. However, it was not clear whether spin–spin correlations sufficed to characterize the collective behavior since neuronal networks have weak pairwise interactions and present higher–order correlations among large groups of elements. Spin models for neuronal networks took special relevance when Schneidman et al. (2006) showed that pairwise correlations alone can describe very precisely their interactions, e.g. in the vertebrate retina and cultured cortical neurons. Tkacik et al. (2009) extended the same conclusion to larger simulated ensembles applying Ising model and found evidence that neuronal networks work near thermodynamic criticality. The reconstruction of couplings between neurons from activity data for small ensembles was optimized by Roudi et al. (2009). Simultaneously, Cocco et al. (2009) provided real-time reconstruction of networks up to $N \simeq 200$. And Schaub and Schultz (2012) demonstrated the practicality of using the Ising model in mean field to decode patterns of heterogeneous activity for larger ensembles $N \sim 10^2 - 10^3$ in a millisecond timescale.

Given the success of the above studies in modeling the behavior of neuronal networks with both percolation and spin models, we explored the possibility to bridge both scenarios to deepen in the understanding of the *percolation experiments* carried out by Jordi Soriano and coworkers at the Weizmann Institute of Science along 2005–2010.

3.2 Percolation experiments

Here we describe in detail the percolation experiments to better comprehend the developed theoretical modeling. We proceed as follows. First, percolation in neural cultures is briefly introduced. Afterwards, the experimental protocol is explained. Then, the contribution of spontaneous and stimulated activity is described. And, finally, the effect of inhibition and the discrimination of glia cells are discussed.

Historically, percolation was studied in the context of porous media and water permeability in order to derive the probability for water to cross (*percolate*) a given system. With such a porous system in mind, a key concept is that a fraction of the sites of the system block water, whereas the rest let it flow through. Tunning the proportion of permeable sites in the system gives rise to a percolation transition that separates two main phases: a first one, with a low fraction of permeable sites and no macroscopic penetration of water in the porous medium; and a second one with a higher fraction of permeable sites, where water has a finite probability of crossing the entire system. In the second phase, one might define the *giant component* g as the largest community of adjacent wet sites at equilibrium. In the first phase, g is non–existent.

In our context of neuronal networks, a parallelism around these concepts can be constructed (Fig. 3.1). Our equivalent to the porous medium is the neuronal network, and the water flow is the propagation of activity between interacting cells, i.e. firing neurons feature wet sites. Then, highly connected neurons correspond to totally permeable sites, whereas those that exhibit little connectivity play the role of blocked sites. Furthermore, the first phase of the percolation approach describes uncorrelated activations at low connectivity values. The second phase, above the percolation transition and with a giant component present, matches the bursting behavior of homogeneous cultures. The *giant component* in this neuroscience parallelism corresponds to the largest community of firing, connected neurons (Breskin et al., 2006; Cohen et al., 2010; Soriano et al., 2008).

Given the parallelism between strongly/weakly connected neurons and permeable/blocked sites, there must be a *connectivity threshold* (or *demand of inputs*) m above which neurons are able to propagate the activity. Since the voltage increase required for the activation of a neuron is about ~ 30 mV with respect to the membrane's resting potential, and since a positive input from another neuron provides an average increase of $\sim 2-3$ mV, then at

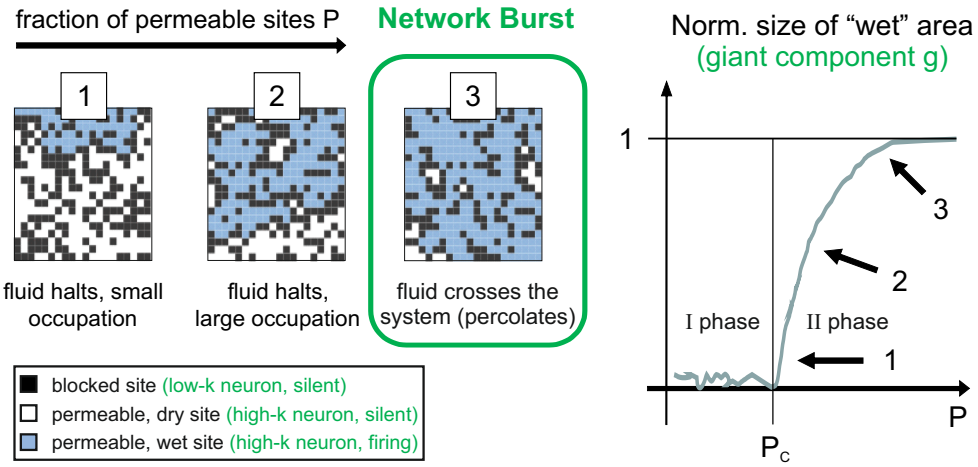

Fig. 3.1 Original percolation and parallelism in neuronal networks. Conceptual sketch of three porous mediums with increasing proportion P (1 to 3) of permeable sites (white and blue squares), decreasing proportion $1-P$ of blocking sites (black squares), and the corresponding fraction of wet sites (blue squares). Blocking sites correspond to low connectivity neurons (low–k); and permeable sites, which are subdivided in dry and wet sites, are featured by silent and firing highly connected neurons (high–k) respectively. The rightmost plot shows the fraction of wet sites in terms of P; with the critical proportion P_c separating the first, non–permeable I phase ($P < P_c$) from the second, finitely permeable II phase ($P > P_c$). The fraction of wet sites is the giant component g of neuronal cultures.

least $m = 15$ 'simultaneous' inputs are needed to activate a neuron (Soriano et al., 2008). We consider two inputs to be simultaneous if the maximum time difference between them is $\Delta t \lesssim 2\tau$, where $\tau \sim 10$ ms is the time constant of the exponential decay of the membrane potential due to leaking currents. Thus, if a neuron receives $m = 15$ or more positive inputs in a time window of ~ 20 ms, it will fire. We conclude that, in a culture with unperturbed conditions, a neuron with $k < 15$ connections is a blocking site, being permeable otherwise.

We note that post–synaptic potentials are strictly not unitary and can cover a broad range, i.e. from 0.1 to 10 mV. However, in our experiments, there are $10^1 - 10^2$ connections per neuron (Soriano et al., 2008). Therefore, the variability in post–synaptic potentials is smoothed out even at a single neuron level to get some average connectivity strength around 2 mV. This average

behavior was reflected experimentally in the fact that, when performing several measures with identical conditions, the macroscopic activity was very similar. Although the particular sequence of neuronal activations could vary, experiments showed that the possible variability of post–synaptic potentials was not relevant at a macroscopic scale.

Deepening in our percolation parallelism, there is a final feature left, namely the ability to tune the fraction of permeable and blocked sites. This would naturally correspond to tune the distribution of connections; however, the structural connectivity in neuronal cultures is virtually inaccessible and cannot be manipulated at will. The feasible option is to tune the connectivity threshold in a functional manner, i.e. by weakening the synaptic strength of all the connections equally through the application of the drug CNQX (pharmacological details provided in a later Section). As the concentration of CNQX increases in the culture medium, a higher fraction of the AMPA-receptors in each synapse is blocked, and the global synaptic strength J is reduced. The initial demand of inputs of $\tilde{m} = 15$ corresponds to the lowest possible, before application of the drug. Afterwards, the connectivity threshold follows $m = \tilde{m} \cdot (1 + \frac{[CNQX]}{\kappa_d})$, with $\kappa_d = 300$ nM the dissociation constant, i.e. the concentration of CNQX at which half of the excitatory AMPA-receptors are blocked (Soriano et al., 2008). The value of the demand of inputs at the percolation transition is defined as $m \equiv m_D$, and is directly related with the average connectivity of the neuronal network, as also stated in Soriano et al. (2008).

Since real neuronal networks exhibit complex dynamics, and percolation approaches characterize equilibrium states of the system, one has to perform percolation experiments that provide some *static* measure of the activity. In order to fulfill this requirement, our experiments assess the fraction of neurons that become active in a time window of $\sim$1 s upon an instantaneous electric stimulation of the culture; and for different levels of disintegration of the neuronal network.

Three major assumptions were considered to fulfill the static condition. First, no neuron activates due to direct or indirect stimulation after $\sim$1 s; second, the culture is in a *global resting state* just before being stimulated; and third, those neurons responding to the stimulation activate only once during the recorded time window. The first assumption ensures that we record the entire activity response, and it is in agreement with experimental data since the observed activity in our cultures reaches the total responding population within a 500 ms window. The second implies that the activations do not arise from spontaneous activity prior to stimulation, i.e. no spontaneous bursting. This is assured by the experimental protocol described in the following Section. Finally, the third assumption does not have to be strictly true for neuronal cultures, since the probability of multiple spiking for excitable neurons in network bursts is reported to be low (Alvarez-Lacalle and Moses, 2009). Indeed, the fluorescent amplitude of bursts evinced single spikes for individual neurons, at least for a broad range of the network disintegration, i.e. for [CNQX] $>$ 200 nM. The latter feature can be observed in the constant fluorescence amplitude of bursts at different disintegration values for a typical culture in Fig. 3.4b. We note that this third assumption has to be stated due to a limitation of the *fluorescence calcium imaging* technique: the refractory time of fluorescence decay after firing is similar to the time window recorded and, therefore, second and higher firings of the neurons cannot be accurately resolved.

3.2.1 Experimental Procedure

Percolation experiments were carried out as described in Refs. Breskin et al. (2006); Cohen et al. (2010); Soriano et al. (2008). Cultures were prepared following the standard procedures for primary brain rat neurons described in Chapter 2. The spatial distribution of neurons varied between a uniform coverage (*homogeneous* configuration) and a highly localized one (*aggregated* configuration), and was set by adjusting neuronal adhesion onto the glass

substrate. In this Chapter we focus on the homogeneous scenario. Although neurons covered an area of about 130 mm^2 (which corresponds to a 13 mm diameter glass coverslip), only a region of 0.8×0.7 mm^2 (Width$\times$Height) was imaged, i.e. about the 0.5% of the culture. All recordings were carried out at room temperature.

Experiments consisted in obtaining the set of *response curves* (Fig. 3.2a) of the neuronal culture at gradually higher CNQX concentrations and upon a series of short, 20 ms biphasic electric stimulations of increasing strengths V, delivered through bath electrodes that stimulated the entire culture. The neuronal network response to stimulation was quantified through fluorescence calcium imaging (Figs. 3.2b-c), and by counting the fraction of neurons ϕ that responded to a given voltage V. A conceptual sketch of the disintegration at the level of individual neurons is presented in Fig. 3.3.

The cultures were spontaneously active at low CNQX concentrations and, therefore, stimulation had to be carefully applied. We proceeded as follows. First, we determined the shortest inter–burst interval (IBI) along 3 min of spontaneous activity at [CNQX]=0. Second, we waited for the occurrence of a spontaneous burst. And, third, once $\sim 90\%$ of the shortest IBI elapsed, the stimulation was applied. At high [CNQX], when no spontaneous bursting is observed, the time of application of the electric stimulation is decided by the experimentalist, with the only constraint that neurons rested for a sufficient time (about 30 s) between two consecutive stimulations.

In general, once the shortest IBI was stated, we could easily build all the *response curve*. The first point corresponded to a voltage of typically 2.2 V. We then counted the fraction ϕ of active neurons, and then repeated the measurement for progressively higher V, which typically increased in steps of 0.2 V, until all neurons responded ($\phi = 1$). Afterwards, the first dose of CNQX was applied, which was followed by 5 min waiting time for the drug to diffuse and take effect, and then the voltage scan procedure was repeated.

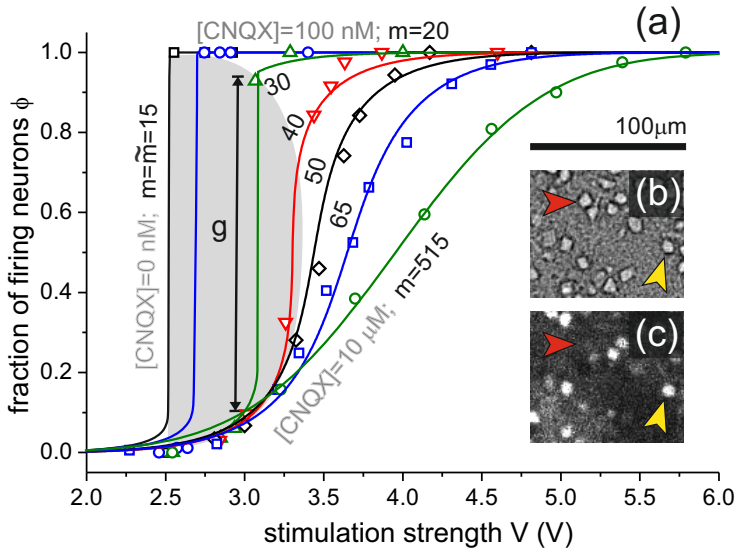

Fig. 3.2 Experimental results and model construction. **(a)** Fraction of responding neurons ϕ at stimulation voltage V for an E–only homogeneous culture. From left to right, symbols are experimental data at $[CNQX] = 0$, 100, 300, 500, 700, 1000 nM and 10 μM. The values of the demand of inputs $m = \tilde{m} \cdot (1 + [\mathrm{CNQX}]/k_d)$ are also indicated, with $\tilde{m} = 15$ and $K_d = 300$ nM. The gray area illustrates the disintegration of the giant component g. The solid lines correspond to the fit of the mean–field approximation to the experiments, and with parameters $H_0 = 4.2 \pm 0.1$ V, $\sigma_h = 0.80 \pm 0.03$ V and $m_D = 39 \pm 1$. **(b)** Bright field image of a small region of a neuronal culture. Round objects are neurons. **(c)** Corresponding fluorescence image. The brightest spots (yellow arrow) are neurons activated as response to the electrical stimulation. Non–firing neurons remain darker (red arrow).

The [CNQX] values explored were typically [CNQX] = 0, 0.1, 0.3, 0.5, 0.7, 1, and 10 μM. Each response curve was analyzed to determine the largest jump in ϕ between two consecutive voltage steps, providing the size of the giant component g at a given concentration of CNQX (Breskin et al., 2006; Cohen et al., 2010; Soriano et al., 2008). Values of $g \lesssim 0.1$ could not be experimentally resolved and g was therefore set to 0.

3.2.2 Fluorescence Probe and Pharmacology

The neuronal culture of interest was placed into a recording chamber that contained a pH–stable medium ('Recording Solution', RS) that maintained

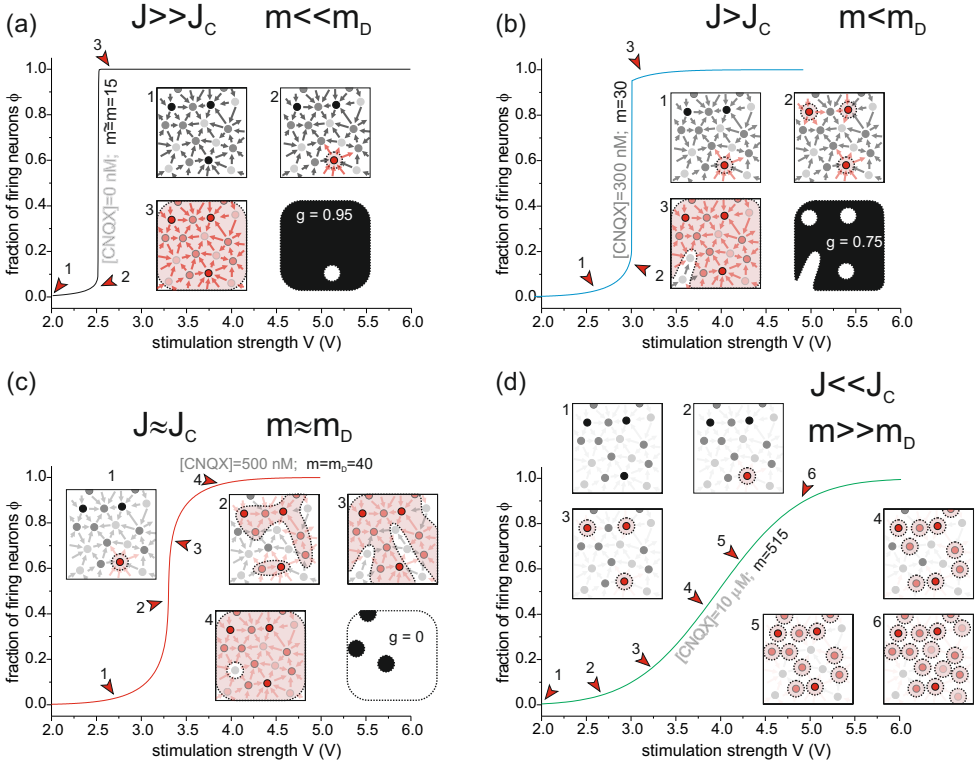

Fig. 3.3 Sketch of neuronal connectivity disintegration. Main plots depict typical response curves at four decreasing values [(a) to (d)] of the neuronal coupling strength J. The (a) and (b) plots correspond to the supercritical regime with finite giant component; the (c) plot presents the response curve at criticality where the giant component vanishes; and (d) shows the subcritical behavior with no giant component. Insets: Circles depict individual neurons, each one with its own sensitivity to the stimulation, and that is coded as three levels of color opacity: light color corresponds to weakly reactive, medium color for moderately sensitive, and dark color for highly reactive neurons. Red circles with black outline show active neurons. Neuronal connections are depicted as directed arrows; inactive (active) connections are drawn in black (red). The connection strength along disintegration is illustrated by the opacity of the arrows: from dark to light gray (red). The communities of active, directly interacting neurons are displayed by light red areas. The black area shows the giant component, defined as the largest avalanche for $J \geq J_c$.

the culture healthy during data acquisition. The chamber was then loaded with the calcium fluorescence probe fluo4-AM and the culture incubated in darkness for 40 min. After washing off residual fluo4 with fresh RS, the

culture was finally placed in an inverted microscope for actual measurements (see Chapter 2).

Cultures contained both excitatory (80%) and inhibitory (20%) connections (Marom and Shahaf, 2002), and the experiments were designed in such a way that networks containing only excitation ('E–only' networks) or both receptor types ('E+I' networks) could be explored. We remark that the applied drug CNQX (6-cyano-7-nitroquinoxaline-2,3-dione) is the antagonist of the AMPA (alpha-amino-3-hydroxy-5-methyl-4-isoxazolepropionic acid) type receptors in the glutamate synapses of excitatory neurons. This CNQX drug, however, cannot target NMDA (N-methyl-D-aspartate) receptors, the second most frequent driver of excitation. Thus, for a neat exploration of the disintegration process, the NMDA excitatory receptors were completely blocked with 20 μM of the corresponding antagonist APV (2-amino-5-phosphonovalerate), enabling the study of network breakdown due solely to CNQX.

We must clarify that the original percolation experiments of Soriano and coworkers explored both excitation and inhibition. In our case, however, and for simplicity in the description of the model, inhibitory synapses were ignored, i.e. in all experiments considered here inhibition was blocked through application of 40 μM bicuculine, a $GABA_A$ (Gamma-aminobutyric acid) receptor antagonist (Breskin et al., 2006). The influence of inhibitory synapses in the results is discussed in Section 3.2.4.

We note that CNQX does not change neurons' membrane properties, and therefore neuronal excitability to electric stimulation is constant. This is supported by the study of Yamada et al. (1989), who observed that CNQX did not modify the current–voltage relationship at the membrane; and by the work of Vergara et al. (2003), who carried out a study in which they measured membrane oscillations in a given neuron, then applied [CNQX] = 10 μM (a saturating concentration), measured again, and observed that oscillations'

strength and frequency remained intact, supporting the insensitivity of membrane characteristics to CNQX.

3.2.3 Spontaneous and stimulated activity

We note that neurons in culture exhibit strong spontaneous activity in the form of bursts that encompass the entire functionally connected culture (Orlandi et al., 2013), and with a typical frequency of $\varphi_0 = 3$ bursts/min. In principle, one could attempt to determine the size of the giant component at a given [CNQX] from the analysis of such spontaneous bursts. However, the construction of disintegration curves $g(m)$ solely from spontaneous activity is not possible due to the rapid decay of the latter with CNQX.

The results shown in Fig. 3.4a illustrate the aforementioned impossibility, and show that spontaneous activity ceases at CNQX values much smaller than the vanishing point of the giant component upon stimulation. For CNQX around 150 nM the bursting frequency has already decreased to half the original, to abruptly become rare or inexistent for [CNQX] $\gtrsim$ 400 nM. By contrast, the size of the giant component g is still around 0.8 at the latter concentration. Hence, lower values of g are totally inaccessible without stimulation, and therefore a complete determination of the $g(m)$ curve is unattainable by means of spontaneous activity. Additionally, we remark that the determination of g through the study of spontaneous bursts would require gradually longer recordings to compensate for the decay in bursting frequency, as shown in Fig. 3.4b. These long recordings would affect the health of the neurons due to photo–damage and would ultimately compromise the quality of the data.

On the other hand, although spontaneous activity rapidly decays with CNQX, for [CNQX] $\lesssim$ 200 nM it is sufficiently strong to interfere with the electric stimulation, as described earlier. Overall, we conclude that, to extract the whole disintegration curve for the giant component, and in a consistent

way thorough the process, it is necessary to record culture response upon electric stimulation while controlling spontaneous activity.

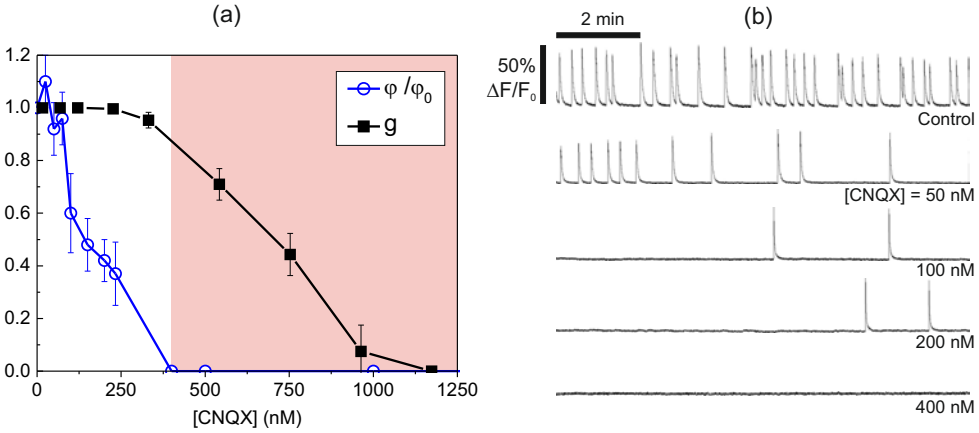

Fig. 3.4 Spontaneous activity of an homogeneous culture in terms of the concentration of CNQX. (a) Normalized spontaneous bursting frecuency φ/φ_0, and giant component g, under increasing concentrations of CNQX. Square data points are an average over 4 cultures. Error bars are standard deviation. The pink area denotes the inaccessible regime for the spontaneous activity. **(b)** Average fluorescence activity traces at different concentrations of CNQX. Vertical axis in normalized arbitrary units.

3.2.4 Effect of inhibition

As described before in Soriano et al. (2008), disintegration curves $g(m)$ could be constructed in conditions in which both excitation and inhibition are active ('E+I' networks) or in conditions in which excitation is only active ('E–only' networks), with inhibition fully blocked through application of bicuculline. That study showed that disintegration curves were almost identical, with the only difference that the 'E+I' networks exhibited a smaller m_D as compared to the 'E–only' ones. This shift was interpreted as an effective increase of the demand of inputs in 'E+I' networks that procured an earlier disintegration.

Although in our study we consider solely 'E–only' networks, we note that, when data is plotted as $g(m/m_D)$, the relative shift between the normalized

disintegration curves for 'E+I' and 'E–only' effectively disappears and both curves collapse (Fig. 3.5). This collapse is fulfilled as far as inhibitory neurons appear uniformly across the network, i.e. that they do not concentrate in particular areas.

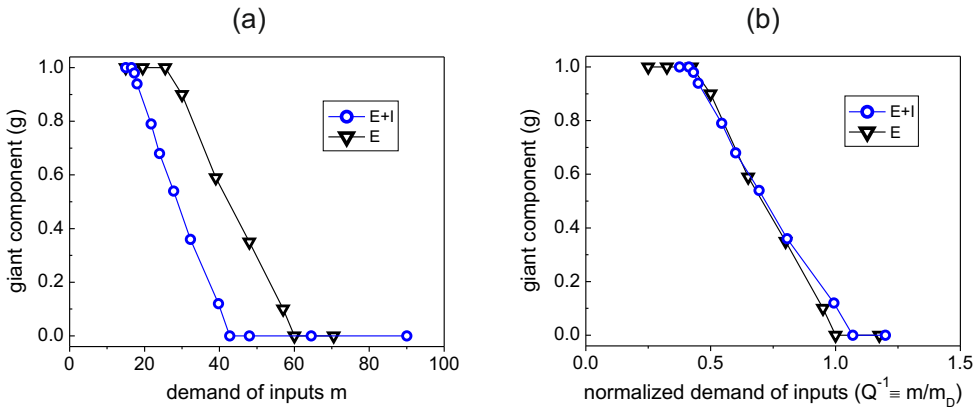

Fig. 3.5 Disintegration curves for 'E+I' and 'E–only' networks. (a) $g(m)$ disintegration curve for the two connectivity scenarios. **(b)** Corresponding normalized disintegration curves, illustrating the good collapse of data points. Data is adapted from Soriano et al. (2008).

3.2.5 Discrimination of glia

Our cortical neuronal cultures present a typical fraction of $\simeq 20\%$ glial cells, which are composed almost completely of astrocytes. In general, astrocytes remain essentially unaffected by the application of external fields, and exhibit a different firing profile than neurons. However, they present slow internal calcium dynamics that can be triggered as a response of neuronal activity. Since astrocytes also incorporate the calcium probe, there was the possibility (though rare) to confuse some particularly bright astrocytes with active neurons.

To rule out such a possibility, we took advantage of the large amplitude of firing upon stimulation at low CNQX to reveal the astrocytes in the network. As shown in Fig. 3.6, a strong stimulation in this regime led to high fluores-

cence amplitudes in the neurons, but also uncovered the indirect, transient response of the astrocytes, in which the maximum in fluorescence amplitude appeared 2–3 s after neuronal activation. This characteristic pattern appeared in all astrocytes, and was therefore straightforward to eliminate them from analysis. Additional strategies to identify astrocytes were treated in Breskin et al. (2006).

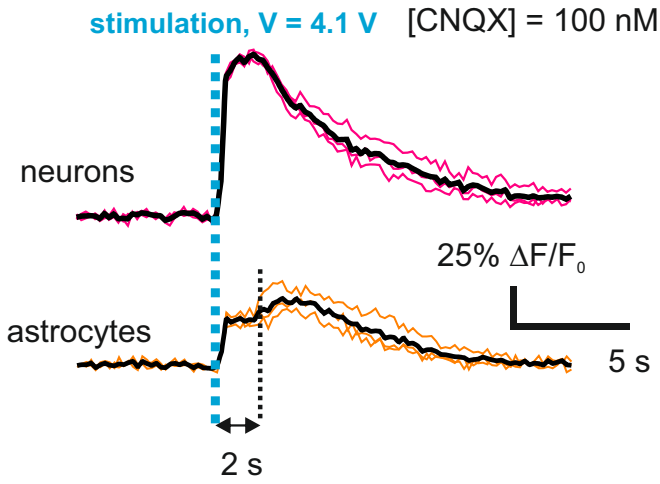

Fig. 3.6 Discrimination of astrocytes. Fluorescent activity traces of three typical neurons (pink) and astrocytes (orange), together with the average fluorescence for clarity. The strong stimulation $V = 4.1$ V served to evoke activity in astrocytes and identify them through their fluorescence pattern, characterized by a maximum in fluorescence that appeared 2–3 s after neuronal stimulation.

3.3 Model

The above experimental observations, specifically the response curves $\phi(V)$ and the behavior of the $g(m)$ curves, caught our attention in the search for new models to understand the role of neuronal connectivity. We finally proposed a new model that significantly improves the predicting power of previous attempts.

Our theoretical scenario is grounded on an ordinary zero–temperature Random Field Ising Model of N spins on a directed network (Dhar et al., 1997; Illa et al., 2006; Sethna et al., 1993). The most general form of the model does not contain any information on the spatial arrangement of the neurons or any other metric–related feature, nor the distribution of connections, and is therefore valid for any network.

3.3.1 Hamiltonian

The Hamiltonian for the Neuronal Network Ising Model (NNIM) reads

$$\mathscr{H} = -\sum_{i=1}^{N} s_i \left(J \sum_{\{j_E\}_i} s_j - \gamma \sum_{\{j_I\}_i} s_j + h_i + \tilde{H} \right), \tag{3.1}$$

where $s_i = 0$ *or* 1 are the spin variables for inactive or active neurons, respectively. $J = J_0/m$ is the excitatory exchange energy with a uniform coupling approximation; J_0 is a constant and m is the experimental control parameter upon disintegration. $\gamma = J_0/m_0$ is the constant inhibitory exchange energy, equal to J only at the initial regime [CNQX] $= 0$ μM. $\{j_E\}_i$ and $\{j_I\}_i$ are the set of excitatory and inhibitory input (presynaptic) neighbors of the ith neuron. h_i are the Gaussian–distributed local random fields that account for neuronal intrinsic variability. And $\tilde{H}$ is the effective external field, defined as $\tilde{H} \equiv H - H_0$, with H_0 a systematic correction. Our observable of interest in the model is the magnetization $M \equiv \langle s \rangle$, i.e. the fraction of active neurons ϕ.

For the complete description of the model, several assumptions require further explanation:

The first one deals with inactive neurons after stimulation, which are treated in the model as spins with value $s_i = 0$, since they do not interact with other neurons. Consequently, they do not contribute to the Hamiltonian and effectively act as temporary removed spins in a diluted system.

The second one accounts for the effect of CNQX in the interaction between neurons: J is assumed to be proportional to the number of functional excitatory receptors in the synapses, which is inversely proportional to the demand of inputs m. Therefore, $J = J_0/m$. We remark that the inhibitory exchange energy γ is constant and does not depend on CNQX as this drug only blocks AMPA excitatory receptors in glutamate synapses, as explained in Section 3.2.2. Additionally, we also consider that the population of neurons obeys the Dale's principle, i.e. excitatory (inhibitory) neurons have solely an excitatory (inhibitory) action, regardless of the nature of the target, post–synaptic neuron.

The third assumption considers that each neuron presents its own sensitivity to the electric stimulation, and that is related to the particular alignment of the axons of pyramidal neurons with respect to the applied external field (Rotem and Moses, 2008). The combination of sensitivity and intrinsic noise of neurons is taken into account in the quenched random fields h_i. The Gaussian nature of these fields in the model is asserted from the experimental response curve at [CNQX] $\to \infty$, i.e. a situation of independent cells that have to be excited one by one. As shown in Fig. 3.2a, the curve $\phi(V)$ in this regime fits well to an error function, indicating that the excitability for individual neurons is indeed Gaussian distributed, and with mean $V_0 \simeq 3.96$ V and width $2\tilde{\sigma} \simeq 1.45$ V.

The fourth assumption is linked to the experimental protocol, devised to provide a resting, non–active culture before stimulation. This initial inactive state implies that we have to introduce a systematic correction $-H_0$ in the value of the external field of the model, otherwise $\phi \neq 0$ at $H = 0$.

The fifth assumption considers that the biphasic pulsed stimulation of 20 ms is equivalent to a continuous driving of the external field, as usually performed for instance in the cycling of a magnetic system. This approach is consistent with experiments, since an increase of the external stimulation from V to $V + \Delta V$ activates those neurons firing at the value V together with some

new ones. In conclusion, we can associate the voltage V with the external field H of Eq. (3.1).

We also note that the experimental response curves in Fig. 3.2a closely resemble branches of hysteresis cycles and can actually be fitted via the NNIM athermal metastability hysteresis curves. Figure 3.7 provides an example of the $M(H)$ theoretical curves obtained from the implicit expression of Eq. (3.10), described in the next section. Although the curves should have the 'hysteretical' behavior of a magnetic system, we consider solely the ascending branch of the hysteresis loop to mimic the experimental data since the system always starts from an inactive state, so that the descending branch is experimentally unfeasible. Since the calcium–dynamics refractory time ($\sim$1 s) is two orders of magnitude larger than the characteristic time of application of the external field ($\sim$ 10 ms), the ascending branch of active states can be effectively viewed as kinetically stable states.

Table 3.1 summarizes the equivalence between the NNIM description and the experiments.

3.3.2 Mean–Field approximation

The model can be solved in the *mean–field* approximation. Mean–field implies that any neuron effectively experiences the same neighborhood (neuronal type and connectivity) and therefore similar response across the network. Hence,

NNIM	Experiments
Spin variables $s_i = 0$ *or* 1	Neuronal state: silent or firing
Magnetization $M \equiv \langle s \rangle$	Fraction of active neurons ϕ
Constant parameter γ	Relative E-I strength
Random fields h_i	Neuronal intrinsic variability
External field H	Applied Voltage V
Constant correction H_0	Initial inactive state

Table 3.1 Equivalence between experiments and NNIM model.

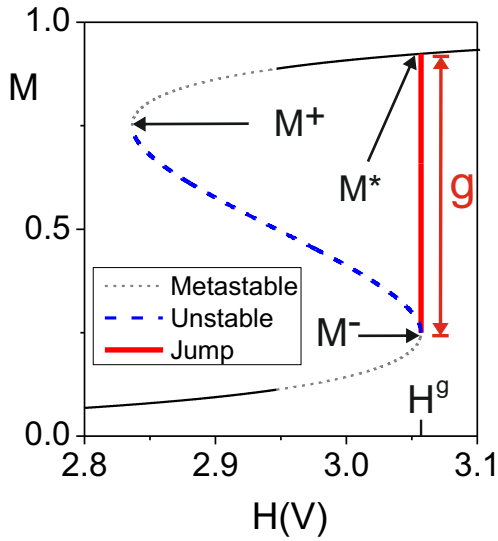

Fig. 3.7 Construction of the response curves. Analytical solution of the total magnetization in the mean–field approach [Eq. (3.10)], and the construction of the giant component g. Two stable curves (solid black lines), two metastable curves (dotted gray lines), and one unstable curve (dashed blue line) compose the theoretical magnetization curve. The giant component is constructed as the jump in the ascending branch of the hysteresis loop (solid red vertical line), from the metastable solution of highest external field (M^- at field H^g) to its counterpart stable solution at the same field (M^*). The final response curves shown in Fig. 3.2a consist of the lower stable and metastable curves, together with the jump of the giant component, followed by the higher stable curve in the range $H > H^g$. The complementary value of the metastable magnetization at the lowest possible external field is denoted as M^+.

we consider that the neighborhood activity is given by $\sum_{\{j_X\}_i} s_j = p_X k_i M$, where p_X is the fraction of excitatory ($X \equiv E$) or inhibitory ($X \equiv I$) neurons, k_i the number of input connections for the ith neuron, and $M \equiv \langle s \rangle$ the magnetization. The local potential of Eq. (3.1) then reads

$$\mathscr{F}_i = J_0 \left(\frac{p_E}{m} - \frac{p_I}{m_0} \right) k_i M + h_i + H - H_0. \tag{3.2}$$

At fixed H, the ith neuron will activate if its k_i and h_i values attain $\mathscr{F}_i > 0$, remaining silent otherwise. Since $s = \{0, 1\}$, then the average spin (magnetization M) is directly the probability of positive local mean–field

potential for an arbitrary neuron, which reads

$$P(\mathscr{F} > 0) = \int_{k_i=-\infty}^{k_i=+\infty} \rho(k_i) \int_{h_i(k_i,\mathscr{F}_i=0)}^{h_i=+\infty} \rho(h_i) dh_i dk_i, \tag{3.3}$$

where $\rho(k_i)$ and $\rho(h_i)$ are, respectively, the distribution of input connections and the Gaussian distribution of the random fields, with zero mean and standard deviation σ_h.

For simplicity, we assume that the neurons have a fixed number of connections $k_i = \bar{k}\ \forall i$. Then

$$M = \Phi\left(\frac{J_0\left(\frac{p_E}{m} - \frac{p_I}{m_0}\right)\bar{k}M + H - H_0}{\sigma_h}\right), \tag{3.4}$$

with Φ the normal cumulative distribution function.

Metastability analysis

As shown in Fig. 3.7, the metastability limits are linked to an infinite derivative of the magnetization with respect to the external field. We calculate these limits by derivating Eq. (3.4) with respect to M on both sides, i.e.

$$1 = J_0\bar{k}\left(\frac{p_E}{m} - \frac{p_I}{m_0}\right)\frac{e^{-\frac{\left(\frac{J_0\left(\frac{p_E}{m} - \frac{p_I}{m_0}\right)\bar{k}M^{\pm} + H^{\pm} - H_0}{\sigma_h}\right)^2}{2}}}{\sqrt{2\pi}\sigma_h}. \tag{3.5}$$

Additionally, we isolate the argument of Φ in Eq. (3.4), which leads to

$$\Phi^{-1}(M) = \frac{J_0\left(\frac{p_E}{m} - \frac{p_I}{m_0}\right)\bar{k}M + H - H_0}{\sigma_h}, \tag{3.6}$$

with Φ^{-1} the inverse of the normal cumulative distribution function.

The combination of Eq. (3.5) and (3.6) allows us to derive an expression for the metastability limits that is independent of both H and H_0, of the form

$$M^{\pm} = \Phi\left(\pm \sqrt{\ln\left[\frac{J_0 \bar{k} \left(\frac{p_E}{m} - \frac{p_I}{m_0} \right)}{\sqrt{2\pi}\sigma_h} \right]^2} \right). \tag{3.7}$$

Since we experimentally explore the culture starting from the network at rest and progressing at ascending values of V (H in the model), we consider solely the ascending branch and the solution M^-.

Magnetization

Taking solely into account the lower branch of the response curves, the emergence of a characteristic jump g (Fig. 3.7), and the disintegration of g at a critical value $m = m_D$, we can obtain a self–consistent equation for the magnetization.

Indeed, the giant component disintegrates at an observed value $m = m_D$ if and only if $M^+ = M^-$ for that value, which implies $M^{\pm} = 1/2$. There is neither instability nor metastability at any H for $m \geq m_D$. Then, from Eq. (3.7) we derive

$$J_0 = \frac{\sqrt{2\pi}\sigma_h}{\bar{k}\left(\frac{p_E}{m_D} - \frac{p_I}{m_0} \right)}. \tag{3.8}$$

We replace J_0 in Eq. (3.4) and obtain the magnetization as

$$M = \Phi\left(\sqrt{2\pi} \frac{\left(\frac{p_E}{m} - \frac{p_I}{m_0} \right)}{\left(\frac{p_E}{m_D} - \frac{p_I}{m_0} \right)} M + \frac{H - H_0}{\sigma_h} \right). \tag{3.9}$$

To further simplify this last expression, we focus on the 'E–only' condition ($p_I = 0$). Then, taking the notation $Q \equiv m_D/m$, we obtain the more compact

expression

$$M = \Phi\left(\sqrt{2\pi}QM + \frac{H - H_0}{\sigma_h}\right). \tag{3.10}$$

We also note that the metastability limits in Eq. (3.7) can now be written as

$$M^{\pm} = \Phi\Big(\pm\sqrt{\ln Q^2}\Big). \tag{3.11}$$

Giant component

The giant component g is obtained as shown in Fig. 3.7, in which one has to pay attention to M^*, and with the giant component given by $M^* - M^-$. The value of M^- is provided by Eq. (3.11). In order to obtain M^* we must know the corresponding external field H^*, which is the same as $H(M^-) \equiv H^-$ since the magnetization is bivaluated at this field. From Eq. (3.10), we infer

$$\frac{H^g - H_0}{\sigma_h} = -\sqrt{2\pi}QM^- + \Phi^{-1}\left(M^-\right), \tag{3.12}$$

where $H^g = H^- = H^*$.

Replacing this external field in Eq. (3.10) we find an implicit equation for M^- and M^*, the two possible values of the magnetization at H^g, i.e.

$$M = \Phi\left(\sqrt{2\pi}Q\Big(M - M^-\Big) + \Phi^{-1}\Big(M^-\Big)\right). \tag{3.13}$$

The solution $M = M^-$ is trivial due to redundancy in the calculations. We take $M = M^*$ and we use the definition $g \equiv M^* - M^-$ to obtain

$$g + M^- = \Phi\left(\sqrt{2\pi}Qg + \Phi^{-1}\Big(M^-\Big)\right). \tag{3.14}$$

Finally, by inserting the M^- expression of Eq. (3.11), we obtain the bivaluated equation

$$g + \Phi\left(-\sqrt{\ln Q^2}\right) = \Phi\left(\sqrt{2\pi}Qg - \sqrt{\ln Q^2}\right), \tag{3.15}$$

where the trivial solution $g = 0$ is not valid. We underline the fact that this equation predicts an universal collapse for 'E-only' cultures when the giant component is plotted in terms of $Q \equiv m_D/m$, which is indeed consistent with the experimental $g(m/m_D)$ data of Soriano et al. (2008).

Critical behavior

We consider the expression for the giant component given by Eq. (3.14). To obtain the critical exponent predicted by the model at transition, the right side of the equation is expanded as a Taylor series around $g = 0^+$ up to third order, i.e.

$$g + M^- \simeq M^- + g - \sqrt{\pi \ln Q}g^2 + \frac{\pi}{3}Q\Big(2\ln Q - 1\Big)g^3. \tag{3.16}$$

Then, the non-vanishing solution near the critical point takes the form

$$g \simeq \frac{3}{\sqrt{\pi}}\frac{\sqrt{\ln Q}}{Q\big(1 - 2\ln Q\big)}. \tag{3.17}$$

The limit $g \to 0^+$ implies $m \to {m_D}^-$, therefore Q can be written as a power series of $\left(1 - \frac{m}{m_D}\right)$ near criticality

$$Q \simeq 1 + \left(1 - \frac{m}{m_D}\right) + O\left[\left(1 - \frac{m}{m_D}\right)^2\right]. \tag{3.18}$$

By inserting this result in Eq. (3.17), we finally obtain

$$g \sim \frac{3}{\sqrt{\pi}}\left(1 - \frac{m}{m_D}\right)^{\frac{1}{2}}, \tag{3.19}$$

with the universal exponent $\beta = 1/2$ consistent with the mean–field universality class and percolation.

3.4 Contrasting Experiments and Model

For clarity in the presentation of results, we show here only data with excitation active.

3.4.1 Response curves

From an experimental point of view, as shown in Fig. 3.2a, the data exhibits the following trend. The connectivity of the network is maximum for [CNQX] $= 0$ and $m = \tilde{m}$, and thus the stimulation of a small group of neurons suffices to light up the entire network. The response curve $\phi(V)$ is then characterized by a sharp jump in the fraction of responding neurons, which is associated to the existence of the *giant component* g in the network, constituted by the largest group of strongly connected neurons. As [CNQX] and m increase, the size of the jump gradually diminishes. At a critical value $m = m_D$ (≈ 40 for the example shown) a jump is no longer identifiable and $g = 0$. At this stage of disintegration the network is formed by small isolated clusters, and in the limit $m \to \infty$ the network is comprised solely of independent neurons. This single–neuron response is well described by an error function, i.e. a Gaussian–distributed neuronal intrinsic variability, which does not change with CNQX (Vergara et al., 2003; Yamada et al., 1989).

From the model point of view, its analysis through Eq. (3.10) provides the set of mean–field response curves $\phi(V)$ with H_0, σ_h and m_D as parameters (solid lines in Fig. 3.2a). We must note here that the simplest case scenario of CNQX saturation, where the system is composed of independent neurons, is almost perfectly characterized by the non–interaction limit $m \to \infty$. From this fit between the experimental saturation curve at $[CNQX] = 10\mu$M and

the mean–field solution at $m = 515$, we extracted the value of the standard deviation $\sigma_h = 0.80 \pm 0.03$ V, and that features the neuronal intrinsic variability. A first approximation for the systematic correction in the external field, i.e. $H_0 = 4.2 \pm 0.1$ V, was also derived from this fitting.

Then, and starting from the previously fixed σ_h and H_0, the best–fit value for the main parameter $m_D = 39 \pm 1$ was obtained for all explored CNQX concentrations. The notably good fits of Fig. 3.2a for the whole CNQX range, and with only three parameters to adjust, evinces the appropriateness of a mean–field approach and validate its corresponding assumptions. Moreover, the final $m_D = 39 \pm 1$ result directly unveils the specific average connectivity of this culture through the equation $m_D \simeq \bar{k}\, p_E$ (Cohen et al., 2010; Soriano et al., 2008), providing $\bar{k} = 49 \pm 1$ for the fraction of exciting neurons $p_E = 1$.

Despite the good agreement between analytical mean–field solution and experiments, second order discrepancies were found when assessing the disintegration curves for the giant component g, as elaborated below.

3.4.2 Disintegration curves

Illustrative experimental disintegration curves $g(m)$ for different culture densities ρ are shown in Fig. 3.8a. The disintegration of the giant component with increasing CNQX concentration presents an initially slow decay, which progressively accentuates and reaches zero at the critical point $m = m_D$, where the giant component vanishes.

Regarding the analytical mean–field model, Eq. (3.15) provided the disintegration curves $g(m)$ with m_D as the only parameter. Since $Q^{-1} \equiv m/m_D$, this equation predicts the existence of a universal disintegration curve when the giant component is plotted as $g(m/m_D)$. Indeed, as shown in Fig. 3.8b, the experimental disintegration curves neatly collapse when plotted as $g(m/m_D)$. Here, the m_D values are particular of each density, and are obtained from the direct evaluation of the vanishing points in Fig. 3.8a.

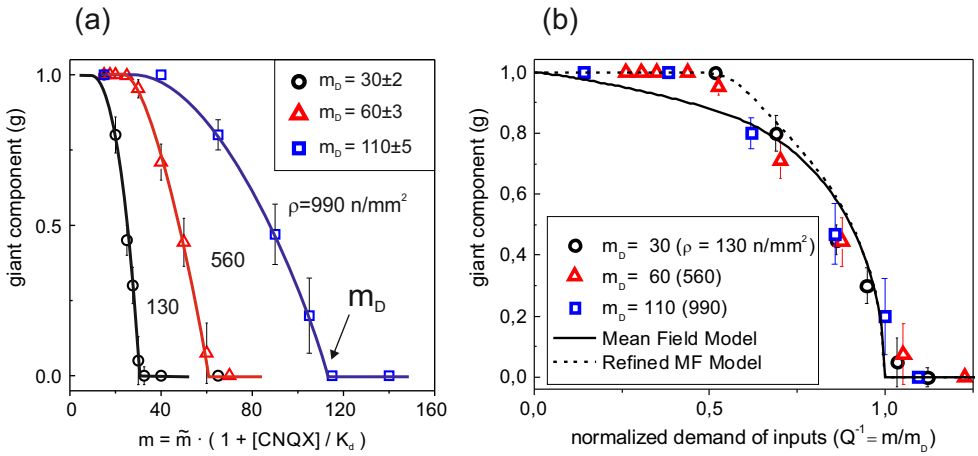

Fig. 3.8 Giant component g**. (a)** Disintegration curve $g(m)$ for 3 different neuronal densities ρ, each data point showing an average over 4 experimental realizations; error bars are standard deviation. m_D marks the critical value of m at transition. Lines are a guide to the eye. **(b)** Collapse of the same experimental data by plotting the size of the giant component g as a function of m/m_D, with m_D the previous critical m value for each culture. The solid line shows the fit for the mean–field NNIM. The dashed line shows the fit of the NNIM with loop-refinement, $\alpha = 5 \cdot 10^{-4}$ and $\xi = 15$.

Even though the former crucial result was obtained by means of our mean–field approach, a clear discrepancy between model and experiments is observed at low m/m_D, where g is constant or decays very slowly. We term this regime *experimental plateau*, which indicates that mean–field may not be sufficient to fully capture the behavior of the culture.

To provide an explanation for this plateau, we introduce a phenomenological refinement of the model that is able to capture this deviation from mean–field at low m/m_D values. This refinement is grounded on the possible action of loops and multiple spiking, which can effectively alter the coupling strength, i.e. neurons appear more connected due to an *excess* of firings per neuron. For clarity, the details of this phenomenological model are elaborated in the next section. This refinement essentially provides two new parameters, namely α and ξ, that can be adjusted to accord the model with the plateau. As illustrated in Fig. 3.8b, the best values that fit the experimental data correspond to $\alpha = 5 \cdot 10^{-4}$ and $\xi = 15$. It is important to mention that we do

not have any prediction for these values, i.e. they are pure phenomenological. However, it is interesting to observe that the contribution of loops and multiple spiking is only relevant at the initial stages of the disintegration of the network, where $m \ll m_D$, and their contribution becomes irrelevant when approaching the critical point m_D.

We note that the aforementioned loops and multiple spiking was a first attempt to understand the origin of this plateau. Along the development of the thesis we realized that they could be elegantly understood in terms of metric correlations in the connectivity, and that are linked to the spatial embedding of neurons and connections during the formation of the neuronal culture. In the following Chapter, an extensive study of the effect of metric correlations in the connectivity of neuronal cultures is presented, and by using numeric simulations of the original, static model that go beyond mean–field. Interestingly, this new view in terms of metric correlations rules out the need for a phenomenological refinement, and evinces the importance of metric constraints when analyzing living neuronal networks.

Phenomenological refinement of the model

This refinement is included here for completeness, and to show the development of different explanations and approaches along the thesis.

The refinement is based on the following. In previous detailed studies (Orlandi et al., 2013) it was shown that an inactive neuron has a higher–than–random probability of releasing neurotransmiters to its postsynaptic neighbors when it receives a sub–threshold input from a presynaptic neighbor. Combined with closed finite loops and finite refractory time, this mechanism could provide multiple spiking for a presynaptic neuron, effectively increasing the amount of possible inputs for the inactive neuron. This excess of bombardment leads to an effective over–connectivity that might originate the experimental plateau in $g(m/m_D)$ observed in Figure 3.8b for low CNQX values.

As a first, tentative approach, we developed the phenomenological refinement considering multiple spiking and first–order loops, which seem to suffice to properly characterize both the the plateau and the disintegration of the giant component in Figure 3.8b. These loops are phenomenologically taken into account by replacing J by $J + f(m)$ in the coupling strength of Eq. (3.1). Since neuron–to–neuron interactions go as $\sim m^{-1}$, we hypothesize that interactions through first–order loops would take the form $f(m) = \bar{\alpha} \cdot m^{-\xi}$. Qualitatively, the higher $\bar{\alpha}$ and ξ, the higher the importance of the loops in the network. Therefore, and considering the E–only scenario, Eq. (3.4) would become

$$M = \Phi\left(\frac{\left(\frac{J_0}{m} + \frac{\bar{\alpha}}{m^{\xi}}\right) p_E \bar{k} M + H - H_0}{\sigma}\right). \tag{3.20}$$

In the following calculations we derive again the main equations of the model taking into account this refinement.

The metastability limits are derived as described previously for the unrefined mean–field, and provide

$$M^{\pm} = \Phi\left(\pm\sqrt{\ln\left[\left(\frac{J_0}{m} + \frac{\bar{\alpha}}{m^{\xi}}\right)\frac{\bar{k} p_E}{\sqrt{2\pi}\sigma}\right]^2}\right). \tag{3.21}$$

The disintegration constraints $m = m_D$ at $M^+ = M^-$ lead to

$$\frac{J_0}{m_D} + \frac{\bar{\alpha}}{m_D^{\xi}} = \frac{\sqrt{2\pi}\sigma}{\bar{k} p_E}. \tag{3.22}$$

And by inserting Eq. (3.22) into Eq. (3.20) we obtain

$$M = \Phi\left(\sqrt{2\pi}\frac{\left(\frac{J_0}{m} + \frac{\bar{\alpha}}{m^{\xi}}\right)}{\left(\frac{J_0}{m_D} + \frac{\bar{\alpha}}{m_D^{\xi}}\right)} M + \frac{H - H_0}{\sigma}\right). \tag{3.23}$$

This expression can be rearranged to provide

$$M = \Phi\left(\sqrt{2\pi}\frac{\left(\frac{m_D}{m}+\frac{\bar{\alpha}m_D}{J_0 m^{\xi}}\right)}{\left(1+\frac{\bar{\alpha}}{J_0 m_D^{\xi-1}}\right)}M + \frac{H-H_0}{\sigma}\right). \tag{3.24}$$

Next, for convenience, we take $\bar{\alpha} = \alpha J_0 m_D^{\xi-1}$, with α constant. Then, the final equation reads

$$M = \Phi\left(\sqrt{2\pi}Q^* M + \frac{H-H_0}{\sigma}\right). \tag{3.25}$$

with $Q^* = (Q+\alpha Q^{\xi})/(1+\alpha)$, where α and ξ would be parameters that account for the abundance of loops in the network, and $Q \equiv m_D/m$.

We note that the metastability limits can be written in this notation as

$$M^{\pm} = \Phi\Big(\pm\sqrt{\ln[Q^*]^2}\Big). \tag{3.26}$$

The giant component for the refined model is obtained as explained in the previous, unrefined derivations, but replacing Q by Q^* in each equation, providing

$$g + \Phi\left(-\sqrt{\ln Q^{*2}}\right) = \Phi\left(\sqrt{2\pi}Q^* g - \sqrt{\ln Q^{*2}}\right). \tag{3.27}$$

Near criticality, Q^* is written as a power series of $\left(1-\frac{m}{m_D}\right)$, and takes the form

$$Q^* \simeq 1 + \frac{1+\alpha\xi}{1+\alpha}\left(1-\frac{m}{m_D}\right) + O\left[\left(1-\frac{m}{m_D}\right)^2\right]. \tag{3.28}$$

Applying this result and replacing Q by Q^* in Eq. (3.17), we finally obtain

$$g \sim 3\sqrt{\frac{1+\alpha\xi}{\pi(1+\alpha)}}\left(1-\frac{m}{m_D}\right)^{\frac{1}{2}}, \tag{3.29}$$

with the same universal exponent $\beta = 1/2$.

3.5 Conclusions

Our analysis of the experiments illustrate that an adapted Neuronal Network Ising Model is sufficient to capture the basis of the behavior of neuronal cultures and their response to external stimulation. Also, the percolation approach proved useful in the characterization of the disintegration of the network, and provided a clear insight of the process.

Our mean–field approximation remarkably matched with experimental data of homogeneous cultures, specially in the response curves, overall validating its assumptions. The former approach even predicted the universal collapse of disintegration curves when normalized in terms of $g(m/m_D)$. This universal behavior is novel, and was not suggested by the previous studies in Refs. Breskin et al. (2006); Cohen et al. (2010); Soriano et al. (2008).

Despite the overall success of the model, a detailed study of the response curves and the disintegration of the giant component showed discrepancies between real homogeneous cultures and mean–field. Particularly, we observed an experimental plateau of $g \simeq 1$ for $m/m_D \lesssim 0.5$ which was not properly characterized by the analytic model. An *ad hoc* refinement of the model was able to mimic this feature. The latter model was constructed in the framework of connectivity loops and multiple spiking, which only influenced the behavior of the curves at low m/m_D values. We note that this first, phenomenological approach is no longer necessary when complete metric simulations of the original are introduced, as elaborated in the next Chapter.

As an overall hallmark of our model, it is woth emphasizing that in homogeneous conditions close to mean–field, the transition point m_D can be neatly determined by analyzing the $g(m/m_D)$ disintegration curves and fitting them to the universal mean–field behavior. Since percolation studies provided $m_D \simeq \bar{k}\, p_E$ in inhibition–free networks (Cohen et al., 2010; Soriano

et al., 2008), our analysis allows for an accurate inference of the network average connectivity by exploiting the information of the whole disintegration curve, without the need of a detailed exploration of the transition point. Moreover, the experimental protocol and accompanying analysis allow for a non–invasive extraction of the average connectivity in cultures, and could be potentially extended to brain slices and other living neuronal networks.

Chapter 4

Dominance of Metric Correlations in Spatial Neuronal Cultures

In this Chapter we introduce complete simulations of the Neuronal Network Ising Model introduced in the previous Chapter. Simulations were implemented on realistic networks that mimicked a number of characteristics observed in neuronal cultures, and their ultimate goal was to assess the importance of metric correlations in cortical circuits *in vitro*.

Indeed, living neuronal circuits, from the smallest culture in a dish up to the brain, exhibit complex collective behavior that is shaped in great measure by the connectivity among neurons (Sporns and Zwi, 2004). Metric correlations arise from both the finite axonal length and the heterogeneity in the spatial arrangement of neurons. Interestingly, in the process of associating specific network properties to key dynamical traits it was usually assumed that the spatial constraints of the neuronal circuit could be disregarded. In fact, the combination of physical embedding, the spatial organization of the neurons, and wiring cost (Bullmore and Sporns, 2012; Chen et al., 2013) not only prevents a neuron to arbitrarily connect with any other, but naturally shapes strong correlations and spatially–inherited features that can be more

important in shaping dynamics than the actual distribution of connections (Horvát et al., 2016).

The importance of metric constraints and their interrelation is focus of great attention in the context of *spatial networks* (Barthélemy, 2011; Bianconi et al., 2009; Brockmann and Helbing, 2013), a framework that analyzes those systems in which nodes and links are embedded in space, and where the physical distance among nodes plays a central role. Following this path, our interest in this Chapter is to take into account two basic spatial aspects, namely the arrangement of neurons over the culture substrate and the typical axonal length, and investigate their influence on the percolation experiments and the Neuronal Network Ising model described in the previous Chapter. These experiments considered the behavior of the giant component g as a function of the demand of inputs m. The shape of the $g(m)$ curve was well reproduced for the mean–field, *metric free* solution of the model, but some interesting discrepancies emerged.

As we will see, the presence of metric correlations precipitates a strong deviation from mean–field. Overall, our theoretic–numerical study show that metric inherited correlations in spatial networks dominate the connectivity blueprint, mask the actual distribution of connections, and may emerge as the asset that shapes network dynamics.

4.1 Simulation details

In this Section, we first describe a fundamental parameter to characterize the importace of metric effects, namely the *degree of aggregation*, and for both experiments and simulated networks. Then we explain the construction of the realistic, metric neuronal networks, and the implementation of the numerical simulations.

The simulations were run by Javier G. Orlandi, postdoc at Soriano's group at the moment of conducting the present investigation.

4.1.1 Computation of the degree of aggregation Λ

To properly extract the contribution of metric correlations, the degree of neuronal spatial aggregation, termed Λ, must be assessed for both real cultures and simulated networks. This quantity characterizes the tendency of neurons to pack together on a given surface. Our interest is that the quantity Λ varies between 0 for a perfectly homogeneous arrangement and 1 for the full concentration of neurons at a given point. We therefore found convenient to quantify Λ through the normalized area under the "Lorenz curve", i.e. the Ginni coefficient presented in Chapter 2, where Lorenz curves provide the ordered cumulated fraction of neurons in an area fraction f, for $0 \leq f \leq 1$.

For the computation of Λ in experiments, the images are first processed to obtain binarized patterns in which neurons appear as black objects over a white background. The bottom–left plot in Fig. 4.1c is an example of the processed images. The experimental values of Λ for a given culture are typically obtained from a snapshot of the camera field of view, i.e. the monitored area of the network. This naturally leads to an intrinsic uncertainty in the values of Λ for a particular experimental realization since other regions of the same culture would in general exhibit slightly different neuronal distributions. When possible, different fields of view of the same culture are analyzed to accurately assess the variability among different regions.

For simulations, we proceed in the same way as in the experiments, but the computation of Λ is over the entire system and thus there is no uncertainty in its measure.

For clarity in the discussion of the results, we define two main spatial arrangements, namely *homogeneous* and *aggregated configurations*, and that correspond to $\Lambda \lesssim 0.5$ and $\Lambda \gtrsim 0.7$, respectively.

Figure 4.2 shows illustrative examples for the homogeneous and the aggregated configurations in both simulations and real cultures.

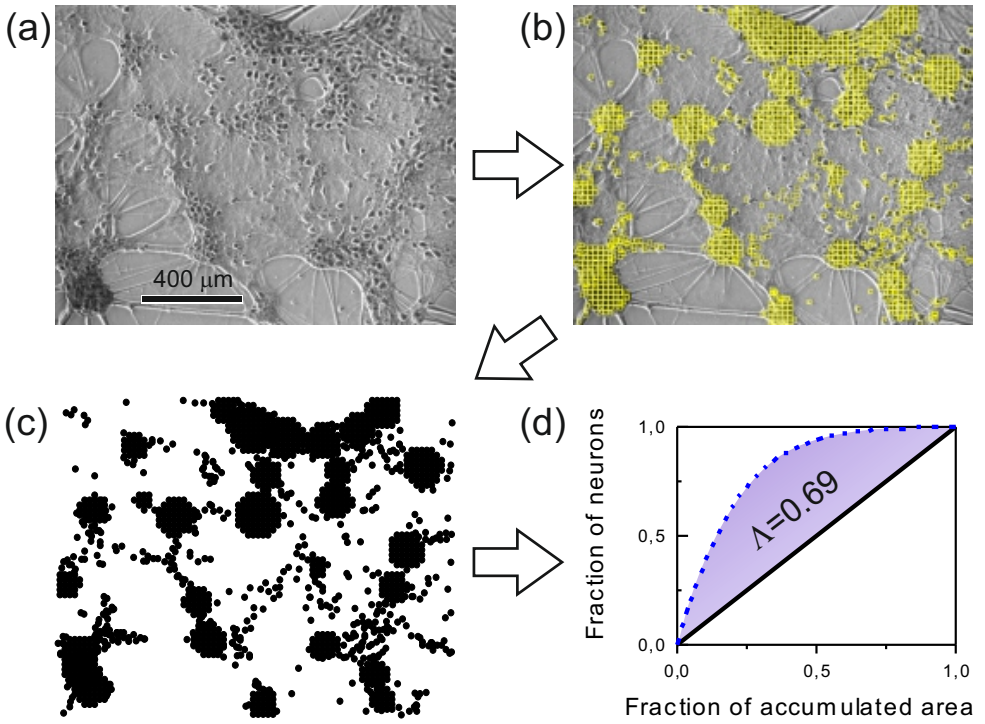

Fig. 4.1 Determination of the degree of aggregation Λ in experiments. **(a)** Optical image of a typical semi–aggregated culture. Scale bar is 400 μm. **(b)** Manual selection of the soma of the neurons in the culture. **(c)** Final post-processed, binarized image. **(d)** Lorenz curve and degree of aggregation $\Lambda = 0.69$.

4.1.2 Network construction

Metric networks were constructed as in Orlandi et al. (2013), as follows. N circular cell bodies (neuronal somas) with a diameter of $\phi_s = 15$ μm were placed on a square substrate of length L, and their spatial distribution was established through a two–step process. First, a two–dimensional probability density function with periodic boundary conditions was built by linear summation of n Gaussian functions with random centers, same amplitude, and fixed width $\sigma_G = 300$ μm. And, second, neurons were placed in the substrate following this distribution. Each of the Gaussians represents an aggregation center with a high neuronal density. The lower n, the higher the aggrega-

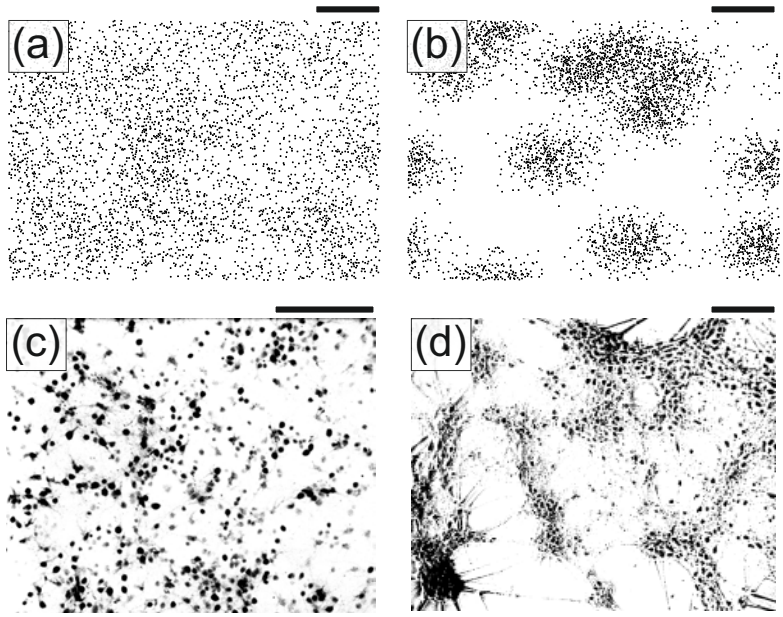

Fig. 4.2 Spatial distribution of neuronal cultures. **(a)** Spatial location of neurons (black dots) in a homogeneous simulated culture. **(b)** Spatial distribution for an aggregated simulated culture. **(c)** Highly contrasted optical image of a homogeneous neuronal culture. **(d)** Highly contrasted optical image of an aggregated neuronal culture. The degrees of aggregation are $\Lambda \simeq 0.2$ and 0.7 for the homogeneous (a,c) and aggregated (b,d) configurations respectively. Scale bars are 500 μm.

tion in the network. The *homogeneous* configuration strictly corresponds to $n \to \infty$, which in the simulations was established as $n = 200$. The *aggregated* configuration was typically bounded in the range $10 \leq n \leq 50$. Examples of the constructed networks are provided in Fig. 4.2a for the homogeneous configuration, and Fig. 4.2b for the aggregated one.

Connectivity among neurons was then set as follows. From each soma an axon was grown following a quasi–straight path as a biased random walk. The total length of each axon was drawn from a Rayleigh distribution with $\sigma_a^2 = 900$ μm. The dendritic tree of each neuron was modeled as a disk with average diameter $\phi_d = 300$ μm and standard deviation $\sigma_d = 40$ μm (drawn from a Gaussian distribution). A directed connection was established with probability p_{conn} from neuron i to neuron j whenever the axon from neuron i

crossed the dendritic tree of neuron j. Network construction is illustrated in Fig. 4.3.

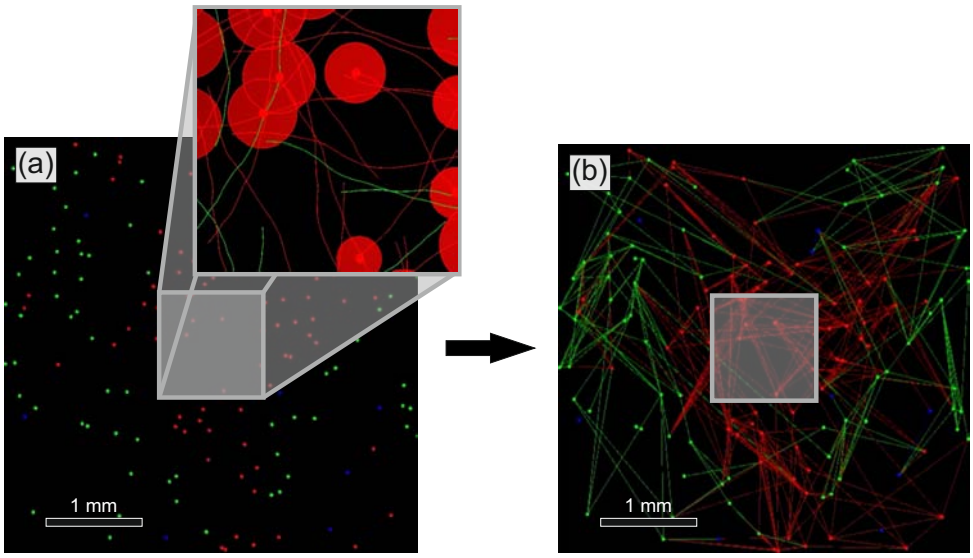

Fig. 4.3 Construction of simulated metric networks. **(a)** Spatial distribution of neurons' somas (color dots) for a simulated homogeneous network; $\Lambda = 0.18$. Inset depicts the construction of the simulated axons (solid lines) and dendritic trees (semitransparent red circles). **(b)** Structural connectivity of the network. Colors indicate highly connected modules. Original images by J. G. Orlandi.

Randomized versions of the aforementioned metric networks, i.e. *null models*, were generated by randomly swapping the output nodes between connection pairs, i.e., $A \to B$ and $C \to D$ turned into $A \to D$ and $C \to B$, if and only if, $A \neq B \neq C \neq D$. This process was repeated until the clustering coefficient CC of the network converged, usually to a value very close the expected one of a random graph with the same average connectivity, i.e. $CC \simeq 1/\bar{k}$. This procedure generates a randomized analog of the networks without modifying their initial distribution of connections. Figure 4.4 shows typical connectivity probability distribution functions for homogeneous and aggregated configurations, which are invariant upon randomization.

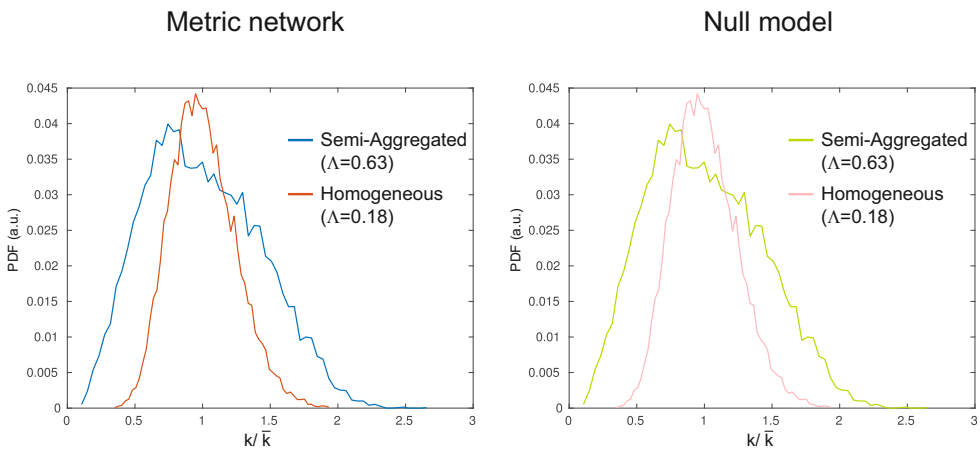

Fig. 4.4 Probability distribution function of the input connectivity in simulated networks before and after the randomization process. Left plot: distribution of input connections of single homogeneous and semi–aggregated realizations, with $\Lambda = 0.18$ and 0.63, respectively. $\bar{k} = 150$ for both network configurations. **Right plot**: The distribution of input connections is unchanged after the randomization.

4.1.3 Simulations Procedure and Numerical Details

As explained in Chapter 3, the Hamiltonian for the Neuronal Network Ising Model (NNIM) reads

$$\mathscr{H} = -\sum_{i=1}^{N} s_i \left(J \sum_{\{j_E\}_i} s_j - \gamma \sum_{\{j_I\}_i} s_j + h_i + \tilde{H} \right), \tag{4.1}$$

where $s_i = 0$ *or* 1 are the spin variables for inactive or active neurons, respectively. $J = J_0/m$ is the excitatory exchange energy with a uniform coupling approximation; J_0 is a constant and m is the experimental control parameter upon disintegration. $\gamma = J_0/m_0$ is the constant inhibitory exchange energy. $\{j_E\}_i$ and $\{j_I\}_i$ are the set of excitatory and inhibitory input (presynaptic) neighbors of the ith neuron. h_i are the Gaussian–distributed local random fields that account for neuronal intrinsic variability. And $\tilde{H}$ is the effective external field, defined as $\tilde{H} \equiv H - H_0$, with H_0 a systematic correction. Our

observable of interest in the model is the magnetization $M \equiv \langle s \rangle$, i.e. the fraction of active neurons ϕ.

Numerical simulations over the previous Hamiltonian are carried out considering the standard zero–temperature random field Ising model (Dhar et al., 1997; Illa et al., 2006). Input parameters are set as $m_D = 150$, $\sigma = 0.8$ V and $H_0 = 4.2$ V. J_0 is chosen as in Eq. (3.8), i.e.,

$$J_0 = \frac{\sqrt{2\pi} m_D \sigma}{\bar{k}}. \tag{4.2}$$

All connections are considered excitatory to mimic the main experimental results and fulfill the Abelian property (Salvat-Pujol et al., 2009). Simulations' pipeline is as follows. For each neuron in each network realization, a local random field value h_i is assigned. An initial field H is then chosen such that the stable solution corresponds to $s_i = 0, \forall\, i$. Then the field is increased until the condition

$$J \left[\sum_{j \in i} s_j \right] + h_i + H - H_0 > 0 \tag{4.3}$$

is satisfied for a given neuron. At this point the corresponding spin is "flipped", i.e., set as $s_i = 1$. The condition given by Eq. (4.3) is then reexamined until no more spins are flipped. The amount of spins that flip for a given field H defines an avalanche and a jump in the magnetization of the system M. The entire process is repeated for gradually higher fields H until $M = 1$. The largest discontinuous jump across the $M(H)$ curve defines the size of the giant component g. Each $g(m/m_D)$ curve was finally averaged over different network realizations.

We note that the difficulties for extending the simulations to networks with inhibition are related to the emergence of *cyclic attractors*, where an *static* steady state at fixed H cannot be determined. The rationale behind this non–collapsing limit cycles in the phase space is illustrated by the following example. The external field H is increased until a first, excitatory spin fulfills

Eq. (4.3) and is therefore activated. The flip of this node directly activates an inhibitory spin, whose action inhibits the firing of the first spin. However, if the first, excitatory node is not activated, the inhibitory spin will not fire. Concurrently, the system gets trapped in a cycle with no stable solution.

As mentioned in the previous Chapter, the studied percolation experiments consider 'E–only' networks, and hence, simulations with inhibition are not necessary to assess these experiments.

4.2 Simulation results and discussion

4.2.1 Response curves

Figure 4.5 (and also Fig. 4.6a) shows that a single realization of a homogeneous configuration exhibits the same features in terms of response curves $\Phi(V)$ as the experimental data. We observe low variability between different network realizations for this configuration, thus, no relevant information is lost when averaging over realizations.

For an aggregated configuration, however, a single realization displays network–specific features, as exemplified in Fig. 4.7. This means that the shape of both the response curves $\phi(V)$ and the disintegration curves $g(m/m_D)$ reflect the spatial arrangement and connectivity of the neurons, and in such a way that the transition point cannot be well determined. As Fig. 4.7 shows, the giant component splits into different sub–components as disintegration progresses. These sub–components manifest the existence of modular traits in aggregated configurations, i.e. neurons are more connected within aggregates than between other neurons in the network. In the example shown, the jump at $m \approx 0.75 \cdot m_D$ signals the disconnection among aggregates, and its numeric value[1] accounts for the average interconnectivity between the

[1] As explained in Soriano et al. (2008), $m_D \simeq \bar{k} p_E$. The fraction of excitatory neurons in our simulations is $p_E = 1$.

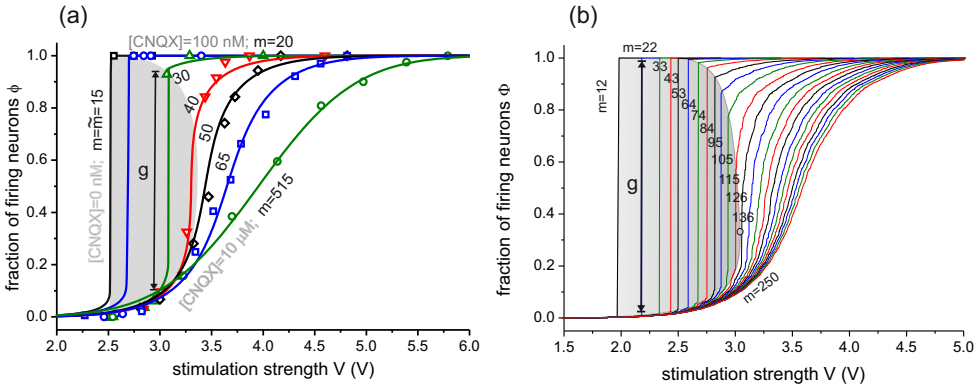

Fig. 4.5 Experimental and simulated response curves for a homogeneous culture. (a) Experimental response curves for gradually larger [CNQX] and m, extracted from Fig. 3.2 of previous Chapter. Symbols are experimental data points. Solid lines depict the fit of the analytical mean–field model to the experiments, and with parameters $H_0 = 4.2 \pm 0.1$ V, $\sigma_h = 0.80 \pm 0.03$ V and $m_D = 39 \pm 1$. **(b)** Response curves for a single realization of an equivalent, simulated culture. The degree of aggregation is $\Lambda = 0.18$.

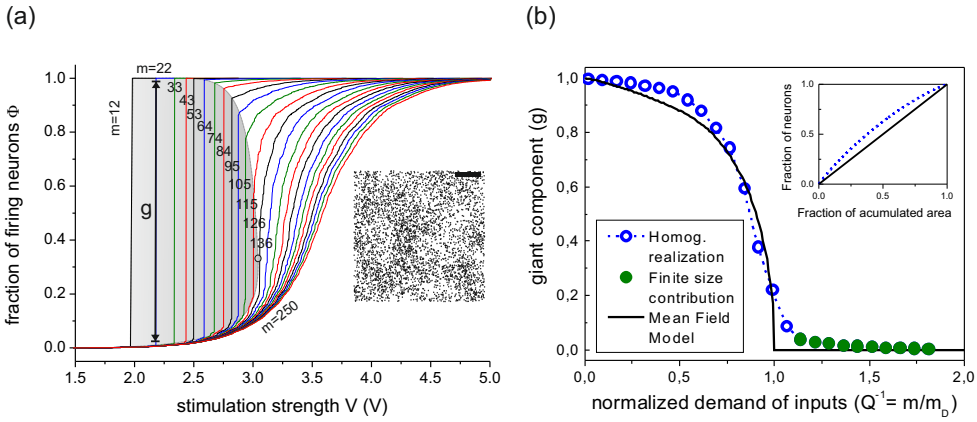

Fig. 4.6 Single realization of a simulated homogeneous culture. (a) Response curves for gradually higher m values. The zoomed–in panel highlights the finite size avalanches. Some avalanches are marked with vertical black bars for easier identification. The bottom–left inset shows the spatial distribution of the network, constructed with $n = 200$ Gaussians. Scale bar is 500 μm. Total size is 5×5 mm^2. **(b)** Disintegration of the giant component $g(m/m_D)$, with the corresponding Lorenz curve depicted on the inset ($\Lambda = 0.18$).

different network modules. Additionally, the total disintegration (i.e. giant component vanishing point) is obtained at $m \approx 1.7 \cdot m_D$.

The existence of two disintegration values indicates that the short range, intra–aggregate connectivity is much stronger than the long range, inter–aggregate connectivity. This result is totally consistent with strong metric correlations, which substantially favor connections among neighboring neurons.

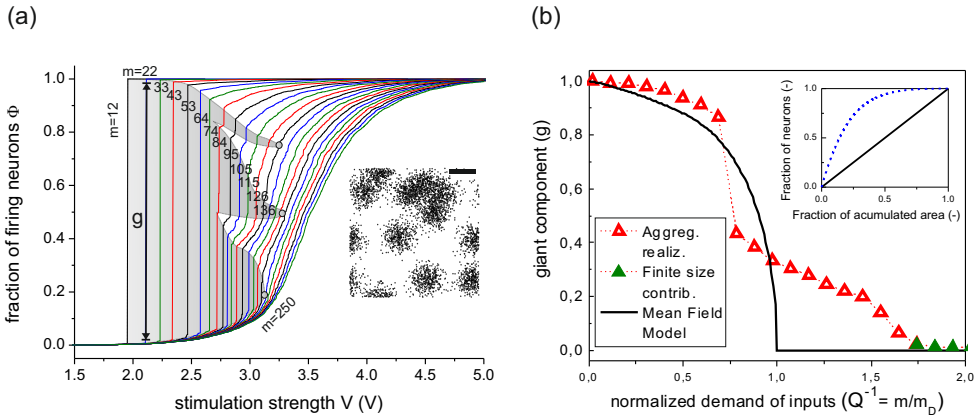

Fig. 4.7 Single realization of a simulated aggregated culture. **(a)** Response curves for gradually higher m values. Different giant components emerge at high values of m, indicating the disintegration of the network onto three modules. The inset shows the spatial distribution of the network, constructed with $n = 10$ Gaussians. Scale bar is 500 μm. Total size is 5×5 mm^2. **(b)** Disintegration of the giant component $g(m/m_D)$. The corresponding Lorenz curve is depicted on the inset, with $\Lambda = 0.63$.

We note that, for the aggregated configuration, the specific values at which the giant component breaks off are totally lost when data is averaged over realizations. Therefore, the averaged disintegration curves present a smoothed behavior, with a fast initial decrease and a slow final disintegration, as illustrated in Fig. 4.10. Hence, one needs to pay special attention to the features of the curves, since strong variations among $g(m/m_D)$ curves reveal a strong sensitivity of the disintegration process to the actual layout of neurons.

We would like to highlight that these network–specific features in the aggregated configuration were also observed experimentally, as shown in Fig. 4.8. Hence, the above analysis provides an enlightening framework to

understand the impact of metric correlations in living neuronal networks. Specifically, spatial heterogeneity in the arrangement of neurons is sufficient to induce metric correlations that in turn shape strong inhomogeneities in the connectivity of the culture.

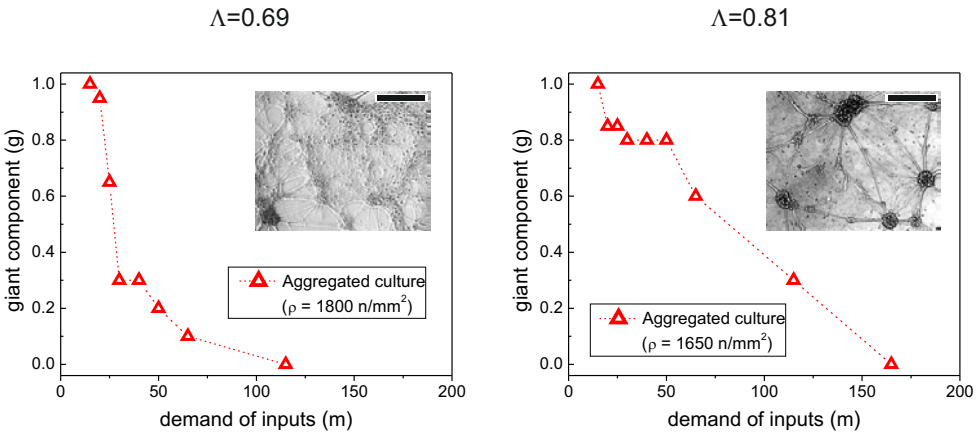

Fig. 4.8 Experimental disintegration curves for two aggregated cultures. Non-normalized disintegration curves $g(m)$ of two cultures of high degree of aggregation. **Insets:** optical images of the corresponding culture. Scale bars are 500 μm.

4.2.2 Disintegration curves

The sensitivity of the response curves $g(m/m_D)$ to metric effects is illustrated in Figure 4.9. The plot compares all the experimental data (with its characteristic plateau at low m/m_D values) with the exact mean–field model and the complete NNIM metric simulations. Experiments and simulations correspond to homogeneous networks. Although a similar plot is possible for aggregated configurations, network specific traits are so strong that the comparison would be misleading.

As displayed in the plot, the results of the simulations are remarkably compatible with the experimental data, specially for the range of low m/m_D values where the mean–field approach did not suffice to capture the observed experimental features. Moreover, the refined model of the previous Chapter

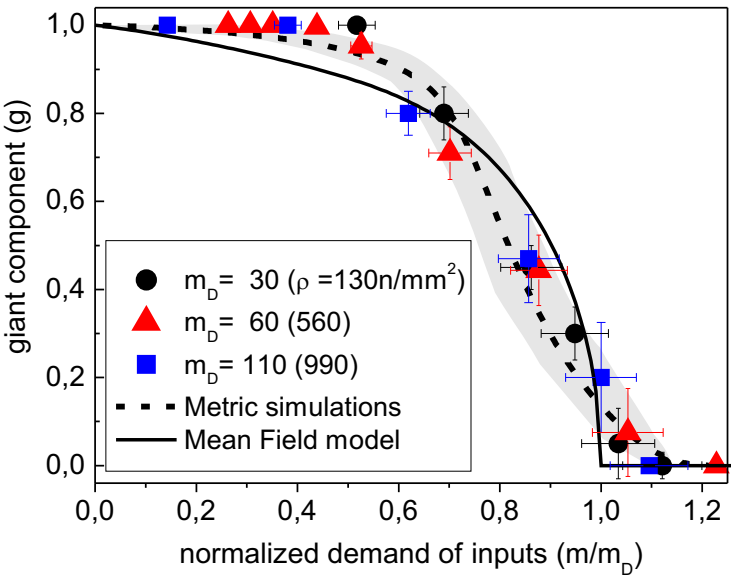

Fig. 4.9 Comparison between homogeneous experiments and complete NNIM model. Experimental $g(m/m_D)$ data points for the three densities ρ of Fig. 3.8 of the previous Chapter, each averaged over 4 cultures. Vertical error bars are standard deviation, and horizontal error bars account for the uncertainty in determining m_D. The solid black line shows the analytical mean–field solution, while the dashed one corresponds to the fit between metric simulations and experimental data. Simulations are an average over 5 homogeneous network realizations, with the light gray area showing the standard deviation.

(Fig. 3.8b) was constructed on the assumption of multiple spiking, whereas the complete simulations do not require these dynamical features at all. Since the simulated data presents an overall better fit and description of the experimental behavior, we conclude that multiple spiking does not significantly contribute to network activity. Hence, we totally discard the refined model for the interpretation of the experimental data.

Our interpretation is that the observed early resilience of networks to disintegration ($m/m_D < 0.75$) arise from the reinforced connectivity at a local scale, inherited from intrinsic metric correlations. The posterior decrease of the giant component with respect to the metric–free, mean–field model ($0.75 \leq m/m_D \leq 1$) would be consistent with the presence of strong connectivity at a local scale. That is because metric correlations would also

weaken connectivity at a larger scale, yielding a semi–isolation of local, coarse–grained networks. The latter process is clearly strong for the aggregated situation, as shown in Fig. 4.7a. The final slower disintegration is due to the average over realizations and finite size effects in the simulations, as explained in Section 4.2.5.

4.2.3 Metric effects and distribution of connections

To properly validate the dominant role of metric correlations one *must separate* the metric contribution from the topological one. By *topological* here we refer to the distribution of connections, disregarding connectivity distances. This raises the following, interesting question: how strongly metric inherited features affect culture's behavior compared to the distribution in the number of connections in the network?

To answer this question, we carried out numerical simulations to compare networks with similar distribution of connections and contrasting Λ, namely $\Lambda = 0.18$ (homogeneous configuration) and $\Lambda = 0.68$ (aggregated). Additionally, we incorporated simulations of the corresponding metric–free *null models*, i.e. randomized network analogs that preserved the distribution of connections (see Section 4.1.2). Averaged $g(m/m_D)$ simulation curves are shown in Fig. 4.10, with insets depicting the spatial arrangement of neurons and the degree distributions $p(k)$ in illustrative networks. Particular realizations of both configurations were provided in former Figs. 4.6 and 4.7.

The results in Fig. 4.10 show that both homogeneous and aggregated configurations deviate from mean–field, although the effect is markedly stronger for the aggregated one. The metric–inherited $g(m/m_D)$ curves contrast with the corresponding null models, which neatly follow mean–field, even though mean–field model totally disregards the distribution of connections (i.e. $k_i = \bar{k}\ \forall i$). We note that the null–models of the homogeneous and aggregated configurations are so similar that they almost coincide in the plot. For this reason, only one null-model curve is shown in the figure.

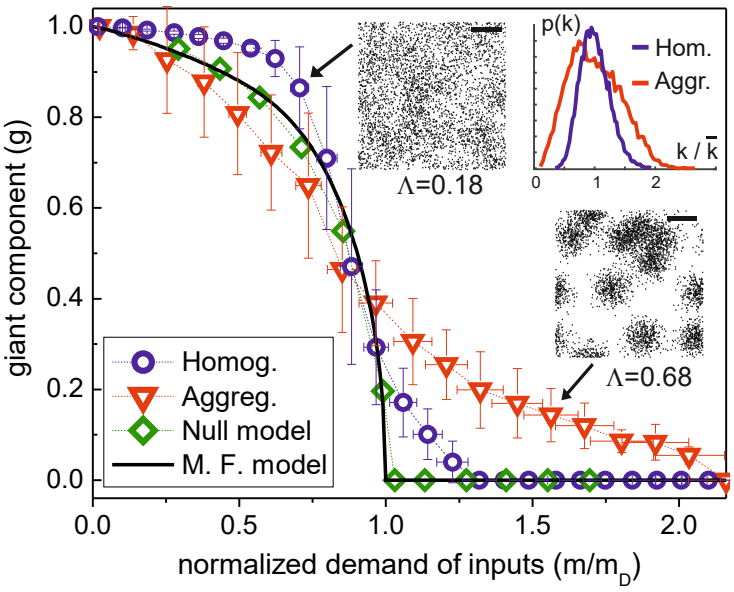

Fig. 4.10 Numerical simulations of $g(m/m_D)$ curves for contrasting Λ. The main plot shows the normalized disintegration curves for homogeneous (circles) and aggregated (triangles) metric configurations. The null models for both configurations are practically indistinguishable, were averaged out for clarity (diamonds), and neatly follow mean–field. The curves are obtained from the numerical integration of the general NNIM model in 10×10 mm^2 networks, and the normalization with m_D is determined through a fit to the mean–field solution (solid line). Each curve is an average over 10 networks. Vertical error bars denote standard deviation, and horizontal bars account for the uncertainty in the determination of m_D. The top left and bottom right spatial maps illustrate, respectively, typical aggregated and homogeneous realizations. Scale bars are 1 mm. The top right inset shows the distribution of connections for both realizations, with $\bar{k} = 150$.

These simulations show that metric correlations, rather than the distribution of connections, shape in great measure the behavior of the $g(m/m_D)$ curves and bound the range of validity for a mean–field approximation.

4.2.4 Quantifying the impact of metric correlations

To provide a measure for the impact of metric correlations in neuronal cultures, we introduce the quantity ε as the mean squared error between the mean–field solution and the $g(m/m_D)$ curve, and for a particular network realization at

a given degree of aggregation Λ. The corresponding results are provided in Fig. 4.11a.

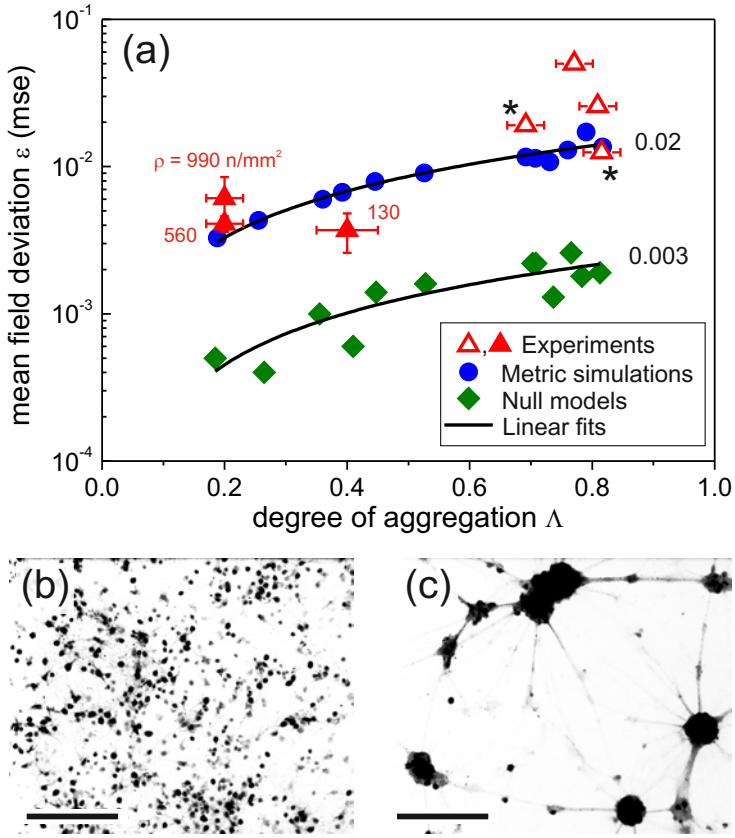

Fig. 4.11 Deviation from mean–field due to metric correlations. (a) Log–linear representation of $\varepsilon(\Lambda)$ for different network blueprints. Each simulation corresponds to a particular network realization. Solid triangles correspond to the experimental data shown in Fig. 4.9, each point averaged over 4 cultures. Vertical error bars are standard deviation. Open triangles correspond to individual cultures; asterisked cultures shown in Fig. 4.8. Horizontal error bars reflect the uncertainty in measuring Λ. Curves are linear fits, with the accompanying value the slope. **(b)** Highly contrasted image of a quasi–homogeneous culture, $\Lambda \simeq 0.2$. **(c)** Corresponding image for a strongly aggregated culture, $\Lambda \simeq 0.8$. Scale bars are 250 μm.

For both experiments and simulations, Fig. 4.11a shows the dependence of ε on Λ. The metric–free, null models should exactly follow mean–field and provide $\varepsilon = 0\ \forall\Lambda$. This occurs, however, for narrow distributions of

connections as in Erdös–Rényi graphs (Li et al., 2011), or as in our mean-field derivation with $k_i = \bar{k}\ \forall i$. Hence, the presence of a broad distribution of connections in simulations (Fig. 4.4 and top right inset of Fig. 4.10) leads to a finite ε and a linear dependence on Λ, though of small slope. By contrast, metric simulations depict ε values that are an order of magnitude higher than the corresponding null models, as well as a linear dependence $\varepsilon(\Lambda)$ characterized by a slope 7 times larger. We note that this different behavior arises solely from metric effects that entirely mask the actual distribution of connections. On the other hand, the experiments agree qualitatively well with metric simulations, and evince that spatial constraints in living neuronal networks cannot be disregarded. Examples of homogeneous and aggregated spatial configurations in experiments are provided in Figs. 4.11b–c.

We anticipate that this discrepancy due to metric correlations is shaped not only by Λ, but also by finite–size effects linked to metrics, assessed in the next Section.

4.2.5 Finite–size effects

In Fig. 4.11a, the importance of metric correlations for a given spatially–embedded network is evaluated as the deviation of its $g(m/m_D)$ behavior from mean–field. However, experiments and simulations were performed over $N \sim 10^3$ neurons and culture size of $L \sim 10$ *mm*, whereas the mean–field model strictly corresponds to $N \to \infty$ with no spatial embedding and arbitrary size. Thus, to properly quantify the impact of metric correlations, the contribution of finite–size effects has to be evaluated.

We distinguish three kinds of finite size effects. The first one corresponds to the contribution of finite size avalanches. The second one is related to a finite connectivity length in an arbitrary system size, and is also related to metric correlations. And the third one arises from the experimental limitation associated to the field of view of the camera, i.e. the monitoring of a small

subset of neurons rather than the entire system. These different contributions are elaborated below.

(A) Finite–size effects related to finite avalanches

In Fig. 4.12, finite size effects can be observed as small jumps or avalanches of activity outside the giant component. They contrast with the continuous response that would be expected in the thermodynamic limit under a quasi–static increase of the external field. Metric correlations do not contribute to finite avalanches since these avalanches are equally present in the simulations with randomized connectivity.

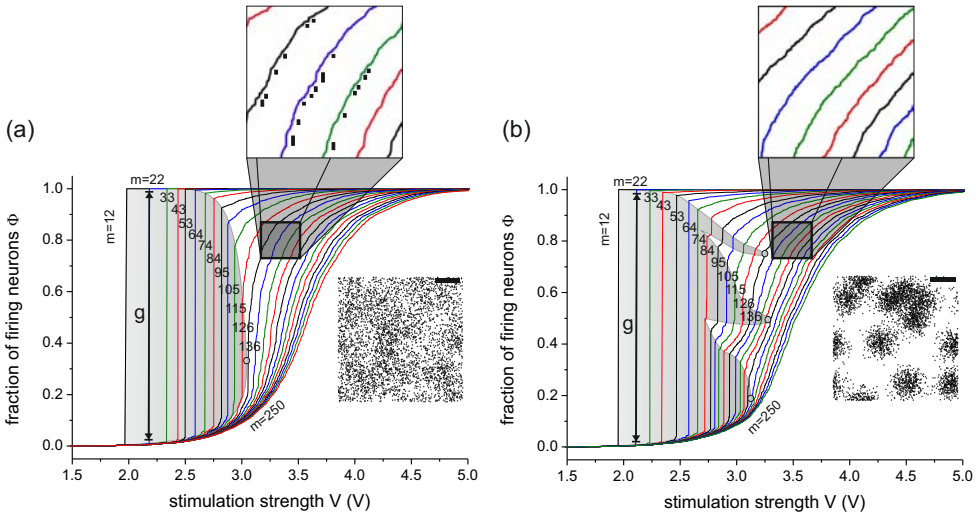

Fig. 4.12 Finite avalanches in simulated response curves. (a) Homogeneous simulated response curves for gradually higher m values ($\Lambda = 0.18$). The zoomed–in panel highlights the finite size avalanches in this homogeneous configuration. Some avalanches are marked with vertical black bars for easier identification. The bottom inset shows the spatial distribution of the network, constructed with $n = 200$ Gaussians. **(b)** Aggregated simulated response curves ($\Lambda = 0.63$). The zoomed–in panel highlights the finite size avalanches in this configuration. The bottom inset shows the spatial distribution of the network, constructed with $n = 10$ Gaussians. Scale bars are 500 μm. Total network size is 5×5 mm^2.

In the disintegration curves of Fig. 4.10, and in Fig. 4.13, the small avalanches are much smaller than the size of the giant component g for low

values of m. This regime is shown as open symbols in Figs. 4.13. However, as disintegration progresses and the giant component decreases, g merges with finite avalanches (green solid symbols in the aforementioned plot). Consequently, we removed the contribution of these finite size avalanches in $g(m/m_D)$ curves by setting g as 0 when it had no significant difference with the noisy background of finite avalanches. This procedure is illustrated in Fig. 4.14, and it has been implemented in Figs. 4.10 and 4.11.

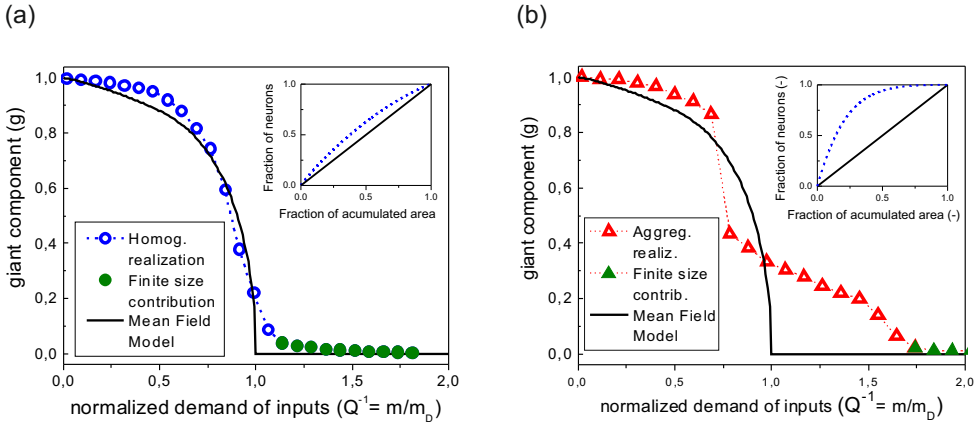

Fig. 4.13 Finite avalanches in simulated disintegration curves. **(a)** Simulated disintegration of the giant component $g(m/m_D)$ for the homogeneous configuration, with the corresponding Lorenz curve depicted on the inset ($\Lambda = 0.18$). **(b)** Simulated disintegration of the giant component $g(m/m_D)$ for the aggregated configuration, with the corresponding Lorenz curve depicted on the inset ($\Lambda = 0.63$). Solid, green symbols depict the contribution of finite size avalanches.

The treatment of finite size avalanches is also implemented in the experiments. g is set to 0 for values lower than 0.1 since it cannot be discriminated from other activity avalanches.

For $N \to \infty$, the absence of these small jumps and the expected continuous response arise from the decrease of the relative size of finite avalanches with N, as shown in Fig. 4.15.

In the case of the aggregated configuration, and assuming a typical size for the clusters of neurons, one would expect an early total disintegration of

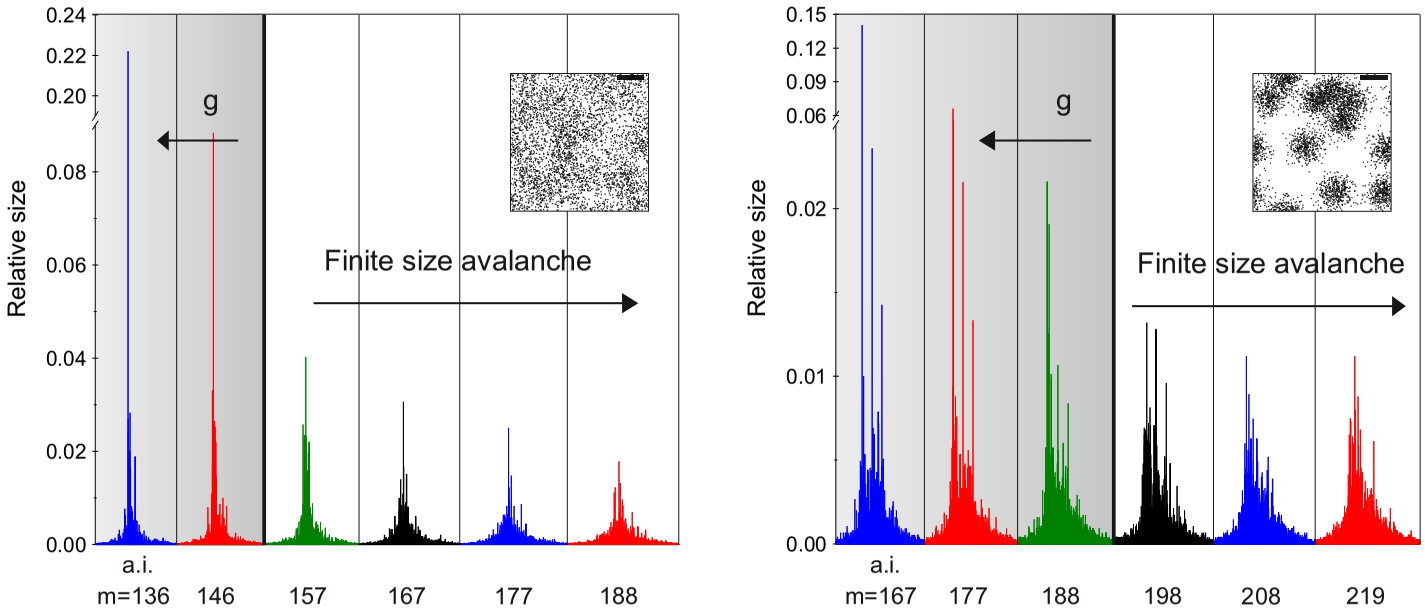

Fig. 4.14 Relative size of avalanches for single homogeneous and aggregated realizations. In the left main plot, each subplot shows the relative size of the jumps of activity for a given m, extracted from the left plot of Fig. 4.6. Inset shows the spatial distribution of the homogeneous network; scale bar is 1 mm. In the right main plot, subplots are extracted from the left plot of Fig. 4.7. The three significant avalanches observed for $m \lesssim 188$ evince the modular traits present in the aggregated configuration. Inset shows the spatial distribution of the aggregated network. The indexes of the avalanches in the x–axis (a.i.) are sorted by increasing external fields for each subplot.

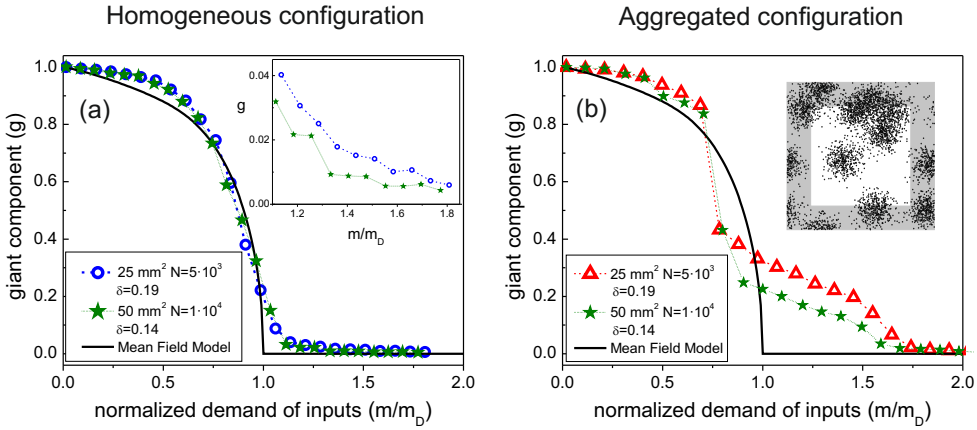

Fig. 4.15 Dependence of finite size avalanches on system size for the homogeneous and aggregated configurations. **(a)** Simulated disintegration curves of two equivalent, quasi-homogeneous networks with different system sizes. Each curve is a single network realization. The inset shows a detail of the curves above transition, and evinces the decrease of finite-size effects with system size. **(b)** Simulated disintegration curves of two equivalent, aggregated networks (single realizations) with different system sizes. The inset shows a typical spatial distribution of an aggregated realization; gray area indicates the difference between the two system sizes.

the giant component in the strict thermodynamic limit. In our simulations, as shown in Fig. 4.15b, this first disintegration is observed as a sudden decrease at $m/m_D \simeq 0.75$, and is related to the isolation of individual clusters. However, since the relative size of the clusters is not negligible with respect to our system size, a late disintegration of the giant component can be extracted, as occurs at $m/m_D \simeq 1.7$. The latter transition is due to the larger local intra–cluster connectivity, as previously explained in Section 4.2.1.

(B) Finite–size effects related to a finite connectivity length

The connectivity length is a parameter of the simulations grounded on the biological axonal length a. Upon construction of the simulated networks, the values of a are drawn from a Rayleigh distribution with mean $\langle a \rangle = 1.1$ mm (see Section 4.1.2). Both the distribution $p(a)$ and $\langle a \rangle$ are grounded on experimental data. Given their biological nature, they were treated as fixed

parameters in all simulations, independently on the number of neurons and system size.

To understand the impact of a fixed connectivity length on the simulations, we introduce the *relative axonal length* $\delta = \langle a \rangle / L$, where L is the characteristic size of the system, defined as an effective diameter $L = 2\sqrt{A/\pi}$, with A the total area of the network. The parameter δ conceptually reflects the capacity of an arbitrary neuron to connect with any other in the network. An illustrative sketch of the concept is shown in Fig. 4.16. The behavior of the system strongly depends on δ, as we elaborate below.

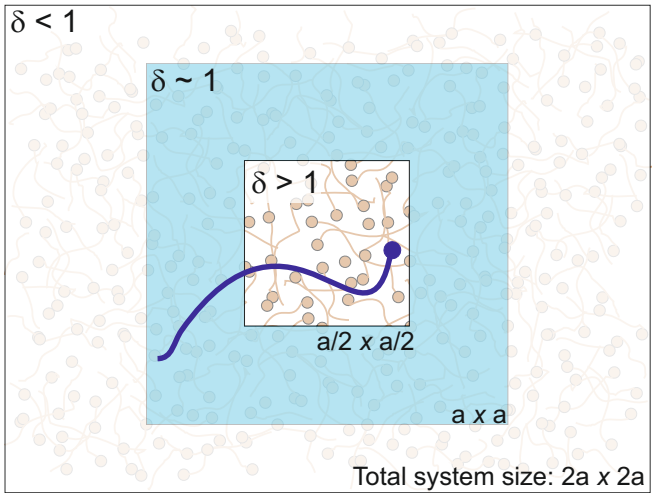

Fig. 4.16 Relative axonal length δ. Conceptual sketch of three system sizes and their relation to δ provided a biologically fixed average axonal length a. The largest network ($2a \times 2a$, $\delta < 1$) contains all axons, whose full–length is linked to a smaller scale than that of this system size. The smallest network ($a/2 \times a/2$, $\delta > 1$) cannot accommodate full–length axons, as illustrated by the purple labeled neuron. The middle–sized network ($a \times a$, $\delta \sim 1$) presents an in–between case.

For sake of clarity, we provide illustrative $g(m)$ simulations at three δ values in Fig. 4.17, and comparing the homogeneous and aggregated configurations. We note that, since $\langle a \rangle$ is a biologically fixed parameter, the different δ are provided by varying system size L.

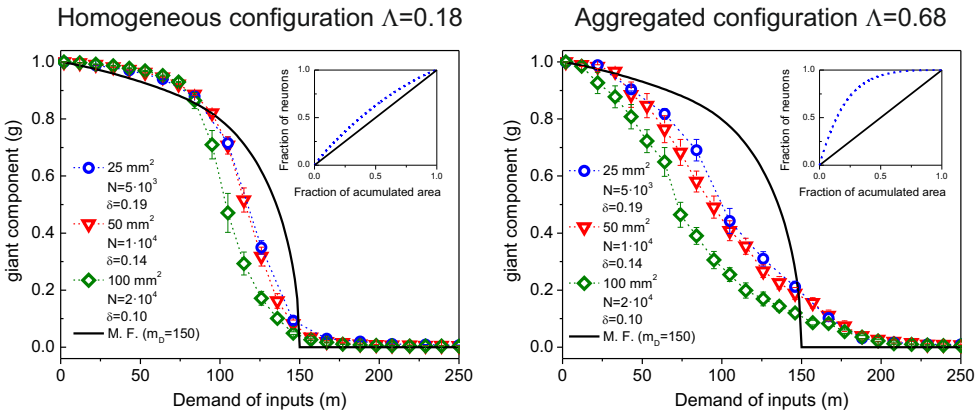

Fig. 4.17 Finite size effects for a varying system size with fixed mean axonal length, density, and degree of aggregation. Main plots show the disintegration curves $g(m)$ simulated for three system sizes in the homogeneous (left) and aggregated (right) configurations. Each data point corresponds to an average over 10 realizations. The insets show the corresponding Lorenz curves. Error bars denote the standard error of the mean.

Depending on the relative importance between axonal length and system size (Fig. 4.16), we distinguish three regimes:

- For $\delta \to 0$, the system size is much larger than $\langle a \rangle$, and therefore metric correlations shape a local connectivity scenario that totally dominates the behavior of the system. Mean–field is not applicable since, in general, the neurons do not experience the same effective neighborhood.

- For $\delta \simeq 1$, any neuron can connect to any other neuron, and therefore the entire system is sufficiently correlated for mean–field to be applicable. Spatial correlations shape local connectivity details that can be viewed as a perturbation to mean–field.

- For $\delta \to \infty$, the axonal length is much larger than the system size. Therefore the relative size of the connectivity length diverges, and mean–field is completely fulfilled since the network is totally connected.

We estimated $\delta \simeq 0.1$ ($\langle a \rangle \simeq 1.1$ mm and $L \simeq 10$ mm) for the experiments and simulations presented in this Chapter and in the previous one, and with

$N \sim 10^4$. The small value of δ indicates that metric correlations are important. In these conditions, simulations reveal that finite–size effects related to a finite connectivity length dominate over those associated to finite–size avalanches. We therefore conclude that the deviation of the network response from mean–field is mainly associated to the preeminence of metric correlations, and strengthens the message that we can use the mean–field solution as a basis to assess the importance of metric correlations in our cultures.

We remark that the different regimes pictured through δ could be related to percolation studies in spatially–embedded Erdös–Rényi graphs (Li et al., 2011; Schmeltzer et al., 2014). These studies, however, considered $\Lambda \to 0$ (lattice–like networks), disregarding a spatial feature that we ascertained as crucial.

As summary of the different behaviors observed, in Fig. 4.18 we provide examples of $g(m)$ and corresponding $g(m/m_D)$ curves for different metric scenarios, and compare them with the mean–field solution and the randomized analogs. Two extreme degrees of aggregation Λ are shown, namely $\Lambda = 0.18$ for homogeneous and $\Lambda = 0.68$ for aggregated configurations.

(C) Finite–size effects related to a limited field of view

The experimental data was obtained from monitoring a small window of 0.7×0.8 mm^2 in a circular culture of total area 133 mm^2 (see previous Chapter). Such a strong difference between the monitored area and the actual system size may give rise to artifacts in the disintegration curves that must be examined.

We carried out such an exploration with simulations, and summarized the results in Fig. 4.19. We first observed that in the mean–field solution, as well as in randomizations of metric networks, the size of the monitored area had no effect on the behavior of the disintegration curves. We next explored metric scenarios, and considered $\delta = 0.1$, i.e. strong metric effects, to mimic our experimental conditions. Figure 4.19a shows disintegration curves for a

typical homogeneous configuration, and evinces that no significant difference is present when the observation window is reduced from 100% the total area to just 0.64% of it. Similarly, the aggregated configuration (Fig. 4.19b) also does not exhibit important discrepancies among the three observation windows assessed. However, the variability is slightly increased in the latter due to the gradual importance of network–specific features of the monitored window, as reflected by the larger error bars.

4.3 Conclusions

In this Chapter, the complete simulations of the NNIM unveiled the sources of discrepancy between the mean–field solution and experiments. The primary agent behind those differences were metric correlations, that translated into the loss of the uniform, mean–field neighborhood. A second agent, but that played a substantially minor secondary order, was the distribution of connections, inherited from the aforementioned spatial embedding as well. We observed that two major ingredients shaped metric correlations. The first one was the *degree of aggregation*, Λ, which accounted for the heterogeneity in the arrangement of neurons over the space. And the second one was the *relative axonal length*, δ, which accounted for the finite maximum connectivity length among neurons relative to the total system size.

As Λ increased, and δ decreased, metric effects grew stronger in the system, and the behavior of the network gradually deviated from that of mean–field. *Homogeneous cultures*, of low Λ, presented highly reproducible activity blueprints, relatively consistent with mean–field calculations. High Λ, *aggregated cultures*, on the other hand, showed network–specific features largely different from the ones expected from mean–field. In the latter case, additional information of the internal structure of the network could be extracted, such as the average intra–connectivity in aggregates, as well as the mean inter–connectivity between them.

Finally, it is worth mentioning in the context of the following Chapter 6, that metric correlations dominated and overshadowed the distribution of connections to such a extreme that truly dictated the dynamic attributes of the network. For instance, the analysis of spontaneous activity fronts in homogeneous neuronal cultures similar to ours ($\delta \simeq 0.1$, $\Lambda \simeq 0.2$) revealed that metric correlations ultimately defined both the location and amplification mechanisms of activity fronts (Orlandi et al., 2013), which appeared periodically and propagated in a circular manner throughout the entire network. At the other extreme, in cultures with $\Lambda \gtrsim 0.6$, as in Fig. 4.11c, the dynamics was characterized by a fast synchronous firing at the scale of the neuronal aggregates combined with a slower sequential activation of small groups of aggregates at the system's scale (Teller et al., 2014).

At the extreme conditions of $\delta \to 0$ and $\Lambda \to 1$ the network switched towards a scenario of *networks of networks* in which the connectivity is markedly distinct at different scales.

In conclusion, our work brings the possibility to predict the dynamical complexity of spatial networks given δ and Λ, spatial features which are not only important to comprehend the structure–function interplay in living neuronal networks, but also in all those systems where spatial embedding is crucial, such as the Internet, transportation, or epidemics.

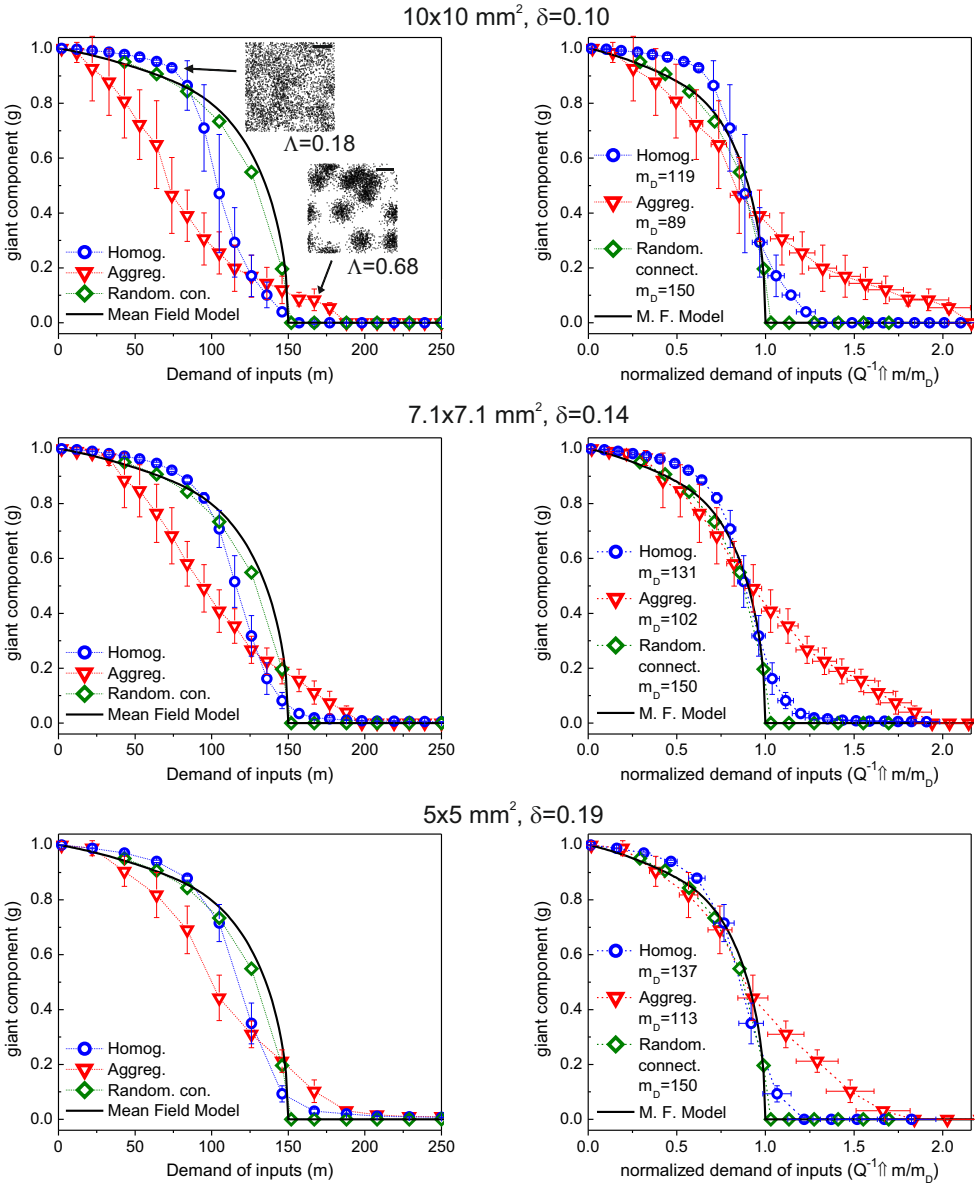

Fig. 4.18 Disintegration curves for complete simulations at varying system size in the homogeneous and aggregated configurations. The left main plots show the disintegration curves $g(m)$. The right main plots show the normalized disintegration curves $g(m/m_D)$, with the corresponding values of m_D derived from the fit to the mean field solution. Data points for 5×5 mm^2 networks are averaged over 50 realizations. The other data points are an average over 10 realizations. Vertical error bars denote standard deviation. Horizontal error bars reflect the variability in the fits. The insets in the top left plot represent typical spatial distributions of neurons for the homogeneous and aggregated configurations. Scale bars are 1 mm.

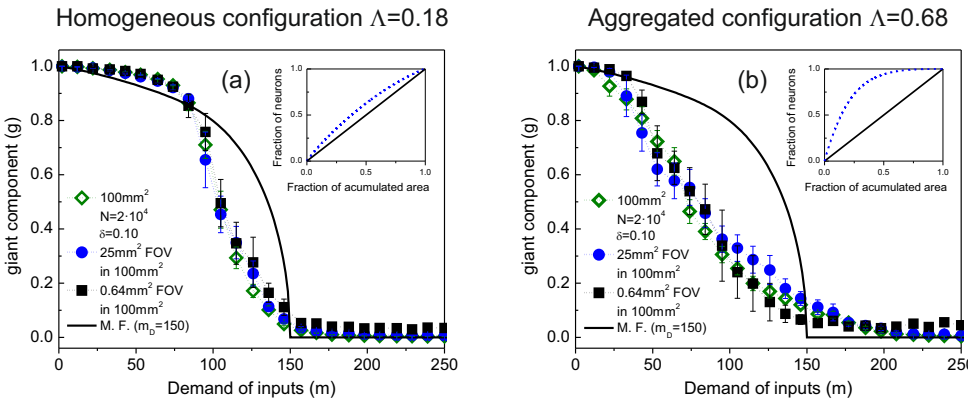

Fig. 4.19 Finite size effects associated to a limited field of view. **(a)** Homogeneous disintegration curves $g(m)$ for simulations with three different field of views. **(b)** Aggregated disintegration curves for the same three field of view sizes. The total area of both network configurations is 100 mm^2, i.e. $\delta \simeq 0.1$. Open diamonds correspond to simulations in which the field of view is the same as the system size; curves are an average over 10 realizations. Solid blue circles represent the behavior of subsets of 25 mm^2, averaged over 5 realizations. And solid black squares show the behavior of subsets of 0.64 mm^2, averaged over 5 realizations. The insets show the corresponding Lorenz curves. Error bars denote the standard error of the mean.

Chapter 5

Analytical Approach for the Initiation of Spontaneous Activity

5.1 Context of the problem

Neurons in cortical cultures exhibit strong spontaneous activity that emerge from a complex interplay between intrinsic neuronal dynamics, connectivity and noise (Orlandi et al., 2013). Noise is pivotal for the initiation of spontaneous activity and, in the context of biophysics, its importance exemplifies the beneficial role of noise in driving dynamical systems without the need of external clocks or forcing. For the particular case of neurons, we can identify two major sources of noise, namely the fluctuations in the membrane potential and the spontaneous release of neurotransmitters in the synaptic boutons of pre–synaptic cells.

This spontaneous activity is present in the form of activity avalanches, which can either die out before activating a macroscopic fraction of the culture (*background avalanches*, BA), or rise a growing cascade of neuronal activations (*ignition avalanches*, IA) that ultimately triggers a *burst*, i.e. the activation of almost the entire network (Orlandi et al., 2013).

A subtle aspect of spontaneous activity that is still not well understood is its *timing*, i.e. the typical time scale between the end of a burst and the initiation of the next one. This characteristic time certainly depends on the activity–connectivity–noise interplay, but its computation is not straightforward. To advance in this quest, in this Chapter we present a simple, non–equilibrium statistical approach to provide an analytical, semi–quantitative approximation for the average bursting frequency and its distribution. The approach is grounded on microscopic variables such as average connectivity, rate of spontaneous independent activations, and cell response to active neighbors.

A first effort in this direction was treated by Orlandi and coworkers in Orlandi et al. (2013) (with extensive details in the Supplemental Information of their publication, section Quorum Percolation Analysis). However, and since derivations were solely based on topological noise amplification, their results turned out to substantially diverge from the expected experimental values. As stated in their publication, "The failure of the percolation estimate dramatically illustrates the importance of dynamic correlations of the neuron firing".

Since our study is intimately related to the work of Orlandi *et al.*, we also use the terms BA and IA for the avalanches. We also remark that, as reported in preparations similar to ours, the typical IA and/or burst frequency observed in experiments is $\varphi_0 \sim 2-3$ bursts/min. We will focus our calculations at a local scale (at system sizes $L \ll 1$ mm). Then, by correctly predicting average burst frequency, we will indeed show that dynamical correlations dominate BA and IA, shape the amplification of noise, and boost the initiation of bursts.

5.2 Introductory framework

Neuronal cultures have been reported as small-world networks, with high clustering coefficient with respect to random graphs (Bettencourt et al., 2007). These metric correlations (Hernández-Navarro et al., 2017) favor local am-

plification of spontaneous activity, so that the activation of a small critical area of the culture, of a typical size of $r_c \simeq 300\mu$m and $N_c \sim 85$ neurons, automatically triggers a burst (Orlandi et al., 2013).

On the other hand, the activation of a single neuron, which is dominated by the interaction with its input neighbors, does not solely depend on the demand of inputs $\tilde{m}$. This threshold implies that a neuron *can only fire* if at least $\tilde{m}$ of its input neighbors activate[1] in a time window $\Delta t \approx 2\tau$, with $\tau = 10$ ms the time constant of the exponential decay of post–synaptic currents. However, and due to noise in the membrane potential and synaptic boutons, a neuron has a finite probability of firing when the number of inputs is lower than $\tilde{m}$. This was captured by Orlandi *et al.* in the framework of dynamical noise amplification of activity in realistic simulations, as shown in Figure 5.1. We also note that, if a neuron were going to fire due to m inputs in the aforementioned time window $\Delta t = 20$ ms, it would activate and excite its output neighbors at $\delta t \sim 2$ ms after receiving its last input. This is due to the time duration of action potentials and the generation of post–synaptic currents.

Summarizing, in order to predict the bursting frequency we have to derive the probability of spontaneous activation of subsets of $N_c \sim$85 neurons. Since topological noise amplification failed to account for realistic *inter–burst–intervals* (IBI), dynamical amplification has to be reconsidered.

5.2.1 Critical number of neurons in a compact area

We note that the critical area, sufficient to induce bursting when active, was already assessed in Orlandi et al. (2013), but it can be qualitatively predicted by means of simple calculations. One can argue that, if an active neuron has $N_c - 1$ active input neighbors, any of its output neighbors would receive at least $1 + (N_c - 1) \cdot cc$ inputs, where cc is the in–clustering coefficient. If

[1] In this Chapter we considered all connections excitatory for clarity and simplicity in the presentation of the theoretical results.

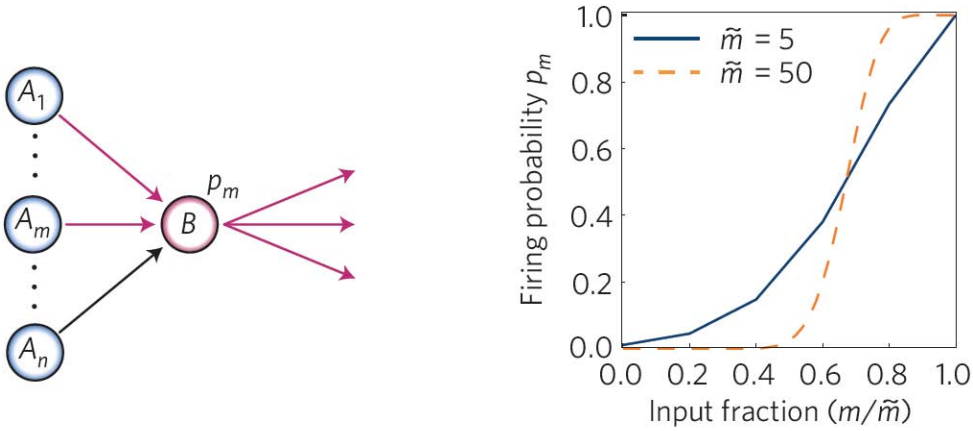

Fig. 5.1 Dynamical amplification mechanism due to connectivity. Left: schematic of the mechanism, where a subset of m (from a total of n) firing neurons projecting over neuron B induces a firing probability p_m (see Section 5.2.2). **Right**: dependence of p_m on the input fraction. The firing probability is greatly amplified before the quorum percolation condition $\tilde{m}$ is met. Figure reproduced from Orlandi et al. (2013).

we impose a critical N_c such that $\tilde{m}_0 = 1 + (N_c - 1) \cdot cc$, where $\tilde{m}_0$ is the initial demand of inputs, all the output neighbors of the first neuron would automatically become active. This would provide a next–step activation of at least 10^1–10^2 neurons and, together with the initial N_c active neurons, it would undoubtedly initiate a burst. Furthermore, the amplification could be enhanced by setting the N_c neurons in a compact area, while preserving the average density of the culture.

Two aspects are important to be clear. First, that the demand of inputs in initial conditions was estimated as $\tilde{m}_0 \simeq 15$ in a time window of $\Delta t = 20$ ms (Breskin et al., 2006; Cohen et al., 2010; Soriano et al., 2008). And, second, that the input clustering coefficient of our homogeneous neuronal cultures was $cc \simeq 0.17 \pm 0.02$ [Orlandi's PhD thesis]. Therefore, we concluded that the critical number of neurons in the critical area is around

$$N_c = 1 + \frac{\tilde{m}_0 - 1}{cc} \sim 83 \; neurons, \tag{5.1}$$

which is consistent with Orlandi et al. (2013).

5.2.2 Firing probability equation

As explained in Orlandi et al. (2013) (detailed in the subsection 'dynamical noise amplification' of the Supplemental Information), the sub–quorum probability of firing could be modeled as a Poisson shot process in the membrane potential, with spontaneous *shot noise* frequency λ in a time window Δt, and where m positive inputs from neighbors[2] would contribute as single, non–spontaneous shots. In brief, the probability of firing is the probability of spontaneously reaching $\tilde{m}_0$ total shots in a time window Δt, starting with m shots. Equation (15) of their SI reads

$$p_m = e^{-\lambda \Delta t} \sum_{i=\tilde{m}_0 - m}^{\infty} \frac{(\lambda \Delta t)^i}{i!} = 1 - \mathscr{P}(\tilde{m}_0 - m, \lambda \Delta t), \tag{5.2}$$

where $\mathscr{P}$ is the regularized gamma function, $\tilde{m}_0$ is the initial demand of inputs, and m is the actual number of positive inputs in the time window Δt.

We extended this last equation by taking into account a change in the demand of inputs $\tilde{m}$, for instance through application of the excitatory connectivity blocker CNQX to the cultures (see Chapter 4.1). Thus, the amplitude of input shots in the membrane potential is modulated by a factor $\tilde{m}_0/\tilde{m}$, and the expression becomes:

$$p_m = 1 - \mathscr{P}\left(\tilde{m}_0 \cdot \left(1 - \frac{m}{\tilde{m}}\right), \lambda \Delta t\right), \tag{5.3}$$

where, in the context of CNQX experiments, the actual demand of inputs takes the form $\tilde{m} = \tilde{m}_0 \cdot \left(1 + [\mathrm{CNQX}]/300nM\right)$.

[2] In this Chapter we followed the notation in Orlandi et al. (2013) instead of maintaining the notation of previous Chapters. Here m is the number of active input neighbors, and the demand of inputs is depicted by $\tilde{m}$.

To assess a realistic value for the average shot noise number $\lambda\Delta t$, and as suggested by Orlandi *et al.*, we use the experimental value for the spontaneous frequency of activation of single neurons in our cultures, namely ω_0=0.4 Hz. By introducing $m = 0$ in Eq. (5.3) we assess the probability for a neuron to spontaneously activate when all neighbors are silent, which must match with the above experimental value

$$p_0 = 1 - \mathscr{P}\left(\tilde{m}_0, \lambda\Delta t\right) = \omega_0\Delta t, \tag{5.4}$$

with the implicit solution providing $\lambda\Delta t = 5.67$ noise–shots on average.

Orlandi *et al.* found that, in general, $\lambda\Delta t \equiv \varepsilon(\tilde{m}_0 - 1)$, with ε a measure of the noise intensity. Our derivations provide a corresponding value of $\varepsilon \simeq 2/5 = 0.4$, similar to the value 1/3 extracted from Figure 5.1.

Finally, the introduced Poisson shot process could be approximated to a normal distributed process. Its mean can be obtained by equating the two arguments in $\mathscr{P}$ of Equation (5.3), isolating m, and adding a continuity correction constant of -1/2, which yields $\mu_{shot} \equiv \tilde{m}/\tilde{m}_0 \cdot (\tilde{m}_0 - \lambda\Delta t) - 1/2 \cong (1-\varepsilon)\tilde{m}$. Its standard deviation is directly $\sigma_{shot} \equiv \sqrt{\lambda\Delta t} \equiv \sqrt{\varepsilon(\tilde{m}_0 - 1)}$. Therefore, the firing probability can be written as

$$p_m = \Phi\left(\frac{m - \mu_{shot}}{\sigma_{shot}}\right) = \Phi\left(\frac{m - (1-\varepsilon)\tilde{m}}{\sqrt{\varepsilon(\tilde{m}_0 - 1)}}\right), \tag{5.5}$$

where Φ is the normal cumulative distribution function.

5.3 Burst frequency

Bursts are emergent phenomena arising from individual spontaneous activity that gets amplified by topological and dynamical interactions between neurons, i.e. ignition avalanches. The topological amplification of noise can be summarized by stating that the ignition of any critical subset of size

N_c suffices to generate a whole–network burst, and therefore the distinction between IA and BA has to be assessed at this small scale. Our main goal in this section is to set a rough threshold to discern between ignition and background avalanches. This threshold is based on the initial number of spontaneously activated neurons n in N_c, and during a characteristic time window of $\Delta t = 20$ ms. Once this threshold is obtained, and knowing the spontaneous rate of individual spikes ω_0, we can compute the probability of activation of any N_c subset in this 20 ms time window by means of the Poisson distribution. Finally, and considering that the network is formed by N/N_c critical subnetworks, the full–culture burst frequency can be extracted.

We note that this is a conservative estimate since we take the whole network as an ensemble of N/N_c independent subnetworks, whereas in real cultures the interaction between critical subnetworks would enhance bursting frequency. However, this approximation is found to be accurate provided the relatively high value of $N_c \simeq 85$ neurons.

5.3.1 The connectivity lottery

At the local scale of N_c, the internal connectivity of the subnetwork could be approximated to a random graph since the characteristic length–scale of $2r_c = 600$ μm is lower than the average axonal length of $\langle \mathrm{a} \rangle \simeq 1$ mm (see Chapter 4).

In our framework, an avalanche starts with n spontaneously active neurons over N_c in a time window of $\Delta t = 20$ ms. Each of the other $N_c - n$ neurons are then connected to $m \leq n$ active input neighbors in this time window. To derive the distribution of m values in terms of N_c-1 possible neighbors, n active neighbors among the subnetwork, and $k \equiv k_{N_c}^{in}$ average input neighbors from $N_c - 1$, we have to calculate all possible combinations.

First we define a single combination as one specific input connectivity set for a neuron, composed of k input connections. Thus, the total number of

possible combinations reads:

$$\binom{N_c-1}{k}. \tag{5.6}$$

Then, once we fix m input connections from the n initially active neurons, and avoiding the connection to the $n-m$ remaining ones, the corresponding number of combinations is

$$\binom{N_c-1-n}{k-m}. \tag{5.7}$$

However, we are dealing with distinguishable neurons, and we have to take into account all possible combinations of m elements over n, i.e. $\binom{n}{m}$, for each combination in Equation (5.7). The final probability distribution function is then

$$\rho(m) = \frac{\binom{n}{m}\binom{N_c-1-n}{k-m}}{\binom{N_c-1}{k}}. \tag{5.8}$$

After a brief bibliographical search, the above equation was identified with the hypergeometric distribution, where the number of successes corresponds to m, in k draws without replacement, from a population of N_c-1 that contains n objects with the desired feature.

For further analytical calculations, we have to perform a normal approximation as well. In this case, the average and the standard deviation of the m–hypergeometric distribution correspond to

$$\mu_{hyp} = n\frac{k}{N_c-1}, \tag{5.9}$$

$$\sigma_{hyp} = \sqrt{\frac{1}{N_c-2}\cdot n(1-\frac{n}{N_c-1})\cdot k(1-\frac{k}{N_c-1})}. \tag{5.10}$$

So that the m–distribution can be approximated to

$$\rho(m) = \phi\left(\frac{m-\mu_{hyp}}{\sigma_{hyp}}\right)/\sigma_{hyp}, \tag{5.11}$$

where $\phi(x)$ is the standard normal density function with 0 mean and standard deviation 1.

5.3.2 Probability of next–step activation

Equation (5.5) characterizes the probability of activation of an arbitrary neuron when m of its input neighbors are active in a time window of $\Delta t = 20$ ms. On the other hand, Equation (5.11) determines the probability for a neuron to be connected to m active input neighbors when the total number of active neurons in a subset N_c is n, and the average input intra–subset connectivity is k. In this Section we combined both results to calculate the probability of activation of an arbitrary neuron depending solely on the initial number of active neurons n in the subset N_c.

The calculation basically implies to average the dynamic correlations over the m–distribution

$$p_n = \sum_{m=1}^{n} p_m \cdot \rho(m), \tag{5.12}$$

which, from Equations (5.5) and (5.11), can be approximated to

$$p_n \simeq \int_{1/2}^{n+1/2} \Phi\left(\frac{m-\mu_{shot}}{\sigma_{shot}}\right) \cdot \phi\left(\frac{m-\mu_{hyp}}{\sigma_{hyp}}\right)/\sigma_{hyp} \cdot dm. \tag{5.13}$$

Now, by redefining $x \equiv \frac{m-\mu_{hyp}}{\sigma_{hyp}}$, and $dx \equiv \frac{dm}{\sigma_{hyp}}$, we obtain

$$p_n \simeq \int_{\frac{1/2-\mu_{hyp}}{\sigma_{hyp}}}^{\frac{1/2+n-\mu_{hyp}}{\sigma_{hyp}}} \Phi\Big(a+b\cdot x\Big) \cdot \phi(x) \cdot dx, \tag{5.14}$$

where $a \equiv \frac{\mu_{hyp}-\mu_{shot}}{\sigma_{shot}}$ and $b \equiv \frac{\sigma_{hyp}}{\sigma_{shot}}$.

The argument of the last integral is similar to a Gaussian whose main area fall within the integration limits, specially for $n \gtrsim 2$. Thus, we can approximate the previous upper and lower integral bounds by $+\infty$ and $-\infty$ respectively. From Owen (1980) we know that

$$\int_{-\infty}^{+\infty} \Phi\Big(a+b\cdot x\Big)\cdot\phi(x)\cdot dx = \Phi\Big(\frac{a}{\sqrt{1+b^2}}\Big). \tag{5.15}$$

Finally, we conclude that the probability of activation of an inactive neuron of N_c in a time window of δt=2 ms, and provided that n neurons had activated in the previous Δt=20 ms, can be approximated to

$$p_n \simeq \Phi\Big(\frac{\mu_{hyp}(n)-\mu_{shot}}{\sqrt{\sigma_{hyp}(n)^2+\sigma_{shot}^2}}\Big) = \Phi\Big(\frac{n\cdot\frac{k}{N_c-1}-3/5\cdot\tilde{m}}{\sqrt{\frac{n(1-\frac{n}{N_c-1})\cdot k(1-\frac{k}{N_c-1})}{N_c-2}+2/5\cdot(\tilde{m}_0-1)}}\Big). \tag{5.16}$$

where $\delta t = 2$ ms to reflect the time duration of action potentials and the generation of post–synaptic currents, as already explained in Section 5.2.

5.3.3 Threshold for ignition avalanches

As a last step we have to extract a threshold for the initial number of spontaneously active neurons n in N_c (and in $\Delta t = 20$ ms) that separates IA from BA. We reason that the threshold is set by the value of n that provides an unstable equilibrium, in the sense that any perturbation in n would drag the system either towards silence, or bursting. Higher n would generate IA, whereas lower values would end up vanishing as BA. This threshold would be an approximate one, since the probability of crossing it would be finite; and the threshold value would be calculated by means of average rates.

To assess equilibrium states of the system, we evaluated those states with compensated average activations and average attenuations, *i.e.* zero mean

rates or zero derivative states. Since we are performing a rough derivative with respect to time, it is sufficient to take solely into account the first time step $\delta t = 2$ ms.

First, we note that the available number of neurons–to–activate[3] is $N_c - n$ and, therefore, the number of neurons that on average would become active at the first time step is $n_1^+ = p_n \cdot (N_c - n)$. On the other hand, we must be aware that a moving time window Δt would gradually lose (or attenuate) the oldest activations at an average initial rate of $n/\Delta t$. Since our time step is set at $\delta t = 2$ ms due to the time duration of action potentials, the number of activations whose effect is lost at the first time step is, on average, $n_1^- = \delta t \cdot n/\Delta t = n/10$.

Both the activation and the attenuation rates follow Poisson distributions, with their corresponding means. The variation in n is then characterized by the difference of two Poisson–distributed variables, whose resulting distribution is the Skellam distribution, of mean $\delta n = n_1^+ - n_1^-$ and standard deviation $\sigma_{\delta n} = \sqrt{n_1^+ + n_1^-}$.

In conclusion, the equilibrium states of the system in terms of n are solutions to

$$p_n \cdot (N_c - n) - n/10 = 0, \tag{5.17}$$

which explicitly reads

$$\Phi\Big(\frac{n \cdot \frac{k}{N_c - 1} - 3/5 \cdot \tilde{m}}{\sqrt{\frac{n(1-\frac{n}{N_c-1}) \cdot k(1-\frac{k}{N_c-1})}{N_c - 2}} + 2/5 \cdot (\tilde{m}_0 - 1)} \Big) \cdot (N_c - n) = n/10, \tag{5.18}$$

where n is the number of active neurons in a critical subset of size N_c and in a time window Δt, k is the average input intra–N_c connectivity, $\tilde{m}$ is the actual demand of inputs, and $\tilde{m}_0$ is the initial, unperturbed demand of inputs.

[3] Here we make an implicit approximation. We do not consider the n active neurons as 'available' to fire since we assume that no neuron will fire twice in $\Delta t = 20$ ms, at least for our activity regime of interest (BA and IA).

Realistic values of the aforementioned quantities are $N_c \sim 85$ neurons; $k \sim 30$ input neurons over N_c; $\tilde{m} = \tilde{m}_0$ (without CNQX); and $\tilde{m}_0 \simeq 15$ (Section 5.2.1). The solutions are then $n_{equilib} = 0.064$, 7.68, and 77.3 neurons. The first solution is stable and corresponds to the background activity $\omega_0 \delta t \simeq 0.068$. The third solution is also stable[4], and is related to peak bursting activity. Finally, the second solution is unstable and corresponds to our threshold for IA. Additionally, a first estimate of the uncertainty of these values can be derived from their Skellam's standard deviation, which corresponds to $\sigma = \sqrt{n^+_{equilib} + n^-_{equilib}} = \sqrt{2 \cdot n^-_{equilib}} = \sqrt{n_{equilib}/5}$. In conclusion, the threshold for the generation of ignition avalanches is

$$n_{thr} \simeq 7.7 \pm 1.2. \tag{5.19}$$

Figure 5.2 illustrates the dynamical process, shows the threshold value that separates BA from IA, and displays typical steps of activations for the latter. Figure 5.3 depicts the 'increment–potential' as a rough parallelism to the usual notion of potentials in classical mechanics. This increment–potential is numerically calculated as $-\int_0^n \Delta n \cdot dn$, so that single–step increments Δn in function of current n can be calculated from the potential as minus its derivative.

5.3.4 Whole–culture bursting: ensemble of N/N_c independent subnetworks

As stated at the beginning of Section 5.3, we made a conservative assumption by considering that the network was formed by N/N_c independent critical subnetworks, disregarding burst–enhancement from the hands of interactions between subsets.

[4] In the strict context of neuronal cultures, it is a kinetically stable solution that decays to lower activity states due to short–term synaptic depression. Here we do not consider STD for simplicity since we are interested in a much lower activity regime.

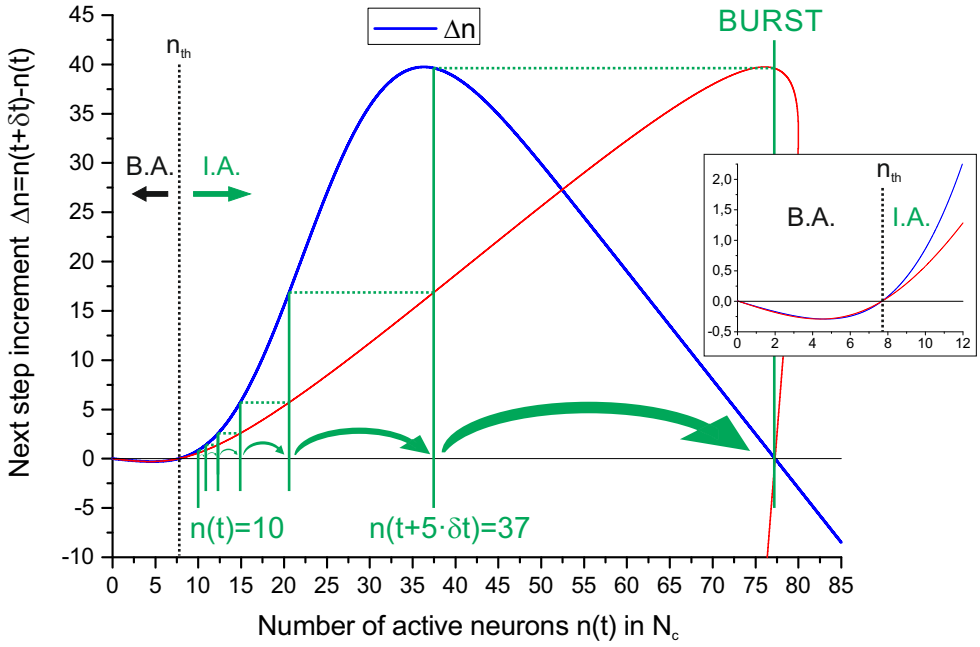

Fig. 5.2 Dynamical profile. Increment in the number of active neurons Δn in the following time step $t+\delta t$ in terms of the number of active neurons n in current time step t (thick solid blue line). Vertical dashed black line illustrates the threshold value n_{th} that separates BA and IA. An example of the dynamical evolution of the system in IA is depicted by vertical thin solid green lines and green arrows. Thin solid red line shows Δn in terms of $n+\Delta n$ as a visual aid for IA dynamics. **Inset**: zoom–in of the threshold region.

Provided the threshold value of n_{thr} active neurons in N_c during Δt, the probability of activation of an arbitrary subnetwork in Δt can be calculated as the probability of spontaneous occurrence of $n \geq n_{thr}$, where n is a Poisson–distributed variable with mean $\omega_0 \Delta t N_c$. That is

$$p^{\Delta t}_{sub-burst} = 1 - \mathscr{P}(n_{thr}, \omega_0 \Delta t N_c), \tag{5.20}$$

where $\mathscr{P}$ is again the regularized gamma function.

To obtain the initiation of a whole–network burst in a Δt time window, at least one subnetwork should have bursted during this time lapse. The bursting

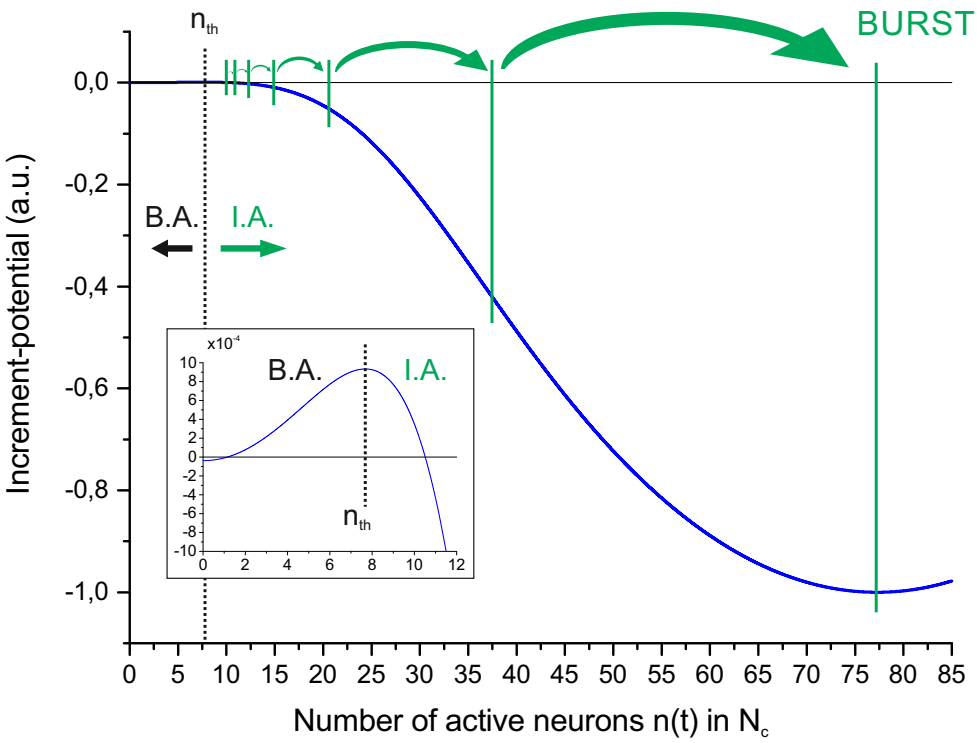

Fig. 5.3 Increment–potential. Illustrative approximate parallelism to the 'potential' concept in classical mechanics. Solid blue line shows $-\int_0^n \Delta n \cdot dn$ derived numerically from data in Fig. 5.2. Vertical dashed black line illustrates the threshold value n_{th} that separates BA and IA. The dynamical evolution of the system in the IA example of Fig. 5.2 is also depicted here by vertical thin solid green lines and green arrows. **Inset**: zoom–in of the threshold region.

probability in Δt is then

$$p_{burst}^{\Delta t} = 1 - (1 - p_{sub-burst}^{\Delta t})^{N/N_c} = 1 - [\mathscr{P}(n_{thr}, \omega_0 \Delta t N_c)]^{N/N_c}. \qquad (5.21)$$

The average inter–burst interval (IBI), which is the inverse of the bursting frequency ν_{burst}, is derived by taking into account the refractory time τ_{ref} that has to elapse for cultures to burst again. The refractory time is experimentally assessed in our lab by electrical stimulation (see following Chapter 8). The observed values are consistent with a Poisson distribution of mean $\tau_{ref} = 10$ s.

The IBI is then

$$\langle IBI \rangle = \tau_{ref} + \frac{\Delta t}{p_{burst}^{\Delta t}} = \tau_{ref} + \frac{\Delta t}{1 - [\mathscr{P}(n_{thr}, \omega_0 \Delta t N_c)]^{N/N_c}} \sim 36\ s, \quad (5.22)$$

where $N = 5 \cdot 10^4$ neurons as in our typical ϕ=13 mm, $\rho \approx$400 n/mm^2 homogeneous cultures. We would like to point out that this result remarkably matched the experimental $\varphi_0 \sim 2-3$ bursts/min (see Section 5.1).

We note that the uncertainty in n_{thr} provides a two–order of magnitude range of possible IBI, i.e. between ∼11 and ∼570 s. And, although this broad range impoverishes the predicting power of these derivations, it is totally consistent with experiments given the extremely high variability of IBIs between identical cultures, and even between different time windows of the same recording of activity.

The bursting frequency can be finally established as

$$\nu_{burst} = \frac{1}{\tau_{ref} + \frac{\Delta t}{1 - [\mathscr{P}(n_{thr}, \omega_0 \Delta t N_c)]^{N/N_c}}} \sim 10^{-2} - 10^{-3}\ Hz. \quad (5.23)$$

Notation and numerical results are summarized in Table 5.1.

5.4 Aggregated cultures

Cultures with strong degrees of aggregation are composed of sets of aggregates or *neurospheres*. These neurospheres are a compact agglomeration of neurons, with a total number of cells that range between 50 and 500 neurons, in a characteristic diameter of $\phi_{aggreg.} \sim 100\ \mu$m (Teller et al., 2014, 2015). Provided these features, clusters can be modeled as compact random networks, with weak interactions between neurons from different clusters. Therefore, the above derivations for critical subsets N_c in homogeneous cultures could be applied as well to whole–aggregates composed of N_c neurons. Then, their

individual spontaneous cluster firing rate could be predicted, and information about their internal connectivity and other characteristics could be extracted.

Notation	Numerical value	Description
BA/IA	–	Background/Ignition avalanche(s)
N	$\sim 5 \cdot 10^4$ neurons	Total neurons in typical culture
N_c	≈ 85 neurons	Total neurons in critical subset
r_c	$\sim 300\ \mu$m	Radius of critical subset
$k \equiv k_{N_c}^{in}$	~ 30 neurons	Average intra–N_c connectivity
cc	0.17 ± 0.02	Clustering coefficient
Δt	20 ms	Time window for recruitment of inputs
δt	2 ms	Time step in activity avalanches
τ_{ref}	~ 10 s	Refractory time for culture recovery
ω_0	~ 0.4 Hz/neuron	Spontaneous single activation rate
λ	≈ 300 Hz/neuron	Shot noise rate in membrane potential
ε	≈ 0.4	Measure of noise in membrane potential
$\tilde{m}_0$	15	Initial demand of inputs
$\tilde{m}$	–	Current demand of inputs
m	–	Inputs from active neighbors in N_c and Δt
n	–	Active neurons in N_c and Δt
μ_{shot}	≈ 9 (for $\tilde{m} = \tilde{m}_0$)	Mean of sub–threshold m to activate
σ_{shot}	≈ 2.4	Std of sub–threshold m to activate
μ_{hyp}	(depends on n)	Mean active neighbors seen in N_c and Δt
σ_{hyp}	(depends on n)	Std of active neighbors seen in N_c and Δt
δn	(depends on n)	Single step (δt) mean increase in n
$\sigma_{\delta n}$	(depends on n)	Single step std of increase in n
n_{th}	7.7 ± 1.2	Threshold in n for BA/IA
$p_{sub-burst}^{\Delta t}$	$\approx 1.3 \cdot 10^{-6}$	Probability of activation of N_c in Δt
$p_{burst}^{\Delta t}$	$\approx 7.7 \cdot 10^{-4}$	Probability of culture burst in Δt
$\langle IBI \rangle$	~ 36 s	Mean inter–burst–interval
ν_{burst}	$\sim 2.8 \cdot 10^{-2}$	Culture bursting frequency

Table 5.1 Notation and numerical values.

Chapter 6

Connectivity and Dynamics in Patterned Neuronal Cultures

In this Chapter we present the results of our patterned experiments, i.e. those in which the cultures do not have a homogeneous substrate but include some sort of obstacle or topographical pattern. As illustrated in Fig. 6.1, experiments comprise two major kind of cultures, namely 'half–PDMS-on–Glass' and 'PDMS patterned' cultures. The analysis of the experimental data

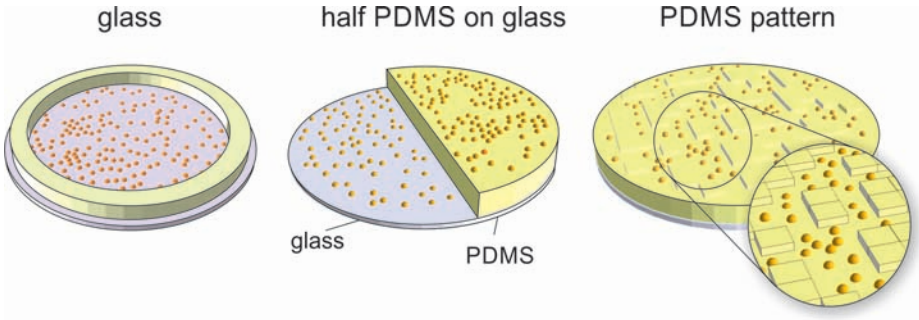

Fig. 6.1 Patterned experiments. Left: sketch of a typical homogeneous culture whose size is constrained by a PDMS ring. **Center**: 'half–PDMS-on–Glass' configuration, where a PDMS slab $\simeq 1$ mm high attached over glass introduces a sharp vertical step that separates the culture into two regions. **Right**: 'PDMS patterned' culture, which provides a topographical disorder constructed with unit squares 250 μm lateral size and 100 μm height.

is explained in Chapter 2, where a sketch of the setup for imaging cultures is also provided.

6.1 Half–PDMS–on–GLASS experiments

These cultures were prepared in a rather simple way. Briefly, we poured and cured a precisely set quantity of PDMS on a plastic petri dish, leading to a PDMS layer of a well–known thickness. We next extracted a 14 mm diameter PDMS disc, cut it in two parts, and bond carefully one of the parts to a clean glass at high temperatures. Neuronal cultures were then prepared, maintained in the incubator, and imaged as usual.

In general, neurons developed healthily in both substrates, although the degree of interconnectivity between the PDMS–neurons and the GLASS–neurons could vary. The *raison d'être* of these experiments was to correlate the structure of network bursts with the connectivity probability among the two distinct sides.

The experimental results shown in this chapter were extracted from 8 *good* cultures (out of 30 total cultures). These selected cultures were the only ones exhibiting sufficient activity and high signal–to–noise ratio for their analysis to be rich from an statistical point of view.

In this section we firstly present the observed number of network bursts, discuss the results and provide an estimation of the crossing probability in both directions between the elevated PDMS crest and the bottom GLASS substrate. Secondly, we present the obtained velocity of propagation of activity for each burst in each side, as well as the distribution of initiation points.

For the investigated cultures, the following three main experimental conditions were explored: standard, *excitation+inhibition* network (NOR); *bicuculline*–treated, *excitation–only* network (BIC); and PDMS–GLASS disconnection (CUT). For the latter we just used a scalpel to cut the connections

along the GLASS–PDMS contact line, effectively separating the two sides (PDMS and GLASS). In all conditions, the two sides were independently studied. We would like to remark that, taking into consideration all combinations of analyzed sides and conditions, each culture involved the equivalent of 6 experiments, i.e. a total of 48 networks were studied in this chapter.

6.1.1 Initial hypothesis

Taking into account solely neuronal structure and neurite growth, we formulate the following two hypotheses: *(i) the sharp step between GLASS and PDMS creates an asymmetric connectivity that leads to a master–slave dynamics, with PDMS being the dominant side*; and *(ii) the degree of asymmetry increases with the height h between the two sides up to some threshold value of complete disconnection*. Hence, activity starting in PDMS will propagate to GLASS much more frequently than the other way around as h increases.

We note that, at the micrometric scale of neurons and connections, gravity does not play any role. Cultures are always submerged in liquid (either culture media or EM) and neurites are attached to the substrate (a process enhanced by the PLL coating). Hence, the vertical orientation of the step would in principle be ignored by the neurites. As we will see, this is not the case and therefore the asymmetry in the interaction between PDMS and GLASS sides should arise from other sources.

We consider the following scenario, in which as a general assumption we consider that neurons attach and develop connections in the same way in both PDMS and GLASS substrates. The PDMS–GLASS step can be visualized as a *fold*, where both the wall and crest are PDMS, and the lower part is GLASS. The crevice at the PDMS is convex, i.e. with an angle of $\simeq 270^\circ$, while the step at the glass surface is concave, with an angle of $\simeq 90^\circ$. Since during plating neurons are placed vertically over the surfaces, there will be no neurons at the wall, and thus all interconnectivity would arise from the ability of the neurons to project connections upwards or downwards (Fig. 6.2a). In

other words, the system is visualized as a single surface, but with no neurons over the tiny window that is the wall.

To account for the possible directionality of axons and dendrites, we argue that the concavity at the bottom and the convexity at the top *are seen differently* by the axons or dendrites, altering neurite growth and breaking the symmetry in interconnectivity. Let us consider a neuron at the bottom layer. Based on our observations, it seems that neurites tend to remain in the

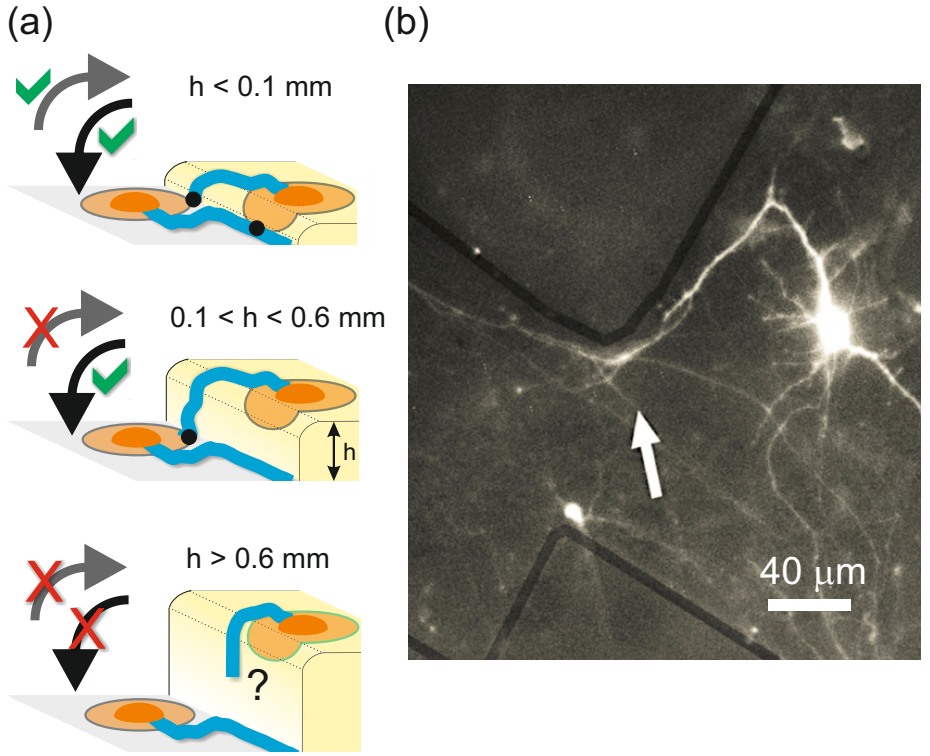

Fig. 6.2 Hypothesis of top–bottom connectivity. **(a)** Sketch of the behavior of axons and dendritic trees for gradually increasing heights h between glass and PDMS. Short heights allow for bidirectional connectivity; medium heights lead to preferentially top–bottom connectivity; and tall heights effectively disconnect the two surfaces. **(b)** Example of the interaction of an axon with a PDMS obstacle, and illustrates that axons growing at the bottom of a topographical pattern tend to grow on the same $x-y$ plane, i.e. they rarely climb obstacles. The axon was visualized using GFP transfection in Soriano's lab.

same plane in which they grow when an obstacle appears. Hence, neurites would touch the wall and they will either be deflected in any direction over the same plane or will just grow along the contact line, without climbing up (Fig. 6.2a). Images taken in our experiments indeed show evidence of this tendency for axons to remain in the same plane (Fig. 6.2b). For a neuron at the top, however, the neurites just keep growing along the bent surface, and either follow the edge or go down.

With this basic scenario in mind, we now introduce the effect of the height difference h between the bottom and top layers. For small heights, top dendrites and axons can interact with bottom ones, facilitating a connectivity in both directions. For intermediate heights, top axons may easily get over the upper edge of the step, to finally reach the lower corner, where they could find an accumulation of dendrites to connect to. However, axons at the bottom would be either trapped along the edge of the wall or go somewhere else, without easily finding top dendrites. This situation would lead to a preferred PDMS–to–GLASS interconnectivity, breaking the symmetry of the network. Finally, for very large heights, top axons would not be able to travel the long distances of the wall, effectively isolating the neurons at the bottom and top layers.

6.1.2 Total number of network bursts

The first direct analysis in our experiments is the computation of the total number of bursts along 30 *min* of recording. Since we performed the analysis of the data separately for the PDMS and for the GLASS sides, we could easily compare their activity. Figure 6.3 presents the results in terms of the total number of observed network bursts for each side. There is high variability between cultures, and even between sides of the same culture; however a minor trend could be observed, in the sense that the total number of bursts presented a relative decrease in CUT conditions, probably reflecting the loss of the PDMS–GLASS interaction. A decrease could be also observed for

results in BIC condition. This drop in activity is related to the release of a larger number of neurotransmitters in the presence of bicuculline, which leads to a larger recovery time after each network burst and, thus, a reduction in bursts' frequency.

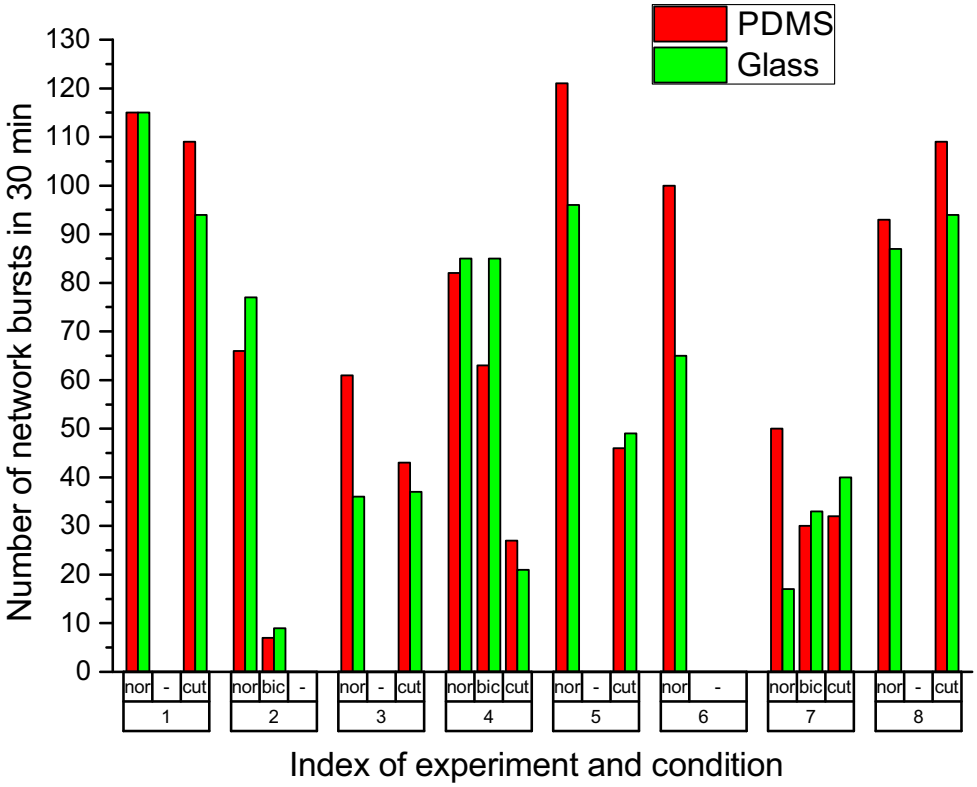

Fig. 6.3 Total number of network bursts. Number of network bursts for PDMS (red) and for GLASS (green) for all measurable experiments and for unperturbed (NOR), blocked–inhibition (BIC), and non–interacting (CUT) experimental conditions.

Figure 6.4 provides a comparison between the number of observed bursts at PDMS and GLASS sides, and by plotting the results at one side as a function of the other. No clear tendency is observed, indicating that the total number of burst may not be a good descriptor to quantify the interaction of the two sides. The plot, however, illustrates in a better way the observed

tendency that the number of bursts decreases for CUT and BIC conditions as compared to the NOR one.

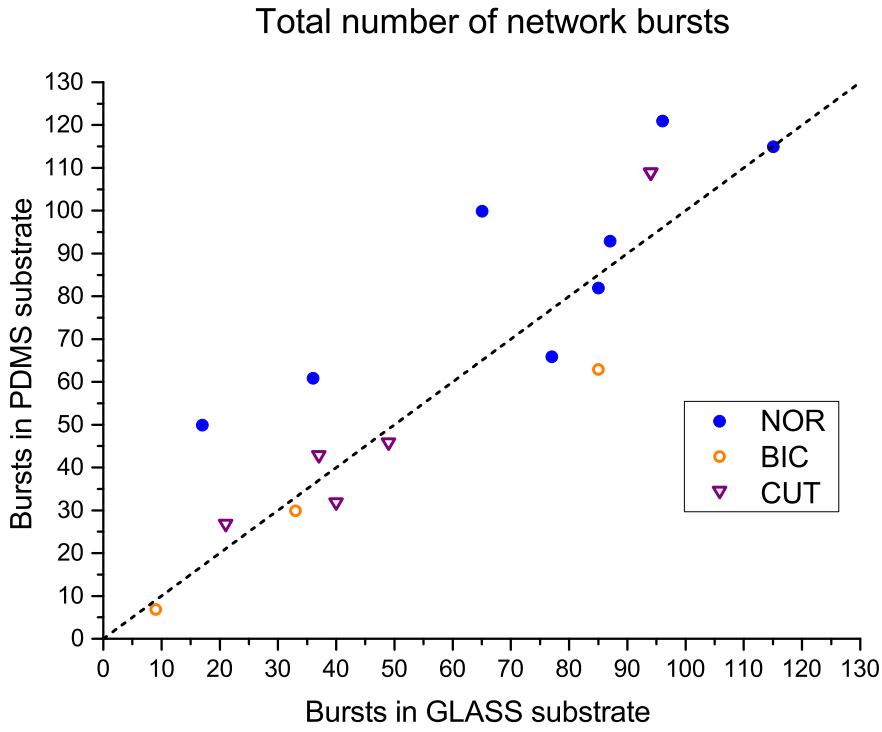

Fig. 6.4 Substrate contribution to number of network bursts. Comparison between PDMS and GLASS number of network bursts for each measurable experiment and condition. Bisector indicates symmetric number of bursts between layers.

6.1.3 Interaction: Crossing probability

To deepen in the analysis, and to assess a possible master–slave dynamics, we need to investigate the initiation of activity and its propagation. Our hypothesis is that there is a preferred PDMS–to–GLASS activity flow for intermediate heights h of the step. This is shown in Section 6.1.1 and Figure 6.1.

To investigate the validity of this hypothesis, we need to introduce the following specific notation.

A *Network Burst* (*NB*) is defined as the quasi–synchronous activation of one of the two sides, either PDMS (NB_P) or GLASS (NB_G). We define a *PDMS–GLASS pair–burst* (PB_{P-G}) as a set of two bursts, one from PDMS and another from GLASS, that are mutually the closest in time, in the sense that the NB_G is the closest to the NB_P and vice versa. The maximum time difference between NB_P and NB_G allowed in a PB_{P-G} is 200 ms, otherwise they are not paired.

Network bursts that participate in PB_{P-G} are designated as *Interacting Network Bursts* (*inter.NB*), and are subdivided in *Initiator Network Bursts* (*init.NB*) and *Follower Network Bursts* ($fw.NB$), which stand for *first* and *last* to fire in their corresponding PB_{P-G}, respectively. The remaining *NB* not included in any PB_{P-G} are defined as *Isolated Network bursts* (*isol.NB*), and all *NB* not included in the $fw.NB$ subset are designated as *Spontaneous Network Burst* (*spo.NB*) since they arose from the spontaneous noise amplification also observed in non–patterned cultures. Notation is summarized in Table 6.1.

NB	Network Burst	NB_P	*NB* in PDMS side
		NB_G	*NB* in GLASS side
PB_{P-G}	Any $\{NB_P, NB_G\}$ pair separated less than 200 ms in time		
inter.NB	Any *NB* in a PB_{P-G}	*init.NB*	First *NB* in a PB_{P-G}
		$fw.NB$	Second *NB* in a PB_{P-G}
isol.NB	Any NB_P or NB_G not included in any PB_{P-G}		
spo.NB	Any *NB* that is not a $fw.NB$		

Table 6.1 Notation in half–PDMS–on–GLASS experiments

We note that causality is assumed for PB_{P-G}. This data processing may provide spurious 'causal' activity when different sides fire independently but close in time. However, these spurious false interactions are upper bounded, as is discussed afterwards.

To properly characterize the interaction between sides, we assess the *crossing probability* for each layer. This probability for a given layer is

computed as the conditional probability of triggering a NB in the other side when the first layer has spontaneously bursted (with a time difference lower than 200 ms) .

The above crossing probability can be estimated by assuming a binomial distribution, where the parameter p is our unknown probability, the m number of trials is the number of $spo.NB$ of the first layer, and the n number of successes is the number of $fw.NB$ of the second layer. Provided m and n, we calculate the likelihood function or distribution for p to obtain its best estimate and its uncertainty. We notice that this likelihood distribution should take the form

$$f_{m,n}(p) = C_{m,n} \cdot p^n \cdot (1-p)^{m-n}, \tag{6.1}$$

where $C_{m,n}$ is a normalization factor that depends on m and n.

To get a proper likelihood distribution we had to normalize the previous expression using integration by parts, which yields

$$\frac{C_{m,n}}{n+1} p^{n+1}(1-p)^{m-n}\Big]_0^1 + \int_0^1 \frac{(m-n)C_{m,n}}{n+1} p^{n+1}(1-p)^{m-n-1} \cdot dp = 1. \tag{6.2}$$

The second term of the sum became zero for $n = m$, and then we derived

$$C_{m,n=m} = m+1. \tag{6.3}$$

For $0 \leq n < m$ the first term vanished, providing

$$\frac{(m-n)C_{m,n}}{n+1} \cdot \int_0^1 p^{n+1}(1-p)^{m-(n+1)} \cdot dp = 1. \tag{6.4}$$

which could be rewritten as

$$\frac{(m-n)C_{m,n}}{n+1} \cdot \int_0^1 \frac{f_{m,n+1}(p)}{C_{m,n+1}} \cdot dp = 1, \tag{6.5}$$

and since $f_{m,n+1}(p)$ is already normalized by definition, we got

$$C_{m,n} \cdot \frac{m-n}{n+1} = C_{m,n+1}, \tag{6.6}$$

which is valid for $n = m$ as well since it provides $C_{m,m+1} = 0$, as should be expected.

From the previous recurrence we derived that

$$C_{m,n} = g(m) \cdot \binom{m}{n}, \tag{6.7}$$

where g(m) is strictly a function of m.

From Eq. 6.7 and 6.3 we concluded that

$$C_{m,n} = (m+1) \cdot \binom{m}{n}. \tag{6.8}$$

And therefore, the likelihood distribution for the crossing probability was

$$f_{m,n}(p) = (m+1) \cdot \binom{m}{n} \cdot p^n \cdot (1-p)^{m-n}, \tag{6.9}$$

which, regarding the literature, corresponded to the beta distribution $Beta(\alpha, \beta)$ with parameters $\alpha \equiv n+1$ and $\beta \equiv m-n+1$.

The best estimate for the crossing probability provided m and n was the mean value of the former distribution, with an uncertainty equal to its standard deviation. To derive both, we calculated a generic equation for non–central moments of the distribution

$$\langle p^k \rangle = \int_0^1 C_{m,n} \cdot p^{n+k} (1-p)^{m-n} \cdot dp, \tag{6.10}$$

that could be reshaped as

$$\langle p^k \rangle = \int_0^1 C_{m,n} \cdot \frac{f_{m+k,n+k}(p)}{C_{m+k,n+k}} \cdot dp, \tag{6.11}$$

in order to get the general result

$$\langle p^k \rangle = \frac{C_{m,n}}{C_{m+k,n+k}} = \frac{(n+k)!}{n!} \cdot \frac{(m+1)!}{(m+k+1)!}, \tag{6.12}$$

which provided the final estimation of the crossing probability from a layer X to a layer Y

$$p_{X \to Y} \simeq \frac{n+1}{m+2} \pm \sqrt{\frac{n+1}{m+2} \cdot \left(\frac{n+2}{m+3} - \frac{n+1}{m+2} \right)}, \tag{6.13}$$

where $m = spo.NB_X$; $n = fw.NB_Y$; and $X = P$ *or* G, while $Y = G$ *or* P.

Figure 6.5 shows the results for the computed crossing probabilities. Two aspects are worth noting. First, that the computed crossing probabilities for the non–interacting (CUT) condition are below $\sim 10\%$ for all experiments, indicating that spurious detections of crossing events are very small. And second, that the application of bicuculline (BIC) did not significantly affect the crossing probabilities, indicating that possible asymmetries in connectivity equally affect excitatory and inhibitory connections.

To better contrast the behavior of the PDMS and glass sides, and to assess their possible asymmetric interconnectivity, Figure 6.6 presents a comparative plot between PDMS and GLASS crossing probabilities. By denoting p_{PG} the crossing probability from PDMS to GLASS, and by p_{GP} the crossing probability from GLASS to PDMS, the figure plots one probability as a function of the other. Cultures with perfectly symmetric connectivity would lead to data points in the bisector of the plot (black dotted line), and any asymmetry would be reflected in deviations from it. In this plot, four data points markedly deviated from the bisector. The deviation followed an interesting

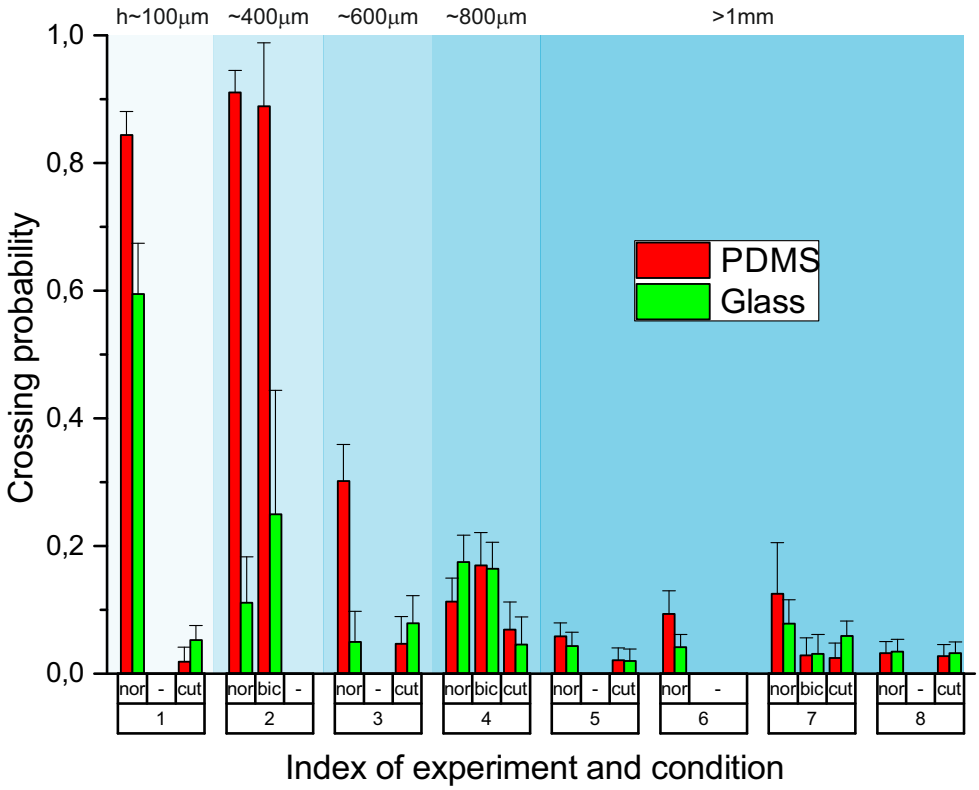

Fig. 6.5 Crossing probabilities. Crossing probability from PDMS (red) and from GLASS (green) for all measurable experiments and for unperturbed (NOR), blocked–inhibition (BIC), and non–interacting (CUT) experimental conditions. Corresponding step heights h indicated on top. Error bars are standard error of the mean.

trend. Experiment number 8, with $h \simeq 0.1$ mm, exhibits $p_{\mathrm{PG}} \simeq 85\%$, and $p_{\mathrm{GP}} \simeq 60\%$. The values are significantly different within experimental error, and proves that small height differences suffice to create an asymmetry that favors the propagation from top to bottom. This effect is increased for experiment number 1, with $h \simeq 0.4$ mm, providing $p_{\mathrm{PG}} \simeq 90\%$, and $p_{\mathrm{GP}} \simeq 15\%$. At the case of large heights, as in experiment number 7 with $h \simeq 0.6$ mm, the probabilities substantially decrease to $p_{\mathrm{PG}} \simeq 30\%$, and $p_{\mathrm{GP}} \simeq 5\%$, indicating that this height is at the verge of completely disconnecting the networks at the two sides.

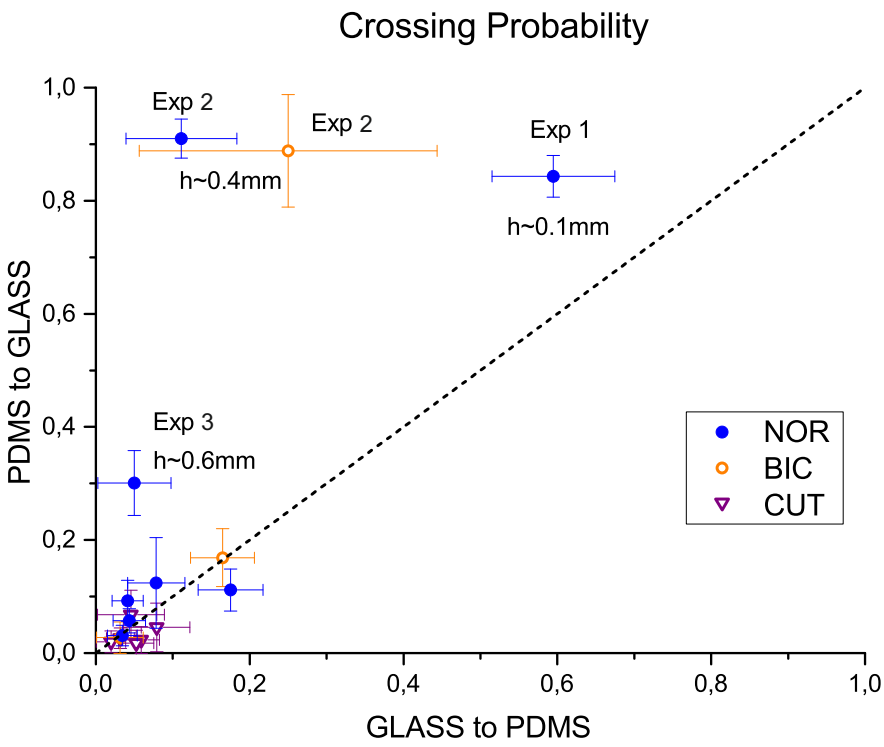

Fig. 6.6 Asymmetric interconnectivity. Comparison between PDMS and GLASS crossing probabilities for each measurable experiment and condition. Bisector indicates symmetric crossing probabilities between layers. Error bars are standard error of the mean. Significantly asymmetric data is labeled by index of experiment and step height h.

Summarizing, these relatively simple experiments identified a qualitative dependency of the crossing probabilities on the step height h that was consistent with our initial hypothesis. Under this assumption, a PDMS step of zero height would provide a practically $\sim 100\%$ crossing probability between sides, with maybe small differences that would arise from the different substrate materials. In the experiments, the crossing probability from GLASS to PDMS substantially decreases as h grows, while it is maintained high in the other direction up to ~ 0.5 *mm*. This situation corresponds to the central sketch in Figure 6.2a, in which few GLASS neurons are able to establish connections with the top PDMS ones. Interestingly, the dependence of p_{PG} on h (or p_{GP} on h) is not linear, reflecting the complex biomechanical processes

associated to connectivity in the presence of obstacles. Values of $h \simeq 0.6$ lead to the interesting situation in which $p_{\mathrm{PG}} > 0$ and $p_{\mathrm{GP}} \simeq 0$, a result that serves as inspiration to design experiments with complex substrate configurations and even more complex spatio–temporal activity patterns. Finally, for $h \gtrsim 0.7$ the two sides are effectively independent, and corresponds to the situation sketched in the bottom panel of Figure 6.2a.

6.1.4 Velocity of propagation

In this analysis we discriminated between initiator bursts (*init.NB*) and follower bursts ($fw.NB$) for the interacting case (PB_{P-G}). Overall, we studied differences in the velocity of activity propagation on PDMS and GLASS substrates. As a first general overview, Figure 6.7 shows the velocity of propagation in each side, experiment and condition.

To refine the analysis, we considered again the idea of plotting the results in a given substrate as a function of the other, and with a bisector indicating any lack of difference. These plots are provided in Figures 6.8 and 6.9. The former pictures possible differences in velocity due to the substrate, for instance associated to different neuronal aggregation levels, cell attachment differences or contrasting axonal lengths. The latter features a comparison of propagation speeds according to the initiator/follower role of each *inter.NB*, in order to evaluate possible differences in velocity related to the initiator role of PDMS and the follower role of GLASS.

The comparison of velocities in the different substrates shown in Figure 6.8 is not sufficiently clear to draw strong conclusions, although there is a tendency for the velocity on PDMS to be higher. We must note that neurons on PDMS are slightly more aggregated and, therefore, in terms of the metric effects exposed in Chapter 4, one could hypothesize that PDMS substrates may induce a higher average connectivity and in turn a higher velocity. However, the strong variability indicates that a thorough investigation is required in order to fully quantify the actors that shape propagation velocity,

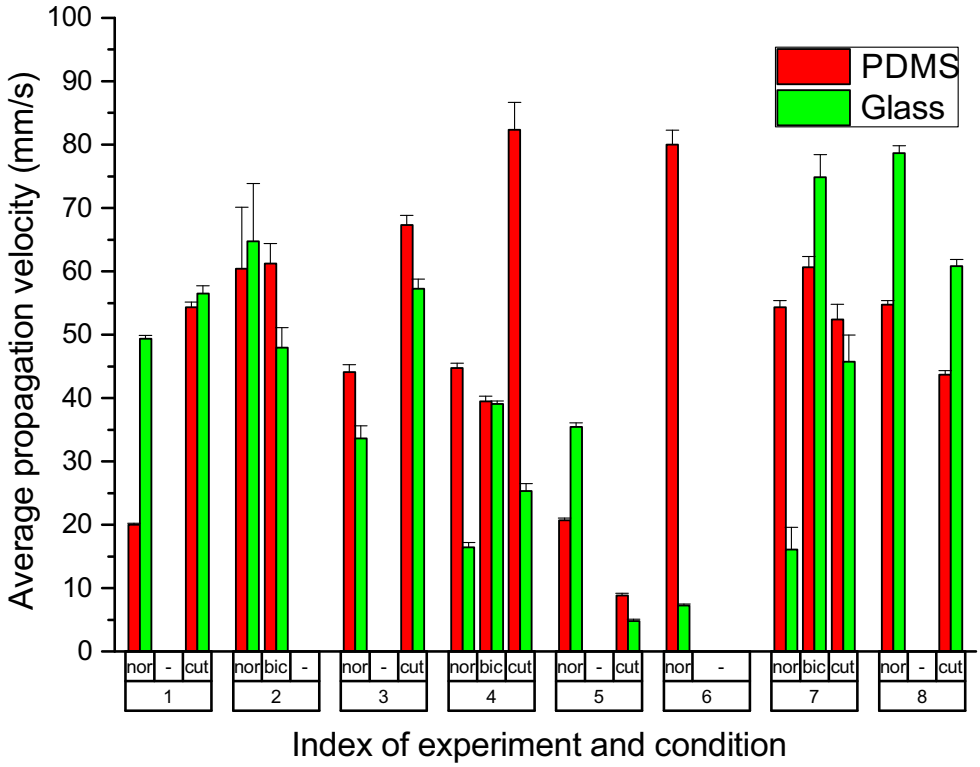

Fig. 6.7 Velocity of propagation. Velocity of propagation in each layer for PDMS (red) and for GLASS (green) for all measurable experiments and for unperturbed (NOR), blocked–inhibition (BIC), and non–interacting (CUT) experimental conditions. Error bars are standard error of the inverse–variance weighted mean.

an endeavor beyond the scope of this thesis. For clarity, those experiments used to quantify the role of the step height h are labeled in the plot, indicating that an assymetry in connectivity is not followed by a change in velocity.

For the initiator/follower role of Figure 6.9 we again could not see any significant difference in the velocity of propagation. This result proves that bursts' initiator or follower role was independent of its velocity of propagation. BIC and CUT data points were omitted in this plot, for clarity in the presentation of the results since they do not provide any additional information.

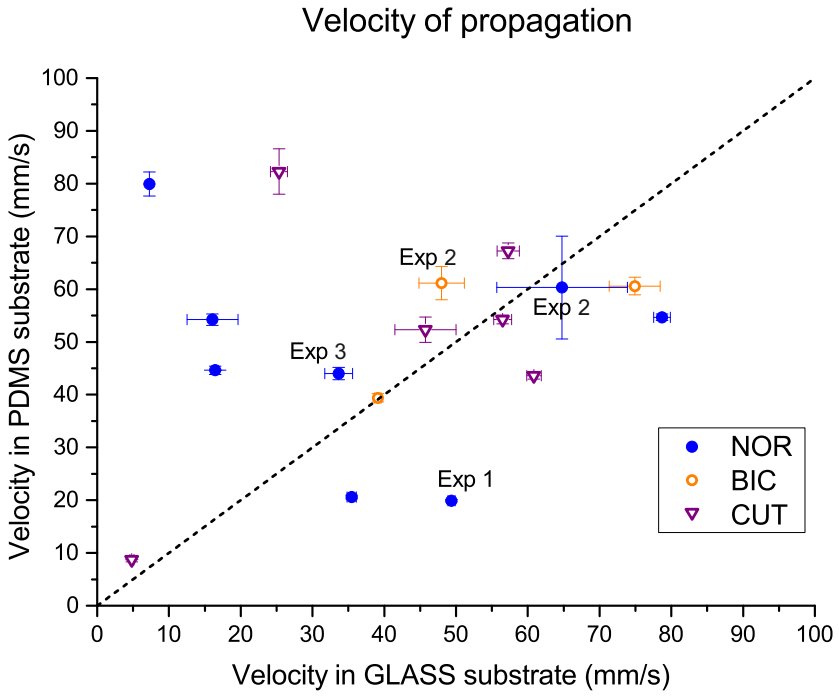

Fig. 6.8 Substrate contribution to velocity of propagation. Comparison between PDMS and GLASS velocities of propagation for each measurable experiment and condition. All bursts have been taken into account. Bisector indicates symmetric velocities between layers. Error bars are standard error of the inverse–variance weighted mean. Significantly asymmetric data is labeled by index of experiment in order to assess possible biases due to interaction between layers.

6.1.5 Initiation points

In this analysis we discriminated between *spo.NB* and *fw.NB* initial points since the latter were a consequence of activity crossing from a layer to the other one. Therefore, we expected the *fw.NB* points to be close to the step, which acted as a boundary between PDMS and GLASS layers. On the other hand, *spo.NB* arose from spontaneous noise amplification independently of the activity developing in the opposite layer. We also note that a distinction between *isol.NB* and *init.NB* was unnecessary.

Figure 6.10 presents the computed probability density function (pdf) of the location of initiation points by means of a Gaussian filter, as explained in

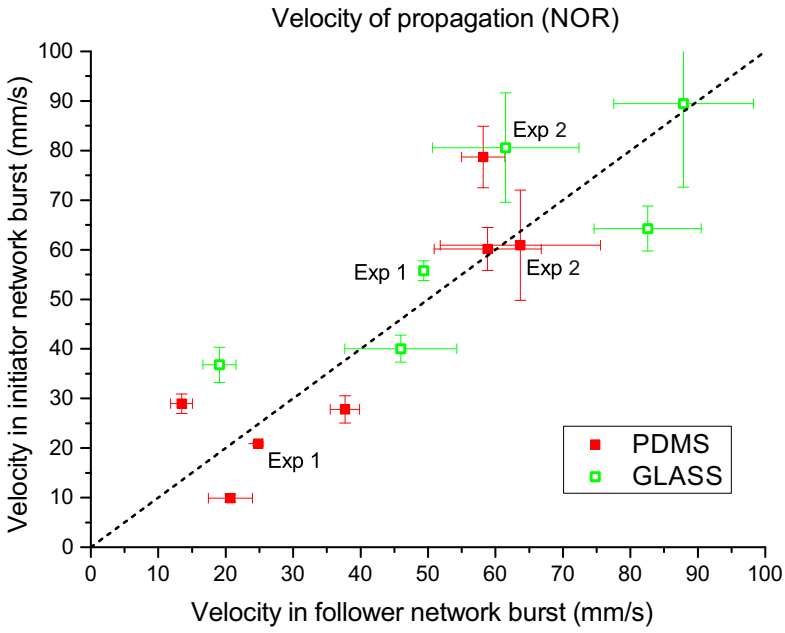

Fig. 6.9 Initiator/follower role contribution to velocity of propagation. Comparison between *init.NB* and *fw.NB* velocities of propagation for each measurable experiment and condition. We note that solely *inter.NB* have been taken into account since *isol.NB* could not be designated as initiators or followers. Bisector indicates symmetric velocities between layers. Error bars are standard error of the inverse–variance weighted mean. Significantly asymmetric data is labeled by index of experiment. Data not shown correspond to data with absence of either initiator or follower bursts.

Section 2.4.4 of Chapter 2. BIC and CUT data were omitted for simplicity. A general shift towards the step between PDMS and GLASS layers was observed for *fw.NB* initiation points (lower plots of each enclosed plot pairs) with respect to *spo.NB* initiation points (upper plots), as expected, and specially for experiments 1–4. Additionally, the pdf of initiation points are highly heterogeneous and network–specific for all cases, with a major fraction of the probability volume encompassed by solely $\sim 15\%$ of culture area, a result that is consistent with the *noise focusing* theoretical framework for their occurrence (Orlandi et al., 2013).

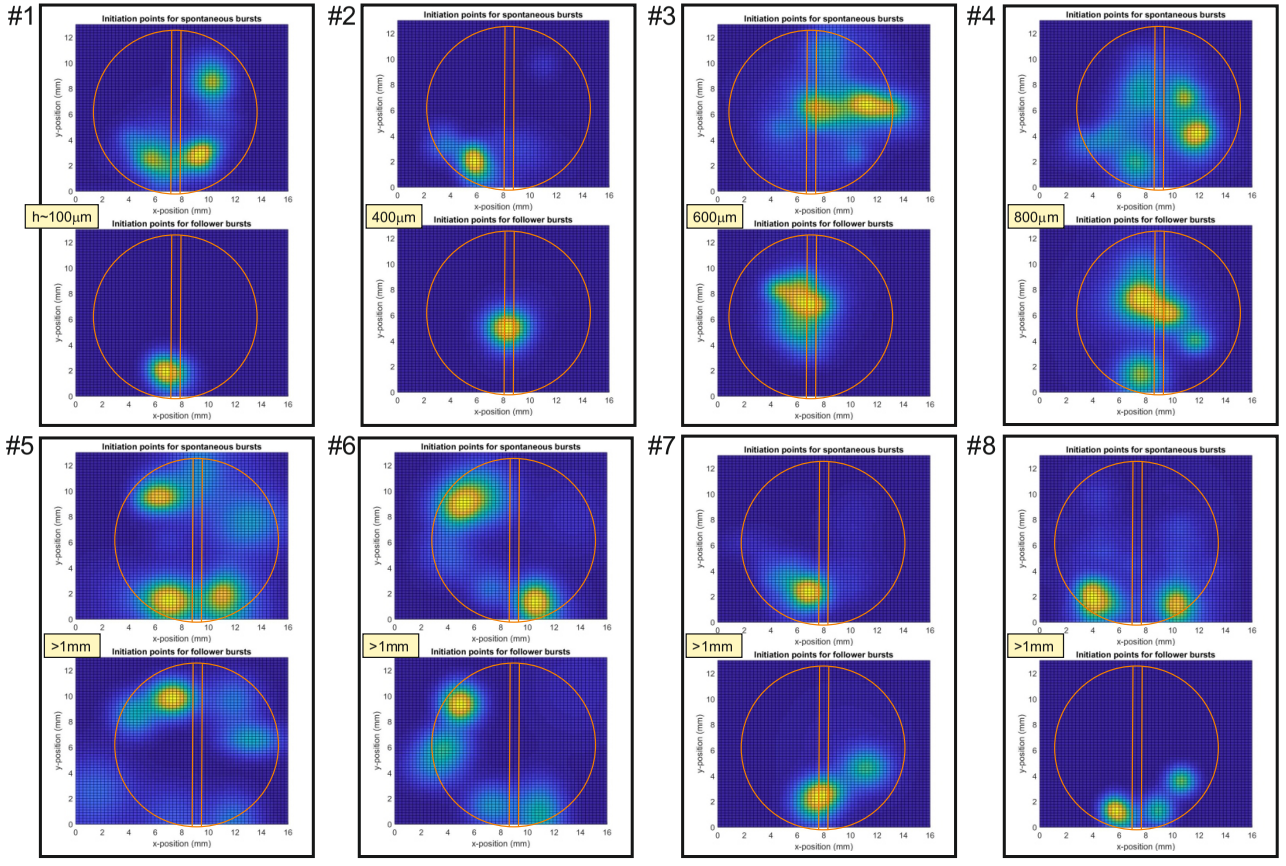

Fig. 6.10 Probability density estimations for the 2D location of initiation points in NOR experiments. Color map of the initiation points pdf, with probability color scale ranging from blue to yellow. Each enclosed pair of plots corresponded to a single experiment, with index equal to their upper–left label. Location of culture and boundary of layers are indicated in solid orange lines. **Upper plots**: initiation points pdf for *spo.NB*, including *isol.NB* and *init.NB*. **Lower plots**: initiation points pdf for *fw.NB*.

6.2 Patterned experiments with PDMS molds

In this Section we present representative experimental results for the random squares patterned cultures (Fig. 6.11). Patterns were set as random squares of $125-250\ \mu$m lateral size and $100\ \mu$m high. We focused on the propagation of activity, and assessed changes in the structure and dynamics of the activity propagating waves with respect to the standard, homogeneous non–patterned cultures. All presented results were obtained at NOR experimental conditions, except for Figure 6.15 which corresponded to the BIC condition.

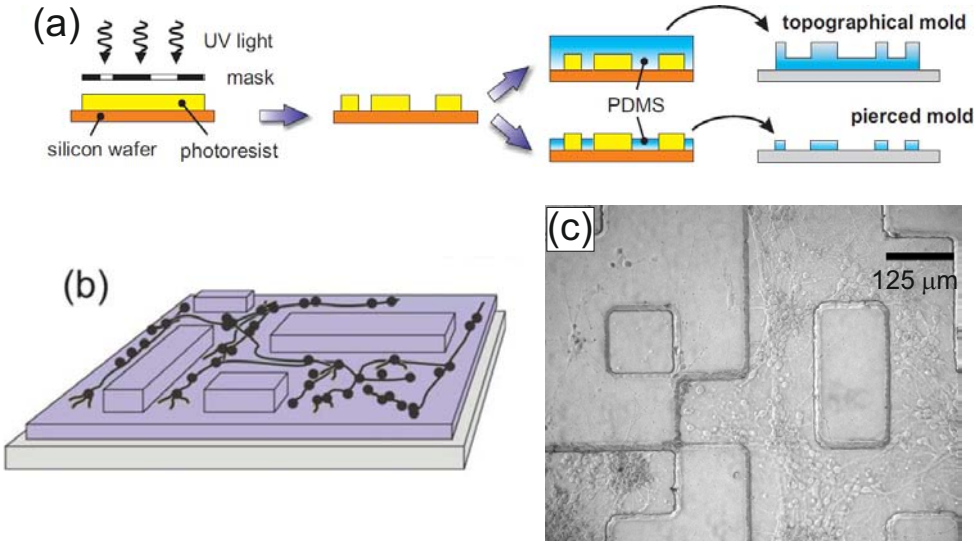

Fig. 6.11 Random squares patterns. **(a)** Photolithography is a process that creates a negative relief of a photo–mask (typically printed on transparency film) out of a resin. The procedure involves a photosensitive resist that is irradiated with UV light through the photo–mask to engrave the desired pattern on the substrate (black areas of the pattern are protected, while the transparent ones are exposed). This process induces cross–linking in the irradiated parts, and after development one obtains a resin mold with the negative relief of the photo–mask. PDMS is next poured over the relief and cured to get the final mould, where the black areas of the original design correspond to the valleys of the PDMS topography. One typically obtains topographical structures that are 50–100 um deep. **(b)** Sketch of the final topographical molds. By chemically treating the bottom parts of the PDMS mold one can prepare cultures that grow solely in the treated area and following complex paths. **(c)** Bright field image of a random squares patterned culture with neurons attached solely to the bottom parts of the PDMS mold.

6.2.1 Experimental data

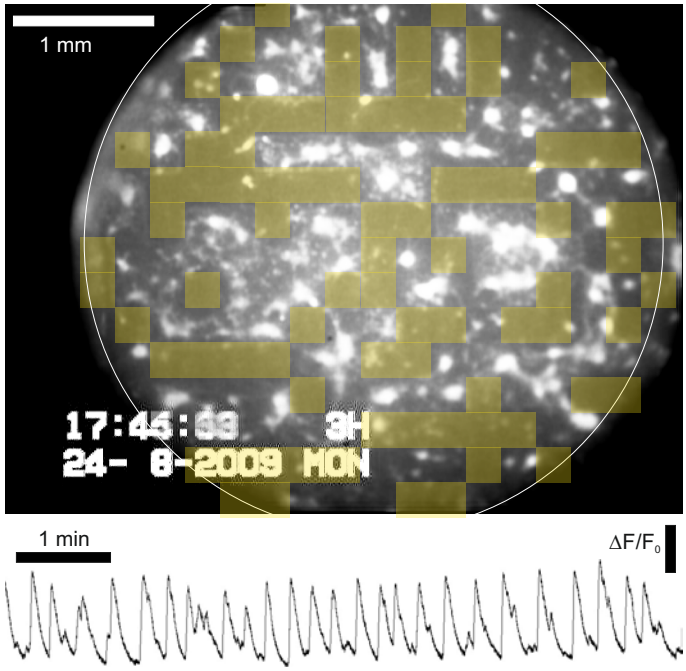

Fig. 6.12 Random topographical pattern experiments. Upper image: accumulated fluorescence image of a typical random pattern culture with superposed sketch of its patterned two–level topography. Yellow areas are obstacles 100 μm high. **Lower image**: average normalized fluorescent activity trace of the culture.

Figure 6.12 shows an example of a random patterned experiment. Typical culture size was $\phi \simeq 4\ mm$. In this experiments neurons preferentially grew in the valleys of the pattern and with clear aggregation, probably due to topographical constraints. Spontaneous activity was recorded and analyzed as usual. The average fluorescence, shown at the bottom of Figure 6.12, indicates a much richer dynamics than non–patterned cultures, with small network bursts at different scales and times. In particular, while homogeneous network showed whole–network bursts combined with silent intervals, in the patterned experiments we observed an almost continuous activity that encompasses different groups of neurons in the culture.

6.2.2 Propagation fronts

Figures 6.13a show two examples of different propagation structures. The observed activity fronts greatly deviated from the typical circular waves observed in homogeneous cultures, showing a rich dynamics that evinced the strongly topography–inherited connectivity blueprint. Specific network bursts dynamics were rarely reproduced since each burst presented a unique activation sequence. Qualitatively, we also observed that the deviation from homogeneous behavior increased as the topographical mold grew in height. The latter data was still under analysis at the moment of writing this thesis and is not shown.

6.2.3 Accumulated activation profiles

Raster plots for the above example bursts are provided in Figs. 6.13b. Here we observed that activity propagation was composed of smaller homogeneous propagations at a local scale, reminiscent of a patched culture composed of small interconnected homogeneous networks. These small propagations accumulated to build the multiple–step curve of accumulated activity (Figs. 6.13c), which was consistent with a connectivity blueprint perturbed by a random topography of characteristic length–scale of 250 μm, as the one shown in Fig. 6.12.

Figure 6.14 presents a comparison between a typical homogeneous accumulated activations profile and the obtained random pattern profile for the second front of Fig. 6.13c (bottom plot). The different scale in the temporal axis evinced a dramatic decrease in the global velocity of propagation of activity in the patterned experiments. This decrease arose mainly from the topographical pattern itself, whose intricacy and bottlenecks slowed down the propagation of activity between the small patches of local networks.

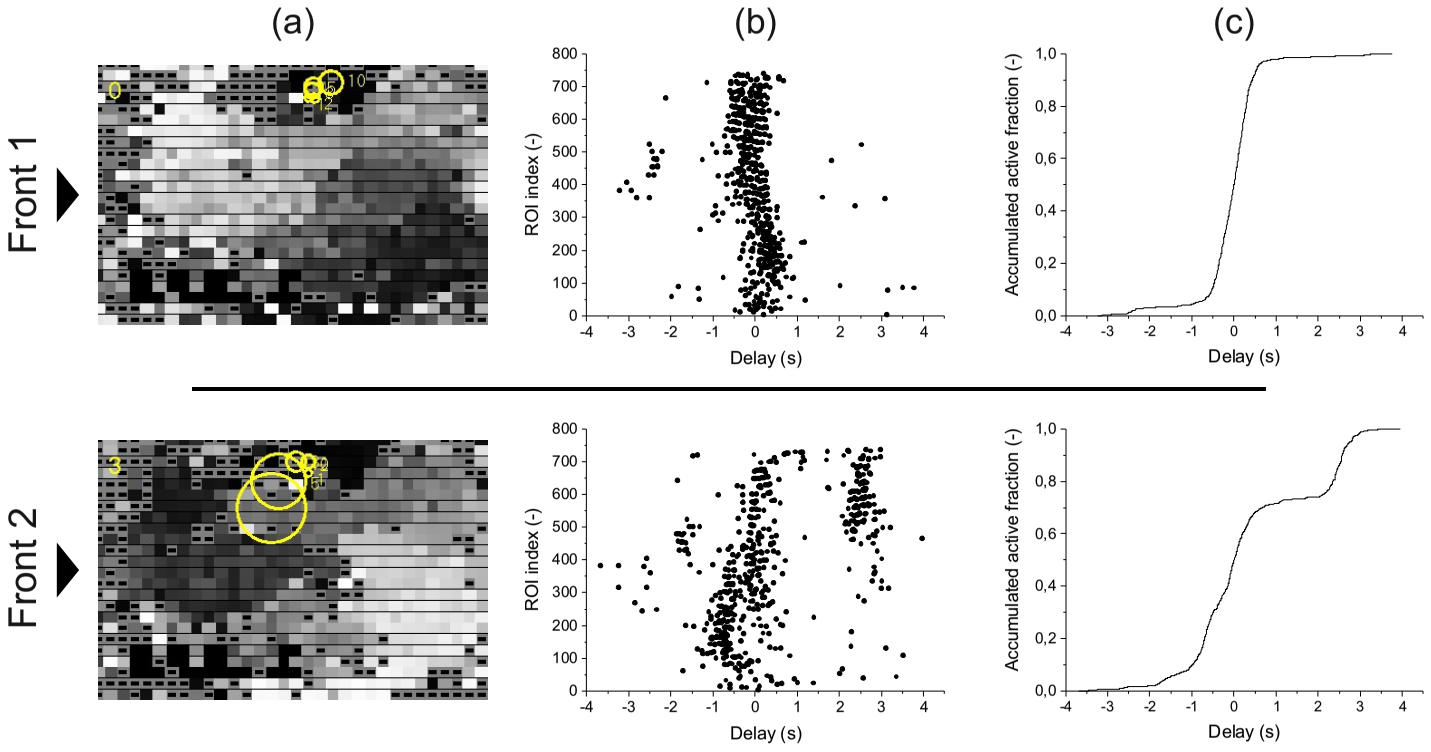

Fig. 6.13 Network burst variability and propagation in random topography experiments. ROIs' activation times color map (a): time increases from black to white color. Yellow circles indicate first firing ROIs. In the first front, a first subset of neurons fire on top of the culture (yellow circles); afterwards, a propagating wave activates the remaining silent ROIs, from bottom–right corner to top–left corner. For the second front, a counterclockwise wave of activation propagates from the top of the culture. **Raster plot of ROIs' activation times (b)**: Front 1 shows a structured burst with sparse delayed activations. Front 2 presents two main sequences of activations in the same burst, with loose structure. **Accumulated activations profile (c)**: In the first propagation, the accumulated number of active ROIs with time present a smooth step–like shape. The second burst resembles a smooth irregular staircase.

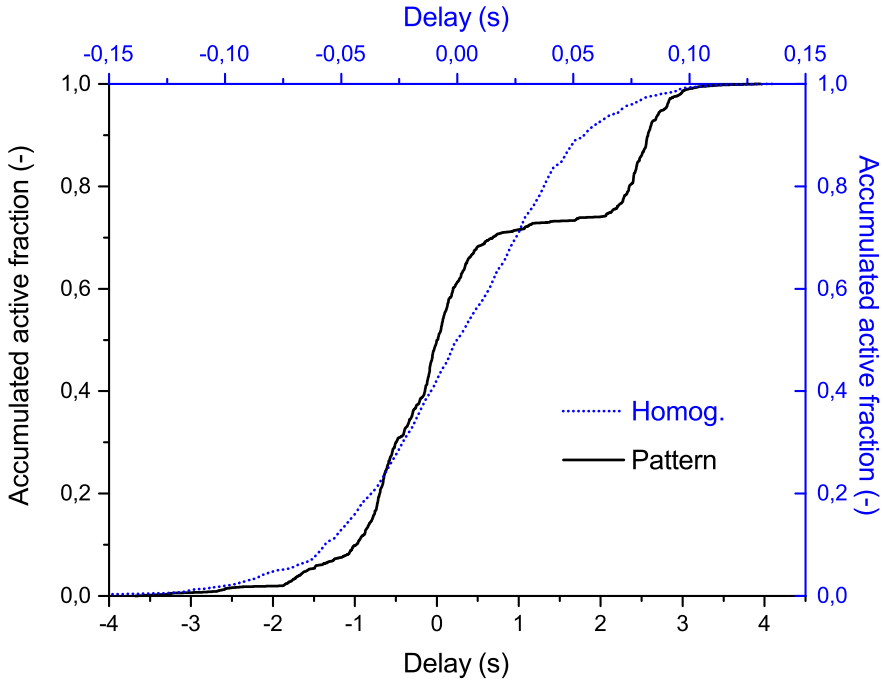

Fig. 6.14 Accumulated activations profile for typical homogeneous and random pattern experiments. Comparisson between the propagation structure for a typical burst in homogeneous cultures (blue dotted line) and for a typical burst in random pattern cultures (black solid line). Two timescales have been used for clarity in the presentation of the results.

6.2.4 Propagation of BIC fronts

Finally, Figure 6.15 shows the propagation wave for a typical burst in a random patterned culture, and with previous application of bicuculline to block inhibition. The behavior is qualitatively similar to that of the previous NOR condition experiments, with similar propagation time durations, fronts and accumulated activation profiles. Specifically for this propagation front, it is interesting to notice that the topographical pattern seems to block activity propagation along the diagonal axis. Indeed, most obstacles fill the diagonal of the culture from the bottom–left corner to the top–right one, and therefore the propagation follows an intricate path in a clock–wise manner.

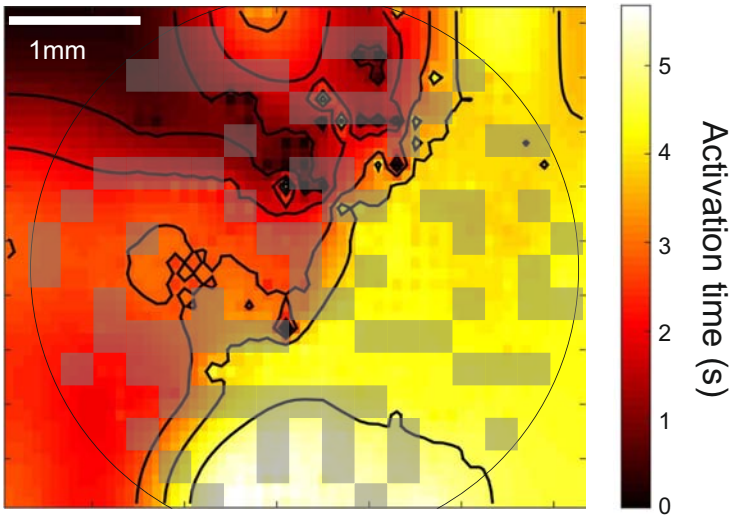

Fig. 6.15 Random pattern propagation wave in BIC condition. Propagation wave for a network burst in a representative patterned experiment under stimulation with drug bicuculline to silent inhibitory neurons. The gray, transparent area indicates the location of the topographical plateaus on the PDMS substrate. The solid line circumference marks culture limits.

6.2.5 Future perspectives

Overall, the above experimental results show that the dynamic activity profile of neuronal cultures can be shaped to some extent by introducing specific metric correlations and constraints. The results call for accurate models and simulations to fully understand the interplay between spatially–inherited features and dynamics. In this direction, we started a collaboration with the Neurophysics group of Dr. S. Bottani, at Paris Diderot University, aimed at reproducing the experimental observations with accurate numerical simulations, including the role of spatial embedding and physical obstacles. Figure 6.16 shows preliminary results for an *in silico* random squares patterned network carried out by one of our collaborators in Bottani's group, the PhD student T. Fardet. We expect that these detailed studies will bring further insight in the relationship between activity and the underlying connectivity structure, and will provide better tools to modulate and dictate neuronal cultures' dynamics.

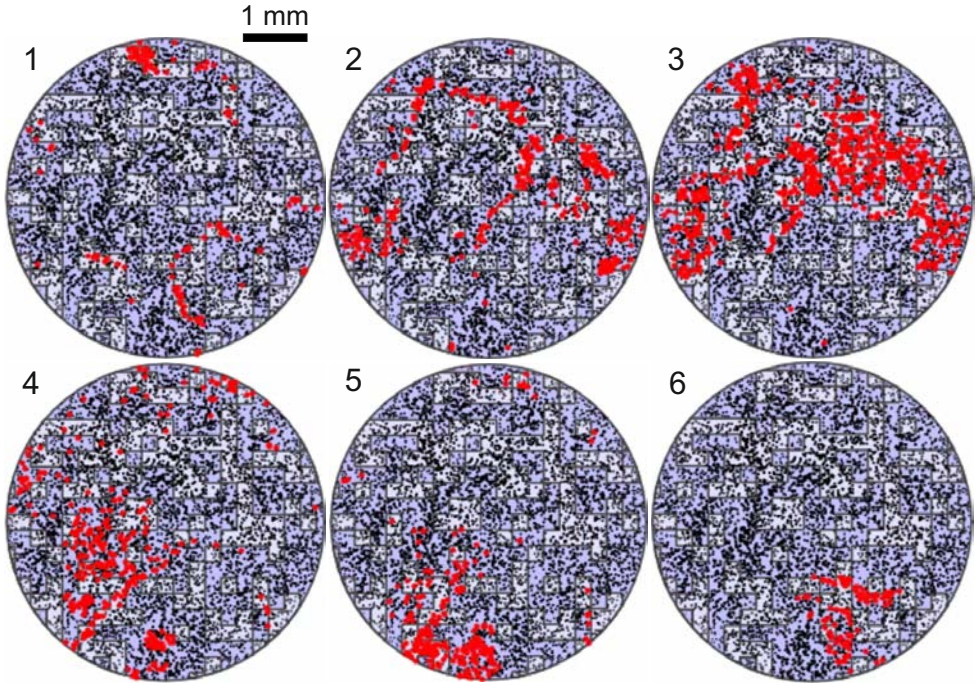

Fig. 6.16 Network bursts propagation in a simulated random squares patterned culture. Activity snapshots of the propagation of simulated activity during a network burst in a random squares patterned culture (from 1 to 6). Red dots indicate active neurons, while silent cells are depicted by black dots. The whole process spans ~ 250 ms, with ~ 40 ms of time separation between snapshots. The underlying simulated topographical mold is shown by solid black lines, with light blue area depicting the upper layer of the mold, and dark blue area displaying the lower one. Simulated data of T. Fardet, reproduced with permission.

Chapter 7

Role of Inhibition and Development in the Dynamics of Neuronal Cultures

In this Chapter we present the results of our inhibition–blocked experiments in cultures, which comprise an initial spontaneous activity measurement without any pharmacological action (NOR condition) followed by another measurement in which the same culture was treated with bicuculline, the antagonist of $GABA_A$ receptors, to completely block their action (BIC condition). An additional goal of these experiments was to complete the results of Orlandi et al. (2013), in which they investigated the initiation mechanisms for spontaneous activity, uncovered the *noise focusing* phenomenon, and described the timing of spontaneous activations as well as the distribution of initiation points, i.e. the area in the culture were spontaneous bursting activity initiated more frequently. The authors concentrated in *small* cultures (about $8-15$ mm^2) and *early mature* cultures, around 10 *days in vitro* (DIV). A question that remained open in their work was an experimental exploration of much larger cultures ($\gtrsim 100$ mm^2) and a broader range of culture ages. The

present Chapter and results aim at filling this gap, as well as at characterizing the role of inhibition in cultures.

In the experiments that we present here we explore changes in culture behavior with and without inhibition in the network, and for a range of culture ages from 6 to 19 DIV. The analysis of the experimental data, and the corresponding setup and protocols are provided in Chapter 2. The neuronal cultures in these experiments were 13 mm in diameter ($\simeq 130$ mm^2 in area), and the entire network was visualized.

The structure of the results is as follows. We firstly present the observed number of network bursts, compare it between the two different experimental conditions, i.e. NOR (E+I) and BIC ('E–only'), and analyze possible trends along culture development. Secondly, we present the obtained average velocity of propagation of activity for each culture, over all bursts, and in each condition; survey the differences between the NOR and BIC conditions; and discuss possible trends and their justification. Finally, experimental initiation points are presented and qualitatively assessed. Experimental results displayed in this chapter were extracted from 19 cultures (out of ~ 40 total measured cultures), which showed sufficiently rich activity and high signal–to–noise ratio to be considered. The total effective number of experiments actually doubles when taking into account both NOR and BIC conditions, adding up to a total of 38 experimental recordings of fluorescent activity.

7.1 Initial hypothesis

In a typical *homogeneous experiment* of whole–culture monitoring of activity, we focused on the characterization of the initiation and propagation of activity fronts. The main goal of the present *inhibition–blocked experiments* was to assess the changes in the activity fronts between the initial NOR condition containing both excitatory–inhibitory connections ('E+I' network), and its

corresponding BIC condition containing excitatory–only connections ('E–only' network).

As stated in Chapter 2, our cortical primary cultures present a reproducible neuronal type distribution of roughly ∼80% excitatory pyramidal neurons and ∼20% inhibitory interneurons. It is important to remark that inhibitory interneurons in culture exhibit an early excitatory action, which switches to their definitive inhibitory role at ∼ 5 DIV. This developmental process is known as 'GABA switch' (Ganguly et al., 2001; Soriano et al., 2008; Tibau et al., 2013b). Provided that we performed experiments at 6–19 DIV, we should have solely observed the interneuron's inhibitory action, although our youngest cultures might have not fully completed the 'GABA switch' process.

As a global trend, when comparing the number of network bursts, a decrease in their total number is expected when switching from NOR to BIC conditions. This decrease has been deeply described in the literature (Orlandi et al., 2013; Tibau et al., 2013b) and is explained in terms of bursts amplitudes and global culture synaptic depression in the context of *short–term plasticity* (STP). Conceptually, an excitation–only culture generates such strong bursts that neurotransmitters reservoirs are strongly depleted, increasing the total recovery time needed for the neurons (and by extension the network) to burst again.

Apropos the propagation velocity of activity, a rough estimate of their order of magnitude could be provided by means of individual neuron structure and propagation time delays. Indeed, let us consider that neurons present dendritic trees with average radius of $\langle r_d \rangle \simeq 150\ \mu$m, axons with average lengths $\langle a \rangle \sim 1$ mm, and an integrate–and–fire time lapse of $\delta t \simeq 2-3$ ms. Then, the propagation velocity can be derived through the ratio between the effective mean connectivity length and the time elapsed for a single propagation. For instance, with an effective connectivity distance of $\sim 200-300\ \mu$m —which takes into account the distribution of connectivity lengths and the random direction of axons— a realistic velocity estimate is about

$\sim$ 100 mm/s, consistent with similar experimental studies (Okujeni et al., 2017). We must note that the velocity may depend on the maturation of the culture. Younger cultures have shorter axons and therefore a shorter effective connectivity distance, which translates into a slower velocity.

Additionally, variations in connectivity should certainly affect the velocity of propagation. Hence, we expect that the average velocity of activity propagation increases when blocking inhibition, since inhibitory interneurons restrain the direct transmission of activity when firing in normal conditions.

As for the initiation points, we suggest that the progressive maturation of the cultures, and therefore the growth in connectivity, provides a richer excitation-inhibition interplay, which should be captured in an increased variability of initiation points.

7.2 Frequency of network bursts

The first statistical analysis that we carried out in the experimental recordings was the frequency of bursts. Since we analyzed independently NOR and BIC data, and with different duration of the recordings, we compared the behavior of the network in both conditions by means of bursting frequencies. Figure 7.1 presents the results. We note that a large variability between neuronal cultures was observed, as usually obtained in our experiments with cortical cultures.

To better compare the NOR and BIC conditions, Fig. 7.2 plots the frequencies of network bursts in NOR conditions as a function of the ones in BIC condition.

Both figures portray a substantial increase in the number of bursts for the NOR condition with respect to BIC ones, ascertained by the larger average height of NOR columns in Figure 7.1 and by the clear overall occupation of the upper–left triangle in Figure 7.2. This experimental observation was consistent with the initial hypothesis discussed in the previous Section.

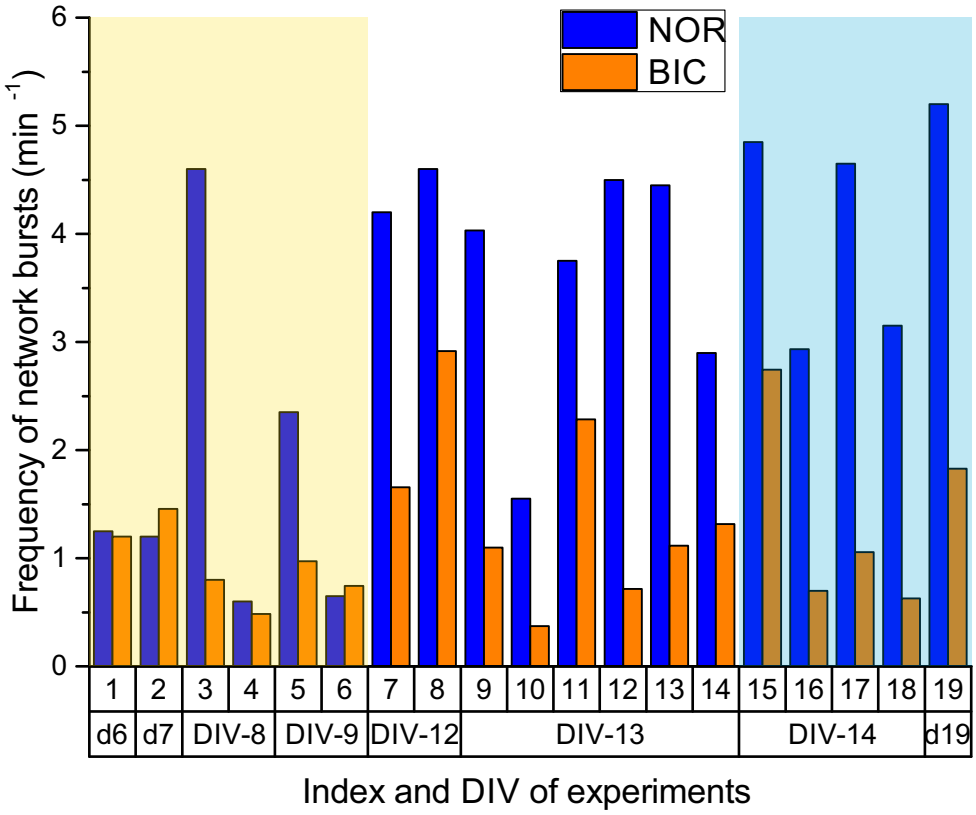

Fig. 7.1 Frequency of network bursts. Frequency of network bursts in NOR (blue) and BIC (orange) conditions for different cultures and *days in vitro*. Light yellow and light blue areas denote young and mature cultures, respectively.

Additionally, we detected a slight but persistent increase in the frequency of network bursts with culture age for the NOR condition. A comparison of column heights between the light yellow and light blue areas of Figure 7.1 revealed this trend, which could be also observed in Figure 7.2 by comparing the projection of those areas onto the bisector line (the farther from the origin in the bisector direction axis, the more bursts observed). A possible explanation for this phenomenon could be related with an increase in connectivity as cultures' axons and dendrites gradually grew; which would lead to a better amplification of activity noise, and therefore an increase in network bursting frequency (see Chapter 5). Furthermore, a lower variability in the number

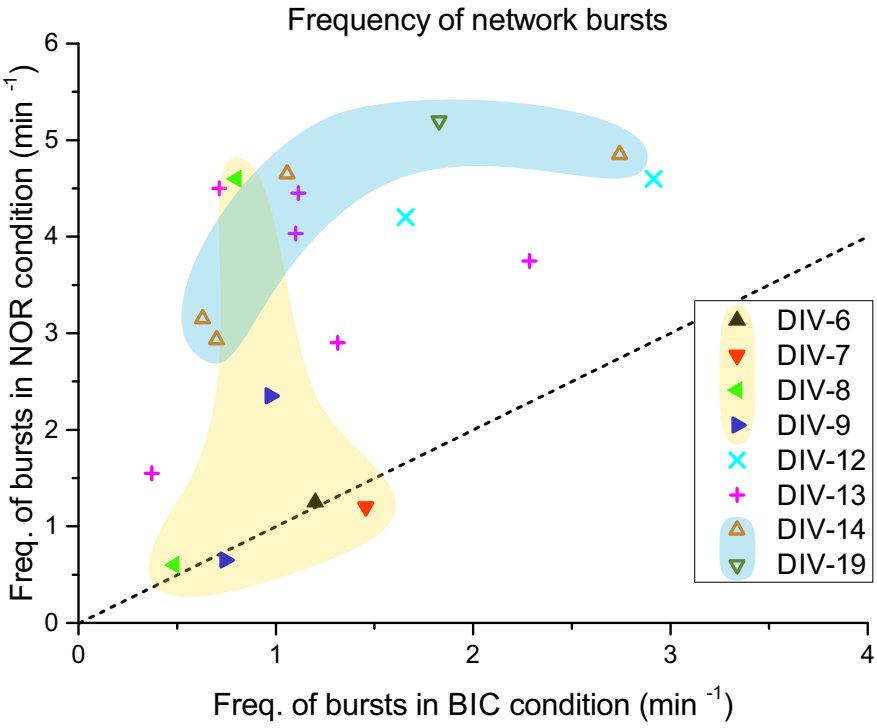

Fig. 7.2 Experimental condition contribution to bursting frequency. Comparison between NOR and BIC frequency of network bursts for each measurable experiment. Bisector indicates equal frequency of bursts between experimental conditions. Light yellow and light blue areas denote young and mature cultures, respectively.

of NOR bursts could be observed for mature cultures, whereas BIC bursts variability increased (light blue area). The latter could be ascribed to a higher complexity in the excitation–inhibition interplay.

Finally, the general trend of a higher number of bursts for the NOR condition was less clear for the majority of the young cultures (light yellow area), specially for cultures at 6 and 7 DIV. This may indicate that the aforementioned *GABA switch* was not completed. In that case, the corresponding GABA action would still be excitatory, and their blockade would have decreased excitation in the network, lowering short–term depression, and allowing higher burst frequency.

7.3 Propagation velocity

Here we compared the average propagation velocity in NOR and BIC conditions, as well as possible variations due to culture age. We would like to point out that, since the extraction of the velocity of propagation was a very difficult and demanding analysis (using the 'cone fit method', see Chapter 2), even moderated fluorescence noise provided spurious average velocity measures not compatible with realistic biophysical activity propagations. Therefore, a velocity threshold of 200 mm/s was set as an upper bound to discriminate between spurious and valid measures. The fact that the noisiest cultures (in terms of fluorescence signal) presented velocities above this threshold value exemplifies the difficulty of analysis and its high error, and calls for more sophisticated methods for determining the velocity of propagating fronts.

Figure 7.3 shows the results for the average velocity of propagation in each condition and for all experiments. And Figure 7.4 presents a comparison of the velocity results between conditions.

We firstly note that these experimental results are totally consistent with the order of magnitude of ~ 100 ms for the velocity of propagation derived in Section 7.1. Secondly, and disregarding noisy data, we note that a slight increase of average velocity with culture age could be observed in both conditions, although this possible trend was not strong. And, thirdly, a general tendency towards the bottom–right corner of Figure 7.4 was observed, either considering all data points or discarding noisy measures. The latter tendency was consistent with the expected behavior of cultures, discussed in Section 7.1 as well.

We remark that the increased velocity with culture age could be ascribed to neurites' growth, which would provide larger mean connectivity lengths and, therefore, an increase in the overall velocity of activity propagation fronts in the cultures.

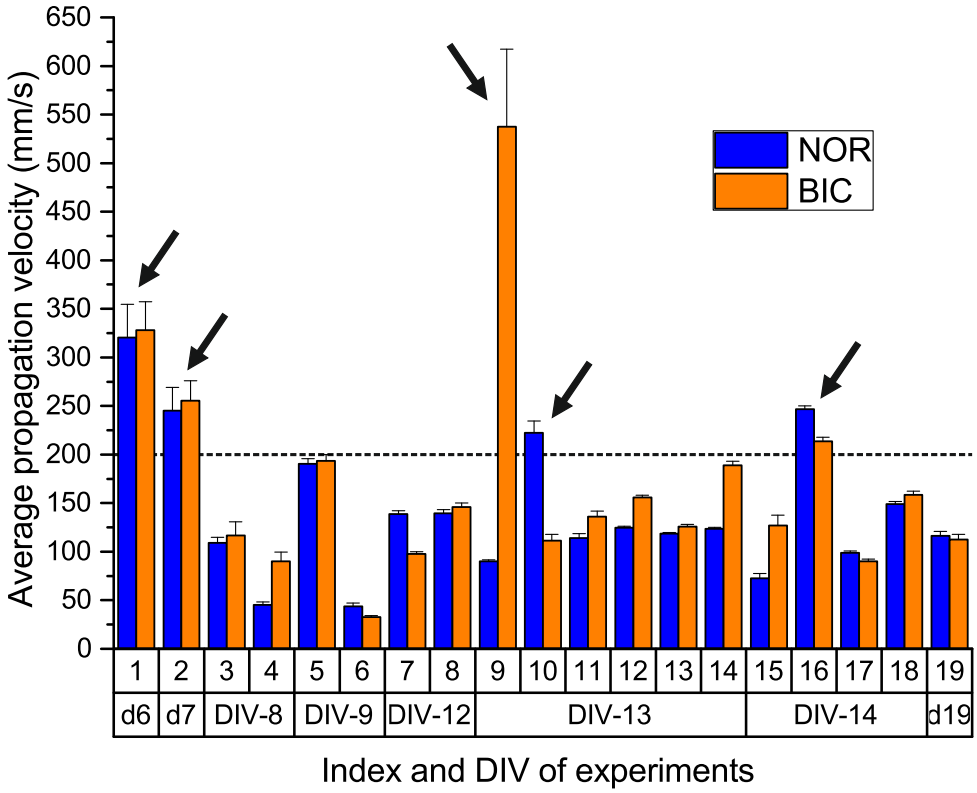

Fig. 7.3 Velocity of propagation. Average velocity of propagation in NOR (blue) and BIC (orange) conditions for all measurable experiments. Error bars are standard error of the inverse–variance weighted mean. The black dashed line denotes the chosen upper bound for biophysically plausible velocities of propagation. Experiments with higher observed average velocities (black arrows) directly correspond to extremely noisy data.

7.4 Initiation points

We would like to highlight that, although the analysis of these experimental results was also performed through the cone fit method, which provided spurious velocities for noisy data in previous Section, here the determination of initiation points was a much more robust analysis, with the 'tip of the cone' providing the spatial location of the first group of neurons that activated.

In these experimental results we compared the distribution of initiation points between the NOR and BIC conditions, and for different culture ages. As

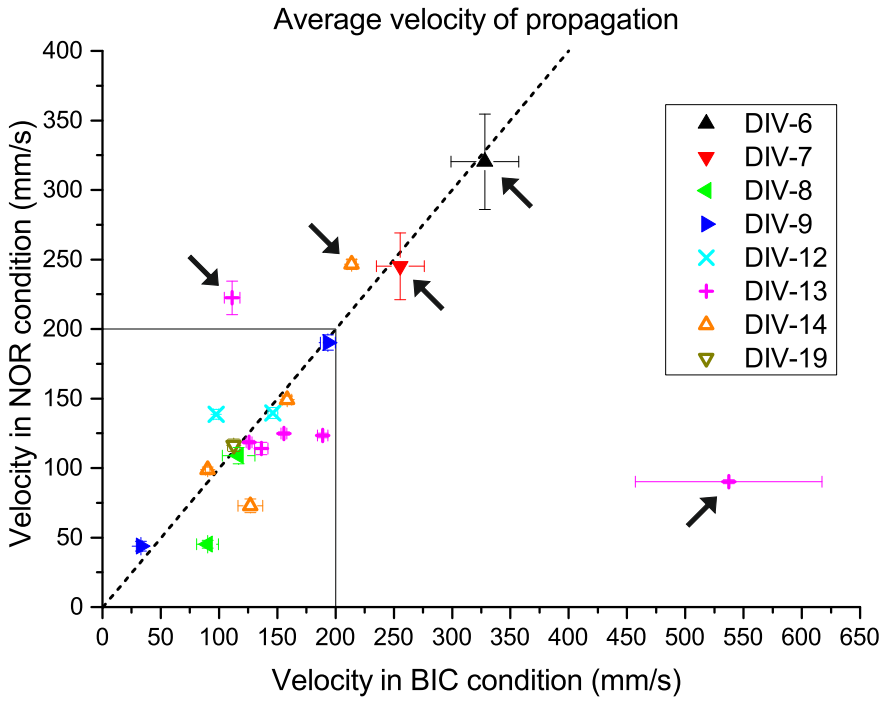

Fig. 7.4 Experimental condition contribution to velocity of propagation. Comparison between NOR and BIC average velocities of propagation for each measurable experiment. All bursts have been taken into account. Bisector indicates equal velocities between experimental conditions. Error bars are standard error of the inverse–variance weighted mean. The encircled rectangular area denotes biophysically plausible propagation velocities. Extremely noisy data is labeled with black arrows.

explained in Section 7.1, we expected a change in the distribution of initiation points between conditions, illustrating the non–trivial role of inhibition in neuronal networks, and evincing the complex excitation–inhibition interplay. Moreover, the maturation of cultures was expected to provide a higher number of initiation points but each covering a smaller area.

Both predictions —a change in the distribution of initiation points upon blockade of inhibition, and more varied and localized initiation upon development— were tested and in general confirmed. Results are shown in Figure 7.5, which presents the estimated probability density function (pdf) of the location of initiation points by means of a Gaussian filter, as explained in Chapter 2.

Single representative experiments are presented for each DIV. The change in the pdf of initiation points is clear in most of the presented data, with 6 DIV culture as main notable exception, which may be due to an incomplete GABA switch at young culture age. Provided the previous assumption, the application of bicuculline would have blocked around $\sim 20\%$ of culture excitatory receptors, reducing the excitation–driven amplification mechanisms of spontaneous activity.

Furthermore, we observed a general change in the heterogeneity of pdf with DIV as predicted, and with its highest value at $13 - 14$ DIV. The apparent loss of spatial richness at 19 DIV may capture a transition in the connectivity for very mature cultures, and one could hypothesize that highly mature networks reinforce the initiation areas of activity, reducing the spatial heterogeneity to few initiation points, in some kind of complex process that may combine specialization, pruning and plasticity.

7.5 Drawbacks and future experiments

A major problem of the presented results is that the neuronal cultures at distinct DIV were *different*. They came from the same culture batch, but due to the Fluo-4 fluorescence loading procedure the monitored cultures could be used only once. This certainly hindered a detailed exploration of the initiation points along cultures' age. To overcome this problem, at the moment of writing this thesis, Soriano's Laboratory implemented the use of genetically encoded calcium indicators (GECIs), which allow the monitoring of the *same* culture along several weeks. The use of GECIs with better signal–to–noise ratio than Fluo-4 will allow for a refinement of the above analysis and much richer statistics.

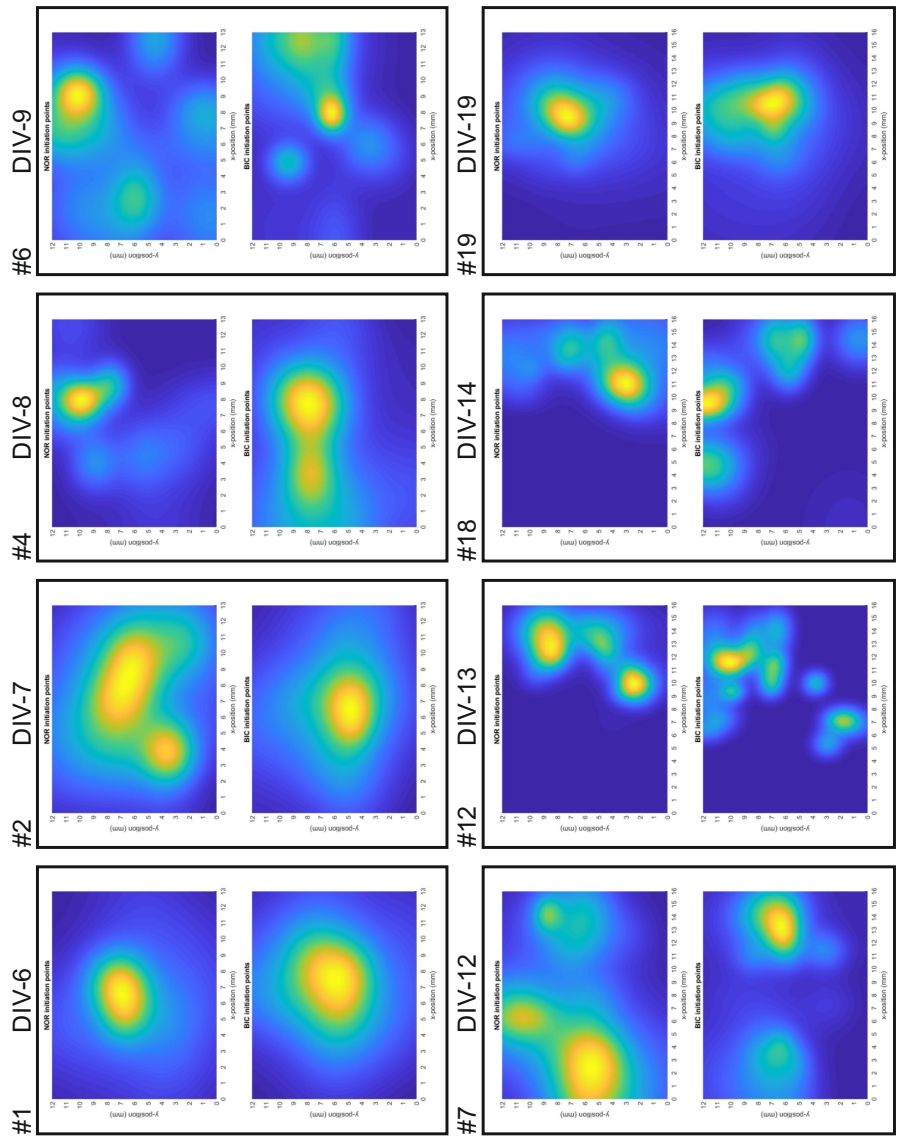

Fig. 7.5 Probability density estimates for the 2D location of initiation points in NOR and BIC conditions. Color maps of the initiation points pdf estimates, with probability color scale ranging from blue (low) to yellow (high). Each enclosed pair of plots corresponded to a single experiment, with index equal to their upper–left label and age equal to their upper DIV tag. **Upper plots in pairs**: initiation points pdf estimates for NOR condition experiments. **Lower plots in pairs**: initiation points pdf estimates for BIC experiments.

Chapter 8

Electrical Stimulation of Neuronal Cultures

In this Chapter we present the results of our electrical stimulation experiments. The motivation for these experiments was to attempt a quantification of the changes in network behavior upon stimulation, in particular the ability of the network to fire at a rate higher than in the spontaneous case, and variations in the velocity of propagation and initiation points between spontaneous and induced fronts.

The experimental exploration included the determination of the appropriate range for the applied potential, the recording of activity in control, 'E+I' cultures (NOR condition), and the recording of activity for the same cultures under electrical stimulation (STM condition). Cultures of different ages were tested, ranging from 7 to 16 DIV. The analysis of the corresponding experimental data and the respective setup and protocols are provided in Chapter 2.

In the experiments presented here we used small cultures 3 mm in diameter, which provided several advantages with respect to larger ones. First, since a single 13 mm coverslip can accommodate up to four independent small cultures, we were able to select the healthiest one out of them for each

recording. We note that the external stimulation increases cells' stress and therefore these experiments required cultures with optimum conditions. Second, we wanted to study the effect of a homogeneous electrical stimulation on neuronal cultures, and this was not possible with cultures much larger that the separation between the macro–electrodes ($\sim$ 5 mm). And third, the cultures that were not directly stimulated served as a valuable control sample to verify that neither the electrodes nor the stimulation caused alterations in the recording solution were neurons are bathed during the monitoring of activity. Figure 8.1 illustrates the typical configurations of the cultures during recording.

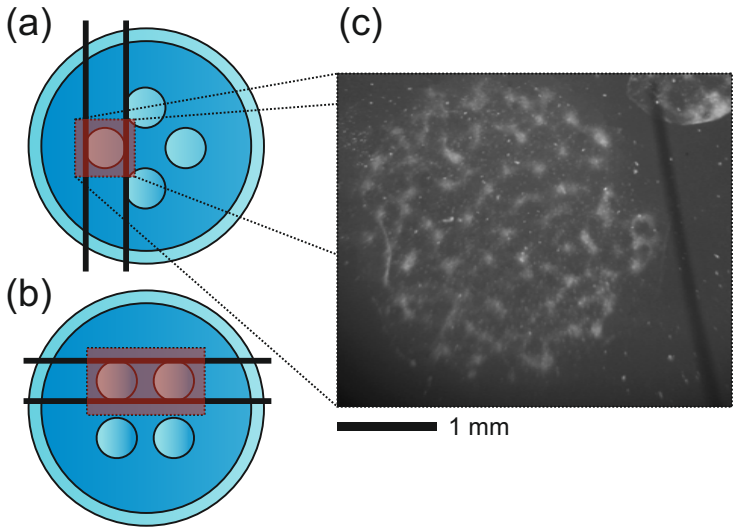

Fig. 8.1 Experimental configuration. **(a)** First recording configuration. 13 mm glass coverslip (light blue) with PDMS mold attached (dark blue) for the preparation of several 3 mm mini–cultures. Solid parallel black lines depict the position of the macroelectrodes. Camera field of view (red area) is limited to the single, healthiest culture. **(b)** Second configuration. Camera field of view is enlarged to cover two stimulated cultures at the same time. **(c)** Fluorescent image of the culture in the first experimental configuration. The thick black line on the right is one of the electrodes.

The presentation of results is as follows. Firstly, we present the framework of preliminary experiments, where the explored electric potentials and

corresponding cultures' responses are discussed. These experiments provided a specific potential to be used in further activity measures. Secondly, the results for a total of 9 cultures are presented. We note that a total of ~ 30 experiments were carried out. However, and due to important difficulties, such as high cellular death and poor signal–to–noise ratios, several experiments were discarded since firing events could not be well resolved, the activity was too poor for reliable statistics, or cultures became quickly damaged. We therefore solely considered those experiments in which the recorded activity was sufficiently rich and cultures were healthy by the end of both (NOR and STM) experiments, which left a total of 18 recordings for 9 cultures.

Similarly as in previous Chapters, the experimental results are divided into three groups, namely number of network bursts, velocity of propagation of activity fronts, and distribution of the initiation points. The comparison between the spontaneous activity traits (NOR) and the stimulated activity features (STM) are presented and discussed for each case, and possible explanations are considered.

8.1 Introduction

Since the basis of neuronal activations are the changes in cells' membrane potential, a wide number of studies have focused on the effect of an electrical or magnetic stimulation to the activation of neuronal networks.

Some studies aimed at mapping brain functions and extract information of neural connectivity *in vivo* through direct electrical stimulation, as reviewed in Borchers et al. (2012) and references therein. Other works used similar methods to: (i) investigate changes in connectivity in neuronal diseases, for example in epilepsy (Matsumoto et al., 2017); (ii) target the visual circuitry to elicit visual sensations in the human retina of blind subjects (Humayun et al., 1999), or even explore the development of prostheses for the visual

cortex (Lewis and Rosenfeld, 2016); and (iii) assess the glial contribution to electrical stimulation responses (Gellner et al., 2016; Monai et al., 2016).

Regarding *in vitro* studies, several works tested electrical stimulations on slices (Bikson et al., 2004). Additionally, and provided their high manipulability, a great effort has been invested in the stimulation of neuronal cultures, since they present an optimal framework. Specifically, a large number of studies used neuronal cultures to report the effects of electrical stimulations on nerve regeneration (Adel et al., 2017; Lichtenstein et al., 2017), guidance of neurites' growth (Hronik-Tupaj et al., 2013), and plasticity (Chao et al., 2007). Additionally, neuronal cultures helped in the study of glial contribution to culture response upon stimulation (Sommakia et al., 2014).

Problems arising from the use of electrodes in electric stimulation of tissues and cultures were already known decades ago (Brummer et al., 1983). Though, in the case of platinum macro–electrodes, such as in our experiments, recent studies deepened in those considerations (Aryan et al., 2015; Leung et al., 2015).

As for the aim of this Chapter, different studies present varied results concerning the enhancement or depletion of burst activity upon electrical stimulation. Hamilton and coworkers (Hamilton et al., 2014) observed a decrease in bursting activity of cortical cultures under a sinusoidal stimulation of 1 Hz and semi–amplitude 500 mV, roughly similar to the stimulation studied in our experiments. Conversely, Bologna et al. (2010) reported an increase in bursts during development and also as a direct response, where the applied potential was a biphasic pulse of 400 μs, 1.5 V peak–to–peak, and with a frequency of 0.2 Hz. Therefore, the effect of an electric stimulation of sinusoidal shape, with 2 V of semi–amplitude, and frequency 0.1 Hz was difficult to predict beforehand.

8.2 Preliminary results

Several possible electrical stimulation protocols could be initially tested to study their impact on cortical neuronal cultures, and also to chose the optimal voltage potential for long series of experiments. In our framework, electrical potentials could be differentiated between *sub–threshold* and *super–threshold* stimulations, where threshold here defines the voltage value at which a direct activation of the culture occurs by means of a triggered burst. Regarding our results and setup, super–threshold responses were obtained for potentials stronger than 5 V (electric field of 10^3 V/m), lasting at least 50 μs, in the case of cultures older than a week.

Super–threshold potentials provided interesting data for the study of synaptic depression and global culture recovery time. Nevertheless, they were intrinsically aggressive, and entailed a fast degradation of the cultures that did not allow long recordings. The minimal average *recovery time* for a whole culture to be excitable again was $\tau_{rec} \simeq 8$ s, and therefore neuronal networks could not follow pulsated super–threshold stimulations of frequency $\nu \gtrsim 0.12$ Hz.

On the other hand, sub–threshold potentials could be viewed as 'enhancers of noise', and therefore they provided a valuable tool for assessing the behavior of cultures with a noise level higher than the intrisic one. This *additional noise* was modulated through the electrical stimulation amplitude, which enhanced activity amplification mechanisms. In this context, moderate electrical stimulation still damaged neuronal cultures, and recordings could not be performed reliably for more than ~ 45 min. For example, a sinusoidal stimulation of semi–amplitude larger than 3 V killed $\sim 90\%$ of the cells before those 45 min elapsed. A continuous, DC potential higher than 500 mV severely damages the cultures as well. We note that DC stimulations dramatically harmed neuronal cultures since they generated unbalanced ionic concentrations across the recording medium, whereas alternating ones roughly compensated ionic fluxes over time.

Thus, from preliminary tests and observations, we extracted an adequate range for the frequency of sub–threshold stimulation. This range varied between the average *spontaneous* bursting frequency of $\nu_{spo} \sim 0.05$ Hz and the inverse of the *recovery* time introduced before, that procured $\nu_{rec} \simeq 0.12$ Hz. This range for the frequency of stimulation defined a first parameter for our optimal stimulation protocol.

The rest of parameters comprised the stimulation pattern and amplitude. After several tests, the optimal electric stimulation pattern was chosen as a sinusoidal wave of semi–amplitude 2 V and frequency $\nu = 0.1$ Hz. Altogether, we decided upon an alternating current, non–lethal along 30 min, and with a frequency sufficiently low to be approximately followed by the culture, yet larger than the spontaneous frequency.

8.3 Initial hypothesis

The former potential was chosen to promote uncorrelated spontaneous individual firings as a contribution to intrinsic neuronal noise. An increase in neuronal activations should boost the amplification of activity noise and the subsequent generation of avalanches in the form of network bursts. Therefore, a first hypothesis is that the electrical stimulation should increase bursting frequency.

This hypothesis, however, may be reject taking into account the following arguments. First, that the stimulation might induce strong bursts with high fluorescence amplitude, yielding a larger recovery time due to the depletion of neurotransmitters (i.e. short–term depression). And second, that the stress induced to the neurons upon stimulation could alter their normal functioning, possibly deteriorating their ability to integrate inputs and propagate information, resulting in a decrease in bursting frequency.

Thus, *a priori*, we do not have sufficient biophysical information to predict the effect of the electrical stimulation on average network activity.

Regarding propagation velocities, the electrical stimulation could hinder or delay the transmission of activity between neurons as a result of the aforementioned short–term depression. Then, a decrease in the velocity of the propagating activity front could be expected.

Finally, regarding initiation points, we note that, in a first approximation, interneurons and pyramidal neurons were depolarized equally by the electric potential, disregarding their inhibitory or excitatory action. Additionally, the suggested increase in the depletion of neurotransmitters would occur homogeneously thorough the entire culture. Thus, an electric stimulation applied via macro–electrodes could modulate the probability of bursting at different initiation points, but should not dramatically change their distribution.

8.4 Total number of network bursts

Our first set of results are the total number of bursts, which are directly computed from the average fluorescence trace of each culture (see Chapter 2). NOR and STM conditions were analyzed independently, with equal recording duration, and a proper comparison of the total number of bursts could be performed. Figure 8.2 presents the results in terms of the total number of observed network bursts in 30 min for both experimental conditions.

Some variability among cultures was observed, as typcially occurs in our cortical cultures, particularly for young ones at $7-9$ DIV. Since the number of bursts showed no average dependency on DIV, we could not draw any strong conclusion on the effect of an electrical stimulation along maturation.

Figure 8.3 shows the direct comparison between the number of bursts at NOR and STM conditions. Either by neglecting the experiments with excessive cellular death or by taking them into account, we could not picture an evident average trend towards a higher number of bursts during stimulation. As proposed in the previous Section 8.3, this might be ascribed to the compensation between, on the one hand, a bursting enhancement under

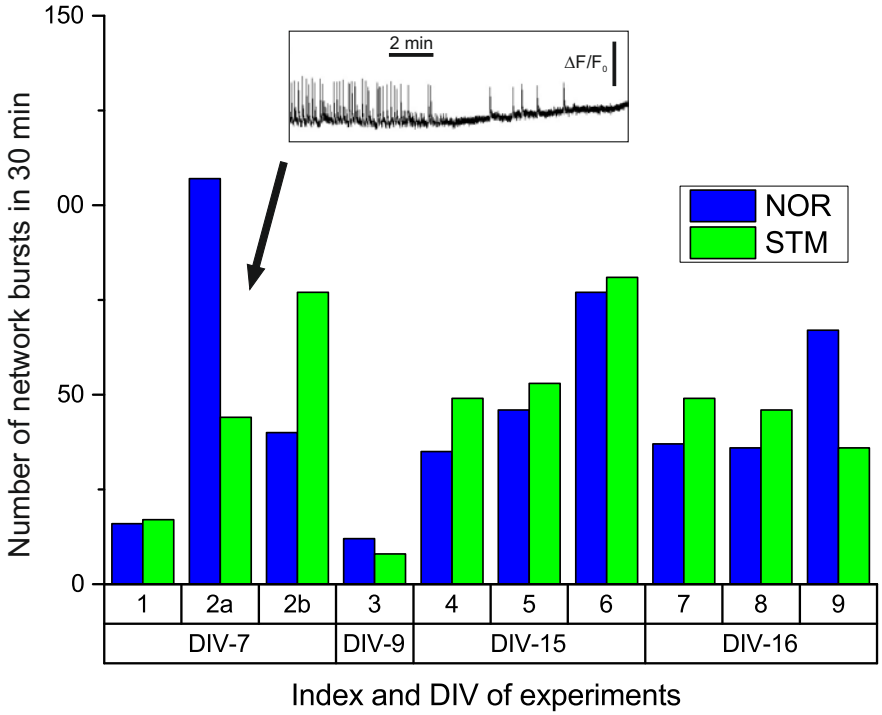

Fig. 8.2 Number of network bursts in 30 min. Number of network bursts in NOR (blue) and STM (green) conditions for different cultures and *days in vitro*. Results of experiment 2 involved two independent cultures, "a" and "b", recorded at the same time. **Upper inset**: fluorescence activity trace of 2a–STM with excessive cellular death at the end of the recording.

electrical stimulation and, on the other hand, a larger synaptic depression and higher cell death.

We would like to note that, although no clear trend could be extracted, a major subset of the experiments presented low variability among them, and showed a weak increase of bursts under electrical stimulation.

8.5 Propagation velocity

The second feature studied in our experiments was the propagation velocity of the activity fronts (bursts), and the comparison between NOR and STM conditions. As previously discussed in Chapter 7, velocities larger than

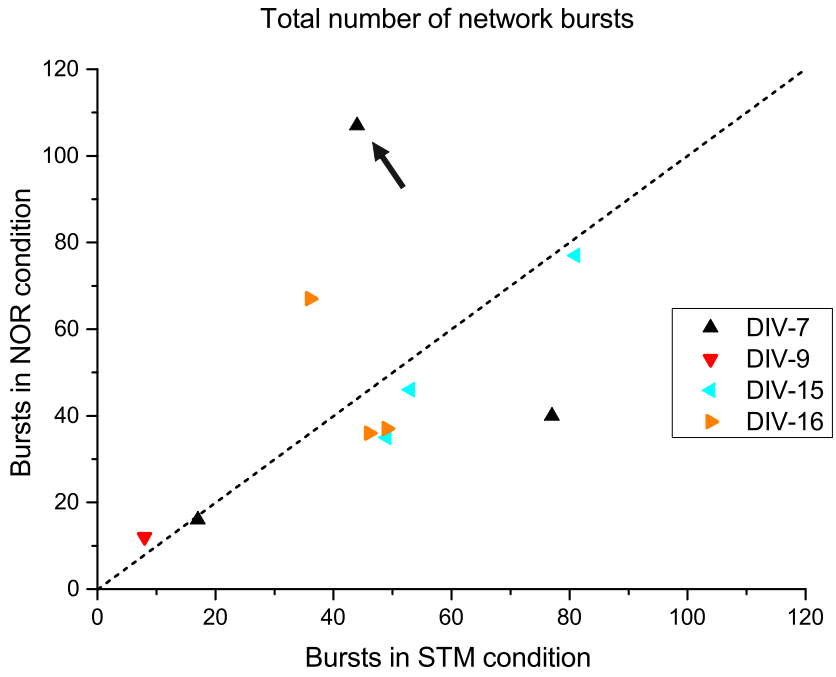

Fig. 8.3 Experimental condition contribution to number of network bursts. Comparison between NOR and STM number of network bursts for each measurable experiment. Bisector indicates equal number of bursts between experimental conditions. Experiment 2a, with excessive cell death, is pinpointed by a black arrow.

200 mm/s were considered spurious due to high signal–to–noise ratios in the fluorescence data. Indeed, the youngest cultures presented the noisiest profile for individual neuronal activation times, and therefore their results are particularly sensitive to error.

Figure 8.4 shows the results for the average velocity of propagation in each condition and for all experiments, and Fig. 8.5 presents a comparison of the obtained velocities by plotting NOR velocities as a function of the STM ones.

We note that the obtained velocities were totally consistent with the coarse prediction of ~ 100 mm/s derived in Chapter 7. Additionally, and disregarding the spurious data obtained for experiment number 1, young cultures at 7 DIV presented lower velocities than maturer ones, evincing the growth of neurites

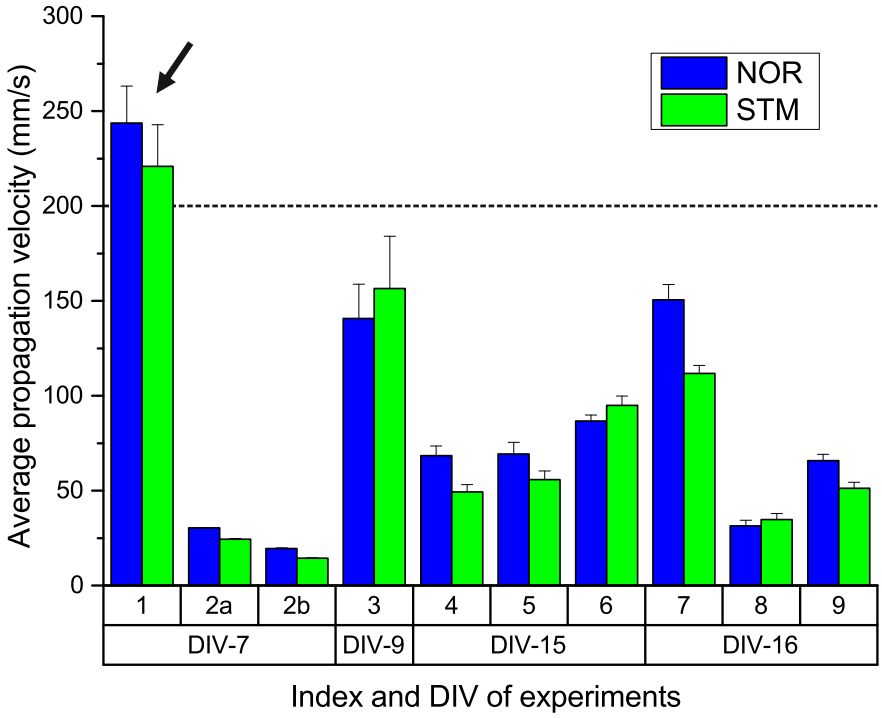

Fig. 8.4 Velocity of propagation. Average velocity of propagation in NOR (blue) and STM (green) conditions for all measurable experiments. Error bars are standard error of the inverse–variance weighted mean. The black dashed line denotes the chosen upper bound for biophysically plausible velocities of propagation. Experiments with higher observed average velocities (black arrows) directly correspond to extremely noisy data.

and the subsequent increase in connectivity that could boost propagation velocities for older cultures, as observed in previous experimental results of this thesis.

By observing Fig. 8.5, and taking into account the uncertainty of each measure, no data points are located below the bisector line. On the contrary, the plot suggests that for some particular experiments at DIV $15-16$, the velocity in NOR conditions is slightly higher than in the STM ones. We therefore conclude that the velocity of propagation is slightly slowed down upon stimulation, as already suggested in Section 8.3. This feature is ascribed to the strengthening of synaptic depression under additional depolarization of

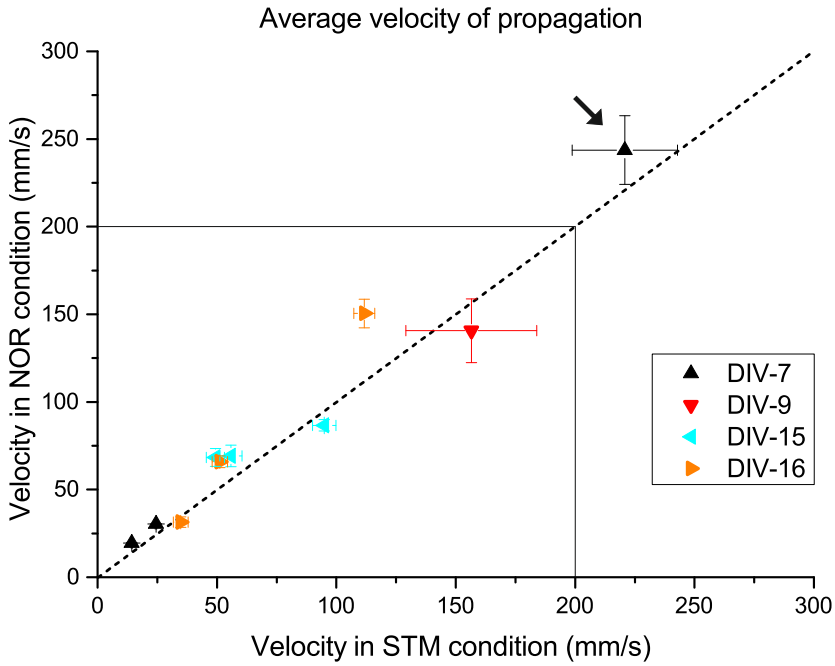

Fig. 8.5 Experimental condition contribution to velocity of propagation. Comparison between NOR and STM average velocities of propagation for each measurable experiment. All bursts have been taken into account. Bisector indicates equal velocities between experimental conditions. Error bars are standard error of the inverse–variance weighted mean. The encircled rectangular area denotes biophysically plausible propagation velocities. Extremely noisy data is labeled with black arrows.

neurons due to the external electric potential. However, the observed changes were small, and indicate that the strengthened short–term depression could play a secondary role. Clearly, an accurate biophysical model and a larger set of experiments is required to understand this data.

8.6 Initiation points

We finally investigated the distribution of initiation points for NOR and STM conditions, for all experiments and different culture ages. As explained in Section 8.3, we expected no fundamental changes in the probability density

functions (pdfs) between the unperturbed and the stimulated cases, since an enhancement of activity should neither destabilize the original inhibition–excitation balance present in cultures nor strongly increase synaptic depression in a heterogeneous way thorough the culture.

As shown in Fig. 8.6, the spatial distribution of initiation points is essentially the same between NOR and STM conditions, and indicates that the above hypothesis does hold. The corresponding data for experiment number 2, composed of two isolated cultures recorded at the same time, is shown in Fig. 8.7. For this figure, the change in the probability density estimates evinces an excessive cellular death for culture "a" in the STM condition, while culture "b" increased its total number of bursts, as discussed in Section 8.4 and shown in Figure 8.2. However, no fundamental changes could be observed in the individual, renormalized pdf estimates of both cultures, which was consistent with the other experiments.

On the other hand, we note that the heterogeneity in pdf estimates expected for mature neural networks could not be resolved due to the small size of cultures in these electrical stimulation experiments, of $\phi = 3$ *mm*, as opposed to the $\phi = 13$ *mm* cultures studied in Chapters 6 and 7.

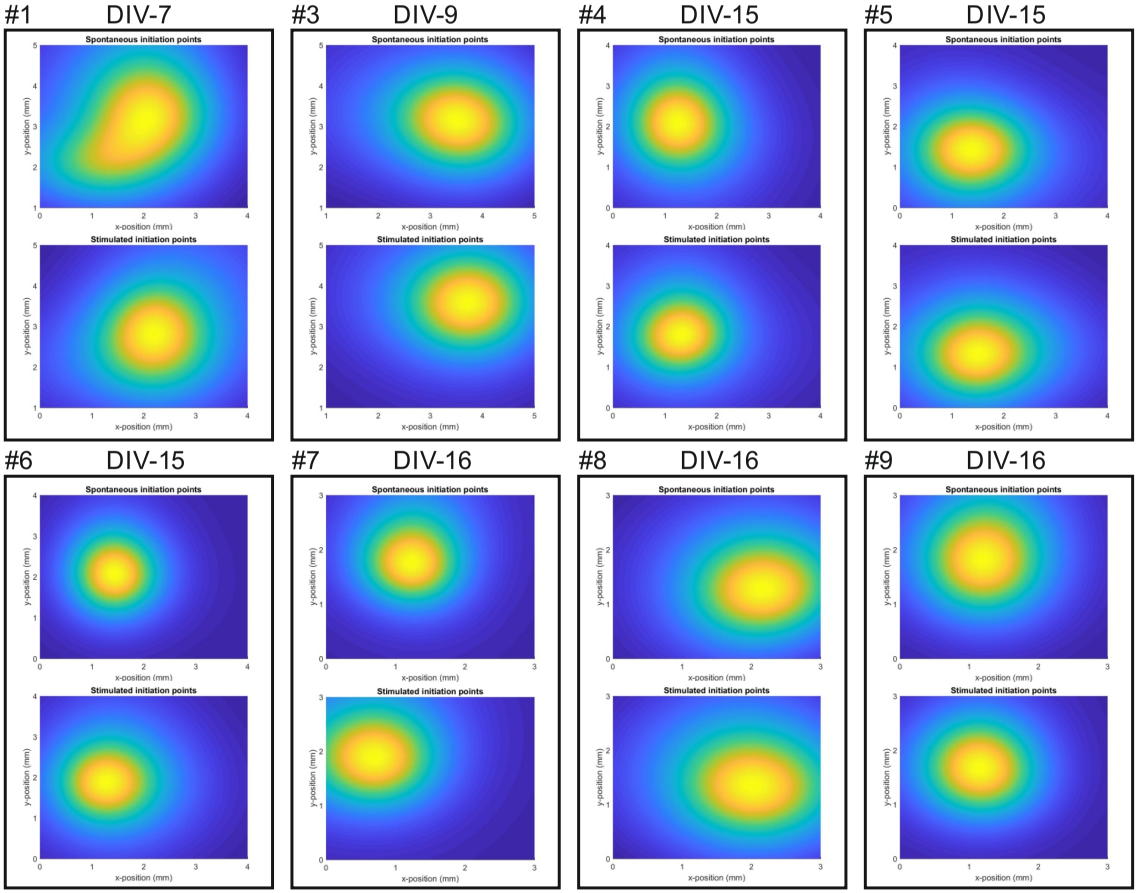

Fig. 8.6 Probability density estimates for the 2D location of initiation points in NOR and STM conditions. Color maps of the initiation points pdf estimates, with probability color scale ranging from blue (low) to yellow (high). Each enclosed pair of plots corresponded to a single experiment, with index equal to their upper–left label and age equal to their upper DIV tag. **Upper plots in pairs**: initiation points pdf estimates for NOR condition experiments. **Lower plots in pairs**: initiation points pdf estimates for STM experiments.

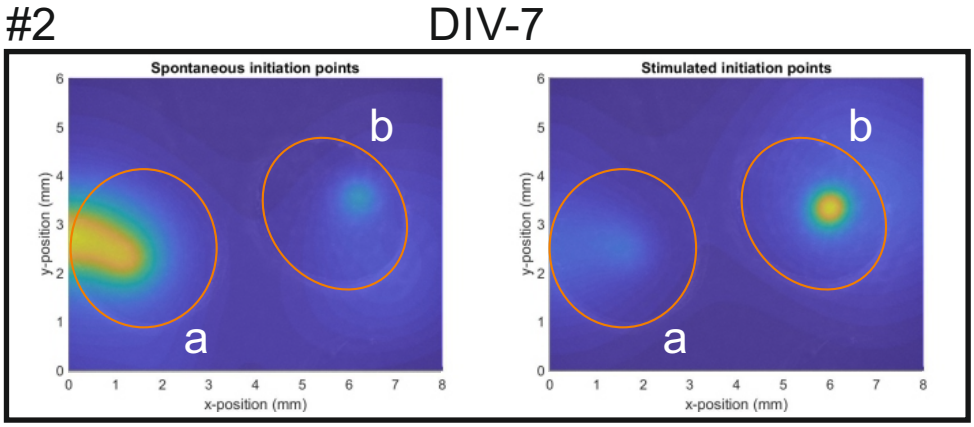

Fig. 8.7 Probability density estimate for the 2D location of initiation points for experiment number 2. Color maps of the initiation points pdf estimates, with probability color scale ranging from blue (low) to yellow (high). Culture age is indicated in the upper DIV label. The boundaries of both cultures are depicted by solid orange lines. **Left plot**: initiation points pdf estimate for NOR condition experiments. **Right plot**: initiation points pdf estimate for STM experiments.

Chapter 9

Conclusions

Here we formulate the general conclusions of this thesis. We summarize the conclusions of each chapter, and in the same order as they have been presented.

Ising model for neuronal networks and metric correlations

- An adapted Neuronal Network Ising Model (NNIM), grounded on percolation experiments, proved sufficient to capture the basis of the response of neuronal cultures upon instantaneous electrical stimulation. An analytical mean–field approach agreed well with the experimental results in the context of homogeneous cultures, and correctly predicted the universal collapse of the giant component disintegration when the demand of inputs m was normalized by its critical value m_D, i.e. $g(m/m_D)$.
- It was possible to extract an estimation of the average connectivity of each culture through a fit of the mean–field solution to the experimental data
- Complete simulations of the NNIM in biologically–inspired metric networks unveiled the dominance of metric correlations in neuronal

cultures, which overshadow the distribution of connections and dictate dynamic attributes of these networks. Metric simulations accounted for the deviation between the above analytical mean–field solution of the model and experimental results, a deviation that arises from the loss of a uniform neighborhood under spatial correlations.

- Two major ingredients modulate the importance of metric correlations, namely $\Lambda \in [0,1]$ the degree of spatial aggregation of neurons' somas in the culture, and $\delta > 0$ the relative mean axonal length with respect to the total system size. Homogeneous cultures ($\Lambda \to 0$) switch from local to mean–field connectivity as δ grows. Aggregated cultures ($\Lambda \to 1$) always present network–specific features.

- The experimental–theoretical approach is a non–invasive protocol that could be potentially extended to brain slices and other living neuronal networks.

Analytical approach for the initiation of spontaneous activity:

- An analytical, non–equilibrium statistical approach semi–quantitatively captured the dynamical activity noise amplification mechanism governing the emergence of spontaneous network bursts in homogeneous neuronal networks.

- The approach was grounded on microscopic variables, such as the mean single–neuron demand of inputs and their average local connectivity, and did not contain any *ad hoc* parameters. These variables could be quantified using biophysically plausible values.

- The approach provided realistic frequencies of spontaneous network bursts, and established the typical range of activity frequency, totally consistent with experimental observations.

- The extension of these results to aggregated cultures is straightforward, and single–aggregate spontaneous activations might be easily modeled to extract their internal characteristics.

Connectivity and dynamics in patterned neuronal cultures:

- PDMS molds placed on cultures' substrate were able to constrain and dictate neuronal network connectivity, and consequently shaped the emergent dynamics of these neuronal populations.

- A PDMS step of height $h \sim 100$ μm attached to glass effectively dictated an asymmetric top–to–bottom connectivity that resulted in a master–slave dynamics between the top layer (PDMS) and the bottom one (GLASS). Large step heights ($h \gtrsim 800$ μm) disconnected them, and small steps ($h \lesssim 100$ μm) allowed a symmetric connectivity that resulted in homogeneous dynamics across the two layers.

- More complex experimental designs were obtained by using soft–lithographic techniques on PDMS, providing a two–height topographical pattern characterized by a set of random squared obstacles 100 μm high and 250 μm of lateral size. The obstacles dictated strong heterogeneity in the connectivity that translated into rich dynamic activity patterns.

- The preliminary exploration of patterned cultures evinced the sensitivity of macroscopic activity patterns to microscopic connectivity traits, and illustrated the complexity in the activity–connectivity interplay.

Role of inhibition and development in the dynamics of neuronal cultures:

- The blockade of inhibitory receptors through bicuculine allowed a comparison of network dynamics between the excitatory and inhibitory condition ('E+I' networks) and the solely excitatory one ('E–only' networks). Big cultures were used, of 13 mm in diameter.

- The spontaneous network bursting frequency decreased in ‘E–only’ networks since short–term synaptic depression increased due to stronger bursts and further depletion of neurotransmitters. The velocity of propagation of activity fronts in network bursts, on the order of 100 mm/s, was slightly enhanced in the ‘E–only’ conditions since the blockade of inhibition effectively increased neuron–to–neuron communication.

- Activity initiation areas exhibited remarkable changes in their spatial distribution and strength between ‘E+I’ and ‘E–only’ networks, reflecting the pivotal role of the connectivity blueprint in shaping burst initiation areas.

- Young cultures (below 10 DIV) presented a lower bursting frequency than maturer ones (for both, ‘E+I’ and ‘E–only’ conditions), indicating that activity increases in accord with the number and length of connections along maturation. In both conditions, early mature cultures ($12 - 14$ DIV) showed faster activity propagation velocities and a more spatially distributed initiation areas than young cultures. And very mature cultures (over 14 DIV) seemed to reinforce fewer initiation points in a complex process probably involving specialization, pruning and plasticity.

Electrical stimulation of neuronal cultures:

- External electrical stimulation via bath electrodes was able to either force network bursting (supra–threshold stimulation) or increase activity noise in neuronal networks (sub–threshold), i.e. enhanced individual uncorrelated activations.

- Sub–threshold electrical stimulation altered the spontaneous, intrinsic neuronal activity patterns without compromising the health of the neuronal culture.

- An alternate current of low frequency and moderate amplitude increased bursting frequency and slightly reduced the velocity of propagation of activity fronts, probably due to the combination of increased neurotransmitters' depletion and enhanced bursting frequency.
- The spatial distribution of activity initiation points seemed to be unaffected by the external stimulation, although only small cultures 3 mm in diameter were explored.

9.1 List of publications

– [Hernández-Navarro et al. (2017)] L. Hernández–Navarro, J. G. Orlandi, B. Cerruti, E. Vives, and J. Soriano. Dominance of metric correlations in two–dimensional neuronal cultures described through a random field Ising model. *Physical review letters*, 118 (20):208101, 2017.

– L. Hernández–Navarro, A. Arché, and J. Soriano. Effect of an electrical stimulation in the activity of neuronal cultures, (in preparation).

– L. Hernández–Navarro and J. Soriano. Dictated connectivity modulates the dynamics of spontaneous activity fronts in neuronal cultures, (in preparation).

– L. Hernández–Navarro, J. G. Orlandi, J. Casademunt and J. Soriano. Theoretical approach to predict bursting frequency in neuronal cultures, (in preparation).

Chapter 10

Resum en Català

L'objectiu d'aquesta tesis és investigar els mecanismes que generen l'activitat espontània i estimulada en xarxes neuronals. Aquest treball es centra en el sistema neuronal tancat més senzill que pot mostrar activitat col·lectiva: els cultius neuronals. En aquest marc, l'activitat col·lectiva consisteix en episodis esporàdics de dispars quasi sincronitzats entre totes les neurones del cultiu, anomenats "esclats de xarxa".

Gràcies a la seva fàcil manipulació i accessibilitat, els cultius neuronals permeten un estudi profund dels factors que modulen l'activitat de xarxes neuronals vives, i que són la base del funcionament del cervell. Aquests factors inclouen tres elements principals: connectivitat entre neurones, dinàmica intrínseca neuronal, i soroll (activacions neuronals aleatòries). En sistemes neuronals més complexes que els cultius, com per exemple el cervell dels mamífers, la relació entre aquests factors és molt més difícil d'analitzar degut al gran nombre de cèl·lules i connexions. A més a més, els cultius neuronals presenten l'avantatge d'una variabilitat cel·lular molt específica que simplifica la seva modelització en el marc de la Biofísica.

Els experiments i la preparació i creixement dels cultius neuronals s'han dut a terme en el laboratori de Neurofísica del Dr. Jordi Soriano, en la facultat de Física de la UB. Els cultius neuronals estudiats s'han obtingut a partir de la

dissecció d'embrions de rata, de 17-19 dies de gestació; i s'han cultivat entre una i tres setmanes en el mateix laboratori a on s'ha mesurat la seva activitat.

L'activitat neuronal ha estat mesurada fent servir la tècnica d'imatge per fluorescència de calci ("fluorescence calcium imaging" en anglès). Aquesta tècnica consisteix en introduir dins de les neurones del cultiu unes molècules específiques que emeten fluorescència quan s'acoblen amb Ca^{+2}. Degut a les característiques biològiques de les neurones, un augment del calci intracel·lular es correlaciona directament amb un dispar d'activitat de la neurona. Així, i gràcies a un microscopi equipat amb una làmpada de fluorescència, i amb una càmera d'altra resolució i alta freqüència d'adquisició d'imatges, hem pogut caracteritzar les activacions a nivell de neurona individual.

La investigació s'ha centrat en cinc línies de recerca: l'estudi de correlacions mètriques en cultius neuronals; el desenvolupament d'un model teòric per descriure i predir l'esclat de xarxa; l'anàlisi de la propagació dels fronts d'activitat experimentals sota pertorbacions estructurals de la connectivitat del cultiu; l'estudi de l'efecte de la inhibició en la iniciació i propagació dels esclats *in vitro*; i l'estudi de la resposta experimental dels cultius sota una estimulació elèctrica moderada de baixa freqüència.

En la primera línia de recerca hem reanalitzat els experiments de percolació en cultius duts a terme pel Dr. Jordi Soriano i col·laboradors entre el 2005 i el 2010 a Israel. En aquests experiments es mesura la resposta en activitat dels cultius sota una estimulació elèctrica instantània, i per a diferents nivells de degradació de la connectivitat mitjançant acció farmacològica. En aquesta tesis hem adaptat un model d'Ising de camps aleatoris al context dels cultius neuronals. La solució analítica del model sota l'aproximació de camp mitjà ens ha permès caracteritzar la resposta dels cultius amb precisió, i fins i tot extreure'n una bona estimació de la connectivitat mitjana per neurona, així com predir característiques universals de l'activitat dels cultius. Simulacions completes del model, aplicades en xarxes biològicament realistes, i dutes a terme per el nostre col·laborador Javier G. Orlandi, ens han

permès estudiar l'efecte de les correlacions mètriques en cultius neuronals (correlacions inexistents en el marc de l'aproximació de camp mitjà). Comparant les xarxes mètriques amb la seva corresponent versió amb connectivitat aleatoritzada, i amb la solució analítica de camp mig, hem comprovat que les correlacions mètriques dominen el comportament dinàmic del cultiu, fins al punt d'emmascarar la contribució de la distribució del nombre de connexions.

La segona línia de recerca s'ha dirigit cap a un model analític estadístic de fora d'equilibri per predir la freqüència dels esclats de xarxa. Aquesta freqüència (d'uns 2-3 esclats per minut) està lligada a l'activació espontània de neurones individuals (soroll d'activitat de xarxa) i a la reamplificació d'aquestes activacions esporàdiques mitjançant mecanismes dinàmics i topològics. Tenint en compte les característiques dinàmiques de les neurones individuals, la seva interacció amb les veïnes, i la connectivitat local mitjana entre neurones, hem desenvolupat un model analític que prediu semi quantitativament la freqüència dels esclats en funció de variables microscòpiques. Les prediccions encaixen amb els valors experimentals mesurats, i permeten extreure informació microscòpica altrament inaccessible.

En la línia de recerca centrada en l'efecte de pertorbacions estructurals en la connectivitat, i en la subseqüent activitat dinàmica, hem modificat el substrat dels cultius a partir de motlles topogràfics predissenyats. Aquests motlles, fets a partir del polímer PDMS, es classifiquen en dos grups: motlles tipus esglaó (de diferents altures), i motlles tipus quadrats aleatoris. El primer grup de motlles s'han utilitzat per imposar una connectivitat asimètrica al cultiu neuronal, entre el nivell inferior i el nivell superior de l'esglaó de PDMS. Aquesta asimetria ha donat com a resultat una dinàmica senyor-esclau, a on les neurones en el nivell superior majoritàriament imposaven el seu ritme d'esclat a les del nivell inferior. El segon grup de motlles, de quadrats aleatoris, s'ha fet servir per pertorbar heterogèniament la connectivitat de les xarxes neuronals. En conseqüència, la dinàmica resultant mostra una gran riquesa en

patrons d'activitat, esclats de xarxa a diferents escales, i propagació altament específica de cada cultiu.

En la quarta línia de recerca s'ha estudiat la contribució de la inhibició en l'activitat dels cultius neuronals. Per dur a terme aquest anàlisi, hem gravat l'activitat neuronal dels cultius amb excitació i inhibició (E+I), i l'hem comparat amb l'activitat dels mateixos cultius amb la inhibició bloquejada (sols-E). Hem bloquejat la inhibició aplicant bicuculina, antagonista dels receptors d'inhibició en les sinapsis de les neurones corticals. Els resultats experimentals han mostrat que les xarxes sols-E disminueixen la seva freqüència d'esclat respecte a les E+I, possiblement degut a que les primeres generen esclats molt intensos que exhaureixen els neurotransmissors disponibles, requerint un major temps de recuperació entre esclat i esclat. Per altra banda, la velocitat de propagació incrementa lleugerament quan s'ha bloquejat la inhibició, fet que es deu a una transmissió purament excitadora de l'activitat. I a més a més, els punts on s'inicien els esclats, els quals solen ser bastant específics, varien entre les dues condicions E+I i sols-E.

Finalment, la cinquena línia de recerca s'ha centrat en la resposta experimental dels cultius sota una estimulació elèctrica suau, de forma sinusoïdal i de baixa freqüència. Estudis preliminars van mostrar que una estimulació intensa forçava directament l'esclat del cultiu, degradant-lo ràpidament per culpa d'una major mort cel·lular. Per contra, l'aplicació d'un camp feble dóna com a resultat un augment en les activacions individuals esporàdiques, sense un augment tant significatiu en la mort cel·lular. Aquest augment en el soroll de xarxa dóna com a resultat un augment en la freqüència d'esclat, la qual és susceptible de ser modificada en funció del corrent extern aplicat. Els punts d'iniciació, per altra banda, no mostren canvis importants deguts al camp extern. I per últim, la velocitat de propagació sembla disminuir sota estimulació, possiblement a causa d'una major freqüència d'esclat.

References

L. F. Abbott and S. B. Nelson. Synaptic plasticity: taming the beast. *Nature neuroscience*, 3(11s):1178, 2000.

S. Achard, R. Salvador, B. Whitcher, J. Suckling, and E. Bullmore. A resilient, low-frequency, small-world human brain functional network with highly connected association cortical hubs. *Journal of Neuroscience*, 26(1):63–72, 2006.

D. Achlioptas, R. M. D'souza, and J. Spencer. Explosive percolation in random networks. *Science*, 323(5920):1453–1455, 2009.

M. Adel, M. Zahmatkeshan, B. Johari, S. Kharrazi, M. Mehdizadeh, B. Bolouri, and S. M. Rezayat. Investigating the effects of electrical stimulation via gold nanoparticles on in vitro neurite outgrowth: Perspective to nerve regeneration. *Microelectronic Engineering*, 173:1–5, 2017.

M. B. Ahrens, M. B. Orger, D. N. Robson, J. M. Li, and P. J. Keller. Whole-brain functional imaging at cellular resolution using light-sheet microscopy. *Nature methods*, 10(5):413–420, 2013.

E. Alvarez-Lacalle and E. Moses. Slow and fast pulses in 1-d cultures of excitatory neurons. *Journal of computational neuroscience*, 26(3):475–493, 2009.

N. P. Aryan, H. Kaim, and A. Rothermel. Electrode materials: State-of-the-art and experiments. In *Stimulation and Recording Electrodes for Neural Prostheses*, pages 45–64. Springer, 2015.

M. Barthélemy. Spatial networks. *Physics Reports*, 499(1):1–101, 2011.

I. Baruchi, V. Volman, N. Raichman, M. Shein, and E. Ben-Jacob. The emergence and properties of mutual synchronization in in vitro coupled

cortical networks. *European Journal of Neuroscience*, 28(9):1825–1835, 2008.

D. Battaglia, A. Witt, F. Wolf, and T. Geisel. Dynamic effective connectivity of inter-areal brain circuits. *PLoS computational biology*, 8(3):e1002438, 2012.

G. J. Baxter, S. N. Dorogovtsev, A. V. Goltsev, and J. F. Mendes. Bootstrap percolation on complex networks. *Physical Review E*, 82(1):011103, 2010.

J. M. Beggs and D. Plenz. Neuronal avalanches in neocortical circuits. *The Journal of neuroscience*, 23(35):11167–11177, 2003.

M. J. Berridge, P. Lipp, and M. D. Bootman. The versatility and universality of calcium signalling. *Nature reviews Molecular cell biology*, 1(1):11–21, 2000.

L. M. Bettencourt, G. J. Stephens, M. I. Ham, and G. W. Gross. Functional structure of cortical neuronal networks grown in vitro. *Physical Review E*, 75(2):021915, 2007.

G. Bianconi, P. Pin, and M. Marsili. Assessing the relevance of node features for network structure. *Proceedings of the National Academy of Sciences*, 106(28):11433–11438, 2009.

M. Bikson, M. Inoue, H. Akiyama, J. K. Deans, J. E. Fox, H. Miyakawa, and J. G. Jefferys. Effects of uniform extracellular dc electric fields on excitability in rat hippocampal slices in vitro. *The Journal of physiology*, 557(1):175–190, 2004.

L. Bologna, T. Nieus, M. Tedesco, M. Chiappalone, F. Benfenati, and S. Martinoia. Low-frequency stimulation enhances burst activity in cortical cultures during development. *Neuroscience*, 165(3):692–704, 2010.

S. Borchers, M. Himmelbach, N. Logothetis, and H.-O. Karnath. Direct electrical stimulation of human cortex—the gold standard for mapping brain functions? *Nature Reviews Neuroscience*, 13(1):63–70, 2012.

I. Breskin, J. Soriano, E. Moses, and T. Tlusty. Percolation in living neural networks. *Physical review letters*, 97(18):188102, 2006.

D. Brockmann and D. Helbing. The hidden geometry of complex, network-driven contagion phenomena. *Science*, 342(6164):1337–1342, 2013.

S. Brummer, L. Robblee, and F. Hambrecht. Criteria for selecting electrodes for electrical stimulation: theoretical and practical considerations. *Annals of the New York Academy of Sciences*, 405(1):159–171, 1983.

N. Brunel, V. Hakim, and M. J. Richardson. Single neuron dynamics and computation. *Current opinion in neurobiology*, 25:149–155, 2014.

E. Bullmore and O. Sporns. The economy of brain network organization. *Nature reviews. Neuroscience*, 13(5):336, 2012.

R. Burioni, M. Casartelli, M. Di Volo, R. Livi, and A. Vezzani. Average synaptic activity and neural networks topology: a global inverse problem. *Scientific reports*, 4, 2014.

G. Buzsáki and A. Draguhn. Neuronal oscillations in cortical networks. *science*, 304(5679):1926–1929, 2004.

D. J. Cahalane, B. Clancy, M. A. Kingsbury, E. Graf, O. Sporns, and B. L. Finlay. Network structure implied by initial axon outgrowth in rodent cortex: Empirical measurement and models. *PLOS ONE*, 6(1):1–16, 01 2011.

C. Carmeli, P. Bonifazi, H. P. Robinson, and M. Small. Quantifying network properties in multi-electrode recordings: spatiotemporal characterization and inter-trial variation of evoked gamma oscillations in mouse somatosensory cortex in vitro. *Frontiers in computational neuroscience*, 7, 2013.

L. Carrillo-Reid, F. Tecuapetla, D. Tapia, A. Hernández-Cruz, E. Galarraga, R. Drucker-Colin, and J. Bargas. Encoding network states by striatal cell assemblies. *Journal of neurophysiology*, 99(3):1435–1450, 2008.

Z. C. Chao, D. J. Bakkum, and S. M. Potter. Region-specific network plasticity in simulated and living cortical networks: comparison of the center of activity trajectory (cat) with other statistics. *Journal of Neural Engineering*, 4(3):294, 2007.

B. L. Chen, D. H. Hall, and D. B. Chklovskii. Wiring optimization can relate neuronal structure and function. *Proceedings of the National Academy of Sciences of the United States of America*, 103(12):4723–4728, 2006.

Y. Chen, B. Stevens, J. Chang, J. Milbrandt, B. A. Barres, and J. W. Hell. Ns21: re-defined and modified supplement b27 for neuronal cultures. *Journal of neuroscience methods*, 171(2):239–247, 2008.

Y. Chen, S. Wang, C. C. Hilgetag, and C. Zhou. Trade-off between multiple constraints enables simultaneous formation of modules and hubs in neural systems. *PLoS computational biology*, 9(3):e1002937, 2013.

D. B. Chklovskii, T. Schikorski, and C. F. Stevens. Wiring optimization in cortical circuits. *Neuron*, 34(3):341–347, 2002.

D. W. Choi, M. Maulucci-Gedde, and A. R. Kriegstein. Glutamate neurotoxicity in cortical cell culture. *The Journal of neuroscience*, 7(2):357–368, 1987.

S. Cocco, S. Leibler, and R. Monasson. Neuronal couplings between retinal ganglion cells inferred by efficient inverse statistical physics methods. *Proceedings of the National Academy of Sciences*, 106(33):14058–14062, 2009.

E. Cohen, M. Ivenshitz, V. Amor-Baroukh, V. Greenberger, and M. Segal. Determinants of spontaneous activity in networks of cultured hippocampus. *Brain research*, 1235:21–30, 2008.

O. Cohen, A. Keselman, E. Moses, M. R. Martínez, J. Soriano, and T. Tlusty. Quorum percolation in living neural networks. *EPL (Europhysics Letters)*, 89(1):18008, 2010.

D. Cordes, V. M. Haughton, K. Arfanakis, G. J. Wendt, P. A. Turski, C. H. Moritz, M. A. Quigley, and M. E. Meyerand. Mapping functionally related regions of brain with functional connectivity mr imaging. *American Journal of Neuroradiology*, 21(9):1636–1644, 2000.

A. Czarnecki, A. Tscherter, and J. Streit. Network activity and spike discharge oscillations in cortical slice cultures from neonatal rat. *European journal of neuroscience*, 35(3):375–388, 2012.

N. R. de Lorente. Studies on the structure of the cerebral cortex,. i: the area entorhinalis. *J Psychol Neurol*, 45:381–438, 1933.

D. de Santos-Sierra, I. Sendiña-Nadal, I. Leyva, J. A. Almendral, S. Anava, A. Ayali, D. Papo, and S. Boccaletti. Emergence of small-world anatomical networks in self-organizing clustered neuronal cultures. *PloS one*, 9(1), 2014.

G. Deco and V. K. Jirsa. Ongoing cortical activity at rest: criticality, multistability, and ghost attractors. *Journal of Neuroscience*, 32(10):3366–3375, 2012.

G. Deco, V. K. Jirsa, and A. R. McIntosh. Emerging concepts for the dynamical organization of resting-state activity in the brain. *Nature Reviews Neuroscience*, 12(1):43–56, 2011.

J. DeFelipe, H. Markram, and K. S. Rockland. The neocortical column. *Frontiers in neuroanatomy*, 6, 2012.

D. Dhar, P. Shukla, and J. P. Sethna. Zero-temperature hysteresis in the random-field ising model on a bethe lattice. *Journal of Physics A: Mathematical and General*, 30(15):5259, 1997.

M. A. Dichter. Rat cortical neurons in cell culture: culture methods, cell morphology, electrophysiology, and synapse formation. *Brain research*, 149(2):279–293, 1978.

S. N. Dorogovtsev, A. V. Goltsev, and J. F. F. Mendes. Ising model on networks with an arbitrary distribution of connections. *Physical Review E*, 66(1):016104, 2002.

S. N. Dorogovtsev, A. V. Goltsev, and J. F. Mendes. Critical phenomena in complex networks. *Reviews of Modern Physics*, 80(4):1275, 2008.

J. H. Downes, M. W. Hammond, D. Xydas, M. C. Spencer, V. M. Becerra, K. Warwick, B. J. Whalley, and S. J. Nasuto. Emergence of a small-world functional network in cultured neurons. *PLoS Comput. Biol*, 8(5):e1002522, 2012.

J.-P. Eckmann, O. Feinerman, L. Gruendlinger, E. Moses, J. Soriano, and T. Tlusty. The physics of living neural networks. *Physics Reports*, 449(1): 54–76, 2007.

J.-P. Eckmann, S. Jacobi, S. Marom, E. Moses, and C. Zbinden. Leader neurons in population bursts of 2d living neural networks. *New Journal of Physics*, 10(1):015011, 2008.

J.-P. Eckmann, E. Moses, O. Stetter, T. Tlusty, and C. Zbinden. Leaders of neuronal cultures in a quorum percolation model. *Frontiers in computational neuroscience*, 4, 2010.

V. M. Eguiluz, D. R. Chialvo, G. A. Cecchi, M. Baliki, and A. V. Apkarian. Scale-free brain functional networks. *Physical review letters*, 94(1):018102, 2005.

D. Eytan and S. Marom. Dynamics and effective topology underlying synchronization in networks of cortical neurons. *Journal of Neuroscience*, 26 (33):8465–8476, 2006.

O. Feinerman and E. Moses. A picoliter 'fountain-pen'using co-axial dual pipettes. *Journal of neuroscience methods*, 127(1):75–84, 2003.

O. Feinerman, M. Segal, and E. Moses. Signal propagation along unidimensional neuronal networks. *Journal of neurophysiology*, 94(5):3406–3416, 2005.

O. Feinerman, M. Segal, and E. Moses. Identification and dynamics of spontaneous burst initiation zones in unidimensional neuronal cultures. *Journal of neurophysiology*, 97(4):2937–2948, 2007.

M. D. Fox and M. E. Raichle. Spontaneous fluctuations in brain activity observed with functional magnetic resonance imaging. *Nature Reviews Neuroscience*, 8(9):700–711, 2007.

M. Frega, V. Pasquale, M. Tedesco, M. Marcoli, A. Contestabile, M. Nanni, L. Bonzano, G. Maura, and M. Chiappalone. Cortical cultures coupled to micro-electrode arrays: a novel approach to perform in vitro excitotoxicity testing. *Neurotoxicology and teratology*, 34(1):116–127, 2012.

K. J. Friston. Functional and effective connectivity: a review. *Brain connectivity*, 1(1):13–36, 2011.

T. Gabay, E. Jakobs, E. Ben-Jacob, and Y. Hanein. Engineered self-organization of neural networks using carbon nanotube clusters. *Physica A: Statistical Mechanics and its Applications*, 350(2-4):611–621, 2005.

K. Ganguly, A. F. Schinder, S. T. Wong, and M.-m. Poo. Gaba itself promotes the developmental switch of neuronal gabaergic responses from excitation to inhibition. *Cell*, 105:521–532, 2001.

M. Garofalo, T. Nieus, P. Massobrio, and S. Martinoia. Evaluation of the performance of information theory-based methods and cross-correlation to estimate the functional connectivity in cortical networks. *PloS one*, 4(8): e6482, 2009.

K. R. Gee, K. Brown, W. U. Chen, J. Bishop-Stewart, D. Gray, and I. Johnson. Chemical and physiological characterization of fluo-4 ca 2+-indicator dyes. *Cell calcium*, 27(2):97–106, 2000.

A.-K. Gellner, J. Reis, and B. Fritsch. Glia: a neglected player in non-invasive direct current brain stimulation. *Frontiers in cellular neuroscience*, 10, 2016.

W. Gobel and F. Helmchen. In vivo calcium imaging of neural network function. *Physiology*, 22(6):358–365, 2007.

A. Goltsev, F. De Abreu, S. Dorogovtsev, and J. Mendes. Stochastic cellular automata model of neural networks. *Physical Review E*, 81(6):061921, 2010.

A. V. Goltsev, S. N. Dorogovtsev, and J. F. F. Mendes. k-core (bootstrap) percolation on complex networks: Critical phenomena and nonlocal effects. *Physical Review E*, 73(5):056101, 2006.

A. V. Goltsev, S. N. Dorogovtsev, and J. Mendes. Percolation on correlated networks. *Physical Review E*, 78(5):051105, 2008.

C. Grienberger and A. Konnerth. Imaging calcium in neurons. *Neuron*, 73(5): 862–885, 2012.

A. Habets, A. Van Dongen, F. Van Huizen, and M. Corner. Spontaneous neuronal firing patterns in fetal rat cortical networks during development in vitro: a quantitative analysis. *Experimental brain research*, 69(1):43–52, 1987.

P. Hagmann, L. Cammoun, X. Gigandet, R. Meuli, C. J. Honey, V. J. Wedeen, and O. Sporns. Mapping the structural core of human cerebral cortex. *PLoS Biol*, 6(7):e159, 07 2008.

M. I. Ham, L. M. Bettencourt, F. D. McDaniel, and G. W. Gross. Spontaneous coordinated activity in cultured networks: analysis of multiple ignition sites, primary circuits, and burst phase delay distributions. *Journal of computational neuroscience*, 24(3):346–357, 2008.

F. Hamilton, A. Akhavian, G. Knaack, H. Charkhkar, S. Minnikanti, W.-J. Kim, J. Kastee, and N. Peixoto. Dynamic steering of in vitro cortical neurons using field stimulation. In *Engineering in Medicine and Biology Society (EMBC), 2014 36th Annual International Conference of the IEEE*, pages 6577–6580. IEEE, 2014.

R. E. Harris, M. G. Coulombe, and M. B. Feller. Dissociated retinal neurons form periodically active synaptic circuits. *Journal of neurophysiology*, 88 (1):188–195, 2002.

S. Herculano-Houzel. The human brain in numbers: a linearly scaled-up primate brain. *Frontiers in human neuroscience*, 3, 2009.

L. Hernández-Navarro, J. G. Orlandi, B. Cerruti, E. Vives, and J. Soriano. Dominance of metric correlations in two-dimensional neuronal cultures described through a random field ising model. *Physical review letters*, 118 (20):208101, 2017.

A. Hierlemann, U. Frey, S. Hafizovic, and F. Heer. Growing cells atop microelectronic chips: interfacing electrogenic cells in vitro with cmos-based microelectrode arrays. *Proceedings of the IEEE*, 99(2):252–284, 2011.

C.-C. Hilgetag, M. A. O'Neill, and M. P. Young. Hierarchical organization of macaque and cat cortical sensory systems explored with a novel network processor. *Philosophical Transactions of the Royal Society of London B: Biological Sciences*, 355(1393):71–89, 2000.

C. J. Honey, R. Kötter, M. Breakspear, and O. Sporns. Network structure of cerebral cortex shapes functional connectivity on multiple time scales. *Proceedings of the National Academy of Sciences*, 104(24):10240–10245, 2007.

J. J. Hopfield. Neural networks and physical systems with emergent collective computational abilities. *Proceedings of the national academy of sciences*, 79(8):2554–2558, 1982.

S. Horvát, R. Gămănuț, M. Ercsey-Ravasz, L. Magrou, B. Gămănuț, D. C. Van Essen, A. Burkhalter, K. Knoblauch, Z. Toroczkai, and H. Kennedy. Spatial embedding and wiring cost constrain the functional layout of the cortical network of rodents and primates. *PLoS biology*, 14(7):e1002512, 2016.

M. Hronik-Tupaj, W. K. Raja, M. Tang-Schomer, F. G. Omenetto, and D. L. Kaplan. Neural responses to electrical stimulation on patterned silk films. *Journal of biomedical materials research Part A*, 101(9):2559–2572, 2013.

Y. Huang and L. Mucke. Alzheimer mechanisms and therapeutic strategies. *Cell*, 148(6):1204–1222, 2012.

D. H. Hubel and T. N. Wiesel. Receptive fields and functional architecture of monkey striate cortex. *The Journal of physiology*, 195(1):215–243, 1968.

M. S. Humayun, E. de Juan Jr, J. D. Weiland, G. Dagnelie, S. Katona, R. Greenberg, and S. Suzuki. Pattern electrical stimulation of the human retina. *Vision research*, 39(15):2569–2576, 1999.

Y. Ikegaya, G. Aaron, R. Cossart, D. Aronov, I. Lampl, D. Ferster, and R. Yuste. Synfire chains and cortical songs: temporal modules of cortical activity. *Science*, 304(5670):559–564, 2004.

X. Illa, P. Shukla, and E. Vives. Zero-temperature hysteresis in a random-field ising model on a bethe lattice: Approach to mean-field behavior with increasing coordination number z. *Physical Review B*, 73(9):092414, 2006.

T. R. Insel, S. C. Landis, and F. S. Collins. The nih brain initiative. *Science*, 340(6133):687–688, 2013.

S. Ito, F.-C. Yeh, E. Hiolski, P. Rydygier, D. E. Gunning, P. Hottowy, N. Timme, A. M. Litke, and J. M. Beggs. Large-scale, high-resolution multielectrode-array recording depicts functional network differences of cortical and hippocampal cultures. 2014.

M. Ivenshitz and M. Segal. Neuronal density determines network connectivity and spontaneous activity in cultured hippocampus. *Journal of neurophysiology*, 104(2):1052–1060, 2010.

S. Jacobi, J. Soriano, M. Segal, and E. Moses. Bdnf and nt-3 increase excitatory input connectivity in rat hippocampal cultures. *European Journal of Neuroscience*, 30(6):998–1010, 2009.

H. Kamioka, E. Maeda, Y. Jimbo, H. P. Robinson, and A. Kawana. Spontaneous periodic synchronized bursting during formation of mature patterns of connections in cortical cultures. *Neuroscience letters*, 206(2):109–112, 1996.

T. Knöpfel. Genetically encoded optical indicators for the analysis of neuronal circuits. *Nature Reviews Neuroscience*, 13(10):687–700, 2012.

M. I. Kotlikoff. Genetically encoded ca2+ indicators: using genetics and molecular design to understand complex physiology. *The Journal of physiology*, 578(1):55–67, 2007.

A. R. Kriegstein and M. A. Dichter. Morphological classification of rat cortical neurons in cell culture. *Journal of Neuroscience*, 3(8):1634–1647, 1983.

K.-E. Lee, M. Lopes, J. Mendes, and A. Goltsev. Critical phenomena and noise-induced phase transitions in neuronal networks. *Physical Review E*, 89(1):012701, 2014.

R. T. Leung, M. N. Shivdasani, D. A. Nayagam, and R. K. Shepherd. In vivo and in vitro comparison of the charge injection capacity of platinum macroelectrodes. *IEEE Transactions on Biomedical Engineering*, 62(3): 849–857, 2015.

M. S. Lewicki. A review of methods for spike sorting: the detection and classification of neural action potentials. *Network: Computation in Neural Systems*, 9(4):R53–R78, 1998.

P. M. Lewis and J. V. Rosenfeld. Electrical stimulation of the brain and the development of cortical visual prostheses: an historical perspective. *Brain research*, 1630:208–224, 2016.

D. Li, G. Li, K. Kosmidis, H. Stanley, A. Bunde, and S. Havlin. Percolation of spatially constraint networks. *EPL (Europhysics Letters)*, 93(6):68004, 2011.

M. Lichtenstein, E. Pérez, L. Ballesteros, C. Suñol, and N. Casañ-Pastor. Short-term electrostimulation enhancing neural repair in vitro using large charge capacity nanostructured electrodes. *Applied Materials Today*, 6: 29–43, 2017.

D. Lonardoni, H. Amin, S. Di Marco, A. Maccione, L. Berdondini, and T. Nieus. Recurrently connected and localized neuronal communities initiate coordinated spontaneous activity in neuronal networks. *PLoS computational biology*, 13(7):e1005672, 2017.

A. R. Luria. *Higher cortical functions in man*. Springer Science & Business Media, 2012.

H. Lütcke, F. Gerhard, F. Zenke, W. Gerstner, and F. Helmchen. Inference of neuronal network spike dynamics and topology from calcium imaging data. *Frontiers in neural circuits*, 7:201, 2013.

A. Maccione, M. Garofalo, T. Nieus, M. Tedesco, L. Berdondini, and S. Martinoia. Multiscale functional connectivity estimation on low-density neuronal cultures recorded by high-density cmos micro electrode arrays. *Journal of neuroscience methods*, 207(2):161–171, 2012.

E. Macis, M. Tedesco, P. Massobrio, R. Raiteri, and S. Martinoia. An automated microdrop delivery system for neuronal network patterning on microelectrode arrays. *Journal of Neuroscience Methods*, 161(1):88–95, 2007.

R. Madhavan, Z. C. Chao, D. Wagenaar, D. J. Bakkum, S. M. Potter, et al. Multi-site stimulation quiets network-wide spontaneous bursts and enhances functional plasticity in cultured cortical networks. In *Engineering in Medicine and Biology Society, 2006. EMBS'06. 28th Annual International Conference of the IEEE*, pages 1593–1596. IEEE, 2006.

R. Madhavan, Z. C. Chao, and S. M. Potter. Plasticity of recurring spatiotemporal activity patterns in cortical networks. *Physical biology*, 4(3):181, 2007.

E. Maeda, H. Robinson, and A. Kawana. The mechanisms of generation and propagation of synchronized bursting in developing networks of cortical neurons. *The Journal of neuroscience*, 15(10):6834–6845, 1995.

H. Markram. The blue brain project. *Nature Reviews Neuroscience*, 7(2): 153–160, 2006.

H. Markram. The human brain project. *Scientific American*, 306(6):50–55, 2012.

S. Marom and G. Shahaf. Development, learning and memory in large random networks of cortical neurons: lessons beyond anatomy. *Quarterly reviews of biophysics*, 35(1):63–87, 2002.

R. Matsumoto, T. Kunieda, and D. Nair. Single pulse electrical stimulation to probe functional and pathological connectivity in epilepsy. *Seizure*, 44: 27–36, 2017.

A. Mazzoni, F. D. Broccard, E. Garcia-Perez, P. Bonifazi, M. E. Ruaro, and V. Torre. On the dynamics of the spontaneous activity in neuronal networks. *PloS one*, 2(5):e439, 2007.

D. Meunier, R. Lambiotte, and E. T. Bullmore. Modular and hierarchically modular organization of brain networks. *Frontiers in neuroscience*, 4, 2010.

H. Monai, M. Ohkura, M. Tanaka, Y. Oe, A. Konno, H. Hirai, K. Mikoshiba, S. Itohara, J. Nakai, Y. Iwai, et al. Calcium imaging reveals glial involvement in transcranial direct current stimulation-induced plasticity in mouse brain. *Nature communications*, 7, 2016.

V. Mountcastle. An organizing principle for cerebral function: the unit module and the distributed system. *The mindful brain*, 1978.

V. B. Mountcastle. *Perceptual neuroscience: the cerebral cortex*. Harvard University Press, 1998.

T. H. Murphy, L. A. Blatter, W. G. Wier, and J. Baraban. Spontaneous synchronous synaptic calcium transients in cultured cortical neurons. *Journal of Neuroscience*, 12(12):4834–4845, 1992.

J. Nagler, A. Levina, and M. Timme. Impact of single links in competitive percolation–how complex networks grow under competition. *arXiv preprint arXiv:1103.0922*, 2011.

A. Ogura, T. Iijima, T. Amano, and Y. Kudo. Optical monitoring of excitatory synaptic activity between cultured hippocampal neurons by a multi-site ca2+ fluorometry. *Neuroscience letters*, 78(1):69–74, 1987.

S. Okujeni, S. Kandler, and U. Egert. Mesoscale architecture shapes initiation and richness of spontaneous network activity. *Journal of Neuroscience*, 37 (14):3972–3987, 2017.

T. Opitz, A. D. De Lima, and T. Voigt. Spontaneous development of synchronous oscillatory activity during maturation of cortical networks in vitro. *Journal of neurophysiology*, 88(5):2196–2206, 2002.

J. G. Orlandi, J. Soriano, E. Alvarez-Lacalle, S. Teller, and J. Casademunt. Noise focusing and the emergence of coherent activity in neuronal cultures. *Nature Physics*, 9(9):582–590, 2013.

J. G. Orlandi, O. Stetter, J. Soriano, T. Geisel, and D. Battaglia. Transfer entropy reconstruction and labeling of neuronal connections from simulated calcium imaging. *PloS one*, 9(6):e98842, 2014.

R. E. Ornstein and R. F. Thompson. *The amazing brain*. Houghton Mifflin Harcourt, 1991.

Y. Otsu and T. H. Murphy. Miniature transmitter release: accident of nature or careful design? *Sci. STKE*, 2003(211):pe54–pe54, 2003.

D. B. Owen. A table of normal integrals. *Communications in Statistics - Simulation and Computation*, 9(4):389–419, 1980.

B. Pakkenberg, D. Pelvig, L. Marner, M. J. Bundgaard, H. J. G. Gundersen, J. R. Nyengaard, and L. Regeur. Aging and the human neocortex. *Experimental gerontology*, 38(1):95–99, 2003.

R. M. Paredes, J. C. Etzler, L. T. Watts, W. Zheng, and J. D. Lechleiter. Chemical calcium indicators. *Methods*, 46(3):143–151, 2008.

V. Pasquale, P. Massobrio, L. Bologna, M. Chiappalone, and S. Martinoia. Self-organization and neuronal avalanches in networks of dissociated cortical neurons. *Neuroscience*, 153(4):1354–1369, 2008.

L. K. Paul, W. S. Brown, R. Adolphs, J. M. Tyszka, L. J. Richards, P. Mukherjee, and E. H. Sherr. Agenesis of the corpus callosum: genetic, developmental and functional aspects of connectivity. *Nature Reviews Neuroscience*, 8 (4):287, 2007.

J. Pu, H. Gong, X. Li, and Q. Luo. Developing neuronal networks: Self-organized criticality predicts the future. *Scientific reports*, 3, 2013.

N. Raichman and E. Ben-Jacob. Identifying repeating motifs in the activation of synchronized bursts in cultured neuronal networks. *Journal of neuroscience methods*, 170(1):96–110, 2008.

H. Robinson, M. Kawahara, Y. Jimbo, K. Torimitsu, Y. Kuroda, and A. Kawana. Periodic synchronized bursting and intracellular calcium transients elicited by low magnesium in cultured cortical neurons. *Journal of neurophysiology*, 70(4):1606–1616, 1993.

N. L. Rochefort, H. Jia, and A. Konnerth. Calcium imaging in the living brain: prospects for molecular medicine. *Trends in molecular medicine*, 14 (9):389–399, 2008.

A. Rotem and E. Moses. Magnetic stimulation of one-dimensional neuronal cultures. *Biophysical Journal*, 94(12):5065–5078, 2008.

Y. Roudi, J. Tyrcha, and J. Hertz. Ising model for neural data: model quality and approximate methods for extracting functional connectivity. *Physical Review E*, 79(5):051915, 2009.

V. Sakkalis. Review of advanced techniques for the estimation of brain connectivity measured with eeg/meg. *Computers in biology and medicine*, 41(12):1110–1117, 2011.

F. Salvat-Pujol, E. Vives, and M.-L. Rosinberg. Hysteresis in the t= 0 random-field ising model: Beyond metastable dynamics. *Physical Review E*, 79(6): 061116, 2009.

M. T. Schaub and S. R. Schultz. The ising decoder: reading out the activity of large neural ensembles. *Journal of computational neuroscience*, 32(1): 101–118, 2012.

C. Schmeltzer, J. Soriano, I. M. Sokolov, and S. Rüdiger. Percolation of spatially constrained erdös-rényi networks with degree correlations. *Phys. Rev. E*, 89:012116, Jan 2014.

E. Schneidman, M. J. Berry, R. S. II, and W. Bialek. Weak pairwise correlations imply strongly correlated network states in a neural population. *Nature*, 440(7087):1007, 2006.

R. Segev, M. Benveniste, Y. Shapira, and E. Ben-Jacob. Formation of electrically active clusterized neural networks. *Physical review letters*, 90(16): 168101, 2003.

R. Segev, I. Baruchi, E. Hulata, and E. Ben-Jacob. Hidden neuronal correlations in cultured networks. *Physical Review Letters*, 92(11):118102, 2004.

M. Serra, M. Guaraldi, and T. B. Shea. Inhibitory neurons modulate spontaneous signaling in cultured cortical neurons: density-dependent regulation of excitatory neuronal signaling. *Physical biology*, 7(2):026009, 2010.

J. P. Sethna, K. Dahmen, S. Kartha, J. A. Krumhansl, B. W. Roberts, and J. D. Shore. Hysteresis and hierarchies: Dynamics of disorder-driven first-order phase transformations. *Physical Review Letters*, 70(21):3347, 1993.

O. Shefi, I. Golding, R. Segev, E. Ben-Jacob, and A. Ayali. Morphological characterization of in vitro neuronal networks. *Physical Review E*, 66(2): 021905, 2002.

M. Shein Idelson, E. Ben-Jacob, and Y. Hanein. Innate synchronous oscillations in freely-organized small neuronal circuits. *PLoS ONE*, 5(12):e14443, 12 2010. doi: 10.1371/journal.pone.0014443.

D. Smetters, A. Majewska, and R. Yuste. Detecting action potentials in neuronal populations with calcium imaging. *Methods*, 18(2):215–221, 1999.

S. Sommakia, S. Wyatt, K. Otto, A. Vadlamani, and A. L. Garner. Nanosecond pulsed electric field interactions with microglia and astrocytes. In *Power Modulator and High Voltage Conference (IPMHVC), 2014 IEEE International*, pages 405–407. IEEE, 2014.

J. Soriano, M. R. Martínez, T. Tlusty, and E. Moses. Development of input connections in neural cultures. *Proceedings of the National Academy of Sciences*, 105(37):13758–13763, 2008.

R. Sorkin, T. Gabay, P. Blinder, D. Baranes, E. Ben-Jacob, and Y. Hanein. Compact self-wiring in cultured neural networks. *J Neural Eng*, 3(2): 95–101, 2006.

O. Sporns. Network attributes for segregation and integration in the human brain. *Current opinion in neurobiology*, 23(2):162–171, 2013.

O. Sporns and J. D. Zwi. The small world of the cerebral cortex. *Neuroinformatics*, 2(2):145–162, 2004.

C. J. Stam. Modern network science of neurological disorders. *Nature Reviews Neuroscience*, 15(10):683–695, 2014.

O. Stetter, D. Battaglia, J. Soriano, and T. Geisel. Model-free reconstruction of excitatory neuronal connectivity from calcium imaging signals. *PLoS computational biology*, 8(8):e1002653, 2012.

J. Streit, A. Tscherter, M. O. Heuschkel, and P. Renaud. The generation of rhythmic activity in dissociated cultures of rat spinal cord. *European journal of neuroscience*, 14(2):191–202, 2001.

J.-J. Sun, W. Kilb, and H. J. Luhmann. Self-organization of repetitive spike patterns in developing neuronal networks in vitro. *European Journal of Neuroscience*, 32(8):1289–1299, 2010.

S. Teller, C. Granell, M. De Domenico, J. Soriano, S. Gómez, and A. Arenas. Emergence of assortative mixing between clusters of cultured neurons. *PLoS computational biology*, 10(9):e1003796, 2014.

S. Teller, I. B. Tahirbegi, M. Mir, J. Samitier, and J. Soriano. Magnetite-amyloid-β deteriorates activity and functional organization in an in vitro model for alzheimer's disease. *Scientific reports*, 5, 2015.

C. Tetzlaff, S. Okujeni, U. Egert, F. Wörgötter, and M. Butz. Self-organized criticality in developing neuronal networks. *PLoS computational biology*, 6(12):e1001013, 2010.

E. Tibau, C. Bendiksen, S. Teller, N. Amigo, and J. Soriano. Interplay activity-connectivity: dynamics in patterned neuronal cultures. In *Physics, computation, and the mind-advances and challenges at interfaces: Proceedings of the 12th Granada seminar on computational and statistical physics*, volume 1510, pages 54–63. AIP Publishing, 2013a.

E. Tibau, M. Valencia, and J. Soriano. Identification of neuronal network properties from the spectral analysis of calcium imaging signals in neuronal cultures. *Frontiers in neural circuits*, 7, 2013b.

G. Tkacik, E. Schneidman, I. Berry, J. Michael, and W. Bialek. Spin glass models for a network of real neurons. *arXiv preprint arXiv:0912.5409*, 2009.

T. Tlusty and J.-P. Eckmann. Remarks on bootstrap percolation in metric networks. *Journal of Physics A: Mathematical and Theoretical*, 42(20): 205004, 2009.

G. Tononi, O. Sporns, and G. M. Edelman. A measure for brain complexity: relating functional segregation and integration in the nervous system. *Proceedings of the National Academy of Sciences*, 91(11):5033–5037, 1994.

G. Tononi, G. M. Edelman, and O. Sporns. Complexity and coherency: integrating information in the brain. *Trends in cognitive sciences*, 2(12): 474–484, 1998.

C.-Y. Tsai and M.-C. Chang. Robustness and variability of pathways in the spontaneous synchronous bursting of clusterized cortical neuronal networks in vitro. *Journal of the Physical Society of Japan*, 77(8):084803, 2008.

G. G. Turrigiano and S. B. Nelson. Homeostatic plasticity in the developing nervous system. *Nature Reviews Neuroscience*, 5(2):97–107, 2004.

M. P. Van Den Heuvel and H. E. H. Pol. Exploring the brain network: a review on resting-state fmri functional connectivity. *European neuropsychopharmacology*, 20(8):519–534, 2010.

J. Van Pelt, M. Corner, P. Wolters, W. Rutten, and G. Ramakers. Longterm stability and developmental changes in spontaneous network burst firing

patterns in dissociated rat cerebral cortex cell cultures on multielectrode arrays. *Neuroscience letters*, 361(1):86–89, 2004.

L. R. Varshney, B. L. Chen, E. Paniagua, D. H. Hall, and D. B. Chklovskii. Structural properties of the caenorhabditis elegans neuronal network. *PLoS computational biology*, 7(2):e1001066, 2011.

R. Vergara, C. Rick, S. Hernández-López, J. Laville, J. Guzman, E. Galarraga, D. Surmeier, and J. Bargas. Spontaneous voltage oscillations in striatal projection neurons in a rat corticostriatal slice. *The Journal of physiology*, 553(1):169–182, 2003.

J. Von Neumann. *The computer and the brain*. Yale University Press, 2012.

D. A. Wagenaar, J. Pine, and S. M. Potter. An extremely rich repertoire of bursting patterns during the development of cortical cultures. *BMC Neurosci.*, 7:11, 2006.

P. Walicke, W. Cowan, N. Ueno, A. Baird, and R. Guillemin. Fibroblast growth factor promotes survival of dissociated hippocampal neurons and enhances neurite extension. *Proceedings of the National Academy of Sciences*, 83(9):3012–3016, 1986.

D. J. Watts et al. Dj watts and sh strogatz, nature (london) 393, 440 (1998). *Nature (London)*, 393:440, 1998.

B. Wheeler and G. Brewer. Designing neural networks in culture. *Proceedings of the IEEE*, 98(3):398–406, 2010.

J. G. White, E. Southgate, J. N. Thomson, and S. Brenner. The structure of the nervous system of the nematode caenorhabditis elegans. *Philos Trans R Soc Lond B Biol Sci*, 314(1165):1–340, 1986.

J. K. Wrosch, V. Von Einem, K. Breininger, M. Dahlmanns, A. Maier, J. Kornhuber, and T. W. Groemer. Rewiring of neuronal networks during synaptic silencing. *Scientific reports*, 7(1):11724, 2017.

K. A. Yamada, J. M. Dubinsky, and S. M. Rothman. Quantitative physiological characterization of a quinoxalinedione non-nmda receptor antagonist. *Journal of Neuroscience*, 9(9):3230–3236, 1989.

R. Yuste. From the neuron doctrine to neural networks. *Nature Reviews Neuroscience*, 16(8):487–497, 2015.

C. Yvon, R. Rubli, and J. Streit. Patterns of spontaneous activity in unstructured and minimally structured spinal networks in culture. *Experimental brain research*, 165(2):139–151, 2005.